



UNIVERSITY OF LEEDS

Timothy James Brown

**Intramolecular Force Mapping at Room
Temperature using Non-Contact Atomic
Force Microscopy**

**Submitted in accordance with the requirements for the
degree of**

Doctor of Philosophy of Physics

To the

University of Leeds

School of Physics and Astronomy

Supervisors

Dr. Adam Sweetman & Dr. Kevin Critchley

Leeds, March 2023

This document is set in Palatino, compiled with [pdfL^AT_EX2_ε](#) and [Biber](#).

The L^AT_EX template from Karl Voit is based on [KOMA script](#) and can be found online: <https://github.com/novoid/LaTeX-KOMA-template>

Intellectual Property and Publication Statement

I declare that the work submitted is my own, except where work was contributed, including that for a jointly-authored publication (detailed in Chapter 4, 10.1021/acsnano.2c09463). While the main body of thesis text acknowledges these instances, they are also explicitly stated below.

Phil Blowey wrote the Python code needed for force inversion of $\Delta f(z)$ data into $F(z)$, introduced in Chapter 1 (Equations 1.23, 1.24, and used throughout Chapters 3, 4, & 5 (whereby Chapter 4 encompasses the jointly-authored publication mentioned above, of which Phil Blowey was a co-author).

Jack Henry provided density function theory data 4.4.1, in addition to the simulated force matrix acquired via the Probe Particle Model 4.4.2 needed for the jointly-authored publication mentioned above, of which Jack Henry is a co-author, written up in Chapter 4.

Adam Sweetman provided experimental images of FePc molecules on a Ag(111) surface used during the discussion in Figure 5.20.

Instances of figures taken from published sources are indicated by the figure captions.

All other experimental data were gathered by myself and similarly all other Python code was written by myself.

Acknowledgements

I am deeply indebted to my supervisor, Adam Sweetman, I could not have written this thesis were it not for his guidance and patience throughout the project. Additionally, this endeavour would not have been possible without the support from the Royal Society, who financed my research.

I would also like to extend sincerest thanks to my dad, for the immense help in editing and providing moral support.

And lastly thank you to Will Menaker, Matt Christman and Felix Biederman for indirect moral support and counsel.

Abstract

Scanning Probe Microscopy (SPM) methods allow for investigations on the molecular and atomistic scale in real space. While Scanning Tunneling Microscopy (STM) images the electronic structure of a molecular sample, its chemical structure can be resolved, and precise conformation can be determined, by Non-Contact Atomic Force Microscopy (NC-AFM). Acquisition of dense, three-dimensional (3D) force fields with intramolecular resolution via NC-AFM has yielded enormous progress in characterizing molecular and two-dimensional materials at the atomic scale.

To date, intramolecular force mapping has been performed exclusively at cryogenic temperatures, due to the stability afforded by low temperature operation, and as the carbon monoxide functionalization of the metallic scanning probe tip, normally required for submolecular resolution, is only stable at low temperature. An additional technical difficulty of operating a STM with atomic precision at room temperature, is the relative positional drift between the tip and sample.

In this thesis, the experimental apparatus and development of the thermal drift correction methodology needed to gather high-resolution 3D force maps at room temperature are described. The physical limitations of room temperature operation are overcome using semiconducting materials to inhibit molecular diffusion and to create robust tip apexes, while the challenge due to thermal drift is overcome with atom tracking based feedforward correction. The results chapters present 3D force maps comparable in spatial and force resolution to those acquired at low temperature, permitting a quantitative analysis of the adsorption induced changes in the geometry of the molecule at the picometer level. The capability of intramolecular force mapping is widened to larger area maps, of multiple molecules for a variety of systems, demonstrating the versatility and flexibility of the drift correction procedure.

Contents

| | |
|---|-----------|
| Abstract | vi |
| 1 Scanning Probe Microscopy Techniques: Background Theory | 1 |
| 1.1 Scanning Tunneling Microscopy | 2 |
| 1.1.1 Quantum Tunneling | 2 |
| 1.1.2 Development of STM | 6 |
| 1.1.3 Scanning Tunneling Spectroscopy | 12 |
| 1.2 Atomic Force Microscopy | 15 |
| 1.2.1 Deflection Sensors | 16 |
| 1.2.2 Tip-Sample Interactions | 17 |
| 1.2.3 Non-contact Atomic Force Microscopy | 19 |
| 1.2.4 qPlus and Needle Sensors | 30 |
| 1.2.5 Force Mapping | 35 |
| References | 36 |
| 2 Experimental Methods | 43 |
| 2.1 Equipment: Omicron VT-STM/NC-AFM | 43 |
| 2.1.1 Sample Preparation | 45 |
| 2.1.2 Molecular Deposition Source | 46 |
| 2.2 STM tip preparation | 47 |
| 2.2.1 Electrochemical Etching | 47 |
| 2.2.2 Focused Ion Beam | 50 |
| 2.2.3 Results: Tip Characterisation | 51 |
| 2.3 Operation of Microscope | 55 |
| 2.4 Feedforward Correction | 56 |
| 2.4.1 Tracking Mechanism | 57 |
| 2.4.2 Lock-in Amplification | 60 |
| 2.4.3 Incorporating Atom Tracking with Data Acquisition | 64 |
| 2.4.4 Piezo Creep | 66 |

| | |
|---|------------|
| References | 66 |
| 3 Development of Experimental Atom Tracking and 3D Spectroscopy Techniques | 69 |
| 3.1 LabVIEW Scripting | 69 |
| 3.1.1 Initial Conditions for Scripted Data Acquisition | 69 |
| 3.1.2 Drift Correction Procedure | 70 |
| 3.1.3 Gathering Constant Height Data in SPM | 73 |
| 3.1.4 LabVIEW Interface | 75 |
| 3.2 Temperature Control | 77 |
| 3.2.1 Results: Temperature Regulation | 79 |
| 3.3 Results: Scripted Data Sets on Si(111)-(7X7) | 81 |
| 3.3.1 Long Term Topographic Measurement | 81 |
| 3.3.2 Constant Height STM Data Sets | 83 |
| 3.3.3 Two-Dimensional Force Mapping in NC-AFM | 85 |
| 3.3.4 Three-Dimensional Force Mapping in NC-AFM | 91 |
| 3.3.5 Method Comparison | 95 |
| 3.4 Data Processing and Force Inversion | 98 |
| References | 101 |
| 4 Intramolecular force mapping at room temperature | 103 |
| 4.1 Force Mapping of Molecules | 103 |
| 4.2 Results: Preliminary Imaging and Force Data of NTCDI | 105 |
| 4.2.1 Adaptive Height Imaging | 105 |
| 4.2.2 Conventional Constant Height Imaging | 110 |
| 4.3 Results: Intramolecular Force Mapping on NTCDI | 111 |
| 4.3.1 2D Force Mapping | 111 |
| 4.3.2 3D Force Mapping | 113 |
| 4.3.3 Adsorption Geometry | 114 |
| 4.3.4 Supporting Data Sets | 117 |
| 4.4 Simulated AFM data | 119 |
| 4.4.1 DFT | 119 |
| 4.4.2 PPM | 120 |
| 4.4.3 Estimating Tip Apex Stiffness | 120 |
| 4.5 Data Processing | 123 |
| 4.5.1 Noise Considerations | 124 |
| 4.5.2 f_0 Drift | 128 |

| | | |
|----------|---|------------|
| 4.5.3 | Tip Asymmetry | 132 |
| 4.5.4 | Estimating Force Resolution | 133 |
| 4.6 | Conclusion | 137 |
| | References | 137 |
| 5 | Force Mapping of Molecular Networks on B:Si(111) – ($\sqrt{3} \times \sqrt{3}$)R30° | 141 |
| 5.1 | Molecular Self-Assembly | 141 |
| 5.1.1 | Substrate Selection | 142 |
| 5.1.2 | B:Si(111) – ($\sqrt{3} \times \sqrt{3}$)R30° Substrate | 143 |
| 5.1.3 | Molecular Self-Assembly on B:Si(111) | 147 |
| 5.2 | Results: NTCDI on B:Si(111) | 147 |
| 5.3 | Results: C ₆₀ on B:Si(111) | 152 |
| 5.3.1 | 3D Force Map Analysis on C ₆₀ | 155 |
| 5.4 | Results: CoPc on B:Si(111) | 162 |
| 5.4.1 | 3D $\Delta f(x, y, z)$ Mapping of CoPc on B:Si(111) | 165 |
| 5.4.2 | Conformation of CoPc Molecules on B:Si(111) | 168 |
| 5.5 | Conclusion | 174 |
| | References | 175 |

List of Figures

| | | |
|------|--|----|
| 1.1 | Particle trapped in one dimensional potential barrier | 2 |
| 1.2 | Quantum tunneling across a tip-sample junction | 5 |
| 1.3 | Scanning tunneling microscope schematic | 7 |
| 1.4 | Atomic resolution in STM | 8 |
| 1.5 | Piezodrive designs | 10 |
| 1.6 | Effect of tip geometry | 12 |
| 1.7 | Scanning tunneling spectra: Ag(111) | 13 |
| 1.8 | Atomic force microscope schematic & Atomic resolution . . . | 14 |
| 1.9 | Optical detection schemes of cantilever deflection | 15 |
| 1.10 | Micromachined Si-based AFM cantilevers | 16 |
| 1.11 | AFM operation modes | 19 |
| 1.12 | Modulation in dynamic AFM & constant force gradient . . . | 20 |
| 1.13 | Initial atomic resolution in NC-AFM | 22 |
| 1.14 | On-off method of background signal subtraction force inversion | 26 |
| 1.15 | Chemical identification of atoms using NC-AFM | 27 |
| 1.16 | Using an 'atomic pen' in NC-AFM | 27 |
| 1.17 | Quartz resonator sensors | 30 |
| 1.18 | Submolecular resolution of Pentacene on Cu(111) | 32 |
| 1.19 | Two-dimensional force mapping of Si(111)-(7x7) surface . . . | 33 |
| 1.20 | Three-dimensional Δf / current maps and bias spectroscopic data | 34 |
| 2.1 | Photos of Omicron VT-STM/AFM microscope | 44 |
| 2.2 | Photos of home-built deposition source | 45 |
| 2.3 | Electrochemical etching set up used for STM fabrication . . . | 48 |
| 2.4 | Electrochemical etching of W STM tip | 49 |
| 2.5 | Sweeping submergence depth of W wires for STM tip etching | 52 |
| 2.6 | Etching of a STM tip using a FIB | 53 |
| 2.7 | Etching of a qPlus sensor tip using a FIB | 53 |

List of Figures

| | | |
|------|--|----|
| 2.8 | STM Tip heat treatment set up photograph | 54 |
| 2.9 | Before and after feedforward correction: $Si(111) - (7 \times 7)$ | 56 |
| 2.10 | Tip motion due to dither signal | 57 |
| 2.11 | Tip tracking surface atom via dither signal | 58 |
| 2.12 | Atom tracking and feedforward correction schematic | 59 |
| 2.13 | Improving S/N with a LIA | 61 |
| 2.14 | Signal mixing for phase-sensitive detection | 62 |
| 2.15 | Piezo creep response to step voltage | 65 |
| | | |
| 3.1 | Iterative position measurement of tracking site for displacement calculation | 70 |
| 3.2 | Tracking protocol for acquiring constant height data in SPM | 72 |
| 3.3 | Constant height slices method protocol | 73 |
| 3.4 | Home-built LabVIEW program interface | 76 |
| 3.5 | Temperature regulation: Temperature measurements and piezo scanner feedforward vectors from scripted experiments | 78 |
| 3.6 | Demonstration of tracking script used to gather long term topographic measurement over $Si(111)-(7 \times 7)$ in both STM and NC-AFM | 82 |
| 3.7 | Demonstration of tracking script used to gather $I(z)$ matrix over bare $Si(111)-(7 \times 7)$ via slices method | 83 |
| 3.8 | Demonstration of tracking script used to gather $I(z)$ matrix in STM via grid method of NTCDI on $Si(111)-(7 \times 7)$ | 84 |
| 3.9 | Demonstration of tracking script used to gather $I(V)$ matrix in STM via slice method over NTCDI molecule on $Si(111)-(7 \times 7)$ | 85 |
| 3.10 | Demonstration of 2D $\Delta f(x, z)$ mapping of $Si(111)-(7 \times 7)$ in NC-AFM using constant height scanning | 86 |
| 3.11 | Inverted 2D Force map of $Si(111)-(7 \times 7)$ using cross-sectional constant height slices Δf data | 87 |
| 3.12 | Demonstration of 2D $\Delta f(x, z)$ mapping of $Si(111)-(7 \times 7)$ in NC-AFM using grid spectroscopy | 89 |
| 3.13 | Inverted 2D Force map of $Si(111)-(7 \times 7)$ using cross-sectional grid spectroscopy $\Delta f(x, z)$ data | 90 |
| 3.14 | Demonstration of 3D Δf mapping of $Si(111)-(7 \times 7)$ in NC-AFM using constant height slices | 92 |
| 3.15 | Demonstration of 3D Δf mapping of $Si(111)-(7 \times 7)$ in NC-AFM using grid spectroscopy | 93 |

| | | |
|------|--|-----|
| 3.16 | Inverted 3D Force map of Si(111)-(7×7) using grid spectroscopy Δf data | 94 |
| 3.17 | Comparison of data acquisition methods, using feedforward corrections and residual drifts calculated during $\Delta f(x, y, z)$ mapping experiments | 96 |
| 3.18 | $\Delta f(z)$ curve inversion into $F(z)$: comparing Lanczos differentiator and spline fit methods of smoothing | 99 |
| 4.1 | Prototypical Naphthalene tetracarboxylic diimide (NTCDI) molecule: High-resolution NC-AFM image and stick & ball model | 105 |
| 4.2 | Schematic of Adaptive Height mode (AH) scanning in NC-AFM | 106 |
| 4.3 | Initial submolecular resolution images of NTCDI via Adaptive height mode | 107 |
| 4.4 | Submolecular & atomic resolution NC-AFM images of NTCDI via Adaptive height mode | 108 |
| 4.5 | Iterative constant height imaging of NTCDI using tracking | 109 |
| 4.6 | 2D Force maps: grid spectroscopy data set 1 | 111 |
| 4.7 | 2D Force maps: grid spectroscopy data set 2 | 112 |
| 4.8 | 3D Force map $F_z(x, y, z)$ slices method data set 1 | 113 |
| 4.9 | Experimental $z^*(x, y)$ maps calculated from Δf signal from 2D and 3D experiments (main results in Figures 4.7 & 4.8), & simulated $z^*(x, y)$ map from PPM | 115 |
| 4.10 | 3D $\Delta f(x, y, z)$ maps via slices method and attempted grid spectroscopy | 117 |
| 4.11 | 3D force map via slices method data set 2 | 118 |
| 4.12 | $z^*(x, y)$ map extracted from additional 3D Δf data set | 118 |
| 4.13 | Adsorption geometry of DFT calculation of NTCDI on Si(111) – (7 × 7). | 120 |
| 4.14 | PPM simulated force map | 121 |
| 4.15 | Bond length measurement for experimental and simulated data | 122 |
| 4.16 | δz_{mech} noise estimation via single point spectra & S/N estimations as a function of tip-sample distance using constant height images. | 125 |
| 4.17 | δz_{mech} estimation via single point Δf spectra & S/N evolution throughout $\Delta f(x, y, z)$ mapping experiments | 126 |

List of Figures

| | | |
|------|--|-----|
| 4.18 | Raw Δf , dissipation, and amplitude channels of the scan of closest approach from force map experiment | 127 |
| 4.19 | Long range Δf alignment and smoothing of cross-sectional $\Delta f(x, z)$ map | 129 |
| 4.20 | Δf^* and $z^*(x, y)$ map comparisons between uncorrected data and plane-corrected, using $\Delta f(x, y, z)$ data from Figure 4.8 . . | 131 |
| 4.21 | Estimating Force resolution 1: 2D grid spectroscopy $F(z)$ map | 134 |
| 4.22 | Estimating Force resolution 2: 3D constant height slices $F(z)$ map | 134 |
| 4.23 | Estimating Force resolution 3: 3D constant height slices $F(z)$ map | 135 |
| 5.1 | STM images of p-type Si(111) reconstructions: Si(111)-(7 \times 7) and B:Si(111) – ($\sqrt{3} \times \sqrt{3}$)R30° | 143 |
| 5.2 | Ball-and-stick models of B:Si(111) reconstruction: Plan and side views | 144 |
| 5.3 | Overview STM image of B:Si(111) with defects | 146 |
| 5.4 | Demonstration of 3D Δf mapping of B:Si(111) in NC-AFM using constant height slices | 148 |
| 5.5 | STM images of molecular assemblies on B:Si(111) surface . . | 149 |
| 5.6 | Overview of Molecules attempted on B:Si(111) | 150 |
| 5.7 | STM and NC-AFM (AH mode) overviews of disordered NTCDI island formation on B:Si(111) | 151 |
| 5.8 | STM overview of disordered NTCDI island formation on B:Si(111) | 152 |
| 5.9 | STM and NC-AFM overviews of C ₆₀ island formation on B:Si(111) | 153 |
| 5.10 | Constant height image of C ₆₀ island Figure 5.9.C) & D) | 154 |
| 5.11 | C ₆₀ on B:Si(111) 3D $\Delta f(x, y, z)$, $F_z(x, y, z)$ maps taken via constant height slices method and $z^*(x, y)$ map data | 156 |
| 5.12 | C ₆₀ on B:Si(111) 3D $\Delta f(x, y, z)$, $F_z(x, y, z)$ maps taken via grid spectroscopy method and $z^*(x, y)$ map data | 157 |
| 5.13 | Respective 'off' curves used in slices and grid spectroscopy experiments, subtracted from $\Delta f(z)$ data for force inversion. . | 158 |
| 5.14 | Plane tilt analysis from Figures 5.11 & 5.12 | 160 |
| 5.15 | STM & NC-AFM overview of CoPc molecules on B:Si(111) . . | 163 |

| | | |
|------|---|-----|
| 5.16 | Constant height NC-AFM images of CoPc on B:Si(111) acquired at room temperature | 164 |
| 5.17 | Constant height NC-AFM images acquired at low temperature. | 164 |
| 5.18 | 3D Δf map over single CoPc on B:Si(111) taken via the slices method in NC-AFM | 166 |
| 5.19 | 3D Δf map over a pair of CoPc taken via the slices method in NC-AFM | 167 |
| 5.20 | Example constant height images in NC-AFM of FePc on Ag(111) at 5 K using qPlus sensor | 169 |
| 5.21 | DFT calculated structures and charge distributions of Cobalt Phthalocyanine on B:Si(111). | 170 |
| 5.22 | Processed $z^*(x, y)$ map plotted using data from Figure 5.18 . | 171 |
| 5.23 | Processed $z^*(x, y)$ map plotted using data from Figure 5.19 . | 172 |

1 Scanning Probe Microscopy Techniques: Background Theory

Since its creation more than four decades ago, Scanning Tunneling Microscopy (STM) (1), has demonstrated the ability to study and map out electronic structures at the atomic (2–5) and molecular (6–8) levels. The invention of the Atomic Force Microscope (AFM) (9), (which originally branched out from the early STM experiments) has similarly gained prominence as a technique routinely capable of atomic (10–12) and sub-molecular resolution (13, 14). These techniques provided new levels of material characterisation owing to their unprecedented resolution. As a result they have contributed massively to the field of Nanoscience and to the collective understanding of phenomena on the atomic scale (15). STM & AFM are the cornerstones of researching and designing catalytic reactions (16, 17), and studying the self-assembly of molecules (18–20). Biological systems of particular interest can now be imaged on the scale of individual molecules (21, 22). Research into various functional groups on the probe tips is pushing the boundaries of possible resolution for many systems and expanding the knowledge of physics on this scale (23–25). In both techniques, the scanning probes used can also be repurposed, to carry out controlled manipulation of adsorbates on surfaces, which can be exploited for the study of single-molecule chemistry (26, 27), in addition to surface patterning and lithography (28–30). This first chapter will cover the theory and background behind STM, AFM, and additional affiliated experimental techniques used in this thesis.

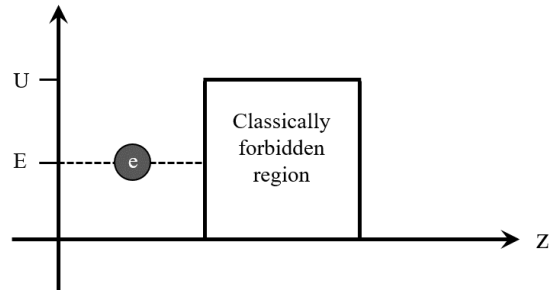


Figure 1.1: An electron of energy E confined outside a one-dimensional potential barrier, of height $U > E$.

1.1 Scanning Tunneling Microscopy

STM operates on the scale of individual atomic and electron interactions, therefore the underlying theory is based on quantum mechanics. In particular, the phenomenon of quantum tunneling.

1.1.1 Quantum Tunneling

The imaging signal of STM is a tunneling current, I . The physical origin can be derived by considering an electron and one-dimensional potential barrier system (presented in Figure 1.1). In classical mechanics, the electron cannot move into the barrier region where $E < U$. However, in quantum mechanics, the position and momentum of the particle are described by a wavefunction $\psi(z)$, the square of which is a probability density:

$$P(z) = |\psi(z)|^2 \quad (1.1)$$

Given the wavefunction satisfies the time independent Schrödinger equation (for one dimension):

$$-\frac{\hbar^2}{2m} \frac{d^2}{dz^2} \psi(z) + U(z)\psi(z) = E\psi(z) \quad (1.2)$$

when applied to the electron on the allowed side of a potential barrier of height U , $\psi(z)$ has the solution:

$$\psi(z) = \psi(0)e^{\pm ikd} \quad (1.3)$$

where wave vector $k = \frac{\sqrt{2m(E-U)}}{\hbar}$, and m is the mass of the electron. Within the forbidden region, Equation 1.2 has the solution:

$$\psi(z) = \psi(0)e^{-\kappa d} \text{ in forbidden region} \quad (1.4)$$

where $\kappa = \frac{\sqrt{2m(U-E)}}{\hbar}$, is the decay constant of an electron state throughout the barrier region. Hence, there is a non-zero value of the probability density within, and beyond, the barrier region:

$$P(z) \propto |\psi(0)|^2 e^{-2\kappa d} \quad (1.5)$$

The particle may 'tunnel' through the barrier (or vacuum) and appear on the other side, see Figure 1.2.A. This potential barrier system serves as a basic model for the physics of STM, which mirrors the piece-wise potential by bringing a metal tip in close proximity to a conducting sample, separated by a vacuum (Figure 1.2.B). The work function, ϕ is defined as the minimum energy required to bring a sample electron from the highest occupied energy state to vacuum. Its magnitude is dependent on the material and also on the surface orientation of the sample (31).

Electrons can tunnel in either direction, as long as there are available states to tunnel into. A net current can be brought about by displacing the Fermi energies of either the tip, E_F^t or sample, E_F^s by some amount, eV , via a bias voltage, V (typically the bias is applied to the sample in most instruments). In Figure 1.2.A a positive bias is applied to the sample, lowering E_F^s . A net flow of electrons from the tip (of state $\psi(z)$) occurs across the vacuum gap and into available states in the sample (of energies between E_F^t and E_F^s). Tip electrons with energies lower than E_F^s cannot tunnel due to the Pauli exclusion principle. Following the convention that the bias is applied to the sample (and the tip is grounded), if $V > 0$, the electrons tunnel from occupied states in the tip into empty sample states, and vice versa if $V < 0$.

Using time-dependent perturbation theory (33), the tunnel current I can be determined by integrating the probability of a state transition (between ψ_t of the tip and ψ_s of the sample) per unit time, over all states. Based on the assumption that the Density of States (DOS) of the tip is constant, Fermi's golden rule (34) stands as a valid approximation for short intervals of time (i.e. ~ 1 ps):

$$I = (4\pi e/\hbar) \int_{-\infty}^{+\infty} [f_t(E_F^t - eV + E) - f_s(E_F^s + E)] \times \rho_t(E_F^t - V + E)\rho_s(E_F^s + E)|M|^2 dE \quad (1.6)$$

where ρ_t and ρ_s are the DOS for the tip and sample respectively, and $|M|$ is the matrix element for transition probability (35). The matrix element is determined by the overlap of the wavefunctions on either side of the potential barrier (32). From Tersoff & Hamann (1985) (36), I can be simplified using the following assumptions: (1) The wavefunction of the tip electrons decay symmetrically about the sphere. (2) The sample electrons can move freely across the sample plane, and their wavefunctions decay normal to the surface. (3) Both the tip and sample share work functions ϕ :

$$I(r_0, V) = (4\pi e/\hbar) \int_{E_F}^{E_F + eV} \rho_t(r_0, E - eV)\rho_s(r_0, E)e^{-2kr_0} dE \quad (1.7)$$

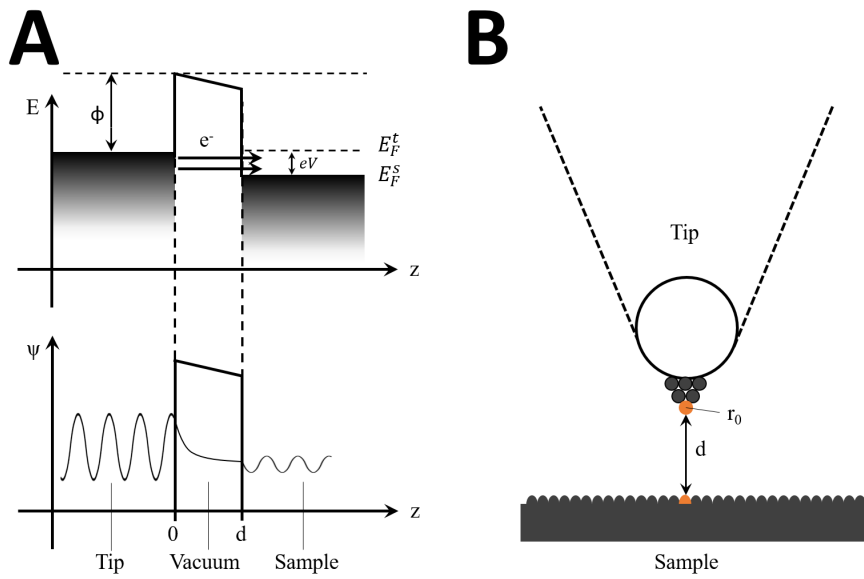


Figure 1.2: A) Top: Electrons of energies between E_F^t and E_F^s tunnel, from occupied states in the tip, into unoccupied states in the sample, overcoming vacuum barrier of height ϕ . The Fermi energy of the sample, E_F^s , is displaced by a bias voltage. Bottom: The electron wavefunction ψ decays in the barrier region, and continues on the other side. Figure adapted from (32). B) Conical model of tip, approached at distance d from sample, capped with spherical apex and terminating in a single atom at position r_0 .

r_0 is the position in the tip where electrons are assumed to be tunneling in/from, i.e. the central position of the terminating atom (see Figure 1.2.B) (35, 36). The matrix element $|M|$ to a one-dimensional probability, which only takes into account tunneling between the terminating atom of the tip and the closest surface atom, i.e. a measurement of maximum resolution. ρ_s and ρ_t being localised in this way means that Equation 1.7 is an integral over the Local Densities of States (LDOS). When the electronic and geometric structures of both the tip and sample are well understood, the true surface topography can be determined from the tunnel current signal I , which is a convolution of the LDOS of both the tip and sample (37, 38). For high energy scales (on the order of eV), the energy dependence of the matrix element $|M|$ cannot be assumed negligible and can be evaluated using the formula by Bardeen (1961) (34). Further simplifications can be made, such as the approximation of the trapezoidal potential barrier in Figure 1.2.A (already a simplification (39)) as a square barrier - its height being the average across both tip and sample. Thus I can be expressed as an exponential that decays inversely proportionally to tip-sample distance z :

$$I(z) = I(0)e^{-2\kappa z} \quad (1.8)$$

where: $\kappa = \frac{\sqrt{2m\phi_{eff}}}{\hbar}$ is the decay constant of a tip state within the tunneling state energy range, ϕ_{eff} is the effective work function, as approximated by the average height of both barriers (35). The high decay constant, κ in metals (on the order of $\sim 1\text{\AA}^{-1}$), gives rise to a highly sensitive distance dependence, resulting in approximately an order of magnitude difference for each \AA increment in z (31).

1.1.2 Development of STM

The first scanning tunneling microscope was built during the initial experiments conducted by Binnig & Rohrer (1982) (1) on metal-vacuum-metal tunneling. This microscope positioned a metal (W) tip, via a piezodrive actuator over the conducting sample of interest (Pt), detecting the flow of

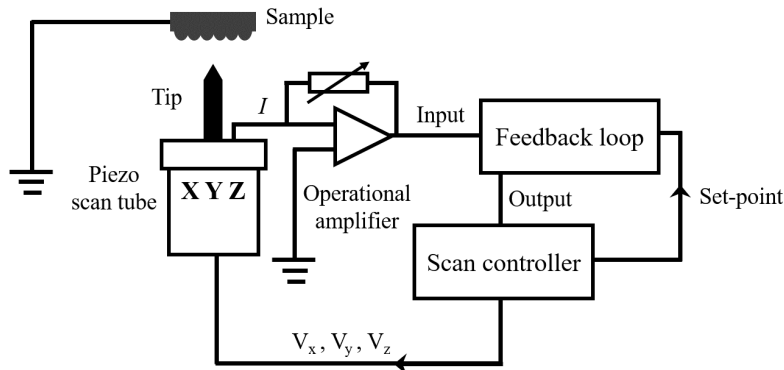


Figure 1.3: Scanning Tunneling Microscope (STM) schematic. A metal tip is brought close to a sample with a bias voltage applied and a tunnel current is detected. This signal is measured whilst the tip is raster scanned in the (x,y) plane across the sample via the piezodrive, typically whilst adjusting z position of the piezo drive in order to maintain some set value of I via a feedback loop. Typically the bias is applied to the sample, whereas for the microscope used in this thesis, the bias is instead applied to the tip.

current across the tip-sample junction. By carrying out a raster scan over the sample whilst detecting a tunnel current, the topography of the sample was able to be mapped. In addition their measurement of the exponential dependence of I on the tip-sample distance showed the high-sensitivity of the microscope they had built. This steep decay of current with respect to distance, enables the STM to resolve atomic sized features, given a sharp tip. This is due to the singular path for current to follow, which originates mainly from the terminating atom of the tip (40) (see Figure 1.2.B).

Following its invention, STM soon yielded atomic resolution imaging (2, 3). Figure 1.4 shows the initial topographic images of atomic resolution of the Si(111)-(7×7) and graphite surfaces. These initial results followed the operation depicted in Figure 1.3, whereby the tunnel current is maintained at some set point. The current detected over each point in (x,y) is converted into a voltage by the operational amplifier, which is then compared to a set-point via a feedback loop, which outputs the necessary voltage for the z -piezo positioning element to return the current to the set-point.

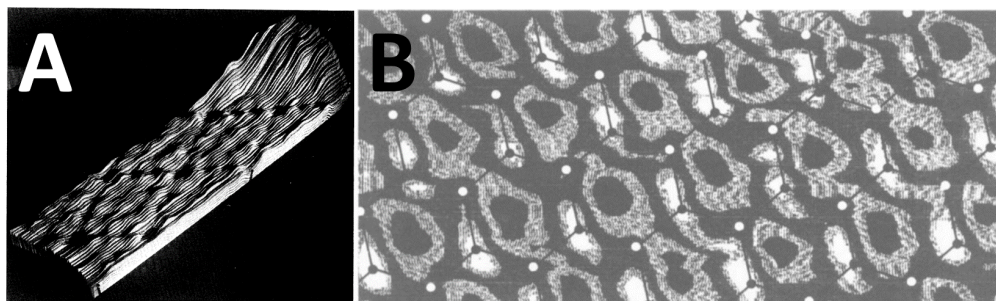


Figure 1.4: A) First STM topograph with atomic resolution of Si(111)-(7×7) reconstruction, taken in ultra high vacuum and room temperature conditions. The semiconductor substrate has become ubiquitous in surface science, owing to its highly corrugated reconstruction, and strong interaction with adsorbates, figure from Binnig et al. (1983) (2). B) STM image of a cleaved surface of highly oriented pyrolytic graphite (HOPG). A lateral resolution better than 2Å was achieved, with inequivalent carbon atoms distinguishable. A honeycomb overlay is superimposed, showing the inequivalent sites. Figure from Binnig et al. (1986) (3).

In ambient conditions, gas atoms and molecules adsorb onto sample surfaces. As such, most materials, with a few exceptions (such as HOPG (3, 41)), cannot be easily studied in ambient conditions. As discussed further in Section 2.1, for sufficient levels of surface cleanliness, ultrahigh vacuum (UHV) conditions are required (42).

1.1.2.1 Feedback Operation

The feedback loop makes adjustments to the tip position in z via the piezodrives to return the current to some set value of the scan controller. In feedback (i.e. constant current) operation, the topography image is a measurement of the DC voltage applied to the z -axis element of the piezodrives, needed to return I to the set-point. The feedback mechanism is a proportional-integral (PI) controller, which responds to tunnel currents exceeding the set-point by retracting the tip away from the sample, and vice versa. The gain, (P) and integration time, (I) loop parameters can be considered as controllers of the magnitude, and the reaction speed of the loop response,

respectively. These are generally fine-tuned to improve the imaging signal to noise ratio (S/N) for a given system and scan speed. For low gain and high time constant values, if the signal undergoes a sudden, significant change (such as a step-change in the surface height), the response of the controller may be insufficient, in both magnitude and speed, to keep the signal at constant current throughout. However, if P and I are too high they may cross resonances causing self excitation in the signal. The PI controller can more easily keep up with changes to I using a slower scan speed.

Alternatively in constant-height mode, the STM is run without the use of feedback. Scanning in this mode can be done at higher speeds, and can provide a more direct map of the LDOS. Constant-height mode runs the risk of a tip-sample collision occurring. For STM data to be valid, it is vital the tip maintains state and does not make physical contact with the surface. Physical contact will mean the measured current is no longer a *tunnel* current, and will likely alter the geometry and electronic structure of the tip.

1.1.2.2 Thermal Drift

A technical difficulty of operating a STM with atomic precision at room temperature, is the relative positional drift between the tip and sample. Due to ever-present temperature gradients across the system, the resultant relaxations cause a continuous change in the relative three-dimensional (3D) position of the tip and sample. Feedback operation adjusts for drifting in the z direction. However, if lateral drift (typically of the order $\sim 100 \text{ pm}/\text{min}$) is left uncorrected, the image will be distorted, limiting the spatial accuracy. This can be alleviated by operating at cryogenic temperatures, wherein the thermal fluctuations of the system are considerably stabilized (43, 44). Low temperature conditions ($\sim 4 \text{ K}$) reduce the thermal gradients throughout the microscope by orders of magnitude, with a commensurate reduction in residual drift. This generally allows for longer acquisition times and hence a higher signal to noise ratio (S/N) for images and data sets (45).

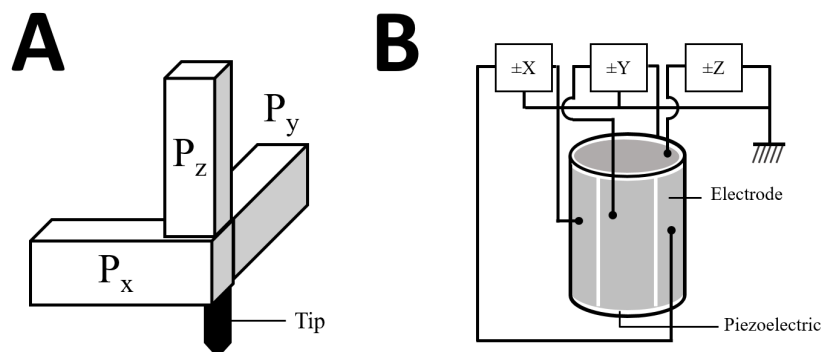


Figure 1.5: A) Original fixed tripod design for piezo scanner (1). B) Single tube design of piezo scanner (46).

1.1.2.3 Fine and Coarse Movement

Figure 1.5 depicts the piezodriven actuators that facilitate the precise 3D movement of the tip. Piezoelectric crystal elements are sandwiched between conducting foils, and applying an electric field across the crystal causes a transverse extension or contraction, depending on polarity (the piezoelectric effect). Following calibration of the crystal extension in response to the voltage applied, piezodriven actuators are able to perform controllable sub-nanometre movements. Typical piezo crystals used in this apparatus include quartz and lead zirconium titanate (47).

Two principal designs of piezodriven actuators exist. First, the 'matchstick box' design consisting of three rigid orthogonal piezo elements, used by Binnig & Rohrer (1982) (1) in the original experiment (see Figure 1.5.A). This design is more prevalent in earlier STM work. Second, the tube-scanner design, introduced by Binnig & Smith (1986) (46), (see Figure 1.5.B) consists of a singular, cylindrical piezo element, able to extend/contract in all three dimensions. This replaced the need for the three individual elements of the previous design. Additionally, tube-scanners have higher mechanical resonance frequencies and therefore contribute less mechanical noise (47).

Tunnel currents are only detectable for tip-sample distances $< 1\text{nm}$. It

is unfeasible for a human to reliably approach the tip to the sample to such a small distance. The coarse motion of the tip is instead controlled by a variety of mechanical designs. These various designs include: the electrostatic clamping "Louse" (10), the differential screw mechanism (48), and the Besocke design, utilising slip-stick motion (49).

1.1.2.4 Mechanical Isolation

A prerequisite for atomic resolution in STM is a mechanical noise level smaller than the atomic corrugation. Thus vibrational isolation is of key importance. Double stage isolation systems of springs and magnetic eddy current damping are widely used in UHV STMs (31, 50). Mechanical vibrations from the external environment transfer to the STM, causing the tip-sample junction to oscillate and serve as the dominant source of noise for the tunnel current (51). These can originate from air-conditioning vents, motors and transformers, and are of the order of a few Hz. The amplitude of the mechanical noise is dampened as the oscillations travel through the springs on which the STM stage is suspended. The amplitude is dampened further by the eddy currents. This is accomplished by surrounding the STM stage with a magnetic field. Eddy current damping, also known as electromagnetic damping (52), is damping due to an induced current produced when a conductor moves through a magnetic field. This current induces a force in the opposite direction to the motion of the conductor.

1.1.2.5 Tip Geometry

Even if the structure of a sample is known, the image is still convoluted with the geometry of the tip. Figure 1.6 shows how sharp and symmetrical tips provide a signal that most closely represents the true topography of the sample, as these minimise the points where there are significant interactions between tip and sample. Blunter, or corrugated tips will have electrons tunneling to/from more points on the tip, that then superimpose over the desired signal at a given point in (x, y) (38). Hence, sharper tips can image surfaces with a higher lateral resolution and contrast.

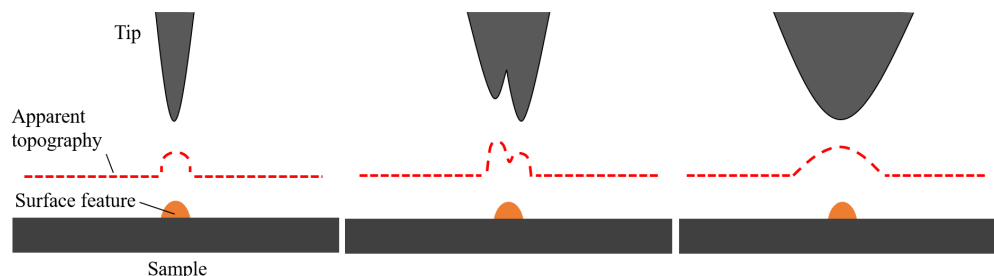


Figure 1.6: Diagram to illustrate how SPM tip geometries provide different apparent line profile traces: A protruding surface feature (e.g. an adsorbed molecule) shows the convolution of the tip shape with the signal of the feature. The sharp, symmetrical tip measures the signal closest to the true profile.

In practice, during STM experiments, the geometry of the tip apex will typically change. Spontaneous restructuring due to atomic forces with the sample may cause the tip to garner clusters of sample atoms, or lose some of its own to the sample (31). Restructuring can manifest itself on the image as corrugation reversals (53), as significant changes to the noise and resolution, or as large defects in the sample where the tip has made contact. Since the early experiments of Binnig et al. (1987) (11), controlled collisions between the tip and sample atoms have provided a viable (if unpredictable) means of sharpening the tip, and improving the contrast in STM. The metal tip atoms can form bonds with the sample adatoms, transferring them to the tip apex. This can result in a dangling bond emanating from the tip, improving the contrast (54). Electrostatically pulsing the tip can also restructure the tip in a beneficial way. Tip atoms lining the blunt tip surface may accumulate toward the apex centre, or electrostatic pulses may expel atoms from the tip, resulting in a sharper geometry (55).

1.1.3 Scanning Tunneling Spectroscopy

The electronic properties of the sample can be characterised with $I(V)$ spectroscopy, also known as Scanning Tunneling Spectroscopy (STS). The tip

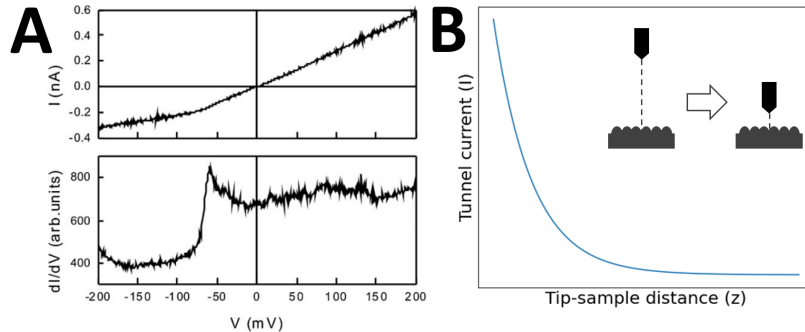


Figure 1.7: A) Example $I(V)$ (top) and $\frac{dI}{dV}$ (bottom) STS data for Ag(111) sample. The change in gradient in the $I(V)$ and the step increase in differential conductance $\frac{dI}{dV}$ indicate the bottom of the surface state band, of energy 69 meV , figure from Morgenstern et al. (2013) (32). B) $I(z)$ curve. The tunnel current exponentially decays proportionally to constant κ as the tip-sample distance is swept (Equation 1.8).

is placed at a set distance from the sample, and the bias voltage sweeps an energy range. By observing the derivative of the tunnel current with respect to bias, $\frac{dI}{dV}$, the differential conductance, dG is obtained. Distinct energy bands that electrons tunnel into (or out of) can be determined from the changes in conductance signal, as their states become available/unavailable for tunneling (see Figure 1.7.A). STS provides information on the electronic structure of a sample, giving insight into its conductivity, chemical reactivity and also its magnetic properties (56).

Additionally, a sample can be characterised by measuring its decay rate κ . From κ the tunnel barrier and work function, ϕ can be estimated. This can be accomplished by sweeping the tip-sample distance z whilst measuring the current: $I(z)$ (see Figure 1.7.B).

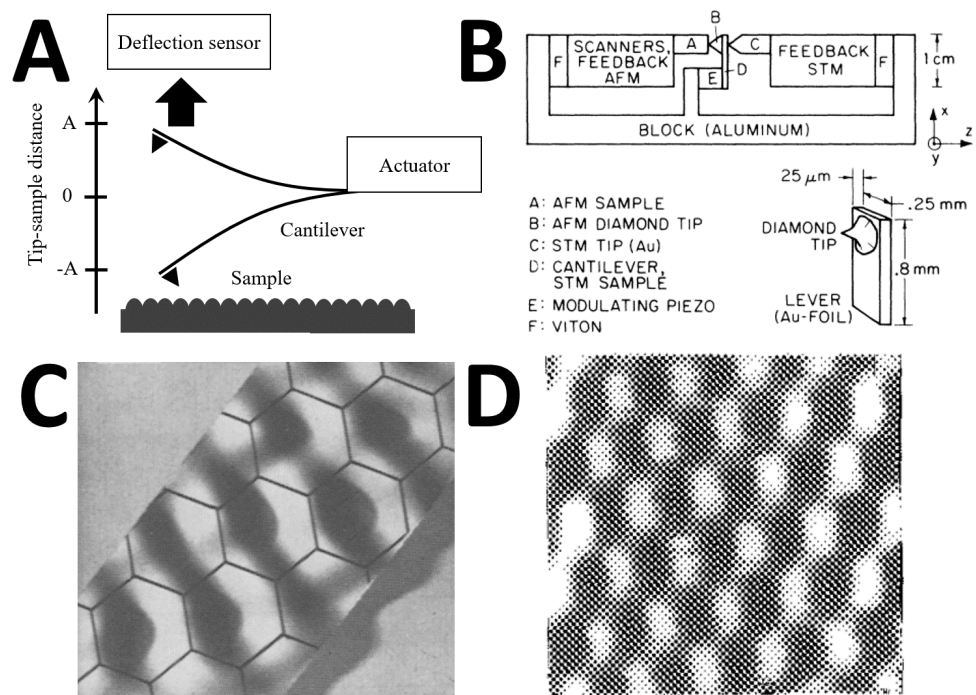


Figure 1.8: A) General schematic for an atomic force microscope (AFM) in regular, transverse flexural mode. B) Original apparatus and cantilever used by Binnig et al. (1986) (9). C) Subsequent image of graphite with atomic resolution and hexagonal structure overlain, figure from Binnig et al. (1987) (41). D) Atomic resolution image of insulating boron nitride sample, figure from Albrecht & Quate (1987) (57).

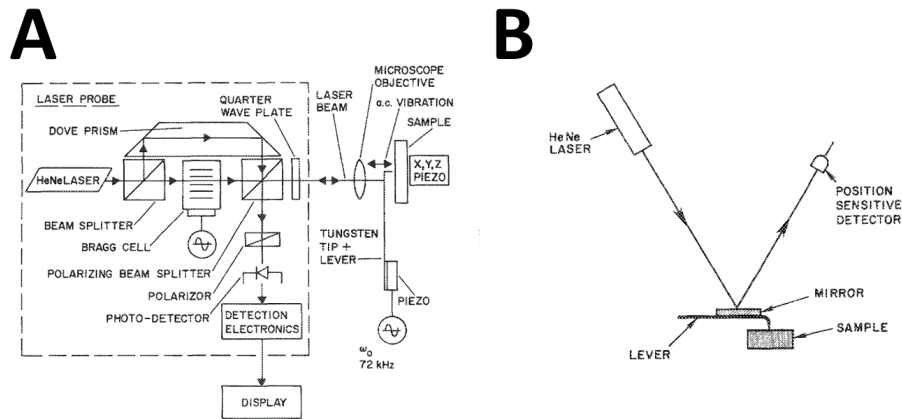


Figure 1.9: A) Initial heterodyne optical interferometer schematic by Martin et al. (1987) (59). B) Optical lever schematic by Meyer and Amer (1988) (60).

1.2 Atomic Force Microscopy

The Atomic Force Microscope (AFM) was invented by Binnig et al. (1986) (9) and operates similarly to STM, but instead measures the force interaction between tip and sample. In an AFM, the tip (typically Si or metal) is mounted to the underside of the free end of a cantilever, and the other end is fixed to the piezodrives of the microscope. The cantilever of stiffness k responds to the tip-sample force F by deflecting in the z axis with magnitude A , see Figure 1.8.A. In this way the cantilever acts as a spring, obeying Hooke's law: $F_{ts} = k.A$ (58). Under static operation, the AFM piezodrives respond to a signal from the feedback loop in order to reverse deviations from a given set deflection. The AFM image therefore depicts a map: $z(x, y, F_{ts} = \text{constant})$. In this way, AFM functions similarly to STM, and often microscopes are designed to facilitate both techniques. Atomic force microscopes on the other hand, have a greater diversity of sensor designs.

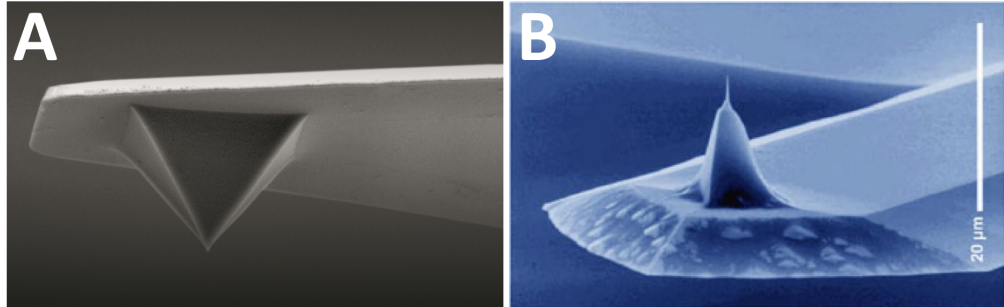


Figure 1.10: A) Scanning electron micrograph of a micro-machined Si_3N_4 cantilever with a Si_3N_4 tip, (61). B) Scanning electron micrograph of a micro-machined Si cantilever with an integrated tip, figure from Wolter et al. (1991) (62).

1.2.1 Deflection Sensors

The deflection was initially detected by measuring the tunnel current from the backside of the cantilever using a STM, by Binnig et al. (1986) (9) (see Figure 1.8.B)). This original cantilever was a gold foil with a diamond tip attached to it, and was sensitive to forces on the order of nN . While the tunnel current is highly sensitive to distance, this apparatus has drawbacks in that it is difficult to reliably position the STM tip to the correct location on the reverse side of the cantilever. Also, there exist forces across the tunnel junction, which convolute the deflection signal (42). Despite this, it was not long until atomic force microscopes showcased atomic resolution on both conducting (41) (C)) and non-conducting surfaces (57) (D)) because, unlike STM, AFM is not limited to conducting samples. A subsequent optical laser heterodyne interferometer apparatus designed by Martin et al. (1987) (59) was then used to measure the deflection (see Figure 1.9.A)). A simpler optical lever technique was designed by Meyer and Amer (1988) (60). A mirror or metallic coating on the reverse side of the cantilever reflects the laser light (B)). Both designs make use of a photosensitive diode to detect a laser light.

Mass-production of micro-machined cantilevers developed quickly too, initially made out of SiO_2 and Si_3N_4 (61, 63) (see Figure 1.10.A)), and later tip-integrated cantilevers made of Si (62) (B)).

1.2.2 Tip-Sample Interactions

There are a variety of interactions that contribute to tip-sample potential U_{ts} and force F_{ts} . These include van der Waals, electrostatic, Pauli repulsion and chemical bonding. In ambient conditions, there may be adhesion forces due to water or hydrocarbons. All these forces (with the exception of Pauli repulsion & chemical bonds) have significant long-range contributions, which can superimpose over the atomic scale forces. Van der Waals interactions arise from fluctuations in the electric dipole moments, polarizing the atoms momentarily. While not as strong as electrostatic forces or covalent bonding, van der Waals forces remain present at both short and long-ranges and are additive. They accumulate over the many atoms of the surface, are always attractive in a vacuum. For a surface-sphere interaction at close proximity (10s of nm), they are given by:

$$V_{vdw} = -\frac{A_H r}{6z} \quad (1.9)$$

where z is the tip-sample distance, r is the radius of a spherical tip apex (see Figure 1.2.B), and A_H is known as the Hamaker constant, which is a function of the density of the material and the square of its polarizability (64). For values of z significantly smaller than tip size, r (and assuming the tip is electrically grounded), the force due to an electrostatic potential V between a spherical tip and flat sample can be given by:

$$F_e(z) = -\frac{\pi\epsilon_0 r V^2}{z} \quad (1.10)$$

where ϵ_0 is the vacuum permittivity (65). Chemical bond forces between two atoms are typically described empirically (due to the complications of accurately describing many-body quantum mechanical systems) via two common methods of treating these forces. First, the Lennard-Jones potential, which is often approximated as:

$$U(z) = \frac{-A}{z^6} + \frac{B}{z^{12}} \quad (1.11)$$

where A and B are constants to be determined through modelling via reference potentials. The formula expresses the attractive forces ($\propto z^{-6}$) and the short-range, repulsive forces ($\propto z^{-12}$), between two atoms due to Pauli and London dispersion forces (66). Second, the Morse potential, which is more commonly used for covalently bonding systems (64):

$$U(z) = D_0(1 - e^{-\alpha(z-z_e)})^2 \quad (1.12)$$

where D_0 is the potential energy minimum, z_e is the equilibrium inter-atomic distance (bond length) and constant α is determined by fitting the functions to reference potentials (67).

In static AFM, in order to achieve atomic sensitivity, the AFM tip must approach close to the surface. But doing so risks the cantilever jumping into contact with the sample due to attractive chemical forces beyond the equilibrium position. As a result the tip is pulled to the surface, to reach an elastic potential energy minima of the cantilever (68). Contact between the tip and sample in AFM can cause damage to both the tip and sample (69, 70). This can be mitigated by using cantilevers of higher stiffness constants k (42). For a desired level of force sensitivity, k needs to be sufficiently small compared to the inter-atomic spring constants of the sample atoms ($k < 10 \text{ N/m}$) (71). Above a certain value of k , the cantilever will not be sensitive enough for atomic resolution. Thus the cantilever spring constant must be well chosen for its given purpose. The value of k is determined by the dimensions and material of the cantilever. For a cantilever of length l , width w and thickness t , its spring constant is given by:

$$k = \frac{Ywt^3}{4L^3} \quad (1.13)$$

where Y is the Young's modulus of the material (31).

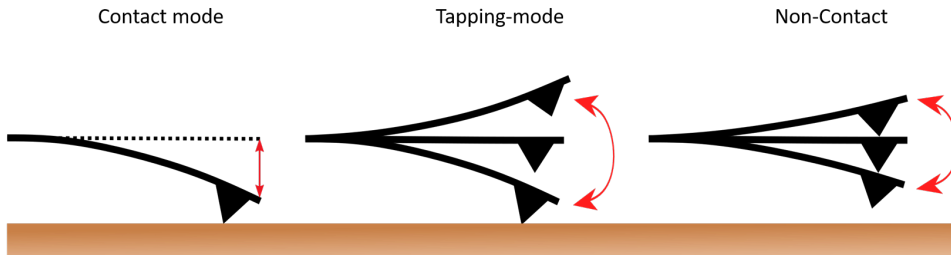


Figure 1.11: Modes of AFM operation. In contact mode, the tip is dragged across the surface, and the displacement of the cantilever (as a result of the tip-sample forces) traces the topography (9). In the tapping and non-contact modes, a driving oscillation keeps the cantilever safe from damage caused by the sample (and vice versa) whilst simultaneously getting close enough to probe the short-range forces, undergoing intermittent contact with the surface (72). In non-contact mode, the tip does not make contact, but operates close enough so that the response of the eigenfrequency reflects the signal coming from the short-range forces, which can be sensitive to changes in force across single atoms (12, 73).

1.2.3 Non-contact Atomic Force Microscopy

In contrast to static operation, Dynamic, or Non-Contact Atomic Force Microscopy (NC-AFM), oscillates the cantilever via a driving voltage (see Figure 1.11). The frequency of the driving voltage is tuned to the resonance, or eigenfrequency, f_0 of the cantilever. As mentioned in Section 1.2.2, for static mode operation, jump-to-contact can be avoided if the cantilever has a higher stiffness than inter-atomic spring constants of the sample. For an oscillating cantilever, stability during scanning requires:

$$kA > \max(-F_{ts}) \quad (1.14)$$

throughout the tip-sample distance the cantilever oscillates over (42). The driving oscillation provides a withdrawing force to the deflected cantilever, affording it greater stability and reduces lateral tip-sample forces, which allows the tip to operate closer to the sample without jump-to-contact occurring (74).

The fundamental eigenfrequency of the cantilever f_0 is given by:

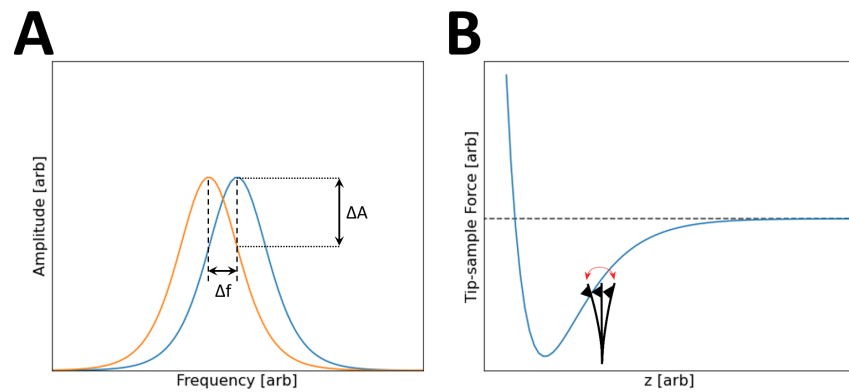


Figure 1.12: A) Frequency and amplitude modulation in NC-AFM: The resonance spectrum of the cantilever (blue curve) changes due to the tip-sample interaction (becoming the orange curve). In FM-AFM the cantilever is actively oscillated at its resonance frequency and the frequency shift Δf is the measured signal. In AM-AFM the cantilever is excited at f_0 and the change in the oscillation amplitude ΔA is the measured signal. B) Force interaction curve resulting from Morse potential (Equation 1.12), between sample and AFM tip. A cantilever is depicted, oscillating at a point in z , and with sufficiently low A , whereby the force gradient can be treated as constant and thus the approximation in Equation 1.19 is valid.

$$f_0 = \frac{1}{2\pi} \sqrt{\frac{k}{m}} \quad (1.15)$$

where m is the mass of the cantilever (42). f_0 changes in response to the presence of a force gradient acting on the tip. Thus, this change in the oscillation response can be measured, either by amplitude modulation (AM-AFM), or frequency modulation (FM-AFM) (see Figure 1.12.A).

With AM-AFM, the change in amplitude, A in response to the tip-sample interaction, (changing the resonance of the cantilever) is modulated and thus forms the feedback imaging signal. The amplitude signal responds on a timescale: $\tau_A \approx 2Q/f_0$ (42), much slower compared to FM-AFM (in vacuum). AM-AFM microscopy has seen particular success when in tapping-mode. In tapping-mode, the tip operates closer to the surface, and undergoes intermittent contact with the surface. The forces acting on the tip are sufficient to cause a measurable change in the amplitude response of the cantilever. It is typically used for liquid state samples in ambient conditions (72, 75, 76).

$$|A| = \frac{|A_{drive}|}{\sqrt{(1 - f_{drive}^2/f_0^2)^2 + f_{drive}^2/(f_0^2 Q^2)}} \quad (1.16)$$

From the measured cantilever deflection an error signal is computed via a PI controller and fed back to drive the actuator. The quality factor of the cantilever, Q is defined as the full width at half maximum (FWHM) of the resonance curve of an oscillator and expresses how underdamped an oscillator is. Typical parameters for a Si cantilever capable of demonstrating atomic resolution in NC-AFM operation are $k \sim 40 \text{ N/m}$, $f_0 \sim 200 \text{ kHz}$ and $Q \sim 50,000$ (42).

Figure 1.13.A depicts the first demonstration of atomic resolution in NC-AFM carried out across several unit cells of the $Si(111) - (7 \times 7)$ reconstructed surface by Giessibl (1995) (12). The region of best contrast exhibited

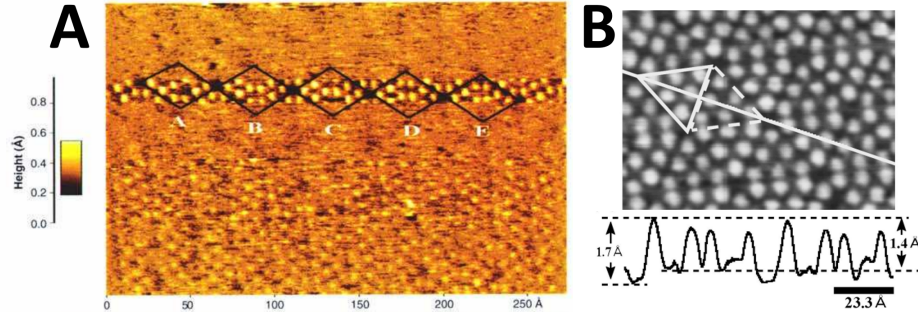


Figure 1.13: A) Demonstration of atomic resolution in NC-AFM across several unit cells of the $Si(111) - (7 \times 7)$ reconstructed surface by Giessibl (1995) (12). B) Topographic image (top) and profile (bottom) depicting differences between non-equivalent surface atoms of the $Si(111) - (7 \times 7)$ (73).

a lateral resolution of 0.6 \AA and a vertical resolution of 0.1 \AA . A cantilever with a spring constant $k = 17 \text{ N/m}$, an eigenfrequency $f_0 = 114 \text{ kHz}$ and quality factor $Q = 28,000$ was oscillated with 340 \AA amplitude and operated in the frequency-modulation mode. The short-range forces responsible for the atomic contrast have a range of only 1 \AA , orders of magnitude smaller than the driving amplitude. Similarly, the contrast over the same surface achieved by Uchihashi et al. (1997) (73) was obtained using a cantilever of $k = 41 \text{ N/m}$, $f_0 = 172 \text{ kHz}$, $Q = 38,000$, being oscillated at 164 \AA .

1.2.3.1 Determining Force from Frequency shift

Compared to static AFM, extraction of the force from the image signal is more complicated for NC-AFM. In NC-AFM, the cantilever follows sinusoidal motion:

$$z(t) = A \cos(2\pi f_0 t) \quad (1.17)$$

where m is the mass of the cantilever, and amplitude A is the max displacement of the oscillation. The oscillation frequency changes in response to tip-sample interaction:

$$f = f_0 + \Delta f \quad (1.18)$$

If the force gradient, $\frac{\partial F_{ts}}{\partial z}$, can be approximated as constant across the range that the cantilever sweeps, the frequency shift is simplified:

$$\Delta f = -\frac{f_0}{2k} \frac{\partial F_{ts}}{\partial z} \quad (1.19)$$

This approximation does not hold when the operational amplitude, A is so large that the force is not linear. Giessibl (1997) (77) extended this result for arbitrary amplitudes:

$$\Delta f = -\frac{f_0}{\pi A k} \int_{-1}^1 F(z_0 + A(1+z)) \frac{z}{\sqrt{1-z^2}} dz \quad (1.20)$$

Where z_0 is the tip-sample distance at the point of closest approach. The expression for force is thus (78):

$$F(z) = 2k \int_z^\infty \left(1 + \frac{A^{1/2}}{8\sqrt{\pi(t-z)}} \right) \Omega(t) - \frac{A^{3/2}}{\sqrt{2(t-z)}} \frac{d\Omega(t)}{dt} dt \quad (1.21)$$

where $\Omega(z) = \Delta f(z) / f_0$. The potential energy is related by:

$$U(z) = 2k \int_z^\infty \Omega(t) \left((t-z) + \frac{A^{1/2}}{4} \sqrt{\frac{t-z}{\pi}} + \frac{A^{3/2}}{\sqrt{2(t-z)}} \right) dt \quad (1.22)$$

An algorithmic approach to calculating Equation 1.22 was presented by Stannard (2015) (79), and written for use in Python throughout this thesis by Phil Blowey. Assuming the tip-sample forces measured are conservative (negligible energy dissipation (80)) the Δf signal can be integrated numerically via the trapezoidal rule, with a non-uniform spacing, to approximate the potential energy, $U(z)$:

$$U_i \approx \frac{4k}{f_0} \sum_{j=i}^{N-1} \left(u_{i,j}^3 + \sqrt{\frac{A}{16\pi}} u_{i,j}^2 + \sqrt{\frac{A^3}{2}} \right) \Delta f_i(u_{i,j+1} - u_{i,j}) \quad (1.23)$$

From there, a corresponding force can be calculated via a Lanczos differentiator, which helps to suppress the noise amplification associated with numerical differentiation (79):

$$F_i \approx -\frac{3}{\Delta z} \sum_{j=1}^m \frac{j(U_{i+j} - U_{i-j})}{m(m+1)(2m+1)} \quad (1.24)$$

where Δz is the spacing between tip-sample distances and m is the span of tip-sample distance included in the differentiator (the higher m is, the greater the degree of smoothing). For measurements across this thesis (wherein A cannot be approximated as far smaller or far greater than the length scales of the interaction forces), Equations 1.23, 1.24 are used to calculate force data. There also exist additional methods for force calculation from the Δf signal, such as the Fourier method (81), or derived from the Morse potential (82). It is important to note that with numerical integration and differentiation, small measurement errors in $\Delta f(z)$ and A can lead to significant errors in $F(z)$. The validity of inverted force measurements can be assessed via an inflection point test (83, 84):

$$\frac{z_{inf}^2}{4} \frac{F'''(z_{inf})}{F'(z_{inf})} \geq -1 \quad (1.25)$$

where Z_{inf} is the tip-sample distance where the curvature of the force changes sign. Code to evaluate the suitability of $\Delta f(z)$ data, via Equation 1.25, was included in the force inversion protocol, written by Phil Blowey, in Python, for use in this thesis.

1.2.3.2 Force Spectroscopy

In NC-AFM experiments, the force displacement curve $F(z)$ can be obtained from $\Delta f(z)$ spectra. Quantitative force measurements provide information of the mechanical properties of samples (and tips) at the atomic scale. Both short and long-range tip-sample interactions contribute to the $F(z)$ and hence $\Delta f(z)$ signal (86, 87). The contribution from short-range forces can be determined by subtracting the long-range elements from the total $\Delta f(z)$ signal (78, 88, 89). Typically during NC-AFM experiments, the bulk electrostatic potential between the tip and sample is compensated by adjusting the applied tip-sample bias. Thus, van der Waals forces are dominant in the long-range regime (40). This method of removing the long-range force over a site of interest, with data taken over a 'null' site, is also referred to as the 'on minus off' method (90). Force inversion of $\Delta f(z)$ curves via this method is depicted in Figure 1.14.

A feature of interest in the converted $F(z)$ spectra, is the maximum attractive force, or minima, and the relative position in z . $F(z)$ minima can be used to quantify the surface reactivity on the atomic scale (44), and hence identify the chemical elements of the sample (91) (see Figure 1.15). The user must therefore make sure the sweep in z encapsulates the attractive minima. But approaching too close will incur a repulsive force due to Pauli exclusion, which increases the likelihood of the tip apex geometry changing.

1.2.3.3 Stability in dynamic AFM

Operating at smaller oscillation amplitudes results in a greater proportion of short-range force acting on the tip during a single oscillation cycle, and hence an increased signal-to-noise ratio (S/N) (40, 92, 93). Small amplitude operation also increases the STM current sensitivity, if simultaneous STM/AFM

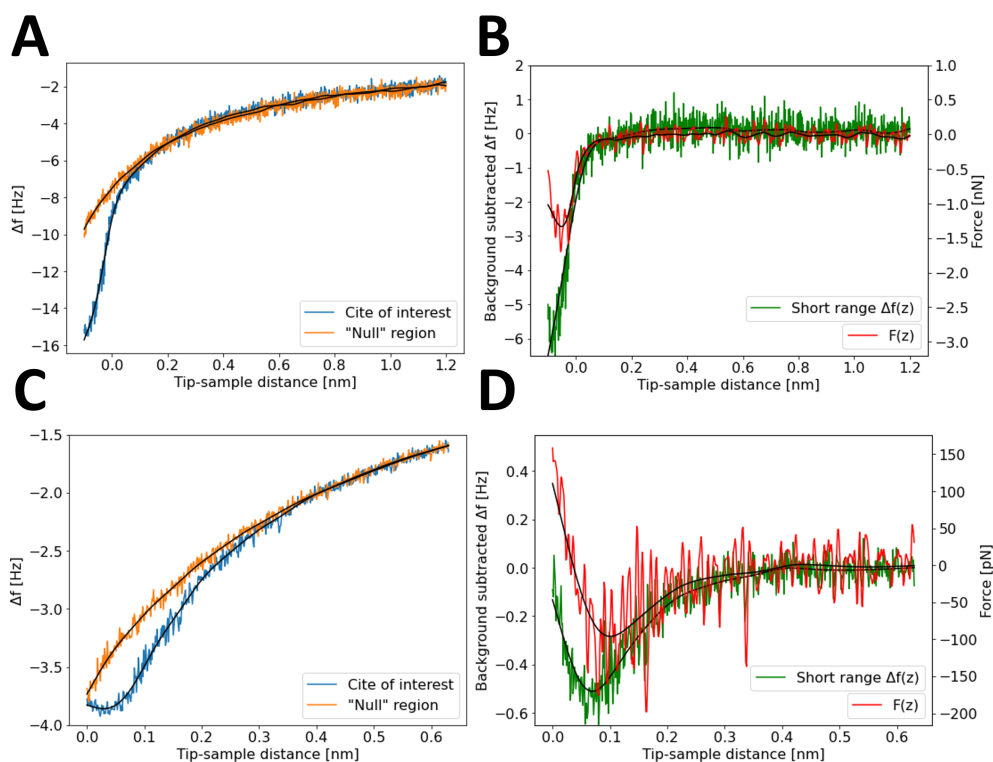


Figure 1.14: A) Example on & off $\Delta f(z)$ curves taken over adatom and 'null' corner hole of a $\text{Si}(111)-(7 \times 7)$ surface. B) With null-site data subtracted, short-range $\Delta f(z)$ signal is plotted alongside the resultant force $F(z)$ inversion (via Lanczos differentiator width, $m = 3$) (79). C) & D) as for A) & B), where on curve is taken over Naphthalene tetracarboxylic diimide (NTCDI) molecule, and off curve taken over $\text{Si}(111)-(7 \times 7)$ substrate. For all subplots the black lines are depicted smoothed data via a scipy spline fit using Python code (85) (smoothing parameter $\lambda = 0.99$).

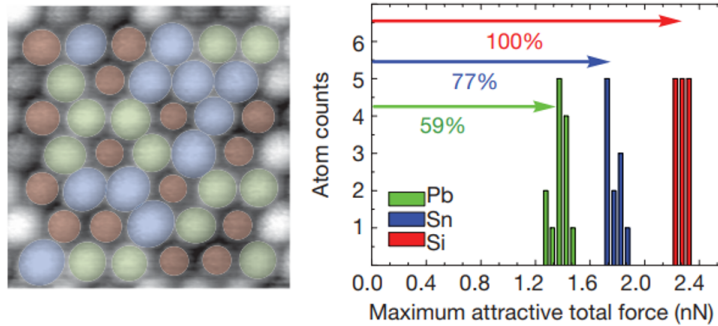


Figure 1.15: Chemical identification across an alloy system consisting of *Pb*, *Sn* and *Si* (imaged on the left, with colour-coding superimposed), distinguishing them via the magnitude of attractive forces measured over them (right). These are elements that otherwise exhibit similar chemical properties, and for which, discrimination through standard topographic images would prove unfeasible, figure from Sugimoto et al. (2007) (91).

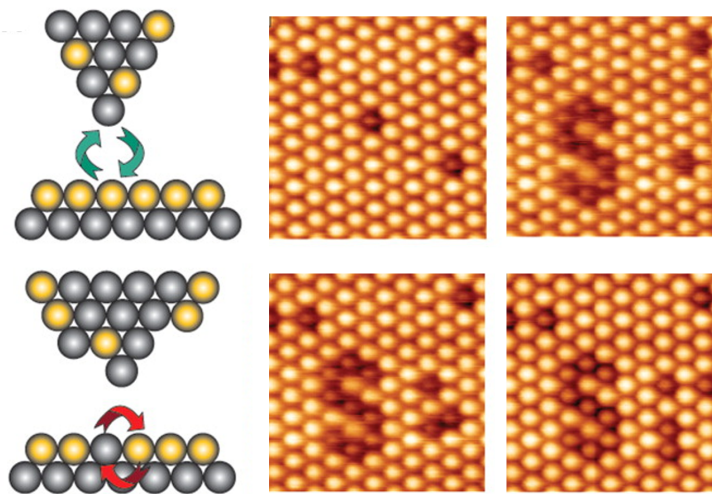


Figure 1.16: Atomic patterning of Si atoms on a Sn layer by means of atomic manipulation via the tip of a Si cantilever (using an 'atomic pen'). Data were gathered in UHV at room temperature. The data were gathered using an oscillation amplitude of 21.9 nm. Data from Sugimoto et al. (2008) (29).

were to be performed (94). The early results in NC-AFM achieved atomic resolution, despite the lower sensitivity of high amplitudes needed to satisfy the stability condition: Equation 1.14. For Si(111)-(7×7), additional criteria for atomic sensitivity: $kA > 100nN$ and $\frac{1}{2}kA^2 \gg \Delta E_{ts}$ also had to be satisfied (where ΔE_{ts} is the energy dissipation of the cantilever, see discussion on non-conservative forces in Section 1.2.3.4).

The thermal and detector noise vary in inverse proportion to the oscillation amplitude ($\propto 1/A$). Hence, measurements conducted at higher A will also have the benefit of reduced Δf noise, but will incur a reduced proportion of short-range forces relative to long-range in the Δf signal. As discussed in Section 1.2.4, the 'qPlus' sensor is able to operate with amplitudes orders of magnitude smaller than conventional cantilevers, whilst maintaining stability. For a given measurement in NC-AFM, the amplitude should be tuned to the scale of the tip-sample interaction in order to optimise the S/N (86). Beyond atomically resolved imaging and force spectroscopy (95), high oscillation amplitude NC-AFM can operate with sufficient stability that controlled atomic manipulation is possible. Figure 1.16 depicts the word Si, written in Si atoms, on a Sn layer (29).

1.2.3.4 Non-conservative forces

Non-conservative tip-sample forces cause hysteresis in the force curve $F(z)$ (80), causing an energy loss in the motion of the cantilever. In addition to internal dissipation of the cantilever (in the absence of tip-sample forces), bringing the tip close to the sample incurs further damping of the oscillation. The driving signal A_{drive} is increased to A'_{drive} by the electronics in order to keep the oscillation amplitude constant. According to Giessibl (2003) (42), $A_{drive} \propto 1/Q$, hence, cantilevers of lower Q values require larger increases to the driving signal in order to maintain a constant oscillation amplitude, due to energy dissipation. The dissipation signal due to tip-sample forces, ΔE_{ts} can be measured using the ratio of driving signals close to the sample (A'_{drive}) and far from the sample (A_{drive}):

$$\Delta E_{ts} = \frac{2\pi E}{Q} \left(\frac{|A'_{drive}|}{|A_{drive}|} - 1 \right) \quad (1.26)$$

Accurate reconstruction of the tip-sample force becomes difficult in the presence of dissipative forces (96–98).

1.2.3.5 Noise Considerations

The frequency noise, δf has three main components, thermal noise $\delta f_{thermal}$, detector noise $\delta f_{detector}$ and mechanical noise $\delta f_{mechanical}(z)$. The total noise can be written as:

$$\delta f = \sqrt{\delta f_{thermal}^2 + \delta f_{detector}^2 + \delta f_{mechanical}^2(z)} \quad (1.27)$$

Albrecht et al. (1991) (99) calculated the thermal noise contribution to the Δf signal of a cantilever to be:

$$\frac{\delta f_{thermal}}{f_0} = \sqrt{\frac{k_B T B}{\pi f_0 k A_{rms}^2 Q}} \quad (1.28)$$

where B is the bandwidth of the frequency detector, and A_{rms} is the root mean square amplitude (99). The detector noise density, n corresponds to the minimum detectable deflection. The corresponding frequency noise is given by (100):

$$\frac{\delta f_{detector}}{f_0} = \frac{n}{\pi A f_0} B^{3/2} \quad (1.29)$$

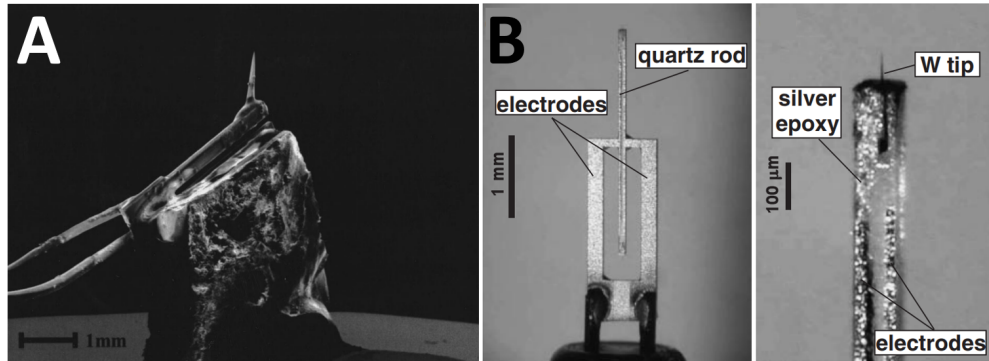


Figure 1.17: A) Photograph of quartz tuning fork resonator (101). B) Left: Photograph of 1MHz quartz length extensional resonator, $k \sim 400kNm^{-1}$. Right: Tungsten tip glued on needle (102).

The mechanical noise in the system $\delta f_{mechanical}(z)$ originates from the fluctuations in the tip-sample distance, z due to external vibrations (87). $\delta f_{mechanical}(z)$ has a dependence on z due to the non-linear nature of the $\Delta f(z)$, increasing with $\frac{d\Delta f}{dz}$. At far tip-sample distances, $\frac{d\Delta f}{dz}$ approaches 0, and $\delta f_{mechanical}$ becomes negligible compared to $\delta f_{thermal}$ and $\delta f_{detector}$. But at close distances (where the highest contrast is observed in NC-AFM), $\delta f_{mechanical}$ dominates.

Over time, the eigenfrequencies, f_0 , of cantilevers can shift slowly due to temperature changes. This shift may manifest as low-frequency noise, (or $1/f$ noise) in the signal (42). Ideally, f_0 should be as stable with respect to temperature as possible.

1.2.4 qPlus and Needle Sensors

Quartz Tuning Forks (QTFs) have long been used as resonators, for instance in time-keeping devices (103). A new sensor design emerged from attaching a probe tip to one end of a QTF resonating normal to the sample surface (104, 105). In Figure 1.17.A, the photograph of the sensor shows one prong of the QTF fixed to a support, while the other prong is free to oscillate, with

a tip attached (made of Tungsten) (101, 106). Effectively the fork is converted to a singular resonating cantilever.

This design boasted higher values of k (and of Q at low temperature) than micro-machined Si cantilevers by orders of magnitude (see Table 1.1). The piezoelectricity of quartz enables self-sensing operation (15), thus qPlus sensors do not rely on optical based detection methods. Moreover, if metal tips are used, simultaneous STM and AFM measurements are possible (94).

For a given tip-sample force in Equation 1.14, the high k of quartz, allows the user to oscillate at amplitudes, orders of magnitude smaller than Silicon cantilevers (86). As mentioned in Section 1.2.3.3, smaller oscillation amplitudes boost the S/N for NC-AFM measurement of short-range forces.

Additionally, QTFs oscillate with a higher stability amidst temperature fluctuations compared to conventional Si cantilevers. For Si, the shift in f_0 , δf_{fluct} is linear with temperature, with typical rates of 35 ppm/K (107). Whereas, for qPlus sensors, the variance in f_0 with temperature can be described semi-empirically as (108):

$$\frac{\delta f_{fluct}}{f_0} \sim -0.00081(1 + \cos(\pi T/T_p)) \quad (1.30)$$

where T_p is the turnover temperature (at which the variation in f_0 due to temperature changes sign). Quartz is typically cut such that $T_p \sim 298K$. This relationship yields minimal variation for quartz (< 10 ppm/K) in f_0 with temperature at both room temperature, and 4K systems (15).

The qPlus sensor demonstrated atomic resolution on Si(111)-(7×7) in NC-AFM shortly after its emergence (92, 106). Atomic resolution on insulating samples (114, 115), studies into atomic friction (116), and atomic manipulation (117) using the qPlus sensor all soon followed suit.

Picking up a CO molecule on the tip apex, was discovered to massively improve the resolution of the Δf signal of a pentacene molecule on a Cu(111) surface, wherein the chemical structure of the molecule is resolved (13) (see

1 Scanning Probe Microscopy Techniques: Background Theory

| Sensor | k (N/m) | f_0 (Hz) | Q at RT | Q at 4K | n (fm/ $\sqrt{\text{Hz}}$) |
|---------------|-----------------|-----------------|-----------------|-----------------|-------------------------------|
| Si Cantilever | 40 | 2×10^5 | 10^4 | 5×10^4 | 10^2 (109, 110) |
| qPlus | 2×10^3 | 5×10^4 | 5×10^3 | 2×10^5 | 50 (93, 111) |
| LER | 10^6 | 10^6 | 5×10^4 | 8×10^4 | 5 (112, 113) |

Table 1.1: Comparison of typical characteristic values of NC-AFM sensors, and noise densities of their detection systems.

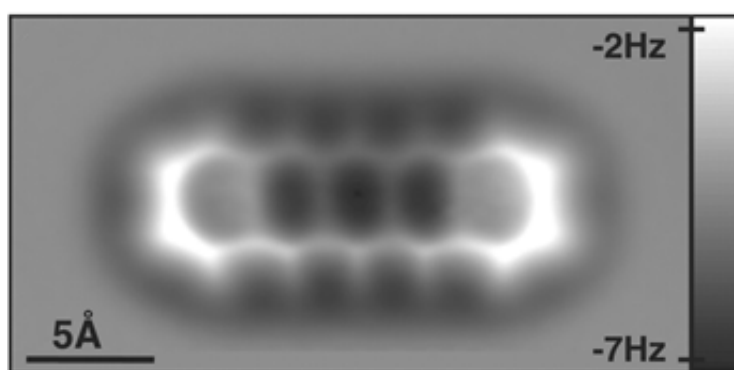


Figure 1.18: First atomically resolved image of a molecule in NC-AFM, Pentacene on Cu(111), imaged using a qPlus sensor and CO-terminating tip operating in constant height, at 4K and in UHV. Figure from Gross et al. (2009) (13).

Figure 1.18). This opened up a new field whereby molecules could be reliably imaged with submolecular resolution using CO terminated tips on qPlus sensors at low temperature (8, 118–120).

A similar design of sensor, the Length Extensional Resonator (LER, or 'needle sensor'), resonates in the longitudinal direction of the cantilever (102, 121) (see Figure 1.17.B). This sensor consists of two quartz rods, which oscillate opposingly, one of which has a tip on its end. LERs are characterised by their high values of f_0 , and Q (see Table 1.1). The resultant stability of these sensors has yielded atomic resolution imaging in ambient conditions (93), and submolecular resolution in cryogenic conditions (122).

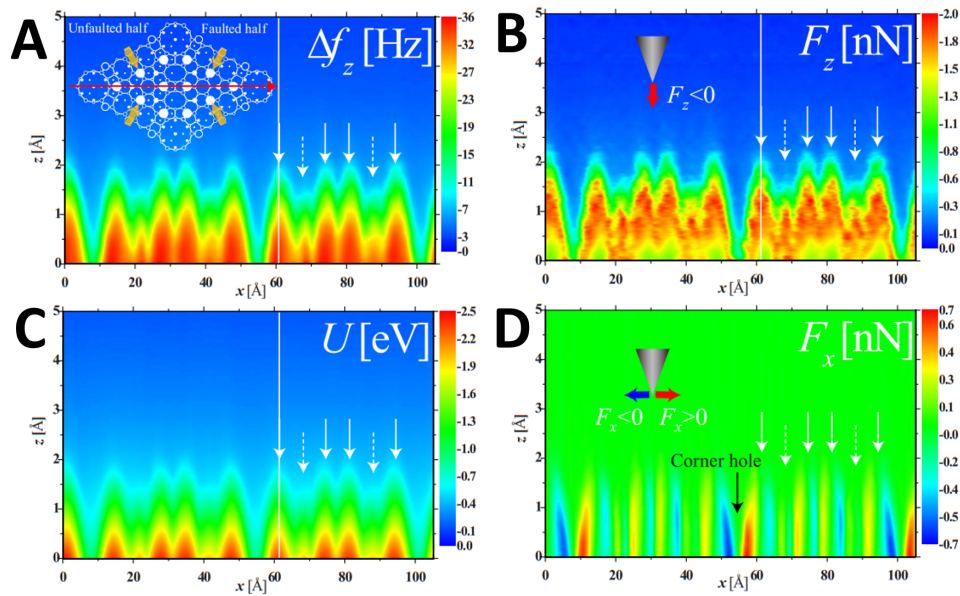


Figure 1.19: Two-dimensional force mapping across two unit cells of Si(111)-(7x7) surface. A) Δf signal measured in NC-AFM. Data were acquired by stacking horizontal line profiles of Δf taken in constant height mode. B) Inverted force signal using the Sader Jarvis algorithm. C) Potential energy, U map calculated from B). D) Lateral force F_x calculated by differentiating C) with respect to x . Dotted arrows indicate positions of substrate adatoms. Figure from Sugimoto et al. (2008) (123).

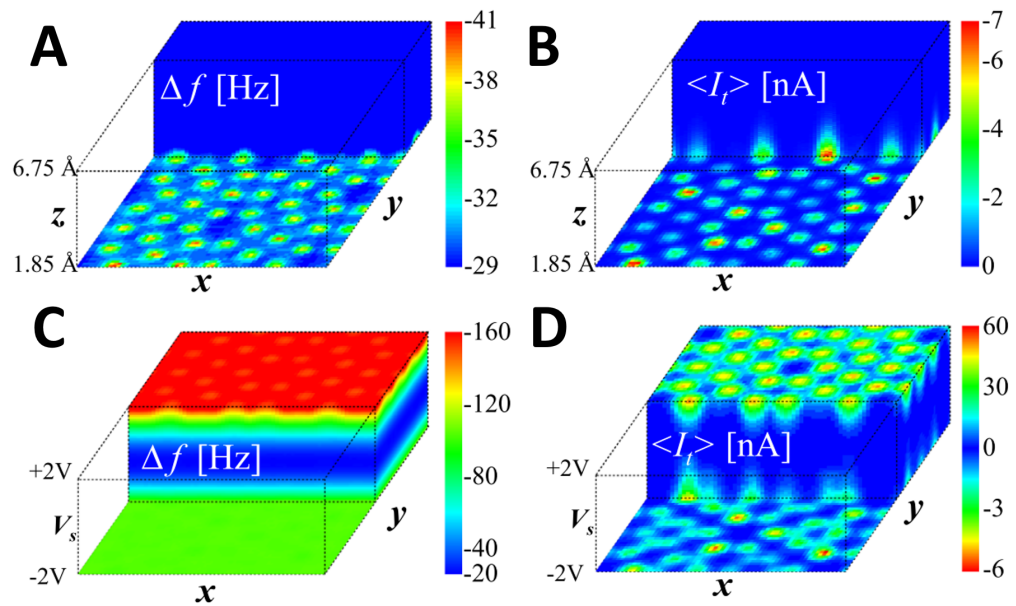


Figure 1.20: Three-dimensional force mapping across unit cell of Si(111)-(7x7). A) $\Delta f(x, y, z)$ map. B) Current, $I_t(x, y, z)$ map simultaneously recorded via a conducting PtIr coating over a Si tip cantilever. C) & D) $\Delta f(x, y, V)$ and $I_t(x, y, V)$ maps throughout bias spectroscopy across the same unit cell. Figure from Sugimoto et al. (2012) (124).

1.2.5 Force Mapping

Rather than one-dimensional spectra, the $\Delta f(z)$ signal can be mapped in 2D $((x, z), (y, z))$ and 3D (x, y, z) . The $\Delta f(z)$ map can then be converted into F_z and potential energy, U maps (123). Figure 1.19 shows a $\Delta f(x, z)$ signal measured in NC-AFM, which can be acquired either by iterating point spectroscopy curves in z , (iterating in x), or horizontal line scans across x , (iterating in z).

The $\Delta f(z)$ curves taken from the data set can be inverted into a map of the force, F_z and potential energy, $U(z)$ using Sader-Jarvis formulae (78). A lateral force map $F_x(x, z)$ can be calculated from a differentiation of the potential map with respect to x . The lateral forces needed for manipulation of a single atom can be determined from lateral force mapping (117).

Further data channels can be simultaneously acquired in multi-dimensional space. Using a conductive PtIr coating over the tip allows one to measure the tunnel current between the tip and the sample (125), or alternatively a qPlus sensor can be used to the same end (126). Force spectroscopy and 3D mapping in NC-AFM have provided physical and chemical insights at the atomic scale (127). Figure 1.20 depicts 3D mapping of the Δf and I signal over a unit cell of the Si(111)-(7x7) surface. The combination of the signals within these maps reveals a modification of the LDOS as a result of chemical bond formation between the tip and Si adatoms (124). 3D force and energy maps of a NaCl(001) surface show individual atomic displacements of the surface atoms as a result of interaction with the tip (128). A 3D Δf on the CaCO₃(10 $\bar{1}$ 4) surface exhibited a lateral precision of 50 pm (45).

For precise force measurements within a multi-dimensional map, experiments require accurate tip-sample positioning. Often, a low temperature environment is more suitable because thermal drift is negligible in such conditions. The experimental work in this thesis is focused on achieving the necessary level of accuracy for multi-dimensional force mapping despite operating at room temperature conditions. It is difficult to build AFM instruments that are not subject to thermal drift at room temperature, but atom-tracking and feedforward techniques can compensate for thermal drift motion. Chapter 2 of this thesis will elaborate on the methodology and the

refinement thereof (using the techniques explained in this chapter), needed to gather force maps at room temperature.

References

1. G. Binnig, H. Rohrer, C. Gerber, E. Weibel, *Phys. Rev. Lett.* **49**, 57–61 (1982).
2. G. Binnig, H. Rohrer, C. Gerber, E. Weibel, *Phys. Rev. Lett.* **50**, 120–123 (1983).
3. G. Binnig *et al.*, *Europhysics Letters (EPL)* **1**, 31–36 (1986).
4. V. M. Hallmark, S. Chiang, J. F. Rabolt, J. D. Swalen, R. J. Wilson, *Phys. Rev. Lett.* **59**, 2879–2882 (1987).
5. C. J. Chen, *Phys. Rev. Lett.* **65**, 448–451 (1990).
6. J. Pascual *et al.*, *Chemical Physics Letters* **321**, 78–82 (2000).
7. J. Repp, G. Meyer, S. M. Stojković, A. Gourdon, C. Joachim, *Phys. Rev. Lett.* **94**, 026803 (2005).
8. L. Gross *et al.*, *Physical Review Letters* **107**, 086101 (2011).
9. G. Binnig, C. F. Quate, C. Gerber, *Phys. Rev. Lett.* **56**, 930–933 (1986).
10. G. Binnig, H. Rohrer, *Surface Science* **126**, 236–244.
11. G. Binnig, H. Rohrer, *Rev. Mod. Phys.* **59**, 615–625 (1987).
12. F. J. Giessibl, *Science* **267**, 68–71 (1995).
13. L. Gross, F. Mohn, N. Moll, P. Liljeroth, G. Meyer, *Science* **325**, 1110–1114 (2009).
14. A. M. Sweetman *et al.*, *Nature Communications* **5** (2014).
15. F. Giessibl, *Review of Scientific Instruments* **90**, 011101 (2019).
16. N. Tao, Z. Shi, *Surface Science* **321**, L149–L156 (1994).
17. Y. Iwasawa, H. Onishi, K. Fukui, *Topics in Catalysis* **14**, 163–172 (2000).
18. K. E. Plass, K. Kim, A. J. Matzger, *Journal of the American Chemical Society* **126**, 9042–9053 (2004).

19. S. D. Feyter, F. D. Schryver, *The Journal of Physical Chemistry B* **109**, 4290–4302 (2005).
20. Y. Makoudi *et al.*, *Surface Science Reports* **72**, 316–349 (Sept. 2017).
21. T. Boland, B. D. Ratner, *Proceedings of the National Academy of Sciences* **92**, 5297–5301 (1995).
22. Y. Kim *et al.*, *Journal of the American Chemical Society* **136**, 13754–13760 (2014).
23. P. Jelinek, *Journal of Physics: Condensed Matter* **29**, 343002 (2017).
24. H. Monig, S. Amirjalayer, A. Timmer, *Nature Nanotech*, 371 (2018).
25. B. Malladal *et al.* (2021).
26. S.-W. Hla, G. Meyer, K.-H. Rieder, *ChemPhysChem* **2**, 361–366 (2001).
27. S.-W. Hla, K.-H. Rieder, *Annual Review of Physical Chemistry* **54**, 307–330 (2003).
28. S. Kraemer, R. R. Fuierrer, C. B. Gorman, *Chemical Reviews* **103**, 4367–4418 (2003).
29. Y. Sugimoto *et al.*, *Science* **322**, 413–417 (2008).
30. R. Achal *et al.*, *Nature Communications* **9** (2018).
31. J. Chen, *Introduction to Scanning Tunneling Microscopy* (Oxford University Press, 1993).
32. K. Morgenstern, N. Lorente, K. H. Rieder, *Controlled manipulation of single atoms and small molecules using the scanning tunneling microscope*, vol. 6, pp. 1315–1455.
33. A. D. Gottlieb, L. Wesoloski, *Nanotechnology* **17**, R57 (2006).
34. J. Bardeen, *Phys. Rev. Lett.* **6**, 57–59 (1961).
35. J. Lawrence, PhD thesis, University of Warwick, 2018, pp. 21–24.
36. J. Tersoff, D. R. Hamann, *Physical Review B* **31**.
37. H. Pfeifer, B. Koslowski, P. Ziemann, *Beilstein J. Nanotechnol.* **2**, 607–617 (2011).
38. K. I. Schiffmann, M. Fryda, G. Goerigk, R. Lauer, P. Hinze, *Ultramicroscopy* **66**, 183–192 (1996).

39. J. Simmons, *Journal of Applied Physics* **34**, 1793 (1963).
40. S. Morita, *Noncontact Atomic Force Microscopy: Volume 2* (Springer, 2009), p. 125.
41. G. Binnig, C. Gerber, E. Stoll, T. R. Albrecht, C. F. Quate, *Europhysics Letters (EPL)* **3**, 1281–1286 (1987).
42. F. J. Giessibl, *Reviews of Modern Physics* **75**, 949–983 (2003).
43. R. Hoffmann *et al.*, *Physical Review B - Condensed Matter and Materials Physics* **67**, 238–244 (2003).
44. M. A. Lantz *et al.*, *Science* **291**, 2580–2583 (2001).
45. P. Rahe *et al.*, *Review of Scientific Instruments* **82** (2011).
46. G. Binnig, D. Smith, *Review of Scientific Instruments* **57**, 1688 (1986).
47. M. A. Gubrud, PhD thesis, University of Maryland, 2010.
48. R. Wiesendanger, D. Anselmetti, H.-J. Gütherodt, *Europhys. News* **21**, 72–73 (1990).
49. J. Frohn, K. Wolf, M. Teske, *Review of Scientific Instruments* **60**, 1200 (1989).
50. Y. Kuk, P. J. Silverman, *Review of Scientific Instruments* **60**, 165–180 (1989).
51. Y. Sugimoto, I. Yi, K.-i. Morita, M. Abe, S. Morita, *Applied Physics Letters* **96**, 263114 (2010).
52. S. Electrical, *Damping Systems – Air friction, Fluid Friction & Eddy Current Damping*, Website accessed: 2022-26-12, 2019, (<https://studyelectrical.com/2019/11/damping-systems-air-friction-eddy-current-fluid-friction-and-electromagnetic.html>).
53. J. V. Barth, H. Brune, G. Ertl, R. J. Behm, *Phys. Rev. B* **42**, 9307–9318 (1990).
54. S. Ohnishi, M. Tsukada, *Solid State Communications* **71**, 391–394 (1989).
55. V. A. Valencia *et al.*, *Journal of Vacuum Science & Technology: A* **33**, 023001 (2015).
56. W. Ho, *J. Chem. Phys.* **117**, 11033 (2002).
57. T. R. Albrecht, C. F. Quate, *Journal of Applied Physics* **62**, 2599 (1987).

58. F. Albrecht, PhD thesis, University of Regensburg, 2016.
59. Y. Martin, C. C. Williams, H. K. Wickramasinghe, *Journal of Applied Physics* **61**, 4723 (1987).
60. G. Meyer, N. M. Amer, *Applied Physics Letters* **53**, 1045–1047 (1988).
61. Nanowerk, *Pyrex-Nitride (PNP) Silicon-Nitride AFM Probes*, Website accessed: 2022-06-10, 2022, (<https://www.nanoworld.com/pyrex-nitride-silicon-nitride-afm-tips>).
62. O. Wolter, T. Bayer, J. Greschner, *Journal of Vacuum Science and Technology B: Microelectronics and Nanometer Structures Processing, Measurement, and Phenomena* **9**, 1353 (1991).
63. T. R. Albrecht, S. Akamine, T. E. Carver, C. F. Quate, *Journal of Vacuum Science & Technology A* **8**, 3386–3396 (1990).
64. J. N. Israelachvili, *Intermolecular and Surface Forces* (Elsevier, 2011).
65. L. Olsson, N. Lin, V. Yakimov, R. Erlandsson, *Journal of Applied Physics* **84**, 4060–4064 (1998).
66. R. H. French, *Journal of the American Ceramic Society* **83**, 2117–2146 (2000).
67. J. R. Hart, A. K. Rappé, *The Journal of Chemical Physics* **97**, 1109–1115 (1992).
68. M. A. S. Quintanilla, *Surface Analysis Using Contact Mode AFM*, ed. by Q. J. Wang, Y.-W. Chung (Springer US, Boston, MA, 2013), pp. 3401–3411.
69. J. B. Pethica, W. C. Oliver, *Physica Scripta* **1987**, 61 (1987).
70. F. Giessibl, G. Binnig, *Ultramicroscopy* **42-44**, 281–289 (1992).
71. D. Rugar, P. Hansma, *Physics Today* **43**, 23–30 (1990).
72. Q. Zhong, D. Inniss, K. Kjoller, V. Elings, *Surface Science* **290**, L688–L692 (1993).
73. T. Uchihashi *et al.*, *Phys. Rev. B* **56**, 9834–9840 (1997).
74. L. Howald, R. Lüthi, E. Meyer, H.-J. Güntherodt, *Phys. Rev. B* **51**, 5484–5487 (1995).

75. R. Erlandsson, L. Olsson, P. Mårtensson, *Phys. Rev. B* **54**, R8309–R8312 (1996).
76. O. Sahin, N. Erina, *Nanotechnology* **19**, 445717 (2008).
77. F. J. Giessibl, *Phys. Rev. B* **56**, 16010–16015 (1997).
78. J. Sader, P. Jarvis S, *Appl. Phys. Lett.* **84**, 1801–1803 (2004).
79. A. Stannard, A. M. Sweetman, *A Considered Approach to Force Extraction from Dynamic Force Microscopy Measurements*, ed. by P. Moriarty, S. Gauthier (Springer International Publishing, 2015), pp. 63–79, ISBN: 978-3-319-17401-3.
80. U. Dürig, *Surface and Interface Analysis* **27**, 467–473 (1999).
81. U. Dürig, *Applied Physics Letters* **75**, 433–435 (1999).
82. F. J. Giessibl, H. Bielefeldt, *Phys. Rev. B* **61**, 9968–9971 (2000).
83. J. E. Sader, B. D. Hughes, F. Huber, F. J. Giessibl, *Nature Nanotechnology* **13**, 1088–1091 (2018).
84. F. Huber, F. J. Giessibl, *Journal of Applied Physics* **127**, 184301 (2020).
85. G. Van Rossum, F. L. Drake Jr, *Python reference manual* (Centrum voor Wiskunde en Informatica Amsterdam, 1995).
86. F. J. Giessibl, S. Hembacher, M. Herz, C. Schiller, J. Mannhart, *Nanotechnology* **15**, 79 (2004).
87. Y. Sugimoto *et al.*, *Physical Review B* **81**, 245322 (2010).
88. M. Abe *et al.*, *Applied Physics Letters* **90**, 203103 (2007).
89. A. Sweetman, A. Stannard, *Beilstein Journal of Nanotechnology* **5**, 386–393 (2014).
90. M. A. Lantz *et al.*, *Phys. Rev. B* **74**, 245426 (2006).
91. Y. Sugimoto *et al.*, *Nature* **446**, 64–67 (2007).
92. F. Giessibl, S. Hembacher, H. Bielefeldt, J. Mannhart., *Science* **289**, 422–425 (2000).
93. B. H, W. T, S. A, *Beilstein Journal of Nanotechnology* **7**, 432–438 (2016).
94. Z. Majzik *et al.*, *Beilstein J Nanotechnol* **3**, 249–259 (2012).
95. Y. Sugimoto *et al.*, *Nature materials* **4**, 156–159 (2005).

96. J. E. Sader *et al.*, *Nanotechnology* **16**, S94 (2005).
97. A. Labuda, Y. Miyahara, L. Cockins, P. H. Grütter, *Phys. Rev. B* **84**, 125433 (2011).
98. H. Söngen, R. Bechstein, A. Kühnle, *Journal of Physics: Condensed Matter* **29**, 274001 (2017).
99. T. R. Albrecht, P. Grütter, D. Horne, D. Rugar, *Journal of Applied Physics* **69**, 668–673 (1991).
100. U. Dürig, H. R. Steinauer, N. Blanc, *Journal of Applied Physics* **82**, 3641–3651 (1997).
101. F. J. Giessibl, *Applied Physics Letters* **73**, 3956–3958 (1998).
102. S. Heike, T. Hashizume, *Japanese Journal of Applied Physics* **45**, 1996 (2006).
103. *Precision frequency control / edited by Eduard A. Gerber, Arthur Ballato.* eng (Academic Press, Orlando, Fla, 1985).
104. K. Karrai, R. D. Grober, *Applied Physics Letters* **66**, 1842–1844 (1995).
105. H. Edwards, L. Taylor, W. Duncan, A. J. Melmed, *Journal of Applied Physics* **82**, 980–984 (1997).
106. F. J. Giessibl, *Applied Physics Letters* **76**, 1470–1472 (2000).
107. U. Gysin *et al.*, *Phys. Rev. B* **69**, 045403 (2004).
108. S. Hembacher, F. Giessibl, J. Mannhart, *Applied Surface Science* **188**, 445–449 (2002).
109. K. Yasumura *et al.*, *Journal of Microelectromechanical Systems* **9**, 117–125 (2000).
110. S. Torbrügge *et al.*, *Review of Scientific Instruments* **79**, 083701 (2008).
111. F. Pielmeier (2014).
112. S. Torbrügge, O. Schaff, J. Rychen, *Journal of Vacuum Science & Technology B* **28**, C4E12–C4E20 (2010).
113. L. Schwab *et al.*, *Microsyst Nanoeng* **8**, 32 (2022).
114. F. J. Giessibl, M. Reichling, *Nanotechnology* **16**, S118 (2005).
115. D. S. Wastl, A. J. Weymouth, F. J. Giessibl, *Phys. Rev. B* **87**, 245415 (2013).

116. A. J. Weymouth *et al.*, *Phys. Rev. Lett.* **111**, 126103 (2013).
117. M. Ternes, C. P. Lutz, C. F. Hirjibehedin, F. J. Giessibl, A. J. Heinrich, *Science* **319**, 1066–1069 (2008).
118. F. Mohn, L. Gross, G. Meyer, *Applied Physics Letters* **99**, 53106 (2011).
119. N. Pavliček *et al.*, *Phys. Rev. Lett.* **108**, 86101 (2012).
120. N. Pavliček, L. Gross, *Nat. Rev. Chem* **1**, 0005 (2017).
121. U. Grunewald, K. Bartzke, T. Antrack, *Thin Solid Films* **264**, 169–171 (1995).
122. T. K. Shimizu *et al.*, *The Journal of Physical Chemistry C* **124**, 26759–26768 (2020).
123. Y. Sugimoto, T. Namikawa, K. Miki, M. Abe, S. Morita, *Phys. Rev. B* **77**, 195424 (2008).
124. Y. Sugimoto, K. Ueda, M. Abe, S. Morita, **24**, 84008 (2012).
125. Y. Sugimoto, I. Yi, K.-i. Morita, M. Abe, S. Morita, *Applied Physics Letters* **96**, 263114 (2010).
126. J. Welker, F. J. Giessibl, *Science* **336**, 444–449 (2012).
127. M. Abe, K. Morita, *NanoScience and Technology* **6**, 15–30 (2009).
128. S. Kawai, T. Glatzel, S. Koch, A. Baratoff, E. Meyer, *Physical Review B - Condensed Matter and Materials Physics* **83**, 1–7 (2011).

2 Experimental Methods

This chapter is an overview of the specific apparatus used to conduct scanning tunneling and non-contact atomic force microscopy for this thesis. The fabrication and preparation of scanning probe tips are described, and particular focus is paid to the atom tracking technique needed for feedforward correction, a cornerstone of high-resolution force measurement in room temperature conditions.

2.1 Equipment: Omicron VT-STM/NC-AFM

The data in this thesis were acquired using a commercial Omicron Nanotechnology variable temperature combined STM/NC-AFM (see Figure 2.1). The microscope is suspended on a double-stage spring suspension system, with additional copper eddy-current damping fins, inside a stainless steel vacuum chamber. This helps to decouple the microscope from its surroundings, thus reducing the mechanical noise. As mentioned in Chapter 1, the required surface cleanliness for atomic and submolecular resolution imaging necessitates pressures lower than the threshold for ultrahigh vacuum (UHV) conditions ($< 1 \times 10^{-9}$ mbar). These pressures were reached using an Agilent ion pump and periodic sublimation of titanium using an Arun Microelectronics TSP controller. The bulk gas pressure is pumped out using a combination of TV 301 Navigator turbomolecular pump and RV5 Edwards oil-sealed rotary vane pump in tandem, together with an initial three-day bakeout of the chamber, which helps to remove water and other molecules adsorbed on the inside walls of the chamber. The pressure during the experiments in the thesis typically ranged from 5×10^{-11} mbar to 1×10^{-10} mbar.

2 Experimental Methods

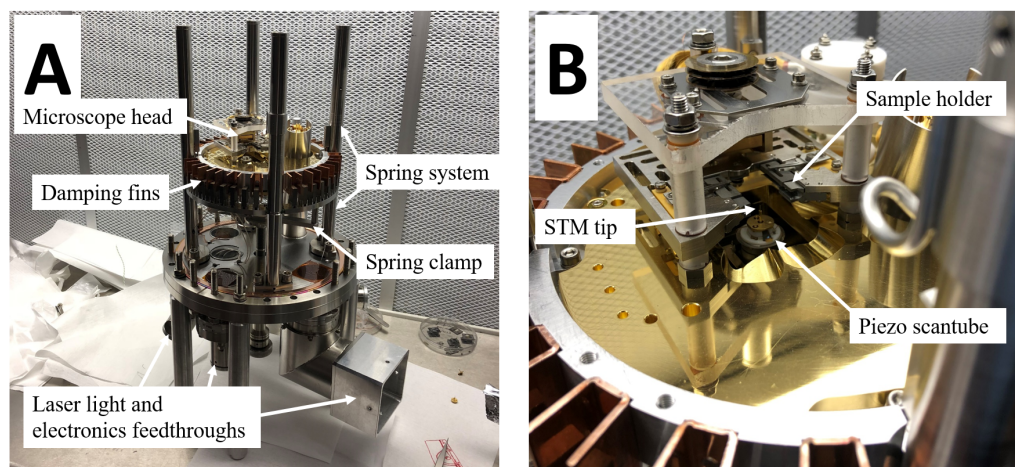


Figure 2.1: Photographs of combined STM/AFM microscope outside of its UHV chamber. A) Shows the microscope head mounted on the mechanical isolation systems of two-stage spring suspension and copper eddy-current damping fins. For tip / sample transfer in and out of the head the spring system should be clamped to stay rigid. Also shown are the laser light and STM/AFM electronics feedthroughs at the base. B) Shows a close-up of the microscope head, with sample holder, STM tip and scanner labelled.

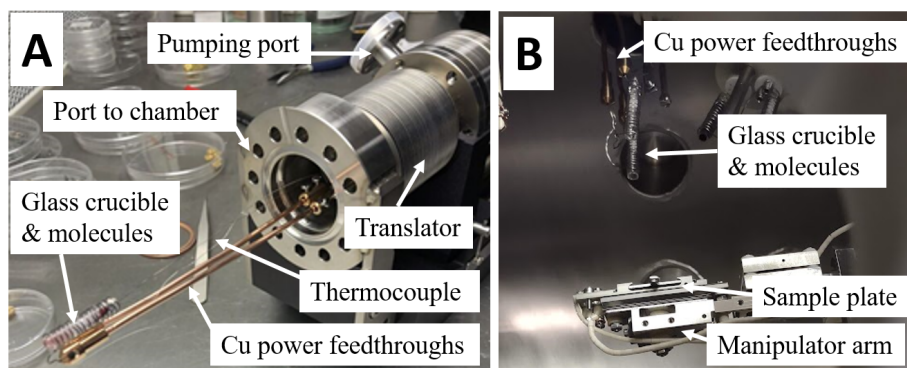


Figure 2.2: A) Photograph of home-built Knudsen cell out of the chamber. The molecular source is contained within the glass crucible using glass wool and is wrapped in tantalum wire which provides a heat source to evaporate the molecules out of the cell, to deposit on a surface. The power is supplied to the wire via copper feedthroughs, and the temperature is monitored using thermocouple wire from inside the glass crucible itself. The whole cell is designed to be pumped to UHV from atmosphere before introduction to the chamber via a gate valve and translator. B) Photograph of the Knudsen cell, pointed at an upturned sample plate, for deposition, inside the UHV chamber.

The chamber is equipped with a load-lock for sample and tip transfer from ambient, a stage for treatment of STM tips, an adjustable manipulator arm, which facilitates the annealing of samples, and an Omicron ISE 5 sputter gun for cleaning AFM tips and metal samples.

2.1.1 Sample Preparation

2.1.1.1 Ag(111)

For use in STM, commercial SPL Ag(111) samples were prepared in the chamber via repeated sputter anneal cycles. During sputtering, 1×10^{-5} mbar pressure of Ar^+ would be introduced with a beam energy of 2 kV from the sputter gun, directly at the Ag(111), in the manipulator arm, for 30 minutes at a time. The sample was annealed after sputtering in the manipulator arm at 500 °C for 30 minutes at a time.

2.1.1.2 Si(111)-(7×7)

Commercial Pi-kem Si(111) crystals were sonicated prior to introduction to the chamber for ~ 5 minutes in various solvents sequentially (Methanol, acetone, and isopropanol). Once in the chamber, the oxide layer was removed using standard flash annealing cycles to 1200 °C for ~ 10 seconds at a time. During flashing, it was ensured that the chamber pressure did not exceed 2×10^{-9} mbar. The (7×7) reconstruction (1), was formed using a quick cool down to 800 °C, followed by a slow cool down back to room temperature (several °C/s).

2.1.1.3 B:Si(111)-($\sqrt{3} \times \sqrt{3}$)R30°

The preparation protocol for this substrate was taken from Spadafora et al. (2014) (2), as this yielded the highest quality reconstructions, with lowest defect densities. Sonicated commercial Pi-Kem Si(111) crystals, with a high density of boron dopants (resistivity $< 0.005 \Omega cm$, approximately $2.6 \times 10^{18} / cm^3$), were flashed annealed to 1200 °C, for 10 seconds at a time, until the ($\sqrt{3} \times \sqrt{3}$) reconstruction would start to appear, indicating that a sufficient amount of boron dopants in the bulk crystal had risen to the surface (3). As with Si(111)-(7×7), it was made sure that the pressure did not exceed 2×10^{-9} mbar during flashing. The surface was then prepared by annealing the crystal at 900 °C for 1 hour (having been flashed repeatedly at 1200 °C), and then cooling to room temperature slowly (~ 1 °C/s). More detail on the B:Si(111)-($\sqrt{3} \times \sqrt{3}$)R30° can be found in Chapter 5 of this thesis.

2.1.2 Molecular Deposition Source

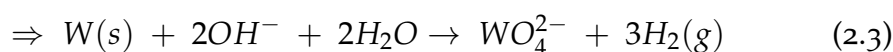
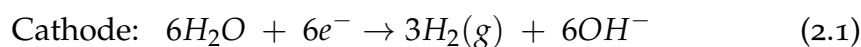
Figure 2.2 shows the homemade Knudsen cell built as a deposition source for various molecules across this thesis. The molecular source is contained within the glass crucible using glass wool and is wrapped in tantalum wire which provides a heat source to sublimate the molecules out of the

cell, to deposit on a surface. The power is supplied to the wire via copper feedthroughs, and the temperature is monitored using thermocouple wire from inside the glass crucible itself. The whole cell is designed to be pumped down before introduction to the chamber. While under vacuum, the Knudsen cells and molecular sources were degassed before introduction to the chamber by heating the tantalum wire around the molecule crucibles. Deposition temperatures and rates were estimated using preliminary experiments of various molecules on Ag(111) in STM.

2.2 STM tip preparation

2.2.1 Electrochemical Etching

The initial studies into STM understood the importance of the tip geometry for achieving atomic resolution, and hence the importance of their fabrication process (5, 6). Before introduction to the chamber, Tungsten (W) STM tips were given sharp, conical shapes, with small apex radii, via electrochemical etching (4, 7, 8) using the set up depicted in Figure 2.3. Lengths of W wire, of thickness 250 μm , suspended from an anode, were partially submerged into a solution of 4M NaOH etchant. A flow of current was made using a cathode in the solution, therefore the following oxidative reactions occur:



2 Experimental Methods

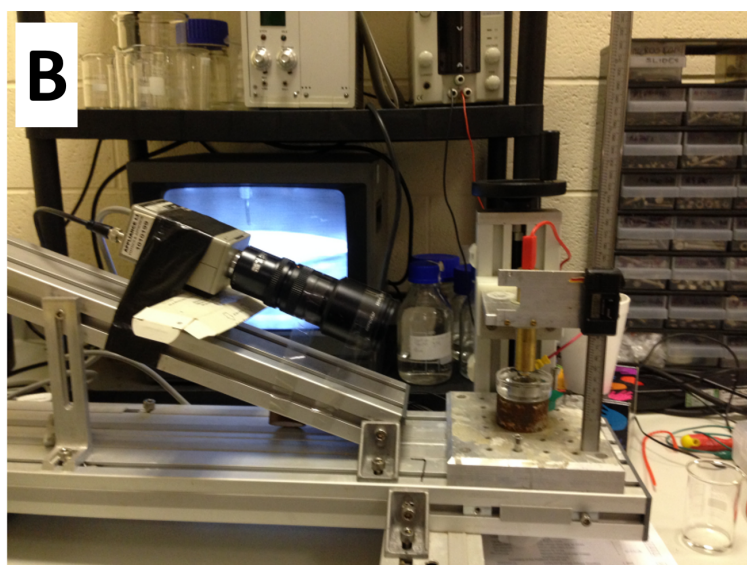
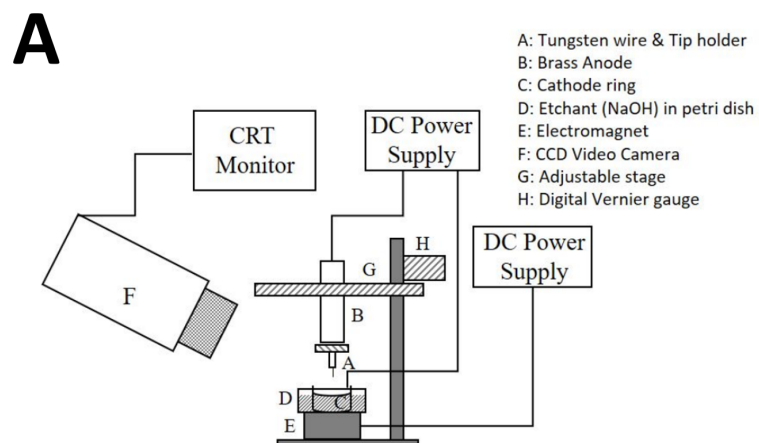


Figure 2.3: A) Labelled diagram to show set up used for etching W STM tips. B) Photo of set up.

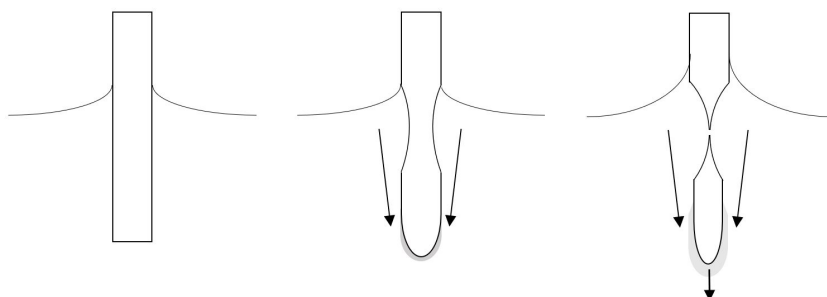


Figure 2.4: Etching process for a W wire segment partially submerged in $NaOH$ solution. The gathering of WO_4^{2-} ions (grey) toward the bottom of the wire leads to a gradient in the etching rate across the meniscus, which in turn leads to the necking and eventual drop-off of the wire, leaving a sharp tip. Figure after Chen (2008) (4).

Figure 2.4 depicts the etching process. A meniscus forms around the submerged tip, and OH^- ions diffuse from the cathode to the wire, creating a concentration gradient. Towards the bottom of the meniscus, the downward flow of WO_4^{2-} ions forms a viscous layer around the wire, protecting it from the build up of OH^- ions and therefore inhibiting etching in the lower region. The wire in the upper region is etched at a faster rate and thus loses more mass compared to the wire more deeply submerged, and the disparity in mass causes necking of the wire due to gravity and subsequent drop-off of the lower mass. The etching process and drop-off of the wire are observed better using a camera and monitor set up (Figure 2.3). Following an optimisation of various experiments the etching process can yield smooth, straight and sharp tips, with apex radii $> 100nm$ and small conical angles.

Post-drop etching is ideally inhibited in order to minimise the blunting of the tip. The power supply can be set to shut-off (with a delay as little as $500ns$) by virtue of the sudden reduction in circuit current after drop off. In addition, the gas products of the reaction (H_2 and O_2) tend to form around the tip at the meniscus level in form of bubbles. These bubbles inhibit the contact of W with the etchant, slowing the rate of etching. As a counter measure, an electromagnet was placed under the electrolyte bath to provide a circular motion of the solution and stir the bubbles. This resulted in the

2 Experimental Methods

reduction of the bubble adhesion on the tip and more acute conical angles of the tip apex. Following the procedure advised in McKendry (2007) (9), the electromagnet was supplied with a DC current of 0.5 A, and 11.4 V.

In practice, the sharpest and most symmetrical tips were consistently made following several previous etches. This is perhaps due to an increased concentration of WO_4^{2-} ions in the solution, which may help to further inhibit the etching around the more deeply submerged portion of the wire. Care was taken to minimise sources of mechanical vibration for a symmetrical necking process.

If the wire is not sufficiently submerged, the mass below the meniscus will not create a strong enough force to neck the wire to the point of drop-off. However, the greater the length of the submerged wire, the more likely a premature drop-off is to occur (7), which is likely to yield a misshapen tip. The optimal submergence depth is also dependent on the wire thickness (10).

For the *W* wire used in the etching set up, the optimal insertion depth was found by sweeping a range: 1.50 mm – 2.25 mm, assessing the shape, and estimating the apex radius. The insertion depth was measured using a mounted digital Vernier gauge. Following the etching, the tips were submerged in water (to wash off the residual *NaOH*) and then photographed through an optical microscope ($\times 10$ magnification). Using the optical microscope images, the tips that exhibited crookedness, bluntness, or a coiled apex (likely due to the recoil from drop off) were discarded. The remaining tips were then further characterised using a Hitachi SU8230 Field emission scanning electron microscopy (FE-SEM), which has a resolution of a few 10s of nm. A random order of depths was used, in efforts to negate any bias provided by the accumulation of WO_4^{2-} ions in the solution.

2.2.2 Focused Ion Beam

An alternative means of metallic tip etching is via focused ion beam (FIB). Gallium ions from a FEI Helios G4 CX Dual Beam FIB/SEM were used to further sharpen a STM tip. Etching via FIB is a lengthy process ($\sim 1 \mu\text{m}$ milled per minute) so instead, a tip that had the bulk material of

its apex already removed via electrochemical etching was used. With the SEM function of the apparatus, the beam shears off the tip material at user defined sections of the tip, and progress can be monitored in real time. The FIB was also used to etch a commercial Omicron qPlus sensor.

2.2.3 Results: Tip Characterisation

Figure 2.5 shows photographs and FE-SEM micrographs of etched tips across a range of insertion depths. The photo Figure 2.5.G revealed a crooked tip, and as such was discarded rather than imaging further in the FE-SEM. The SEM micrographs do not reveal any definitive trend of tip radii or quality of shape due to submergence depth across the range used. Both Figure 2.5.B2 (1.63 mm) and Figure 2.5.H2 (2.25 mm) share similar size and shape. Defects of apices appear throughout the sweep (Figure 2.5.A2, C2), F2). The tip that best exhibited a smooth, symmetric, sharp apex was Figure 2.5.E1 & E2), which was submerged in the electrolyte by 1.90 mm. From the SEM image, the tip radius was likely less than 10 nm. In comparison, SEM images of commercial qPlus quartz sensors with W tips, (already electrochemically etched out the box), were found to have tip radii on the order of 100 nm (see Figure 2.7.A). While no trend was observed, 1.90 mm was taken as a sensible depth to etch STM tips throughout this thesis, which corroborates well with the findings of McKendry (2007) (9), which suggests 2.00 mm as the optimal depth for STM tip etching.

Figures 2.6 & 2.7 depict before and after SEM micrographs of further etching via a FIB, a STM tip and qPlus tip respectively. With SEM microscopy being the most precise technique for tip apex characterisation, the FIB could not etch tips smaller than 10 nm. As such, it cannot be said here that the use of FIB is capable of producing sharper tips than standard electrochemical etching. The FIB apparatus could not etch tips smaller than 10 nm, as it is constrained to the resolution of the SEM microscope. But the FIB/SEM set up has the benefit of imaging in real time. Thus, it is a more reliable method of etching sharp tips than only electrochemically.

STM tips that were then introduced to the chamber were further treated to remove the oxide layer (that forms when exposed to atmospheric conditions).

2 Experimental Methods

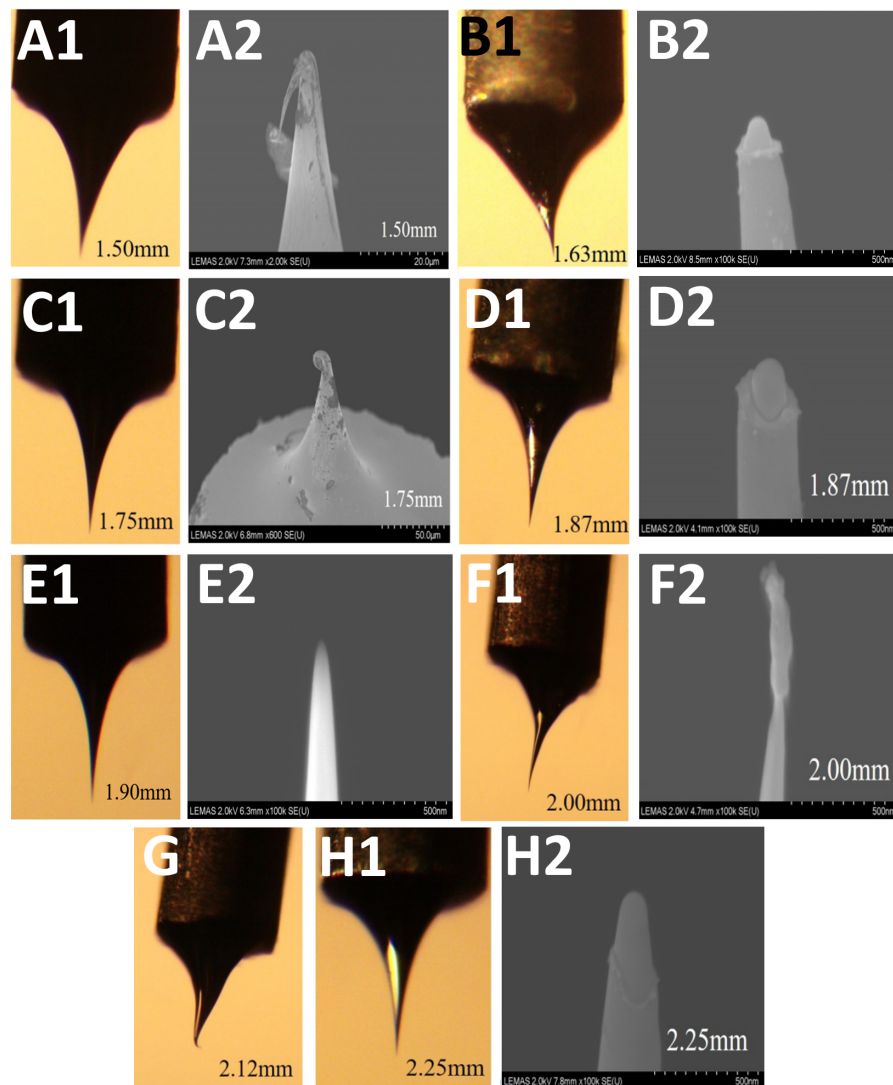


Figure 2.5: All letters labelled: 1) Optical microscope photographs of etched STM tips sweeping a range of insertion depths 1.50 mm to 2.25 mm. All letters labelled: 2) SEM micrographs of corresponding tips. From these micrographs, the size and shape of the tip apices were characterised. The most successful etch was carried out using a submersion depth of 1.90 mm (E1 & E2)), which yielded an approximate radius of 10 nm. The misshapen tip in G) was discarded and hence not further characterised in the SEM.

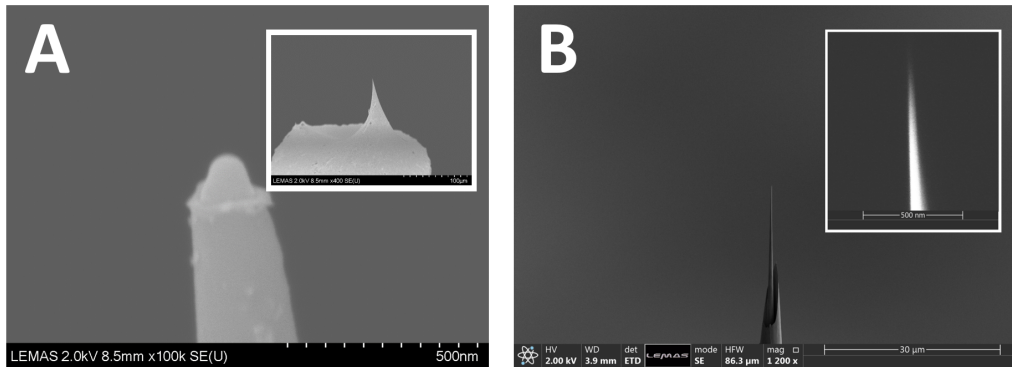


Figure 2.6: A) Hitachi SEM micrograph of STM tip (already electrochemically etched from Figure 2.5.B1&2) before FIB etching. Insert depicts the tip zoomed out enough to see bulk wire material. B) SEM image of same STM tip after milling with Helios FIB machine. Insert depicts higher magnification image of tip apex. Radius of FIB'd tip approximately a few 10s of *nm*.

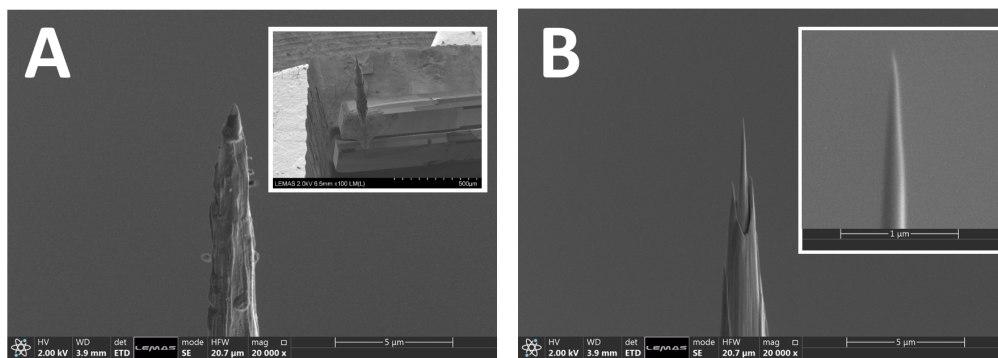


Figure 2.7: A) Hitachi SEM micrograph of commercial qPlus sensor tip before FIB etching. Insert depicts the sensor. B) SEM image of same sensor after milling with Helios FIB machine. Insert depicts higher magnification image of tip apex. Radius of FIB'd tip approximately a few 10s of *nm*.

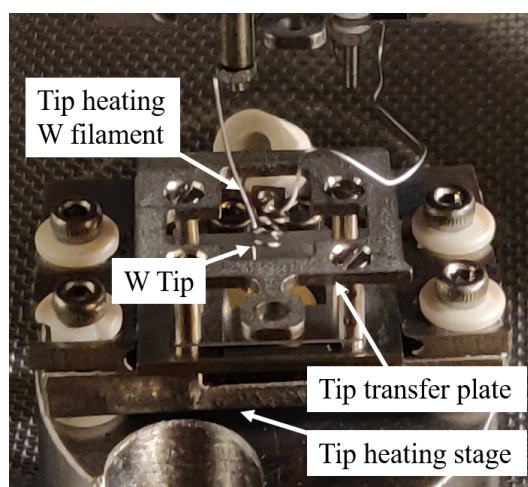


Figure 2.8: STM Tip heat treatment set up photograph

Bombardment of electrons can strip off this outer oxide layer. The tips were transferred to the treatment stage in the UHV chamber, and a W filament is introduced very close to the tip (see Figure 2.8). A direct current of 5.0 A (8.2 V) is passed through the filament, increasing its temperature to ~ 3000 °C, causing it to eject electrons. The tip in the stage is biased with 1.1 kV to attract the ejected electrons. The tip is exposed to an electron bombardment of ~ 5 mA for 1 minute. The heat treatment was assessed by imaging a Si(111)-(7 \times 7) surface and checking the contamination levels were sufficiently low to conduct long term imaging over the same scan area.

2.2.3.1 AFM Tip Preparation

Commercial Nanoworld silicon cantilever chips were glued onto tip holders before insertion into the load lock using EPO-TEK thermal adhesives. A conducting channel is made from the holder to the cantilever by use of a conductive epoxy glue. Surrounding this portion of glue is an insulating epoxy. Both glues were cured by heat treatment at 150°C for an hour. After introduction to the chamber, NC-AFM tips were then treated by argon sputtering for 5 minutes (with 1×10^{-5} mbar of Ar^+ and beam energy 2 kV) to remove the native oxide layer and other contaminant elements, and also to

sharpen the tip. A drawback of the positioning of both manipulator arm and sputter constrain is that the angle of the sputter gun beam is perpendicular to the AFM tip. In theory, it would be best to sputter normal to the tip, to ensure a complete etching of the oxide layer.

During imaging, both NC-AFM and STM tips were treated in-situ to improve resolution by gentle indentation into the surface or voltage pulses as described in Section 1.1.2.5.

2.3 Operation of Microscope

Data were acquired using a commercial Omicron Nanotechnology VT-STM/NC-AFM, operated using a RC5 Nanonis controller and PLL (OC4). All experiments were performed in Ultra High Vacuum (UHV) at room temperature.

W wire tips were typically biased between +1.5 – +2 V for STM experiments. Nanoworld cantilevers manufactured with spring constant, $k \sim 48 \text{ N/m}$, resonant frequency, $f_0 \sim 170.021 \text{ kHz}$, were used in the NC-AFM experiments. It was found that operating at large oscillation amplitudes did not inhibit the desired resolution (sub-molecular contrast), and provided lower Δf noise (see Section 4.5.1). As such, large oscillation amplitudes (A_0) were used $\sim 20 \text{ nm}$ throughout the NC-AFM experiments in the thesis.

The calibration between the excitation (V) and deflection (nm) of the cantilever was estimated using the γ method described by Simon et al. (2007) (11). The cantilevers used throughout the thesis typically exhibited calibration factors $\sim 50 - 70 \text{ nm/V}$. Cantilever deflection was measured using a standard four quadrant photodetector.

NC-AFM imaging was performed with a small voltage applied to the tip (typically +0.3 - +0.4V) to remove the electrostatic force due to the contact potential difference (CPD). Due to the semiconducting nature of the tips, STM based techniques were not used to prepare the tip apex (12, 13). Typically no tunnel was observed, but this was not the case for some of the NC-AFM experiments carried out on C_{60} molecules.

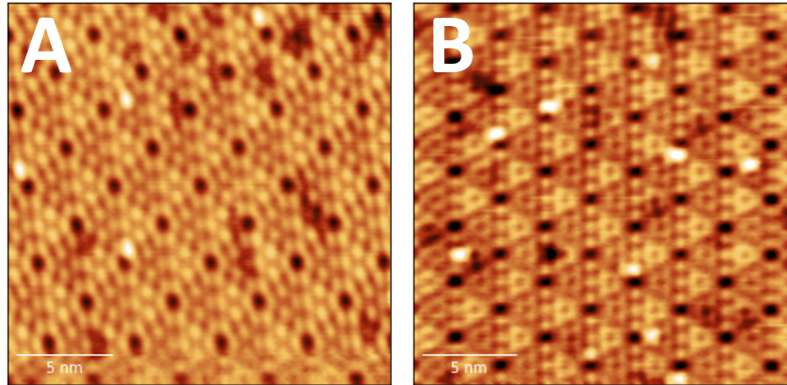


Figure 2.9: STM images of $Si(111) - (7 \times 7)$ scanned A) before feedforward correction and B) after. Feedforward correction helps to prevent distortion of the features during the scan.

The microscope was operated using a RC5 Nanonis controller and PLL (OC₄). The controller, with a built-in lock-in amplifier, facilitates atom tracking and feedforward correction for reducing the effects of thermal drift in the system. Furthermore, the Nanonis interface can implement custom home-built scripts, which are used to give instruction to the microscope (further details in Section 3.1).

2.4 Feedforward Correction

The feedforward correction technique (14), can help compensate thermal drift in STM / NC-AFM. A before-and-after example can be seen in Figure 2.9. The distortion of the $Si(111) - (7 \times 7)$ due to thermal drift is evident beforehand. After applying feedforward correction, the 'after' scan takes corrected data in-situ, and the surface is seen undistorted. For this reason, its implementation is almost essential for high-precision measurements when not operating under cryogenic conditions e.g. room temperature (15, 16). The technique relies on operating the SPM in a tracking mode (17), also referred to as 'atom tracking' (18), in order to measure the thermal drift. Atom tracking was originally implemented in SPM systems in order to lock

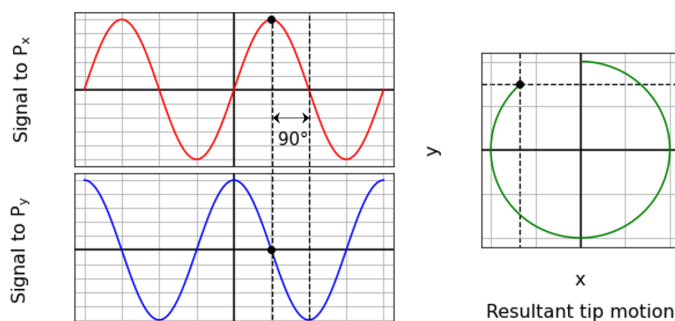


Figure 2.10: Tip motion due to dither signal: the tip traces a circular path (right) through the summation of sine curves sent to P_x and P_y piezos (left) - with a phase shift of 90° .

onto and study dynamic phenomena on surfaces. The applications include studying diffusion rates of molecules across surfaces (19, 20), thermally induced rotation of molecules (21) and the rearrangement of atoms within a cluster (22).

2.4.1 Tracking Mechanism

In tracking mode, small amplitude AC signals (of a set frequency ω) are applied to the P_x and P_y elements of the scan tube (17). A phase shift of 90° between the signals induces circular motion of the tip, see Figure 2.10.

Applying feedback control during this motion maintains the Δf or I signal by adjustments made in z . Due to these adjustments, $\delta z_{x,y}$, the resultant tip path is a circle which extends out of the xy plane. The tracking electronics measure the tilt of the circle (δz_x and δz_y) via a lock-in amplifier. Figure 2.11 depicts the case of a tip dithering with amplitude R around a 'hill-like' atom, wherein $\delta z_{x,y} \sim 0$ at the apex, the slope around this point results in some non-zero value of δz_x (and of δz_y , not depicted in figure).

Figure 2.12 depicts the schematic of a lateral feedback set up using a two-phase lock-in amplifier for tracking mode. The lock-in amplifier measures

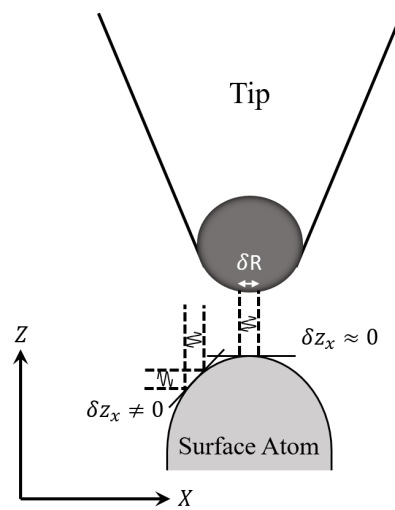


Figure 2.11: Tip dithers in lateral space with magnitude δR while modulating z . The slope of the tracked surface atom, δz is measured using a lock-in amplifier and lateral feedback adjusts the tip position back to the atom apex (where $\delta z \sim 0$).

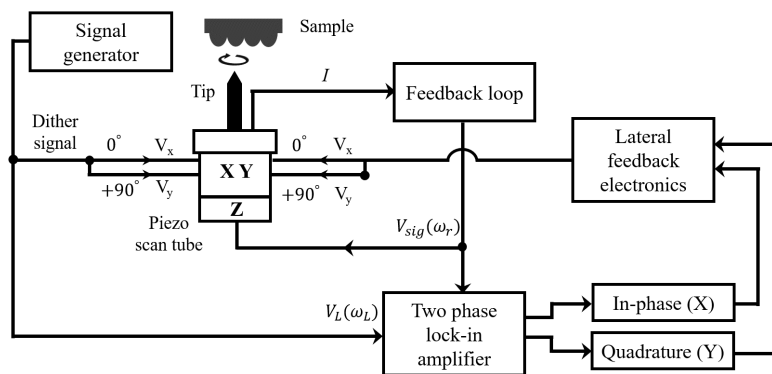


Figure 2.12: Schematic of atom tracking procedure using a two phase lock-in amplifier (LIA). The feedback signal $V_{sig}(\omega_r)$ is measured whilst dithering laterally and tip-sample distance feedback is engaged. The measured signal, along with the reference dither signal are mixed in the LIA, and then decomposed into in-phase and quadrature components. These are used to calculate δz_x and δz_y and hence the misplacement of the tip from the tracking point (where $\delta z_{x,y} \sim 0$). Corrective feedback signals can then sent to the piezo scanner. Figure after Abe and Morita (2009) (23).

the small perturbations $\delta z_{x,y}$. Using the reference dither signal, the return signal has components corresponding to δz_x and δz_y , generally referred to as the in-phase (X) and quadrature (Y) components (24). Using the respective δz_x and δz_y signals, the misplacement of the tip from the tracking site can be calculated and corrected using independent feedback loops. The tip, while dithering, therefore moves toward the apex of the feature, i.e. 'climbing the hill'. Any small changes in tip-sample distance via a lateral displacement (drift) are reversed, hence the tip is locked onto the feature.

Following an apparent, continuous measurement of the position of the tracked feature for a fixed period of time, an average velocity can be calculated, and countervailing DC offsets can be applied to the x, y, z elements of the scan tube. This moves the scan tube with the drifting sample, such that the net tip-sample displacement due to thermal relaxation is compensated for, during scanning and spectroscopy measurements (18). This technique of drift correction is known as 'feedforward correction'. In the electronic schematic Figure 2.12 the DC correction signals are added to the scan controller signals to the scan tube (14, 24).

When tracking highly mobile features, the tip dither speed ωR should be higher than the diffusion velocity (19). Otherwise the feature may displace outside the tip dither radius within a single cycle and would therefore no longer be able to lock onto the feature. The feedback mechanism can also be modified to a positive loop i.e. the DC signals generated move the tip in the direction of greatest slope, in order to lock onto depressions (17).

2.4.2 Lock-in Amplification

Lock-in amplifiers (LIAs) are used to detect desired constituents of a signal (i.e. δz_x and δz_y), of specified frequency ω and phase θ , where S/N ratios are small, and regular amplification and filtering schemes fail. A LIA 'locks in' to a known frequency, and can track changes to the amplitude and phase of that signal, despite large proportions of noise (25).

Figure 2.13 follows an example provided by Stanford Research Systems (26), wherein a desired measurable is a $10nV, 10kHz$ AC signal. If an amplifier has a gain of 1000, the amplified signal will be $10\mu V$. Even a low-noise amplifier

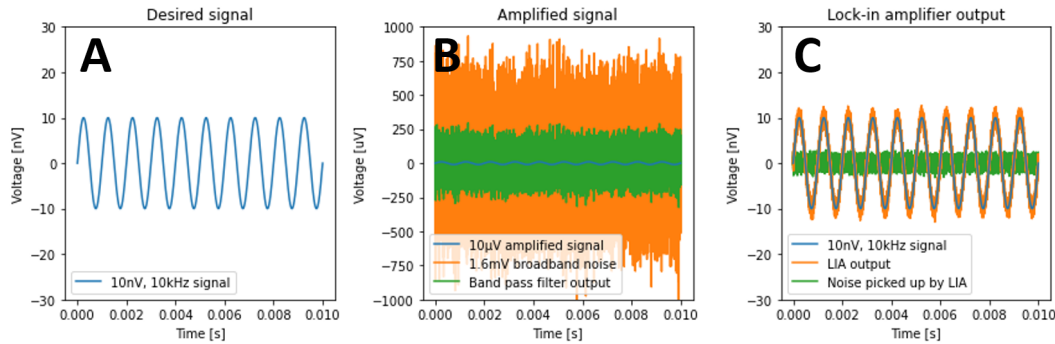


Figure 2.13: A) Example AC signal of amplitude 10 nV and frequency 10 kHz . B) Measurement of the signal through conventional methods requires amplification, which contributes a large amount of broadband noise (1.6 mV). The S/N ratio of the amplified signal is only ~ 0.01 . Feeding the amplifier signal through a band pass filter (of Q factor 100) still detects signals $\pm 100\text{ Hz}$ around the signal frequency but only increases the S/N ratio to 0.2. C) Alternatively the signal can be detected using a lock-in amplifier, where the detection bandwidth is on the order $\pm 0.01\text{ Hz}$. This increases the S/N ratio to 20.

(with example bandwidth 100 kHz) will input $\sim 5\text{ nV}/\sqrt{\text{Hz}}$, which will incur 1.6 mV broadband noise. After amplification the signal is still masked within the instrument noise, and as it is proportional to the gain, changing this parameter will not improve the S/N ratio.

If one makes use of a band pass filter on the signal, only signals within the bandwidth of the filter will be detected. A band pass filter of $Q = 100$ (very small bandwidth), centered on the signal frequency (10 kHz), will detect signals in the range $\pm 100\text{ Hz}$. The noise that passes through the filter will be $50\text{ }\mu\text{V}$ ($5\text{ nV}/\sqrt{\text{Hz}} \times \sqrt{100\text{ Hz}} \times 1000$), which still only yields a S/N ratio of 0.2.

In comparison, LIAs have bandwidths as narrow as 0.01 Hz . The resultant detection noise is $\sim 0.5\text{ }\mu\text{V}$, a S/N ratio of 20.

2.4.2.1 Phase-Sensitive Detection

LIAs operate in experiments where the subject of experiment is excited with a generated AC signal: $V_L \sin(\omega_L t + \theta_{ref})$, this signal is also sent to the

2 Experimental Methods

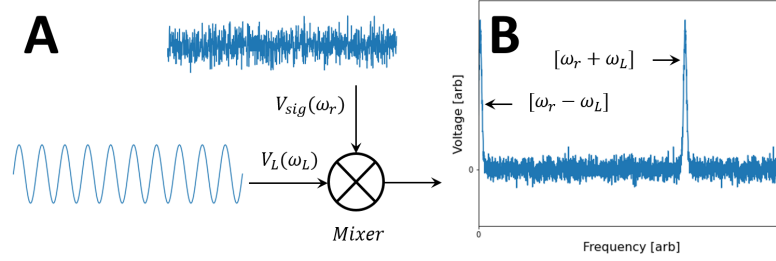


Figure 2.14: A) Return (buried in noise) and reference signals $V_{sig}(\omega_r)$ and $V_L(\omega_L)$ are multiplied together using a signal mixer in the LIA. B) The output of the mixer has two peaks in the frequency domain at $[\omega_{ref} - \omega_L]$ and $[\omega_{ref} + \omega_L]$. In the case where $\omega_r = \omega_L$, the peak associated with the frequency difference, resides at 0 Hz, i.e. a DC component proportional to V_{sig} . A low pass filter can then be applied to the mixer output, which helps to filter all other contributions.

lock-in amplifier as a reference signal.

Using a phase-sensitive detector (PSD), the LIA amplifies and multiplies the return signal V_{sig} (with return frequency ω_r) by the reference signal. The output of the PSD is:

$$V_{PSD} = V_{sig} \sin(\omega_r t + \theta_{sig}) \times V_L \sin(\omega_L t + \theta_{ref}) \quad (2.4)$$

$$= \frac{1}{2} V_{sig} V_L \cos([\omega_r - \omega_L]t + \theta_{sig} - \theta_{ref}) - \frac{1}{2} V_{sig} V_L \cos([\omega_r + \omega_L]t + \theta_{sig} + \theta_{ref}) \quad (2.5)$$

In the frequency domain, the mixed signal output in (Equation 2.5) has two peaks, each corresponding to the summation frequency $[\omega_r + \omega_L]$, see Figure 2.14.B (27). Following this mixing of signals, the use of a low pass filter helps to remove remove all the output of the PSD except for the peak associated with $\omega_r = \omega_L$, which resides at 0 Hz, i.e. a DC signal, which is proportional to V_{sig} and the cosine of the phase difference $\theta_{sig} - \theta_{ref}$:

$$V_{PSD} = \frac{1}{2} V_{sig} V_L \cos(\theta_{sig} - \theta_{ref}) \quad (2.6)$$

After passing through the low pass filter, the output V_{PSD} in (Equation 2.6), is proportional to the observable signal of interest: V_{sig} . In the case of atom tracking, a function generator sends the signal: $V_L \sin(\omega_L t + \theta_{ref})$ to both P_x and P_y of the scan tube and LIA as the reference signal. During tracking mode in SPM, the signal from the tip-sample distance feedback loop is fed into the LIA, and the signal component that matches the reference frequency ω_L is drawn out. This signal, δz is the response of the feedback loop due to the lateral dithering signal.

Noise of frequency $\sim \omega_L$ may pass through the filter, and this can be reduced by use of a narrower bandwidth, however this will require longer durations of data acquisition and thus the filter limits the time resolution of the measurement. The choice of bandwidth is a trade off between S/N and time resolution.

Measuring a DC signal in (Equation 2.8), requires that $\cos(\theta_{sig} - \theta_{ref})$ remains constant, i.e. the reference signal used in the LIA must be phase-locked to the original signal from the function generator. LIAs typically use a phase-locked-loop (PLL) to accomplish this. The PLL actively tracks the external reference signal, and ω_L and θ_{ref} are adjusted to keep up with changes made to the external reference signal. Sometimes however the function generator is within the LIA itself, in which case there is no need for a PLL.

2.4.2.2 Two-Phase Synchronous Detection

In tracking mode, two PSDs with reference signals 90° apart are used to decompose the response signal δz into orthogonal components $\delta z(X)$ (in-phase) and $\delta z(Y)$ (quadrature) (24). The use of the second PSD removes the phase dependency by multiplying the signal from the first, V_{PSD1} by the reference signal of the LIA, phase-shifted by 90° . The outputs are:

$$V_{PSD1} = V_{sig} \cos(\theta_{sig} - \theta_{ref}) \quad (2.7)$$

$$V_{PSD2} = V_L \sin(\omega_L t + \theta_{ref} + 90^\circ) \times V_{sig} = \frac{1}{2} V_{sig} V_L \sin(\theta_{sig} - \theta_{ref}) \quad (2.8)$$

$$\sim V_{sig} \sin(\theta_{sig} - \theta_{ref})$$

The in-phase and quadrature signal, whether in Cartesian (x, y) or polar form (R, θ) represent the signal (δz_x in the case of atom tracking set up in Figures 2.11, 2.12) as vector relative to the LIAs reference oscillation. The in-phase component measures signals of zero phase difference. Signals with a non-zero phase difference are picked up in the quadrature output. For tracking both the δz_x and δz_y signals, two lock-in amplifiers are used in the Nanonis controller. The reference signals of each LIA are phase shifted by a value adjusted to optimise the tracking in both x and y directions (28).

2.4.3 Incorporating Atom Tracking with Data Acquisition

The resultant drift velocity between tip and sample is only constant for a finite duration of time, due to non-linearities in the drift behaviour (24). Thus, for a given level of precision, there is a maximum duration t for which the drift velocity can be assumed constant before it becomes necessary to re-measure it. Assuming quadratic behaviour of each vector, $r(t) = 1/2 a_{drift} t^2$, with acceleration a_{drift} , then the time until a correction can be considered incorrect is given by:

$$t < \sqrt{\frac{2\Delta g}{a_{drift}}} \quad (2.9)$$

where Δg is the desired precision of the lateral positioning, and has to be small enough for a given a to reliably return to the same feature if iterative tracking events are to take place over the same feature (24).

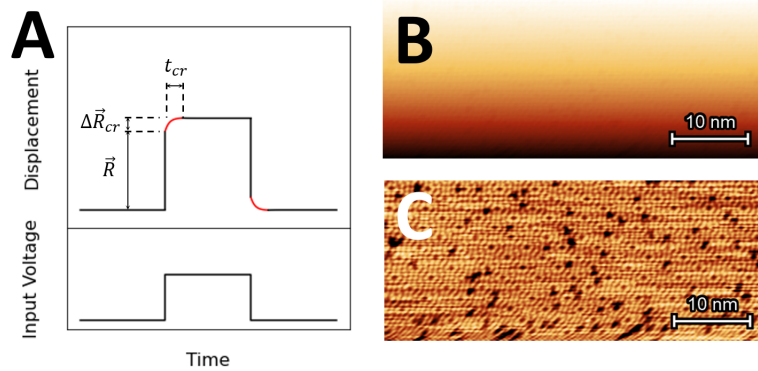


Figure 2.15: A) Piezo creep response to a step voltage. The scan tube immediately extends \vec{R} . It continues to extend $\Delta\vec{R}_{cr}$ over a duration t_{cr} due to creep (red curved portion of displacement). Figure after Habibullah. 2020 (33). B) Raw data depicting the creep effect distorting imaging, in a STM image of the Si(111)-(7x7) surface, following approach of the tip. The scan begins from the bottom, wherein the distorting effect of the piezo creep is most prominent. Image parameters: Set point = 20 A, $V_{gap} = +2$ V, scan speed = 130 nm/s. C) As B), with a median plane subtraction has been applied, removing the creep in the z direction, and the plane flattened in Gwyddion (34), so that the lateral creep can be more clearly observed.

The principle behind feedforward correction (modelling the drift and hence compensating image distortion) had previously been demonstrated without the use of atom tracking. Such methods rely on well-studied crystal lattices in order to either, calculate a constant drift post-hoc (29, 30), or to reverse the slow scan direction and examine the change in average reciprocal lattice vectors (31), or via other more complicated algorithms (32). However, modelling the drift based on the tip trajectory during tracking requires only a feature to lock onto, and the tracking measurement is simple to iterate for the non-linear elements of the thermal drift.

2.4.4 Piezo Creep

Piezoelectric scanners exhibit the creep effect, wherein the piezo crystal continues to deform after a voltage has been applied. Figure 2.15.A depicts a step voltage sent to a scan tube to displace the tip along some intended vector, \vec{R} . The majority of the piezo extension will be covered in less than a millisecond. However, the crystal 'creeps' asymptotically for the remaining extension, $\Delta\vec{R}_{cr}$, taking significantly longer to reach (t_{cr}). $\Delta\vec{R}_{cr}$ is typically $\sim 10\%$ of the full extension (33, 35, 36).

Piezo creep contributes to image distortion following tip movements (see Figure 2.15.B). The effect is more easily observed if $\Delta\vec{R}_{cr}$ is of the order of the surface features or larger, hence it follows that the creep effect is more prominent following larger tip movements. In particular, scanning soon after initial approach to surface (where P_z undergoes repeated full extension & contraction, upwards of 100s of times), typically introduces significant levels of creep. Additionally, the effects of hysteresis of, and cross-talk between, the piezo elements contribute further errors to the tip positioning mechanism following large movements (30, 33).

Whilst conducting SPM experiments, creep can be avoided by waiting several hours following any large movements, (like the surface approach) (31), and minimising tip movements during data acquisition.

References

1. D. Petrovykh, *Si(111) Surface and 7×7 Reconstruction*, Website Website accessed: 2023-01-19, 2008, (<https://nanowiz.tripod.com/sisteps/si111.htm>).
2. E. J. Spadafora *et al.*, *The Journal of Physical Chemistry C* **118**, 15744–15753 (2014).
3. B. Baris *et al.*, *ACS Nano* **6**, 6905–6911 (2012).
4. J. Chen, *Introduction to Scanning Tunneling Microscopy* (Oxford University Press, 1993).

5. G. Binnig, H. Rohrer, C. Gerber, E. Weibel, *Phys. Rev. Lett.* **49**, 57–61 (1982).
6. G. Binnig, D. Smith, *Review of Scientific Instruments* **57**, 1688 (1986).
7. J. P. Ibe *et al.*, *Journal of Vacuum Science & Technology A* **8**, 3570–3575 (1990).
8. A.-s. Lucier, PhD thesis, McGill University, 2004.
9. J. E. McKendry, PhD thesis, University of Leeds, 2007.
10. A. I. Oliva, A. G. Romero, J. L. Pena, *Review of Scientific Instruments* **67** (1996).
11. G. H. Simon, M. Heyde, H.-P. Rust, *Nanotechnology* **18**, 255503 (2007).
12. L. Gross, F. Mohn, N. Moll, P. Liljeroth, G. Meyer, *Science* **325**, 1110–1114 (2009).
13. A. M. Sweetman *et al.*, *Nature Communications* **5** (2014).
14. M. Abe *et al.*, *Applied Physics Letters* **90**, 203103 (2007).
15. Y. Sugimoto, K. Ueda, M. Abe, S. Morita, **24**, 84008 (2012).
16. K. Iwata *et al.*, *Nature Communications* **6**, 7766 (2015).
17. D. W. Pohl, R. Möller, *Review of Scientific Instruments* **59**, 840–842 (1988).
18. M. Abe, Y. Sugimoto, O. Custance, S. Morita, *Applied Physics Letters* **87**, 173503 (2005).
19. B. S. Swartzentruber, A. P. Smith, H. Jónsson, *Physical Review Letters* **77**, 2518–2521 (1996).
20. C. Dri *et al.*, *Ultramicroscopy* **205**, 49–56 (2019).
21. L. J. Lauhon, W. Ho, *Journal of Chemical Physics* **111**, 5633–5636 (1999).
22. E. Inami *et al.*, *Nature Communications* **6**, 6231 (2015).
23. S. Morita, *Noncontact Atomic Force Microscopy: Volume 2* (Springer, 2009), p. 125.
24. P. Rahe *et al.*, *Review of Scientific Instruments* **82** (2011).
25. P. Horowitz, *The art of electronics*, eng (Cambridge University Press, New York, Third edition. 2015), ISBN: 9780521809269.

26. S. R. Systems, *About Lock-In Amplifiers*, Website accessed: 2022-06-24, 2022, (<https://www.thinksrs.com/downloads/pdfs/applicationnotes/AboutLIAs.pdf>).
27. Z. Instruments, *Principals of Lock-in Detection*, Website accessed: 2022-06-25, 2022, (zhinst.com/americas/en/resources/principles-of-lock-in-detection).
28. Specs, *Nanonis STM simulator Tutorial: Manual Version 4.0* (Specs-Zurich, 2015).
29. V. Y. Yurov, A. N. Klimov, *Review of Scientific Instruments* **65**, 1551–1557 (1994).
30. D. K. Schwartz, J. Garnaes, R. Viswanathan, S. Chiruvolu, J. A. N. Zasadzinski, **47** (1993).
31. J. T. Woodward, D. K. Schwartz, *Journal of Vacuum Science and Technology B: Microelectronics and Nanometer Structures* **16**, 51–53 (1998).
32. K. J. Ito, Y. Uehara, S. Ushioda, K. Ito, *Review of Scientific Instruments* **71**, 420–423 (2000).
33. H. Habibullah, *Measurement: Journal of the International Measurement Confederation* **159**, 107776 (2020).
34. D. Nečas, P. Klapetek, *Central European Journal of Physics* **10**, 181–188, (<http://gwyddion.net/>) (2012).
35. A. J. Fleming, K. K. Leang, *Ultramicroscopy* **108**, 1551–1557 (2008).
36. N. D. Follin, K. D. Taylor, C. J. Musalo, M. L. Trawick, *Review of Scientific Instruments* **83** (2012).

3 Development of Experimental Atom Tracking and 3D Spectroscopy Techniques

This chapter details the development of the techniques required to gather and process high-resolution 3D force maps in NC-AFM at room temperature. It covers the scripted experimental procedures written and implemented using Laboratory Virtual Instrument Engineering Workbench (LabVIEW) visual programming language (1), and how the data are processed using code written in Python (2). In addition, the steps made to optimise the drift correction procedure and the different script types are described. The final results of the finished LabVIEW scripts are presented in chapters 4 & 5.

The scripts used in this thesis fall into various categories. The most basic is iterative topographic scans of the same area in SPM. Beyond that data can be acquired in constant height (without feedback operation), to obtain spectroscopic data sets. The constant height data sets were acquired via raster scan and grid spectroscopy.

3.1 LabVIEW Scripting

3.1.1 Initial Conditions for Scripted Data Acquisition

For the purposes of gathering high-resolution 3D data sets in NC-AFM, several conditions should be satisfied prior to the experiment. The piezo creep should be minimised, having waited a few hours following approach.

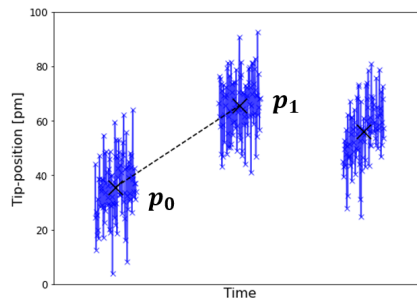


Figure 3.1: Graph of tip position and average coordinate for a given dimension (x, y, z) whilst the tip is locked onto surface feature for a few seconds, before resuming data acquisition. The LabVIEW script uses the distance between sequential average positions to calculate the residual drift (indicated by dotted line) and update the feedforward correction.

The tip state should already give the desired contrast, using in-situ preparation (gentle indentation, on semi-conducting surfaces (3)). The surface region to be measured using the script, should ideally be free of adsorbed contaminants or surface defects, and be flat (adjustments to the (x, y) plane for any sample tilt were made using the Nanonis controller). Lastly, the bulk thermal drift at a given time should already be compensated manually using feedforward correction. In practice this is typically done by a simple tracking measurement (for ~ 1 minute) of the displacement of a substrate adatom, and applying linear fit of the trajectory as a feedforward correction to the scan tube. This is necessary because the scripting is suited only to calculating and correcting the *residual* thermal drift as it changes over time. These changes are smaller in magnitude compared to the bulk drift.

3.1.2 Drift Correction Procedure

The central premise of all scripts is to take data intermittently, whilst regularly updating the feedforward correction applied to the piezo scanner. Conventionally feedforward correction vectors are calculated via a linear fit of a continuous displacement of a feature the tip is locked on to. To achieve acceptable accuracy for the calculated linear fit, the tip should track the feature for ideally ~ 1 minute (4, 5). Doing so significantly increases the

duration of the experiment, and can be prone to errors when the thermal drift behaves non-linearly.

Alternatively the thermal drift can be calculated by measuring the change in position of a tracked feature before and after a period of data acquisition (e.g. a raster scan). When in tracking mode, LabVIEW continuously measures the x , y and z positions of the tip over a short period of time (~ 10 seconds) whilst it dithers around a 'hill-like' feature. Figure 3.1 shows the burst measurement position and the calculated average position in 3D space (p_0). It is not necessary to leave the tip in tracking any longer than is needed to estimate the apex position. Tracking mode is then disengaged, and data can be acquired for a period of time that satisfies Equation 2.9. Afterwards the tip is brought back to p_0 and tracking is re-engaged. The position of the tracked feature is likely to have displaced slightly due to thermal drift, so the tip (via the lateral feedback mechanism) must spend some duration of time 'finding' the apex. The new position is reached, p_1 , and a set of feedforward correction vectors (V_x, V_y, V_z) is calculated from the difference, $p_1 - p_0$, divided by the time taken between tracking measurements, $t_1 - t_0$. These feedforward correction vectors, V_x, V_y and V_z , are applied to the piezo scanner via the Nanonis controller. Subsequent measurements would then be conducted with a more accurate compensation of the thermal drift, and the process is continually repeated.

In addition to regularly updating the feedforward vectors, it is also necessary to compensate for the displacement $p_1 - p_0$. This vector is applied by the LabVIEW script, via the Nanonis controller, to the (x, y) coordinates of the next scan frame (or point spectra location). Displacement in z due to thermal drift is already corrected by virtue of feedback operation during tracking. The latter position, p_1 of one measurement, becomes the former position, p_0 of the next measurement. However, this was only the case for data presented in Chapter 5. The data presented in this chapter, and Chapter 4, were gathered using an early version of the drift correction program, whereby the p_0 and p_1 are used only once and then 'forgotten'. The script required a fresh pair of position values for each calculation of displacements and drift velocity. Thus, this unfinished version of the program required shorter acquisition times (in between tracking) than was strictly necessary.

Figure 3.2 depicts a timing diagram, for constant height data acquisition in

3 Development of Experimental Atom Tracking and 3D Spectroscopy Techniques

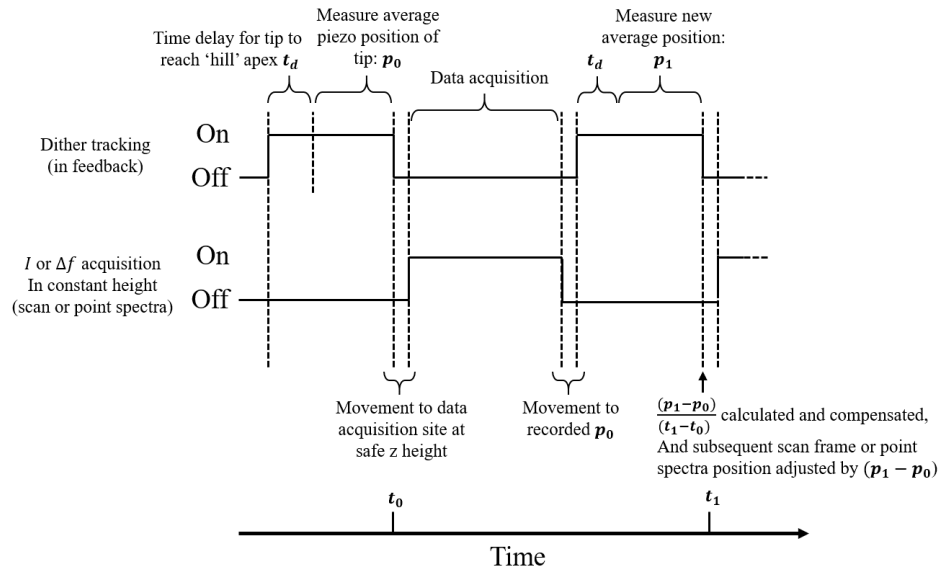


Figure 3.2: Timing diagram for acquisition of large multi-dimensional data sets without feedback in SPM. Starting from tracking mode, an average piezo position of the tip, p_0 is measured after waiting sufficient time, t_d for the tip position to stabilise. The dither signal and feedback are then both disengaged. The tip then moves in constant height to its intended lateral position (with an offset applied to P_z to ensure a safe distance is maintained whilst in transit). Next, the I and Δf signals are recorded whilst conducting a scan, or point spectra. The constant height data measured will be relative to the z component of p_0 . Afterwards, the tip is moved back to p_0 , and the feedback and tracking electronics are re-engaged. The position of the tracking apex (or hill) will have changed slightly due to residual thermal drift. A time, t_d is waited to allow the tip to stabilise at the new position, p_1 following a measurement of the average position of the tip. The vector $p_1 - p_0$ is calculated at that moment and then applied as an offset to the next intended position of the tip, helping to reverse the displacement. By recording the time when the position is measured, the current velocity of the drift can be estimated. This velocity is applied to the piezo as a feedforward correction, such that the DC signal sent to piezo scanner has an up to date compensation vector through the subsequent data acquisition. This process iterates, as more elements of the data set are acquired. Figure after Abe et al. (2005) (4).

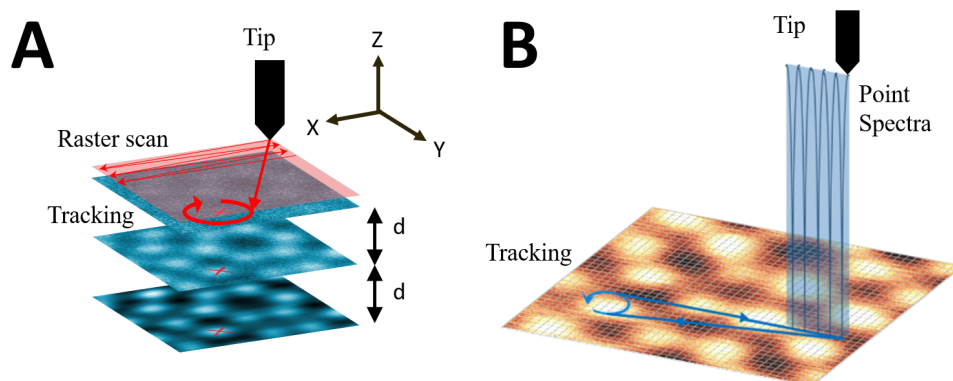


Figure 3.3: A) Constant height slices method protocol: The script alternates between scanning in constant height mode and tracking mode (with feedback on), using a consistent feature of the surface. n constant height images sweep in z with spacing d to produce a 3D matrix of data, whereby the regular feedforward correction maintains the lateral field of view and reduces z -drift across each scan. B) Matrix collated via single point spectroscopy curves, which comprise a grid coordinate system. Feedback and tracking is resumed after every (for example) 5 spectra.

SPM, with the LabVIEW drift correction protocol. To mitigate the risk of tip-changes in the absence of feedback, it was necessary to keep the tip high above the surface during lateral tip movements across the sample (moving to and from the tracking position).

3.1.3 Gathering Constant Height Data in SPM

As explained by Gross et al. (2009) (6), it is generally only possible to obtain sub-molecular contrast during NC-AFM imaging of organic molecules by operating in the repulsive part of the tip-sample interaction, where Pauli repulsion becomes dominant. Typically in NC-AFM, the set Δf value for feedback operation corresponds to the attractive force regime. It is impractical to operate the feedback loop in the repulsive regime across sites of different reactivity, due to issues of feedback loop and tip instability. For

this reason, constant height operation is usually required in order to enter the repulsive regime and obtain sub-molecular contrast.

For force mapping in particular, it is necessary that the tip traverses both the attractive and repulsive regimes in the data sets. Therefore to obtain the desired result (3D force maps of sub-molecular resolution), the use of constant height imaging is required, which, at room temperature, necessitates highly effective correction of the thermal drift. This is extremely challenging, and is likely the reason why thus far, room temperature force maps of submolecular resolution have not yet been reported in the literature.

Figure 3.3 depicts the two principal methods used in this thesis for acquiring multi-dimensional constant height data sets in SPM: stacking constant height images as slices A), and grid spectroscopy B).

3.1.3.1 Constant Height Slices

Figure 3.3.A depicts the procedure for gathering constant height images iteratively, over the same region of the sample, whilst altering the tip-sample distance, z , by some incremental spacing d . Acquiring data in this manner has previously seen success in mapping intramolecular forces at cryogenic temperatures (6–9), and mapping the forces over atoms at room temperature (10, 11). Similar to the method described by Sugimoto et al. (2010) (12), the script engages tracking mode between scans over a desired site, in order to update the feedforward correction. This is a necessity for taking constant height data at room temperature. The scan speed must be sufficiently fast to satisfy Equation 2.9, allowing the tip to always return to the same feature being tracked (indicated by the red 'x' in A)). If the time difference between tracking events, $t_1 - t_0$ is large enough that the tip locks onto a different feature, the script loses the ability to accurately calculate the displacement and drift. The script is unlikely to stabilise from that point and should be shut off. All tip-sample distances are relative to the z height associated with the feedback set point during tracking. No *post-hoc* alignment was applied to the images gathered throughout this thesis. Sufficient alignment was already provided by the in-situ drift correction procedure.

3.1.3.2 Grid Spectroscopy

Conversely, the grid spectroscopy method collates single-point spectra, taken in z , which collectively comprise a grid in the (x, y) plane (13–15). As with the constant height slices method, acquisition of the multi-dimensional data set via grid spectroscopy is regularly interrupted in order to engage tracking mode, so that the feedforward correction can be calculated and updated. Figure 3.3.B shows an example grid spectroscopy protocol, where the SPM tip performs 5 point spectra, before entering tracking mode on a desired adatom. When it resumes data acquisition, the tip moves to the position for the 6th spectra and so on. Alongside each update to the feedforward vectors, the past displacement is calculated and reversed by shifting the coordinates of each element in the grid (x, y) . A comparison of each of these methods is discussed in Section 3.3.5.

3.1.4 LabVIEW Interface

All data sets were acquired using a single LabVIEW program, whose layout is divided across three tabs. The first tab allows the user to change the dithering parameters of tracking, and carry out manual bulk corrections to the drift via a linear fit which is modelled on user-chosen limits on the tip position data (this is also possible using merely the Nanonis software). The contents for the second tab allow the user to define the data acquisition parameter. Switches are set prior to the experiment that decide whether data will be gathered with or without feedback operation. In the case of constant height data sets, the furthest and closest tip-sample distances are set by the user. Additional parameters, such as the safe tip-sample distance and number of repeat measurements can be set too. The tip bias, both for data acquisition, and for tracking are set (changes to the bias are slewed to avoid pulsing the tip). Once the user is satisfied that the feedback set point and tracking parameters provide stable lateral feedback, a button press triggers the automatic data acquisition and drift correction procedure. The third tab presents the graphs that continually plot the output of the tip position measurement, the vectors calculated via average positions, and

3 Development of Experimental Atom Tracking and 3D Spectroscopy Techniques

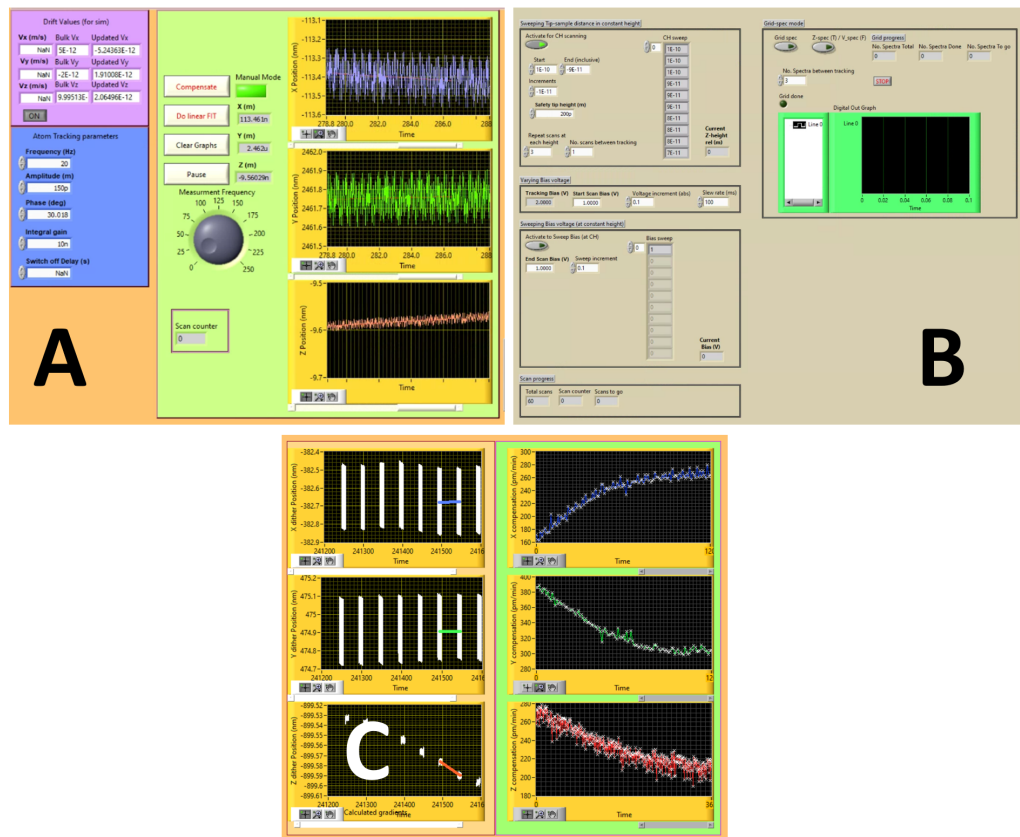


Figure 3.4: Home-built LabVIEW program interface A) The first tab, which is for manual bulk correction of thermal drift and for setting dithering parameters. The three graphs plot the tip position as it enters tracking mode. Linear fits and feedforward corrections are made to flatten x , y and z position read-outs. B) The second tab, is for the switches and limits that set the parameters for the experiment. The data acquisition method (slices or grid spectroscopy), and the grid dimensions are all selected in this tab. C) The third tab, which displays the tip position and calculated drift vectors which are plotted over the course of the experiment.

finally the feedforward correction vectors (these are also saved into a data file in LabVIEW).

3.2 Temperature Control

The temperature of the scan head of the microscope was measured using a Lakeshore temperature controller 331 (connected to a Pt-100 Ω resistance temperature detector, mounted at the scan head) during the scripted experiments, as was the temperature of the surrounding laboratory. The scan head temperature was also regulated using the same Lakeshore unit and a built in heater at the scan head. It functions using a PID control loop, with variables: proportional (P), integral (I), and derivative (D). The PID equation in the Lakeshore Model 331 is:

$$\text{Heater Output} = P \left[e + I \int (e) dt + D \frac{de}{dt} \right] \quad (3.1)$$

where the error, $e = (\text{Set temperature} - \text{Feedback reading})$ (16). These parameters were manually tuned until a stability of $\pm 2 \text{ mK}$ was observed. Empirically, parameters of $P = 100, I = 10, D = 50$ were found to give the best stability. The lab temperature was regulated using a thermostat. It was not possible to tune this regulation, beyond adjusting the set point (which was generally held at 293 K).

It should be noted that the scan head temperature readout (and hence, the set points that were used) was offset by $\sim +20 \text{ K}$ above room temperature, due to a systematic error caused by mismatched corrections to the scan head diode. This was not deemed significant, because the quantity of interest was in the temperature stability merely as a comparative tool. As a result, the diode readings at the scan head have not been calibrated to the thermocouple used to measure the lab temperature.

3 Development of Experimental Atom Tracking and 3D Spectroscopy Techniques

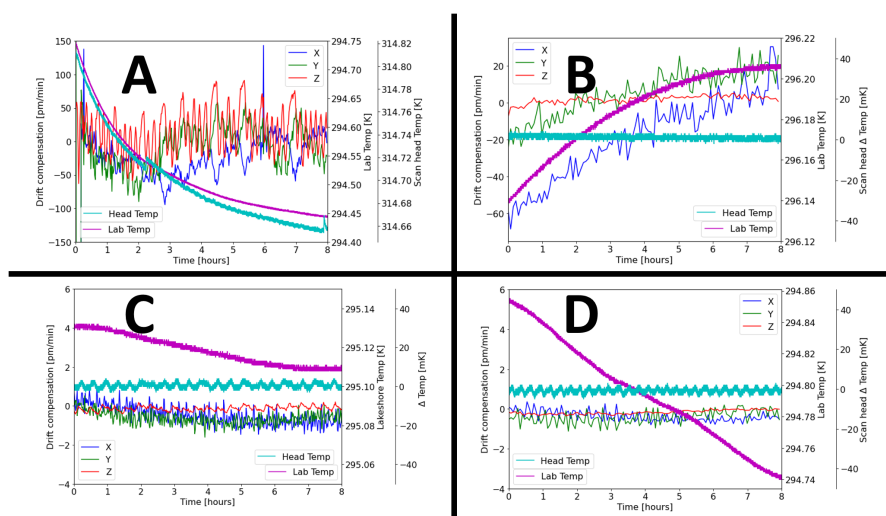


Figure 3.5: From four scripted experiments, the temperature readouts of both of the temperature measured at the scan head & temperature of the surrounding laboratory. Plotted alongside are the piezo scanner feedforward correction vectors (V_x, V_y, V_z), required to return the tip to its tracking site consistently. The behaviour of the drift vectors serves as a measure of the positional stability of the system. The values of the feedforward vectors are shown on the y axis on the left hand side of each graph. The temperatures are plotted across the two y axes on the right hand side of the plots. The surrounding lab temperature occupies the inner y axis, and the scan head temperature the outer y axis. A) Data set of continuous topographic measurement of Si(111)-(7 \times 7) in STM, $t_{acq} \approx 1$ minute, was carried out on Si adatom (main data not presented in this thesis). The scan head temperature was not regulated. Lab temperature scale = 350 mK, scan head temperature = 180 mK. B) Data set of Δf map taken via slices method, $t_{acq} \approx 2$ minutes, tracking was carried out on NTCDI molecule (see main result in Figure 4.8). The scan head temperature was regulated at a set point = 316.65 K, using $P = 100, I = 10, D = 50$. Lab temperature scale = 100 mK, scan head temperature = 100 mK. C) Data set of Δf map taken via grid spectroscopy, $t_{acq} \approx 1$ minute, tracking was carried out on C₆₀ molecule (see main result in Figure 5.12). The scan head temperature was regulated at a set point = 315.65 K, using $P = 100, I = 10, D = 50$. Lab temperature scale = 100 mK, scan head temperature = 100 mK. D) Data set of Δf map taken via slices method, $t_{acq} \approx 2$ minutes, tracking was carried out on CoPc molecule (see main result in Figure 5.18). The scan head temperature was regulated at a set point = 315.65 K, using $P = 100, I = 10, D = 50$. Lab temperature scale = 130 mK, scan head temperature = 100 mK. In each case a duration of 8 hours was plotted for simplicity, however, the duration of scripted experiments A) & C) both exceed this duration (15+ hours), and hence have been truncated.

3.2.1 Results: Temperature Regulation

The temperature readouts of both the Lakeshore thermocouples used (temperature measured at the scan head & temperature of the surrounding laboratory), and the feedforward drift correction vectors (V_x , V_y and V_z , required to return the tip to its tracking site consistently), are plotted across four subplots (four separate experiments) in Figure 3.5. The behaviour of the drift vectors serves as a measure of the positional stability of the system.

In the case of Figure 3.5.A, the temperature and feedforward vectors were recorded during an experiment to take iterative topographic scans over Si(111)-(7×7) in STM (not presented in this thesis). In this experiment, the Lakeshore controller set point was below the temperature of the surroundings (311.15 K set point $< \sim 314.65^\circ\text{C}$). The Lakeshore was therefore unable to regulate the temperature of the scan head, resulting in poor temperature stability of the feedforward vectors. The scan head temperature follows a similar trend to the surrounding lab temperature. The magnitude of the ΔT is diminished by roughly a factor 1/2 for the scan head temperature, likely owing to the UHV chamber, that helps to insulate the scan head from external temperature changes. Without any regulation of the scan head temperature, it is difficult for feedforward correction to stabilise the thermal drift: V_x , V_y and V_z may vary on the order of 100 pm/min between each update made to the piezo scanner (every 1 – 2 minutes).

Hence, temperature regulation was employed across all subsequent scripted data sets present in this thesis.

The temperature was regulated for 3D Δf mapping experiments: B)-D), each using the optimised PID values: $P = 100$, $I = 10$, $D = 50$. The temperature data plotted in B) (main experimental result in Figure 4.8) shows the most stable scan head temperature observed throughout the scripted experiments ($316.65\text{ K} \pm 2\text{ mK}$), remaining unaffected by the change in lab temperature. For clarity, the scale for the scan head temperature is reduced to the range +50 to –50 mK. Regulating the temperature a few K above room temperature has a stabilising effect on the feedforward vectors needed to compensate for the thermal drift. V_z in particular, is significantly more stable than V_x and V_y ($\Delta V_z < 1\text{ pm/min}$ per update, $\Delta V_{x,y} \sim 1 - 10\text{ pm/min}$ per update). This is likely because the experiment was carried out using an

unfinished version of the drift correction procedure (3.1.2) whereby a new set of positional values (p_0, p_1) are needed for each correction of the lateral displacement and update made to the feedforward correction. Under these circumstances, the z element of the position change, $p_1 - p_0$ was always less than the lateral displacement by virtue of returning to feedback after each batch of data acquisition. This meant the x and y elements of p_1 had twice as much time to deviate from p_0 than z did. As a result V_x and V_y were not as stable as V_z . Another contributing factor is the fact that the tip was tracking a molecule throughout the experiment, rather than a substrate atom. The mostly planar molecule, would have a less precise lateral apex position than for a Si adatom. Nevertheless B) is still included in Figure 3.5 as an example of long term (8 hours), optimal regulation of ± 2 mK.

Figure 3.5.C (main experimental result in Figure 5.12) depicts the scan head temperature oscillating slightly (~ 315.65 K ± 4 mK), likely due to a ringing effect in the regulation control loop. This ringing (oscillation time period ~ 20 minutes) is also seen in V_z plot, highlighting the connection between tip-sample drift and temperature gradients within the system. Despite this oscillation, the feedforward vectors are an order of magnitude smaller than for B). This is likely owing to the improved drift correction procedure (3.1.2), whereby each p_1 is used as p_0 in the following displacement calculation, which effectively doubles the rate of correction made to the piezo scanner. As with B), the tip made use of a molecule as a tracking feature, which may explain why V_x and V_y are less stable ($\Delta V_{x,y} \sim 1$ pm/min per update) than V_z ($\Delta V_z \sim 0.1$ pm/min per update).

Figure 3.5.D (main experimental result in Figure 5.18) depicts similar values to that of C), highlighting the reproducibility of the results. However, while the ringing is present again in the scan head temperature (315.65 K ± 4 mK), it is not seen in the plot of V_z , which is much flatter in D) ($\Delta V_z < 0.1$ pm/min per update) compared to C).

The results across Figure 3.5 show the benefit of regulating the temperature whilst operating room temperature SPM. Without regulation, the temperature of the microscope is subject to the changes in the surrounding temperature. This in turn creates further temperature gradients within the microscope, changing the tip-sample drift. Hence, temperature regulation is

essential and a prerequisite for environments sufficiently stable to gather high-resolution force map data at room temperature.

Furthermore, the regulation of the scan head temperature could be as steady as ± 2 mK using $P = 100, I = 10, D = 50$, in the control loop. However, the control loop was inconsistent at this level, and would often start and stop ringing unpredictably. Figure 3.5.C shows this ringing in the control loop having an effect on the scan head temperature and on V_z . But this was also not always the case, as the V_z in D) does not appear to be influenced by the oscillation seen in the scan head temperature. Moreover, V_x, V_y and V_z across C) & D) are markedly more stable than for A) and B). Therefore, beyond a certain level of temperature stability, the limiting factor for stability in V_x, V_y and V_z is instead the acquisition time, t_{acq} afforded by the more efficient procedure of the drift correction.

3.3 Results: Scripted Data Sets on Si(111)-(7X7)

3.3.1 Long Term Topographic Measurement

The simplest procedure for scripted data acquisition is for repeated topographic scanning (feedback in operation). Figure 3.6 shows three examples of using this tracking protocol to take long term topographic measurement over a prototypical surface: Si(111)-(7 \times 7). First, in images A) & B), the script was used in STM over a conservatively small area (3.87 nm²) covering only a unit cell, and with a faster scan speed such that the image acquisition time was only ~ 26 s. The positional changes of the adatoms over iterative scans were negligible. The experiment comprised over 10,000 individual scans. While images A) & B) look very similar, occasional tip-changes were observed throughout the whole data set. However, despite this, the tracking script was sufficiently robust to resume tracking in the correct position. Second, for C) & D), the acquisition time spent in between tracking was approximately doubled, to 1 minute, to scan a larger area: 20 nm². The script lasted a 24 hour span, without any tracking faults, and again, shows almost identical contrast to the first image in the data set. Third, for E) & F) the

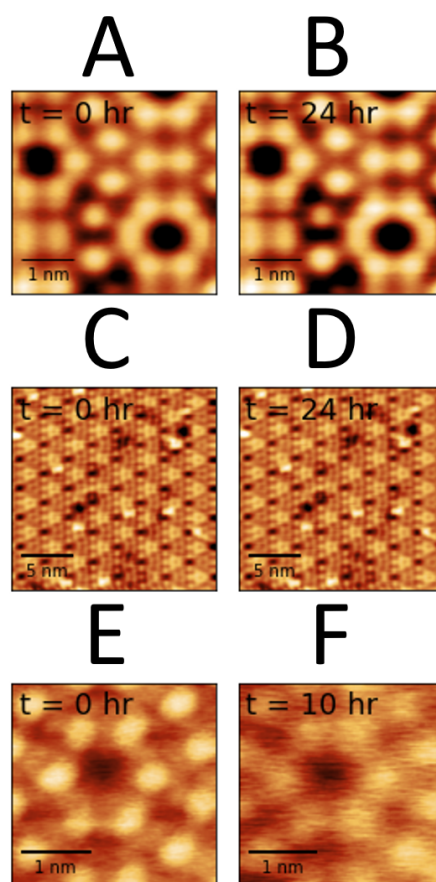


Figure 3.6: Example image sequences (of Si(111)-(7×7) surface) taken using a LabVIEW script using atom tracking, feedforward correction, and past displacement correction. The same area was scanned iteratively over long periods of time to assess the stability of the drift correction procedure. The relative times are included in each image. A) & B) Topographic map of a unit cell of Si(111)-(7×7) in STM. Imaging parameters: set point = 20 pA, 496 × 496 pixels, 3.87 nm × 3.87 nm area, $V_{gap} = +2$ V, $t_{acq} = 26$ s. C) & D) Topographic map taken over a larger area of Si(111)-(7×7) surface in STM. Imaging parameters: set point = 20 pA, 304 × 304 pixels, 20 nm × 20 nm area, $V_{gap} = +2$ V, $t_{acq} = 146$ s. E) & F) Topographic map of Si(111)-(7×7) atoms taken in NC-AFM. Imaging parameters: set point = -10 Hz, $A_0 = 18$ nm, 256 × 256 pixels, 3 nm × 3 nm area, $V_{gap} = 0$ V, $t_{acq} = 151$ s.

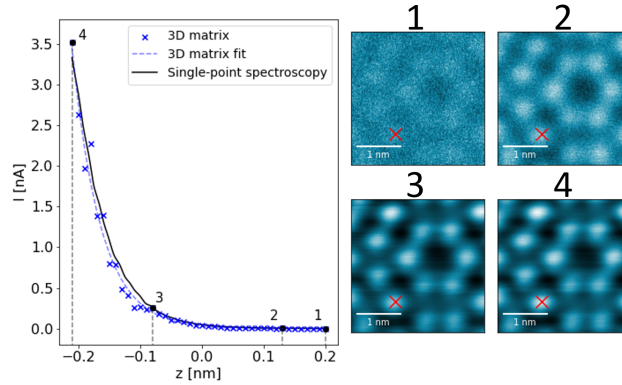


Figure 3.7: Demonstration of tracking script used to gather $I(z)$ matrix over bare Si(111)-(7x7) via slices method. Imaging parameters: set point = 50 pA, 304 x 304 pixels, 3 nm x 3 nm area, $V_{gap} = +2$ V, $t_{acq} = 37$ s. The tip-sample distance was varied from +200 pm to -200 pm. $I(z)$ curve from 3D matrix is a 5 x 5 pixel average around the point marked by the red x on each image. The preliminary single point spectroscopy is an average of 5 curves taken over tracked atom indicated by the red x. The preliminary single point spectroscopy is an average of 5 curves taken over the same tracked atom indicated.

protocol was applied in NC-AFM. Not only are tips capable of atomic resolution on Si(111)-(7x7) less stable compared to STM, but NC-AFM also demands significantly slower scan speeds for an acceptable S/N. This limits the scan area, thus the experiment was conducted over a 3 nm area, with an image acquisition time of 2.5 minutes. The experiment lasted 10 hours before a tracking failure, which led to a drift miscalculation that lost the field of view.

The results of the topographic scripts in Figure 3.6 establish the robust and effective nature of the LabVIEW tracking program, as a basis for gathering high-resolution 3D force map data in NC-AFM.

3.3.2 Constant Height STM Data Sets

The scripted constant height protocol depicted in Figure 3.3.A was first tested in STM, as imaging and tip stability are generally superior to NC-AFM. Figure 3.7 shows a successful execution of a scripted experiment to

3 Development of Experimental Atom Tracking and 3D Spectroscopy Techniques

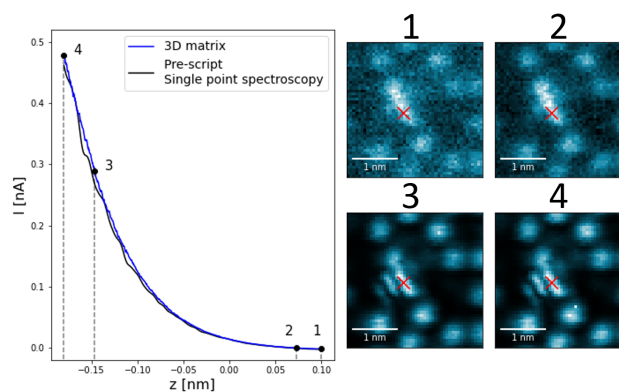


Figure 3.8: $I(z)$ matrix taken via grid spectroscopy. Tracking resumed after every 5 spectra, $t_{acq} \approx 40$ s in between tracking events. Experiment parameters: tracking set point = 12 pA, 48×48 pixels, $3 \text{ nm} \times 3 \text{ nm}$ area, $V_{gap} = +1.5 \text{ V}$. Spectra sweep from +100 pm above the height of the tracking point, to -180 pm below, with 1024 pixel density in z . $I(z)$ curve from 3D matrix is a 5×5 pixel average around the point marked by the red \times on each image. The preliminary single point spectroscopy is an average of 5 curves taken over the same tracked atom indicated.

take constant height slice data of the bare Si(111)-(7 \times 7) surface. The constant height scans were stacked into a 3D matrix using Python (see discussion of data processing in Section 3.4), from which spectroscopic data through z could be extracted at the point indicated by the red \times in the example scans. The $I(z)$ extracted from the 3D grid showed good agreement with a preliminary $I(z)$ spectra taken over the same atom, which demonstrates the robust nature of the tracking procedure, and furthermore that spectroscopic data could be gathered using the slices method.

The grid spectroscopy script was tested on a NTCDI molecule on the Si(111)-(7 \times 7) surface in Figure 3.8. The tracking was resumed after 5 spectra, and the agreement between the 3D matrix and a curve taken over the equivalent position over the molecule prior to the experiment demonstrated the low positional error of the tracking mechanism and scripted protocol. As the tip gets closer toward the surface, the orbital structure of the NTCDI molecule can be observed (17). This data set also demonstrates how constant height images can be retrieved from 3D grid spectroscopic data, i.e. the equivalence

3.3 Results: Scripted Data Sets on Si(111)-(7X7)

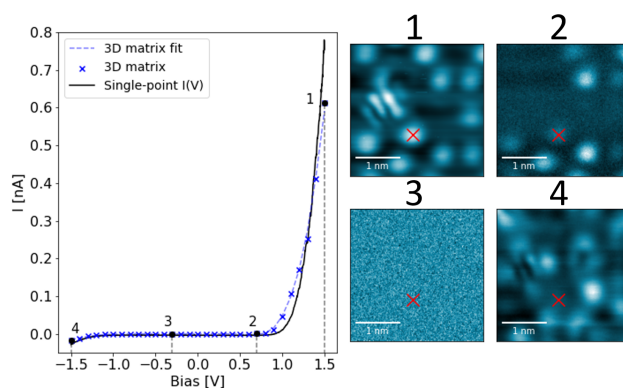


Figure 3.9: Demonstration of tracking script used to gather $I(V)$ matrix in STM via slice method over NTCDI molecule on Si(111)-(7 \times 7). Imaging parameters: set point = 12 pA, 256 \times 256 pixels, 3 nm \times 3 nm area, $V_{gap} = 1.5$ V during tracking, bias was varied +1.5 V to -1.5 V, $t_{acq} = 39$ s. Scans were taken -200 pm below the height of the tracking position. $I(V)$ curve from 3D matrix is a 5 \times 5 pixel average around the point marked by the red \times . The preliminary single point spectroscopy is an average of 5 curves taken over the same tracked atom indicated.

of both methods.

Likewise, $I(V)$ spectroscopy data can also be recreated using constant height imaging. In this case, a suitable tip-sample distance for imaging is chosen, and the bias applied during imaging is varied through a desired range, rather than changing the z height. The script slews the changes to the tip bias, to avoid electrostatically pulsing the tip. Figure 3.9 shows a $I(V)$ matrix constructed from constant height scans, sweeping from -1.5 V to +1.5 V, also taken over a NTCDI molecule on Si(111)-(7 \times 7).

3.3.3 Two-Dimensional Force Mapping in NC-AFM

3.3.3.1 2D Constant Height Slices

A major challenge of applying the scripted procedures to NC-AFM is pursuing sufficiently high S/N (via longer acquisition time) whilst maintaining tip stability, and ensuring thermal drift does not crash the tip into the surface.

3 Development of Experimental Atom Tracking and 3D Spectroscopy Techniques

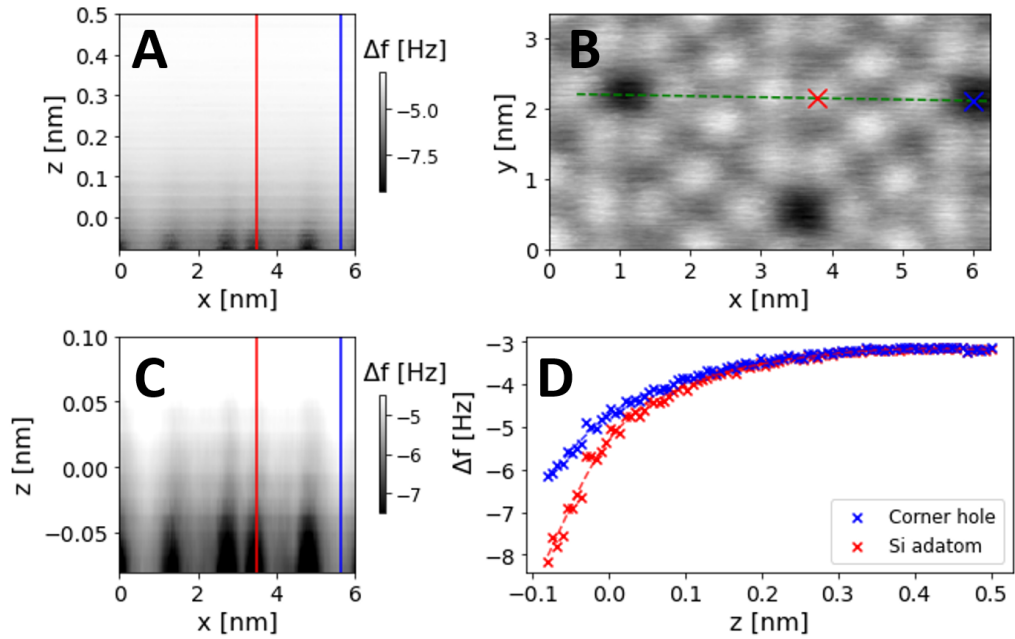


Figure 3.10: A) $\Delta f(x, z)$ cross-sectional map across $\text{Si}(111)$ - (7×7) unit cell, gathered via constant height slices method in NC-AFM. Map size: 512×93 pixels, $6 \text{ nm} \times 0.58 \text{ nm}$ (x, z), tracking set point = -4 Hz , $V_{\text{gap}} = +0.1 \text{ V}$, $A_0 = 18 \text{ nm}$. Map averaged in x using 10 pixel averaging window ($\sim 100 \text{ pm}$). B) Constant Δf image of unit cell taken prior to experiment. The position of the cross-sectional map is indicated by the green dotted line. Image parameters: Δf set point = -4 Hz , 300×256 pixels, $6.24 \text{ nm} \times 4.34 \text{ nm}$ scan area (x, y), $V_{\text{gap}} = +0.1 \text{ V}$. C) Δf map scaled to highlight the signal at closest approach around the Si adatoms. D) $\Delta f(z)$ curves extracted from grid data over 'on' and 'off' sites, marked by the red and blue lines respectively in A) & C). Dotted lines in plot are Δf curves spline smoothed in z using the *splrep* function from the *scipy.interpolate* python library (smoothing parameter $\lambda = 0.99$).

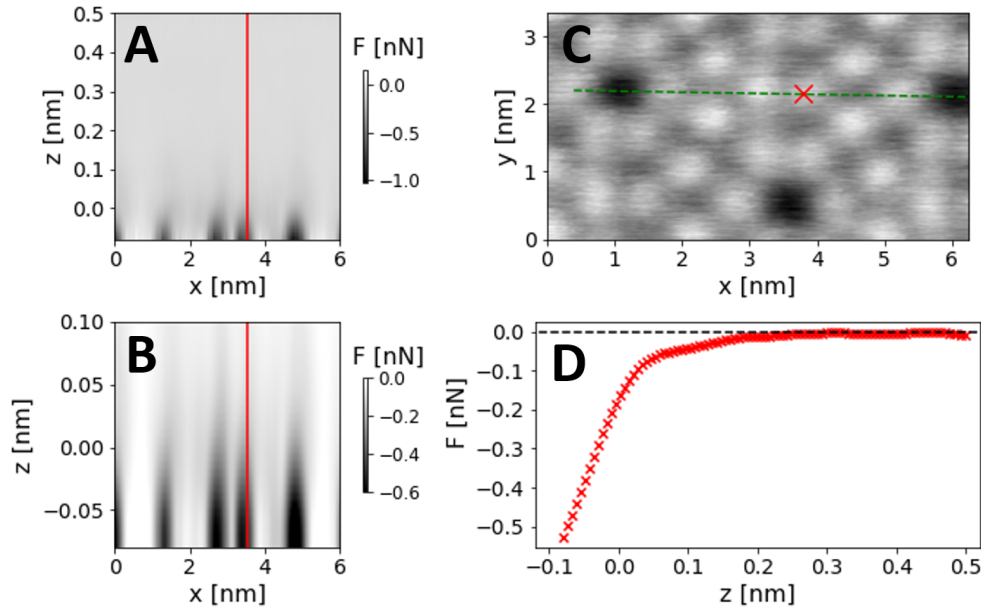


Figure 3.11: $\Delta f(x, z)$ map of Si(111)-(7 \times 7) from Figure 3.10 inverted into 2D force map of the same dimensions. $\Delta f(z)$ curve over corner hole site taken as 'off' curve and subtracted from all others for the inversion. The force matrix was smoothed across x using a 10 pixel average, and extracted $F(z)$ curve was smoothed using the *splrep* function from the *scipy.interpolate* python library (smoothing parameter $\lambda = 0.99$). A) Inverted force of cross-section. B) Constant Δf of unit cell taken prior to experiment. The cross-sectional map is indicated by the green dotted line. C) Force map scaled up to highlight force around Si adatoms. D) $F(z)$ curve extracted from grid data over 'on site'. Its position in the unit cell is indicated by the red lines in A) & C), and the red 'x' in B). The tip did not approach the surface close enough to measure a force turnaround. The most attractive force measured was only ~ -0.5 nN.

Because of the increase in acquisition time of the whole experiment, the chances of a random, unexpected tip-change also increases. For situations where a full 3D data set is not necessary, e.g. finding the variation of force minima across just the key points of a single molecule, the total acquisition time can be significantly reduced by only gathering 2D cross-sectional data sets. Both the slice and grid spectroscopy methods can be used to acquire 2D cross-sectional Δf maps, reducing the total time of the experiment to 1 – 2 hours. In the case of the constant height slices method, each scan is a $1 \times n$ pixel profile, which was then stacked in z , as before. Several line profiles can be taken before the tracking has to resume to update the feedforward vectors. Figure 3.10 is a cross-sectional Δf map across 4 adatoms and two corner holes of the Si(111)-(7×7) unit cell. The data were acquired by stacking constant height line profiles in z , similar to Sugimoto et al. (2008) (18). Example $\Delta f(z)$ curves extracted from the map are plotted also in D), corresponding to Si adatom and corner hole sites.

3.3.3.2 2D Grid Spectroscopy

For grid spectroscopy, the procedure is the same as for 3D maps, except with only a single row of single point spectra ($1 \times n$ pixel). Figure 3.12 shows a cross-sectional Δf map, over the equivalent atomic sites as Figures 3.10 & 3.11, measured using grid spectroscopy. In this data set, the $\Delta f(z)$ curves over the Si adatom approach close enough for the $\Delta f(z)$ to reach a minimum, indicating the tip had reached the repulsive regime. The steps taken in data processing and force inversion of the $\Delta f(z)$ signal into $F(z)$ maps are discussed in Section 3.4. Using the constant height slices method Δf map data from Figure 3.10, a force map of the Si(111)-(7×7) substrate was calculated and plotted in Figure 3.11. Note that in this force map, the tip did not approach close enough to enter the repulsive regime, and hence no force minima was detected over the adatoms.

Using the grid spectroscopy method Δf map data from Figure 3.12, a force map of the Si(111)-(7×7) substrate was calculated and plotted in Figure 3.13. For this data set, the tip did approach close enough to the surface to reach a force minima over the adatoms. Over the selected adatom (indicated by red line in Figure 3.13.A & C)), the attractive force minimum is ~ -1.2 nN.

3.3 Results: Scripted Data Sets on Si(111)-(7X7)

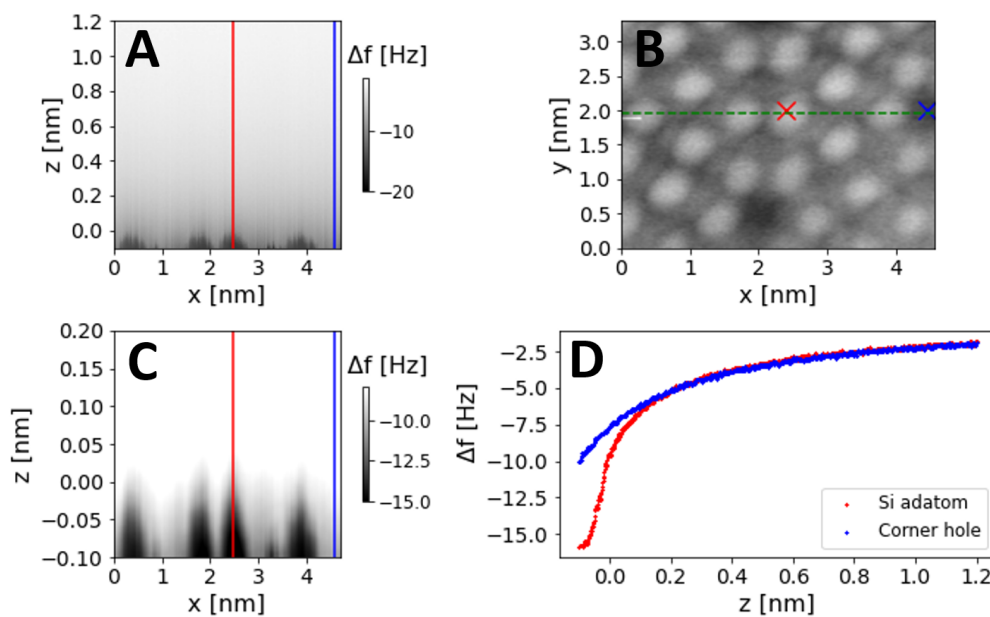


Figure 3.12: A) $\Delta f(x, z)$ cross-sectional map across Si(111)-(7 \times 7) unit cell, gathered via grid spectroscopy method in NC-AFM. Map size: 256 \times 1024 pixels, 4.7 nm \times 1.3 nm (x, z), tracking set point = -10 Hz, $V_{gap} = 0$ V, $A_0 = 18$ nm. Map smoothed in xz using 3 \times 3 pixel average. B) Constant Δf image of unit cell taken prior to experiment. The position of the cross-sectional map is indicated by the green dotted line. Image parameters: Δf set point = -10 Hz, 256 \times 206 pixels, 4.55 nm \times 3.66 nm scan area (x, y), $V_{gap} = 0$ V. C) Δf map scaled to highlight the signal at closest approach around the Si adatoms. D) $\Delta f(z)$ curves extracted from grid data over 'on' and 'off' sites, marked by the red and blue lines respectively in A) & C).

3 Development of Experimental Atom Tracking and 3D Spectroscopy Techniques

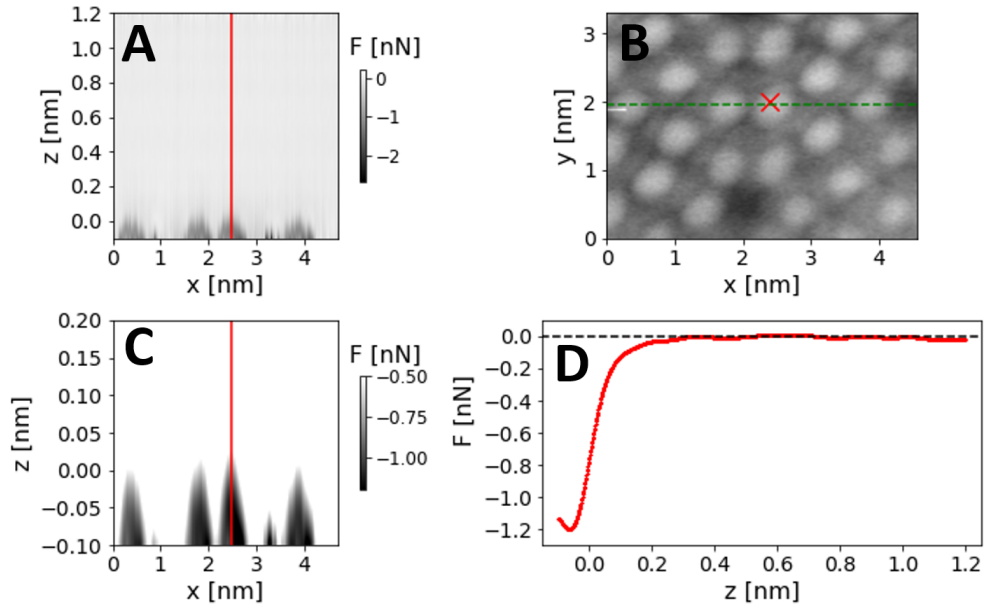


Figure 3.13: $\Delta f(x, z)$ map of Si(111)-(7 \times 7) from Figure 3.12 inverted into 2D force map of the same dimensions. $\Delta f(z)$ curve over corner hole site taken as 'off' curve and subtracted from all others for the inversion. The force matrix was smoothed in x using a 10 pixel average, and extracted $F(z)$ curve was smoothed using the *splrep* function from the *scipy.interpolate* python library (smoothing parameter $\lambda = 0.99$). A) Inverted force of cross-section. B) Constant Δf of unit cell taken prior to experiment. The cross-sectional map is indicated by the green dotted line. C) Force map scaled up to highlight force around Si adatoms. D) $F(z)$ curve extracted from grid data over 'on site'. Its position in the unit cell is indicated by the red lines in A) & C), and the red 'x' in B). The force minimum of the 'on' site is ~ -1.2 nN.

This value is of the same order as that measured by Sugimoto et al. (2008) (18), who also used Si tip cantilevers.

The 2D cross-sectional map scripts proved capable of yielding reasonable force data. Thus, the next step was to apply them to 3D.

3.3.4 Three-Dimensional Force Mapping in NC-AFM

3.3.4.1 3D Constant Height Slices

Conducting scripts for three-dimensional force mapping requires especially stable tips, due to the long acquisition times. The S/N ratio was improved for the constant height slices experiment by repeating the scans at each height (generally 3 times), and calculating an average image. This allows the user to scan each single image at a faster speed in order to ensure that the tip is always able to return to the correct tracking site, and that residual drift in z does not become significant. Figure 3.14 depicts a 3D Δf map acquired via the constant height slices method over Si(111)-(7 \times 7). The evolution in Δf contrast in Figure 3.14 is somewhat complex, and is indicative of a 'non-standard' tip. As the tip approaches the surface, the adatoms of the top layer appear as faint, attractive circles, however, the rest atoms below start to show strong attractive contrast. Closer to the surface, the attractive contrast of the rest atoms dominates the repulsive contrast of the adatoms. With an unknown tip geometry (but likely still Si-terminating), it is difficult to speculate as to where the unusual Δf / force behaviour originates. However, the stability of the tracking demonstrated the success of the 3D mapping experimental protocol.

3.3.4.2 3D Grid Spectroscopy

Finally a 3D grid spectroscopy Δf map was conducted over adatoms surrounding a corner hole of the Si(111)-(7 \times 7) surface in Figure 3.15. Both the red, 'on', and blue 'off' curves (left) are in good agreement with the preliminary single point $\Delta f(z)$ curves (black) over the same positions, prior to the scripted experiment, providing further indication of the stable tip

3 Development of Experimental Atom Tracking and 3D Spectroscopy Techniques

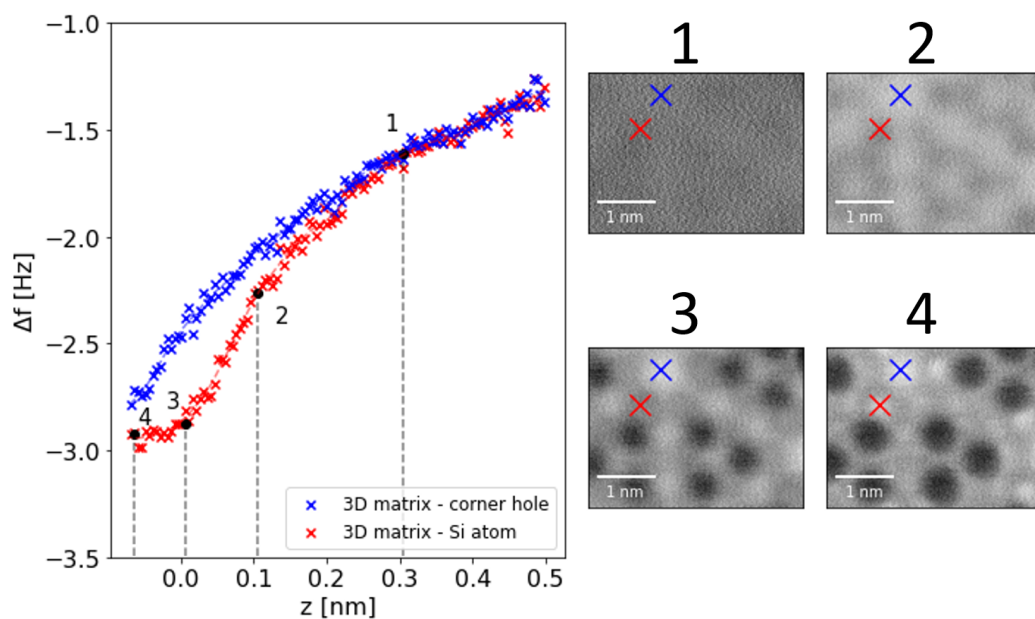


Figure 3.14: 3D $\Delta f(x, y, z)$ map of Si(111)-(7 \times 7) in NC-AFM using constant height slices. Each slice in data set was scanned 3 times and an average image was calculated. Map dimensions: 368 \times 256 \times 115 pixels, 3.76 nm \times 2.78 nm \times 0.57 nm. Tracking set point = -3.25 Hz, $V_{gap} = +0.15$ V, $A_0 = 20$ nm, scan time = 94 s. Total $t_{acq} \sim 5$ hours. Left) Extracted $\Delta f(z)$ curves across various sites in data set. Curves smoothed by initially averaging the 3D data set in (x, y) with 5 \times 5 pixel average. Then Δf signal spline smoothed in z using the *splrep* function from the *scipy.interpolate* python library (smoothing parameter $\lambda = 0.99$). Right) Example images 1)-4) from data set, showing evolution in contrast of Si atoms.

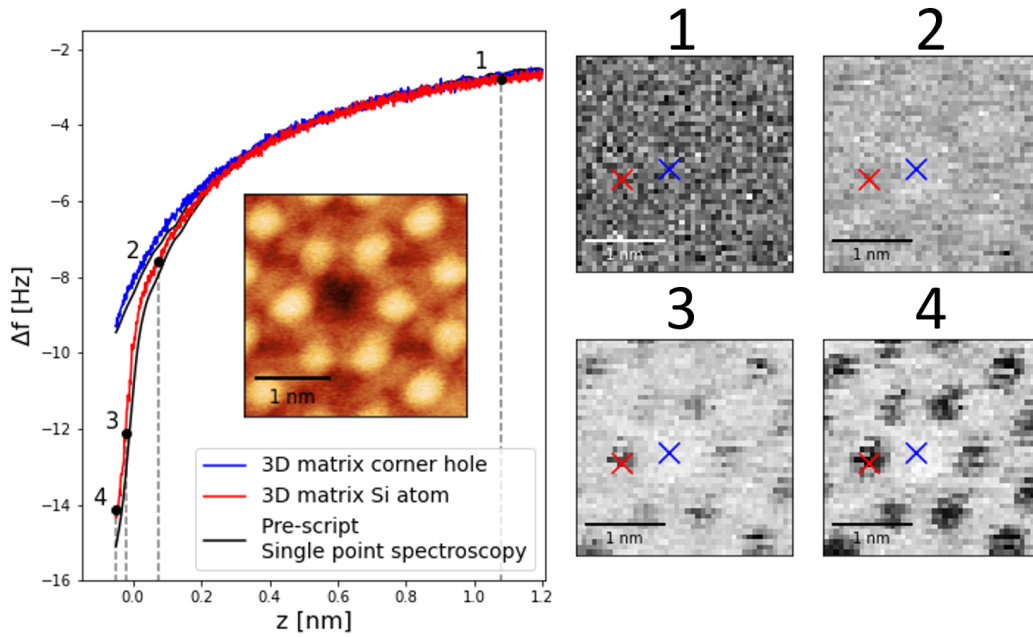


Figure 3.15: $\Delta f(x, y, z)$ map of Si(111)-(7 \times 7) gathered using 3D grid spectroscopy. Matrix dimensions: $42 \times 42 \times 1024$ pixels, $3 \text{ nm} \times 3 \text{ nm} \times 1.25 \text{ nm}$. Tracking set point = -10 Hz , $V_{\text{gap}} = 0 \text{ V}$, $A_0 = 18 \text{ nm}$. t_{acq} for 5 spectra = 35 s (5 spectra were taken between tracking events), total $t_{\text{acq}} \sim 6$ hours. Left) Example $\Delta f(z)$ curves over 'on' and 'off' sites. Also plotted is $\Delta f(z)$ curve taken prior to experiment over equivalent site. Curves smoothed by initially averaging the 3D data set in (x, y) with 3×3 pixel average. Then Δf signal spline smoothed in z using the *splrep* function from the *scipy.interpolate* python library (smoothing parameter $\lambda = 0.99$). Insert in graph shows constant Δf taken following grid experiment over same region. Image parameters: Δf set point = -10 Hz , 256×256 pixels, $3 \text{ nm} \times 3 \text{ nm}$ scan area (x, y) , $V_{\text{gap}} = +0 \text{ V}$, $t_{\text{acq}} = 440 \text{ s}$. Right) Example (x, y) slices 1) - 4) through 3D data set, getting progressively closer to the surface, showing the evolution of the contrast of the Si adatoms.

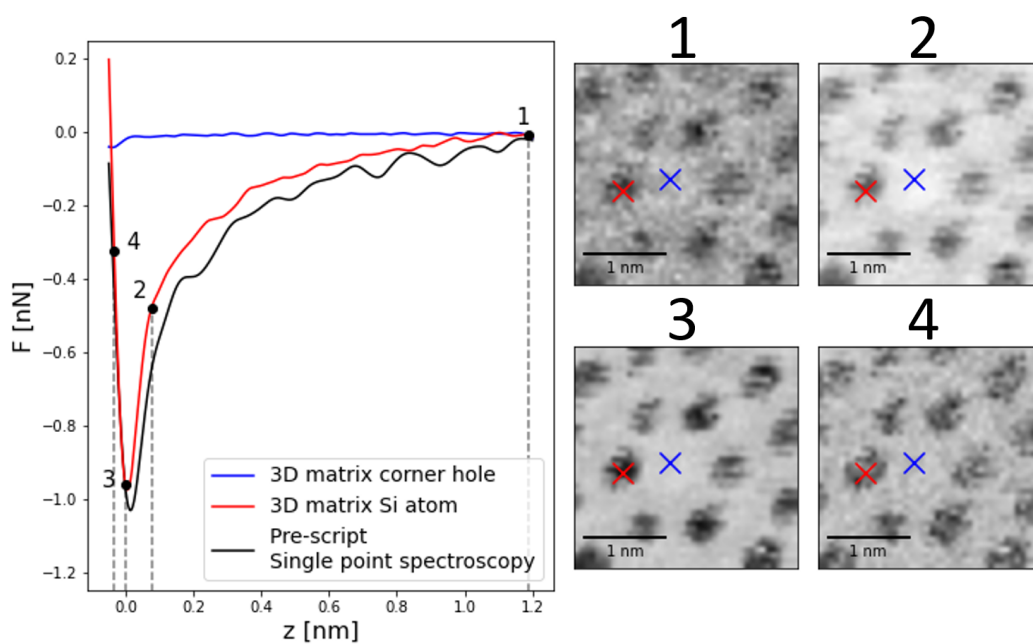


Figure 3.16: $F_z(x, y, z)$ map of Si(111)-(7×7) from Figure 3.15 inverted into 3D force map of the same dimensions. $\Delta f(z)$ curve over corner hole site taken as 'off' curve and subtracted from all others for the inversion. The force matrix was smoothed in (x, y) using 3×3 pixel average, and extracted $F(z)$ curve was spline smoothed using the *splrep* function from the *scipy.interpolate* python library (smoothing parameter $\lambda = 0.99$). Left) Example $F(z)$ curve over 'on' site. Also plotted is $F(z)$ curve taken prior to experiment over equivalent site. The force minima of both curves is ~ -1 nN. Right) Example (x, y) slices 1) - 4) through 3D data set, getting progressively closer to the surface, showing the evolution of the contrast of the Si adatoms.

state and low positioning error, which lasted the duration of the entire experiment (~ 6 hours). The relative placements of the adatoms in the 3D matrix, close to the surface, match well with the constant Δf image shown in the insert. This scan was conducted immediately after the script, using the set tracking set point. A constant height image was not taken, unfortunately, which would have enabled a more direct comparison of the Δf signal at close approach acquired via both scanning and grid spectroscopy methods. The force minima over the 'on' site was calculated to be ~ -1 nN for the preliminary point spectroscopy and for the 3D grid depicted in Figure 3.16. This value is consistent with that measured in the 2D grid spectroscopy data set in Figure 3.13 (same tip used for both experiments), and with previous force measurement on Si(111)-(7 \times 7) via multiple dimensional Δf mapping (18, 19).

3.3.5 Method Comparison

The two principle methods of force map data acquisition: constant height slices and grid spectroscopy, should theoretically produce the same data. However, in practice they each have differing strengths and weaknesses. When trying to minimise the necessary time spent between tracking events, grid spectroscopy has an advantage. A single element (one curve), may be carried out (with acceptable S/N) in only a few seconds, whereas a full scan, particularly in NC-AFM, takes longer for an acceptable S/N, on the order of minutes. More time spent with inaccurate feedforward vectors increases the risk of erroneously tracking a different feature upon subsequent engagement of tracking mode. The larger acquisition time of scanning also increases the uncertainty in z -position during a constant height scan. For simple conversion of Δf maps into force maps, it is necessary to assume that the tip is truly scanning in *constant* height. If the tip drifts more than the desired precision in z , (Δg), this assumption is no longer valid. In extreme cases the residual z drift can cause the tip to approach too close to the surface, incurring either tip-change or crash, terminating the force mapping experiment. In the case of the slices method, however, if the user carries out the script protocol from high z to low z , in the event of tip-change, there is still a fully retrievable data set down to that point in z where the

3 Development of Experimental Atom Tracking and 3D Spectroscopy Techniques

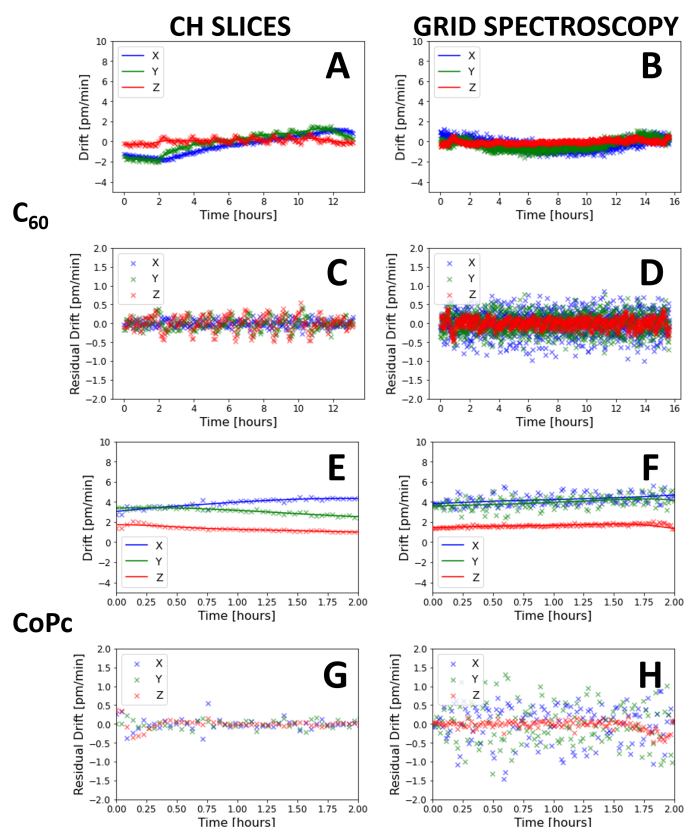


Figure 3.17: Feedforward corrections and residual drifts calculated during $\Delta f(x, y, z)$ mapping experiments, using both methods of data acquisition: constant height slices and grid spectroscopy. A) & C) Applied feedforward vectors and calculated residual drifts (respectively) for constant height slice map over C_{60} molecules (main result in Figure 5.11). B) & D) Applied feedforward vectors and calculated residual drifts for grid spectroscopy map over C_{60} molecules (main result in Figure 5.12). E) & G) Applied feedforward vectors and calculated residual drifts for constant height slice map over CoPc molecules (main result in Figure 5.19). F) & H) Applied feedforward vectors and calculated residual drifts for grid spectroscopy map over CoPc molecules (main result not included in this thesis). For all experiments the temperature of the microscope head was regulated to ± 4 mK. The residual drifts were calculated by subtracting a heavily smoothed spline fit ($\lambda = 0.99$) from the data.

change occurred. In contrast it is often harder to retrieve usable data when a tip change occurs during a grid spectroscopy experiment, since the tip approaches the closest point in z at each (x, y) coordinate.

The two methods can be assessed from stability they afford the system via the drift correction procedure. Figure 3.17 depicts the feedforward vectors (V_x, V_y, V_z) applied and estimated residual thermal drifts across multiple Δf mapping experiments. Both C_{60} (see main result in Figure 5.11 (slices) & 5.12 (grid spec)) and CoPc (Figure 5.19 (slices)) were mapped in $\Delta f(x, y, z)$ (four experiments in total), during which the feedforward vectors applied to the piezo scanner during the scripted drift correction procedure were recorded. For all experiments, the scan head temperature was regulated at $315.65 \text{ K} \pm 2 \text{ mK}$. For the slices experiments, $t_{acq} \approx 2$ minutes, and for the grid spectroscopy, $t_{acq} \approx 1$ minute. For each molecule, the methods were conducted concurrently, using the same tip, in order to provide the best comparison.

First, the residual drift of the C_{60} slices experiment (plotted in Figure 3.17.C) was most prominent in z , but still $< 1 \text{ pm}/\text{min}$ for all directions. The drift in z followed the oscillation of the sub-optimal temperature regulation. For the grid spectroscopy (D), the variation in magnitude of residual z drift is similar to the slices experiment, but has higher values for x and y ($\sim 1 \text{ pm}/\text{min}$). This would imply that even with just half the acquisition time of the slices method, grid spectroscopy suffers from slightly worse positional accuracy for drift calculation and data gathering. A possible explanation for the poorer performance of the grid spectroscopy could be the piezo-creep. After moving distances of the order of 1 nm in z , the tip re-engages feedback and resumes tracking, and thus, the piezo crystal may be still relaxing during the measurement of its average position. In which case an increased of the delay time, t_d (see Figure 3.2) would be necessary. Ultimately however, displacement on the order of 1 pm is insignificant when compared to the dither radius for a tip tracking molecular sized features (100s of pm). It follows that the small residual drifts measured in C) & D) would allow for greater acquisition times, hence higher values of S/N could be achieved in the images / $\Delta f(z)$ spectra: a trade-off for lower positional accuracy.

Second, the residual drifts from the CoPc experiments plotted across Figure 3.17.E - H) are of similar values to those of the C_{60} , but the drift in z across

both methods is significantly smaller. For the slices method, the residual drift in all directions is roughly equal. For the grid spectroscopy, the lateral positional accuracy is still poorer compared to z , and the values from the slices.

It is notable that Rahe et al. (2011) (13) reported the use of feedforward correction with grid spectroscopy, yielding a maximum residual drift velocity of $25 \text{ pm}/\text{min}$ for an experiment that updated the feedforward correction after intervals of ~ 15 minutes. In their experiment, the tip was re-centred on the point of tracking after intervals of 18.5s in order to keep the displacement due to thermal drift under the desired precision / pixel density. Thus, $25 \times (18.5/60) \sim 8 \text{ pm}$ maximum displacement due to residual drift. This satisfied Equation 2.9: $8 \text{ pm} < \Delta g \sim 50 \text{ pm}$, despite the lengthy durations between updates to the feedforward vectors. Similarly, the residual drift vectors presented in Figure 3.17 also all satisfy the constraint in Equation 2.9, for the respective pixel densities. Therefore the residual thermal drift is not a limiting factor of the lateral precision throughout the experiments in this thesis (likely the limiting factor is the tip state). An estimate for the lateral resolution is made in Section 4.5.4.

To conclude, both methods are capable of gathering high resolution force map data sets at room temperature with positional errors of the order 1 pm . The better performance in lateral stability of the slices experiment is insignificant when compared to the size of dither radii used. However, empirically, grid spectroscopy experiments (particular when attempted in 3D), are more prone to unexpected tip-changes. This is likely because the tip reaches the point of closest approach for each pixel in (x, y) .

3.4 Data Processing and Force Inversion

The Nanonis image and spectroscopy data files were processed and analysed using code written in Python (2). For data on $\text{Si}(111)$ - (7×7) surfaces, $\Delta f(z)$ curves conducted over a corner hole site were considered the background ('off') signal and were subtracted from the 'on' site $\Delta f(z)$ curves (21), leaving the site-specific Δf signal. The $\Delta f(z)$ signal was converted to $F(z)$ using Equations 1.23 & 1.24 (20). Without any smoothing, this would

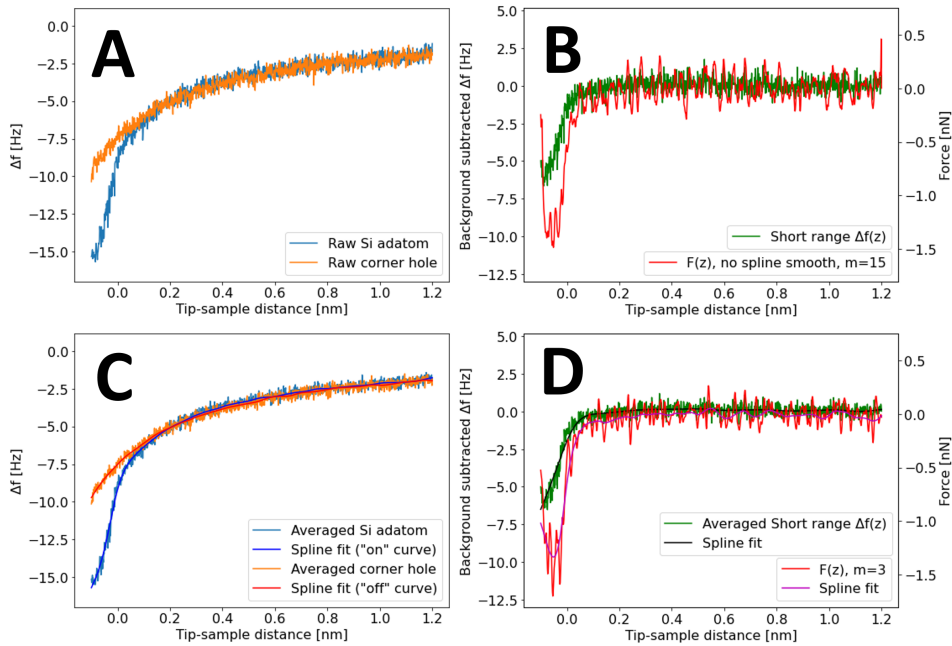


Figure 3.18: $\Delta f(z)$ curve inversion into $F(z)$: comparing Lanczos differentiator and spline fit methods of smoothing. A) plots the raw $\Delta f(z)$ curves taken over adatom (blue) and corner hole (orange) sites of Si(111)-(7×7). The difference between these raw curves is plotted in B) (green), alongside the output of the force inversion code (red), with a smoothing window size, $m = 15$. A result of smoothing only with the differentiator is the fictitious variation in force at the edge positions in z , typically more prominent at the end far from the surface. C) plots the average of forward and backward sweep channels, for both 'on' (light blue) and 'off' (orange) curves, with spline fit smoothing ($\lambda = 0.999$) for each (dark blue and red respectively). These spline smoothed $\Delta f(z)$ curves were converted into $F(z)$ (of the 'on' site) and plotted in D). The green curve is the difference between the averaged $\Delta f(z)$ curves, the black line is the difference between the spline smoothed $\Delta f(z)$ curves. The red curve is the output of the force inversion using $m = 3$ (the minimum window width (2σ)). The purple curve is the spline fit of the red curve ($\lambda = 0.99$).

result in $F(z)$ curves that exhibited a high degree of noise due to the numerical differentiation in the algorithm. Smoothing by merely increasing the differentiator width smoothing window, m led to large deviations in the force in the far end of the $F(z)$ curve, rather than plateauing to $F(z) = 0$ as expected, due to the smoothing window being constrained to smaller widths at the edge positions in z . Figure 3.18.A & B) show this effect. Graph A) plots the raw $\Delta f(z)$ curves taken over adatom (blue) and corner hole (orange) sites of Si(111)-(7×7). The difference between these raw curves is plotted in Graph B) (green), alongside the output of the force inversion code (red), with a smoothing window size, $m = 15$. At the furthest point in z , there is an apparent repulsive data point by virtue of the differentiator being unable to apply a wide window m , at the edge position. The $F(z)$ signal at the point of closest approach can be similarly affected.

In contrast, Figure 3.18.C & D) depict an alternative force inversion protocol adopted throughout this thesis. In the case of single Δf point spectra (C)), the data in the forward and backward sweep were averaged, reducing noise by $\sim 50\%$. It was, of course, necessary to check first check for any systematic differences in these directions (e.g. due to tip-change or significant creep or thermal drift in z). In the case of the multiple preliminary spectra preceding the scripted experiments (Figures 3.7 - 3.9, 3.15) these would be averaged too, assuming they were taken over the same site. Next, a spline fit via the *splrep* function (from the *scipy.interpolate* python library) would be used to smooth both the 'on' and 'off' $\Delta f(z)$ curves. Following the force inversion of the short range $\Delta f(z)$ (calculated using the difference between the smoothed 'on' and 'off' curves), the $F(z)$ curve would be smoothed with another spline fit. The smoothing parameter, λ would be tuned in each case to suit the level of noise in the data, and care was taken to ensure the smoothing did not distort the result of the force curve data (e.g. over-smoothing will tend to reduce the magnitude of the force minima). Typically the spline smoothing parameter, λ was set between 0.99 – 0.9999.

For multiple dimensional Δf maps, the data are imported into appropriately size *numpy* array prior to any further processing. For the 2D grid spectroscopy $\Delta f(x, z)$ map depicted in Figure 3.12, the averaging conducted prior to the spline smoothing and force inversion was carried out using a rolling average across the x axis. This rolling average was 10 pixels wide, equating to ~ 180 pm in x . Following inversion the force grid was smoothed

further using the same rolling average method, and then splines smoothed using $\lambda = 0.99$. This process was repeated for the 3D grid spectroscopy $\Delta f(x, y, z)$ map in Figure 3.15, save for the averaging, which was carried out across (x, y) over a 3×3 pixel grid, equating to an area $\sim 200 \text{ pm}^2$. For the constant height slices data sets, scan data taken at equivalent height were averaged. As with the spectroscopy data files, the forward and backward scan channels were also averaged (having checked there were no systematic differences in each case). In the case of the 2D slices $\Delta f(x, z)$ map (Figure 3.10), the $\Delta f(x, z)$ map was smoothed in x with a rolling average, with a window size 10 pixels, equating to $\sim 100 \text{ pm}$. The extracted $\Delta f(z)$ curves were smoothed in z using a spline fit as before (typically $\lambda = 0.99$). The smoothed $\Delta f(z)$ data was then inverted into $F(z)$ as with the spectra data files. Finally, for the 3D slices $\Delta f(x, y, z)$ map (Figure 3.14), the forward and backward Δf channels, and equivalent height scans were averaged as well. The data was averaged in (x, y) using a 5×5 pixel sized ($\sim 250 \text{ pm}^2$) rolling average window.

The data sets across this chapter chart the progress of the tracking scripts, and showcase the required robustness and stability for gathering force maps in NC-AFM at room temperature. In Chapter 4 this methodology is applied to gather force maps over single molecules adsorbed on Si surfaces.

References

1. R. Bitter, T. Mohiuddin, M. Nawrocki, *LabVIEW: Advanced programming techniques* (Crc Press, 2006).
2. G. Van Rossum, F. L. Drake Jr, *Python reference manual* (Centrum voor Wiskunde en Informatica Amsterdam, 1995).
3. K. Iwata *et al.*, *Nature Communications* **6**, 7766 (2015).
4. M. Abe, Y. Sugimoto, O. Custance, S. Morita, *Applied Physics Letters* **87**, 173503 (2005).
5. Y. Sugimoto *et al.*, *Physical review letters* **98**, 106104 (2007).
6. L. Gross, F. Mohn, N. Moll, P. Liljeroth, G. Meyer, *Science* **325**, 1110–1114 (2009).

3 Development of Experimental Atom Tracking and 3D Spectroscopy Techniques

7. L. Gross *et al.*, *Physical Review Letters* **107**, 086101 (2011).
8. C. Moreno, O. Stetsovych, T. K. Shimizu, O. Custance, *Nano Letters* **15**, 2257–2262 (2015).
9. A. M. Sweetman *et al.*, *Nature Communications* **5** (2014).
10. Y. Sugimoto *et al.*, *Science* **322**, 413–417 (2008).
11. Y. Sugimoto *et al.*, *ACS Nano* **7**, 7370–7376 (2013).
12. Y. Sugimoto *et al.*, *Physical Review B* **81**, 245322 (2010).
13. P. Rahe *et al.*, *Review of Scientific Instruments* **82** (2011).
14. S. Kawai, T. Glatzel, S. Koch, A. Baratoff, E. Meyer, *Physical Review B - Condensed Matter and Materials Physics* **83**, 1–7 (2011).
15. S. Fremy *et al.*, *Nanotechnology* **23** (2012).
16. Lakeshore, *User's Manual Model 331 Temperature Controller* (Lake Shore Cryotronics, Inc., Westerville, OH, 2009).
17. S. P. Jarvis *et al.*, *Journal of Physics Condensed Matter* **27** (2015).
18. Y. Sugimoto, T. Namikawa, K. Miki, M. Abe, S. Morita, *Phys. Rev. B* **77**, 195424 (2008).
19. Y. Sugimoto, K. Ueda, M. Abe, S. Morita, **24**, 84008 (2012).
20. A. Stannard, A. M. Sweetman, *A Considered Approach to Force Extraction from Dynamic Force Microscopy Measurements*, ed. by P. Moriarty, S. Gauthier (Springer International Publishing, 2015), pp. 63–79, ISBN: 978-3-319-17401-3.
21. M. Ternes *et al.*, *Phys. Rev. Lett* **106**, 16802 (2011).

4 Intramolecular force mapping at room temperature

This results chapter describes the experiments carried out to gather the first reported force maps of submolecular resolution, over a single molecule at room temperature (this chapter is adapted from a research paper recently published during the project (1)). The scripted procedures for thermal drift correction described in Chapter 3 enable the user to reproducibly acquire dense 2D and 3D force field maps over a small organic molecule adsorbed on a semi conducting surface.

4.1 Force Mapping of Molecules

The demonstration of submolecular resolution by Gross et al. (2009) (2) showed the unparalleled ability of NC-AFM, using CO functionalised tips, to image the detailed substructure of molecules adsorbed on metal surfaces (see Figure 1.18). Since then, the technique has produced a wealth of impressive results, including the ability to observe bond order in organic molecules (3), localisation of charge within a molecule (4), imaging the stages of a chemical reaction (5), molecular manipulation at the single bond level (6), and detailed investigation of on-surface synthesised 2D materials such as graphene nano-ribbons (7), amongst many others (8–10). In particular, many of these results make use of force mapping to elucidate key information about the molecule - substrate system, beyond that obtained via conventional imaging. Imaging can provide simple characterisation of the chemical structure for planar molecular systems, but in order to identify more complex quantities such as the adsorption angle, distortion in the molecular configuration due to surface-molecule interaction (2, 11, 12), and

deflection of the tip apex (13), it is necessary to acquire $\Delta f(z)$ data across multiple dimensions in order to allow the direct visualisation of the complex force field arising between the tip and the molecule. Two-dimensional force maps, in concert with conventional constant height imaging provide a relatively quick and convenient way of capturing most of the key information over high symmetry systems, and are particularly useful under challenging experimental conditions where acquisition times are limited. However, for more complex systems with a high degree of asymmetry, or where more sophisticated analysis (11, 13–15) is required, it is necessary to capture complete 3D force fields, with commensurately longer acquisition times and even stricter requirements for long-term tip and system stability.

Although demonstrating unparalleled resolution and sensitivity, these results have been almost exclusively limited to operation on planar metallic substrates at low temperature (approximately 5 K via liquid helium cooling). This is due to the requirements of both creating and maintaining a functionalised probe by controlled pickup of a single CO molecule (unstable at temperatures above ~ 10 K (16)), and the need for an extremely stable environment with negligible thermal drift (as the tip must approach extremely close to the adsorbed molecule in constant height in order to probe the Pauli repulsion regime (2)). These practical considerations drastically limit the accessibility of the technique and its use in studying systems under conditions relevant to real-world applications. Also, it has previously been demonstrated that intramolecular contrast can be obtained on nonmetallic substrates at elevated cryogenic temperatures without deliberate tip functionalisation (17–19), including demonstration of single images showing submolecular resolution at room temperature (20). In each of these works, the use of semiconducting materials for both tip and substrate inhibits diffusion of the molecules.

In order to assess the feasibility of room temperature intramolecular force mapping, a prototypical molecule - substrate system was chosen that was known to be stable at room temperature, and which had already demonstrated amenability to submolecular resolution imaging at cryogenic temperatures. Naphthalene tetracarboxylic diimide (NTCDI) adsorbed onto the $Si(111) - (7 \times 7)$ surface has been shown to have a commensurability between the reactive oxygen end groups of the molecule, and the silicon adatom spacing, which allows it to adsorb in an almost planar configuration

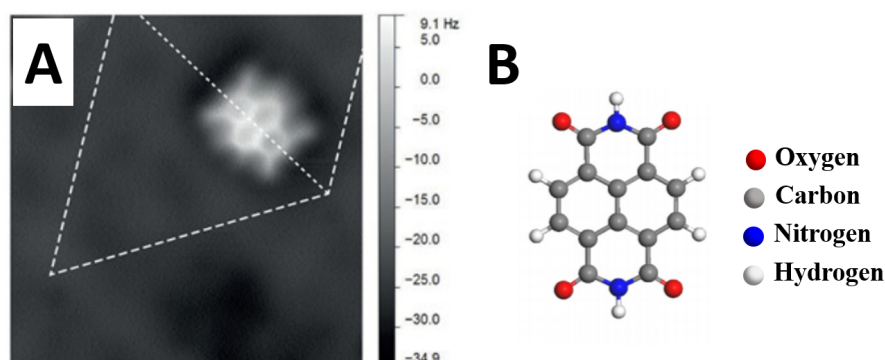


Figure 4.1: A) High-resolution NC-AFM image of prototypical Naphthalene tetracarboxylic diimide (NTCDI) molecule on Si(111)-(7×7), with substrate unit cell indicated by dotted white line. Image from Jarvis et al. (2015) (10). B) Stick & ball model of NTCDI.

in a number of sites in the Si(111) – (7 × 7) unit cell (see Figure 4.1), as demonstrated in previous combined STM/NC-AFM studies at cryogenic temperatures (10, 17).

4.2 Results: Preliminary Imaging and Force Data of NTCDI

To prepare the experiment, NTCDI molecules were deposited on a Si(111)-(7×7) surface via the Knudsen cell (see Section 2.1.1.2). A low coverage (< 0.1 ML) was achieved by heating the cell at 175°C for 30 minutes. Without the use of STM based techniques, adaptive height operation in NC-AFM was used for taking large overview images, and tip preparation.

4.2.1 Adaptive Height Imaging

In adaptive height (AH) mode, each line in the slow-scan direction is scanned twice, first with Δf feedback applied, to maintain the tip-sample

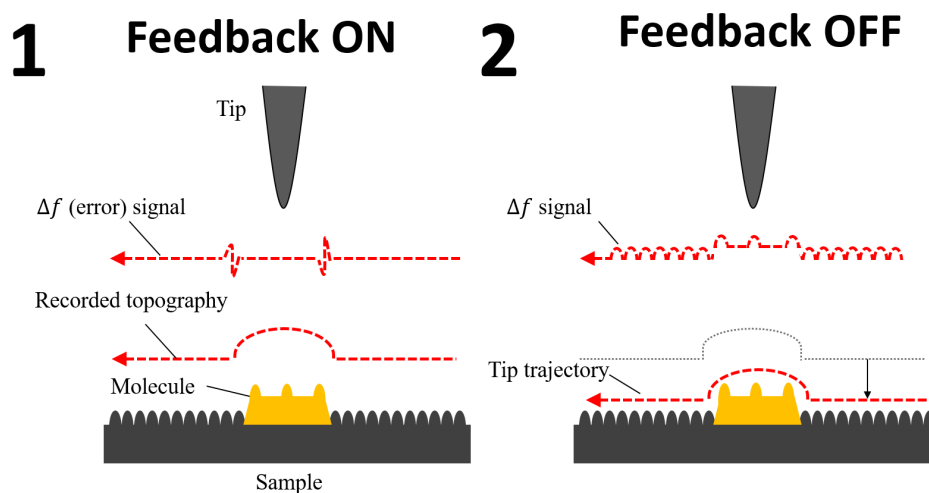


Figure 4.2: Schematic of Adaptive Height mode (AH) scanning in NC-AFM (19).

distance. This is followed by a scan without feedback. However this second pass traces the line profile of the previous pass (see Figure 4.2). This ensures the tip remains at a suitably safe distance from any large features/contaminants. In order to get closer to the surface, an additional offset to the tip height can be added to the pass with feedback disengaged. Adaptive height mode allows close approach of the surface features in order to observe intramolecular contrast whilst mitigating the risk of a tip-change due to thermal drift, because a safe feedback height is resumed after each line in the fast-scan direction.

Prior to performing the scripted experiments on NTCDI, larger ($> 10 \text{ nm}^2$) overview scans were conducted in adaptive height mode (introduced by Moreno et al. (2015) (19)) in order to locate the NTCDI molecules, as well as evaluate the tip state for potential further tip reconfiguration (20) and the cleanliness of the surrounding substrate. Applying conventional constant height scanning to such large areas is normally unfeasible at room temperature, due to high levels of instability and residual thermal drift compared with cryogenic conditions. However, reconstruction of a 3D force field acquired by this technique becomes extremely complicated due to the

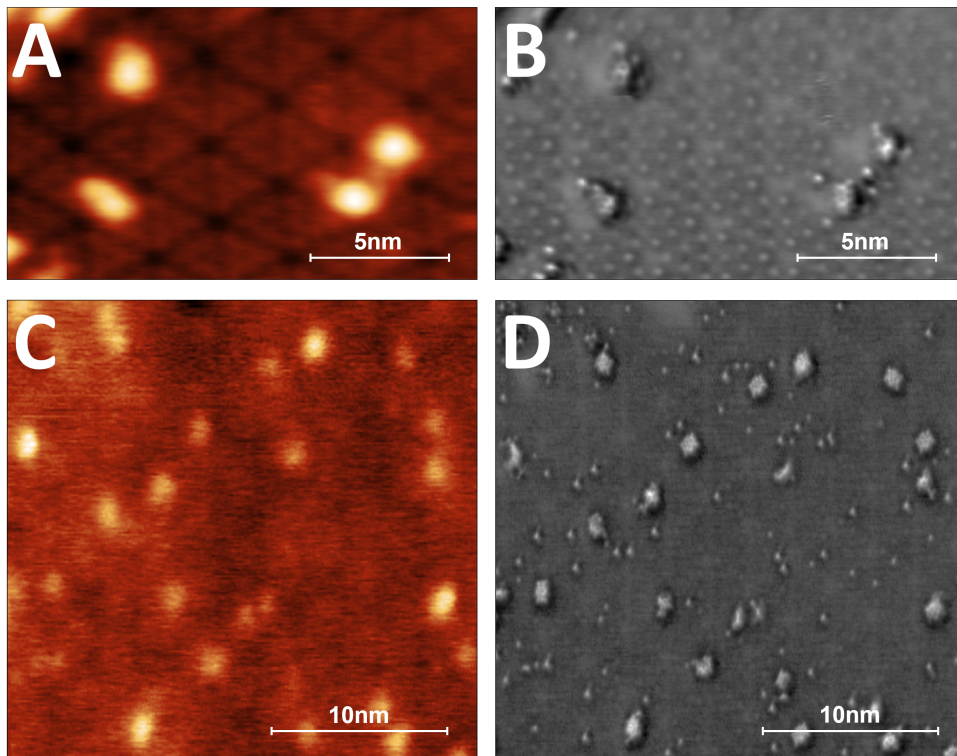


Figure 4.3: Two examples of scanning in adaptive height mode NC-AFM, of NTCDI molecules deposited on a Si(111)-(7x7) surface. A) & C) are topography images with Δf set points -0.9 Hz and -5.2 Hz and gap voltages, $V_{gap} +0.45 \text{ V}$, $+0.35 \text{ V}$, respectively. Oscillation amplitude, $A_0 = 21 \text{ nm}$. B) & D) are the respective corresponding Δf channels recorded without feedback in z . The offsets in z , when measuring in constant height mode, for B) & D) are -192 pm and -230 pm respectively.

4 Intramolecular force mapping at room temperature

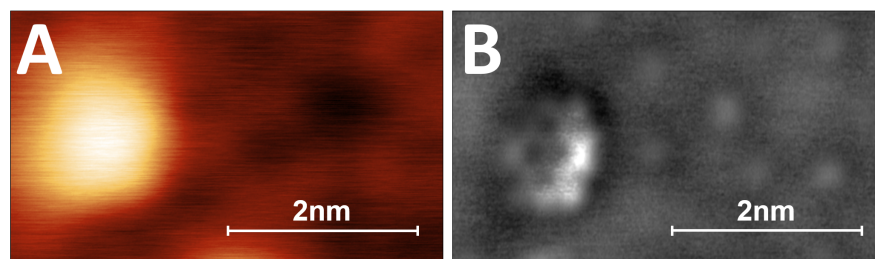


Figure 4.4: Examples of adaptive height mode scan over NTCDI molecule on Si(111)-(7×7) surface in NC-AFM. A) Image from topographic channel (the pass of constant Δf). B) Image from Δf channel (from adaptive constant height pass) with -150 pm offset applied. Image parameters: set $\Delta f = -0.8 \text{ Hz}$, $V_{gap} +1 \text{ V}$, $A_0 = 21 \text{ nm}$.

intrinsic misalignment of the absolute z position of adjacent spectra (19).

Figure 4.3 shows two examples of using AH scanning to survey the surface and to find suitable molecules. The submolecular resolution in the Δf channel during the second pass B) & D) allows the user to assess the specific adsorption geometry and intramolecular contrast. Figure 4.4 shows a higher resolution AH image, in which the Δf channel reveals the chemical structure of NTCDI. As with Figure 4.4.B, simultaneous submolecular contrast over the NTCDI & atomic resolution over the Si adatoms was sometimes observed. In this image, the repulsive contrast over silicon adatoms indicates the tip was passivated, potentially terminating with a OH^- group, which has been observed to improve contrast (20). This is in line with earlier low temperature studies, and density functional theory (DFT) simulations, that show that both Si - OH terminated and Si - terminated probes do not react strongly with adsorbed organic molecules (15, 17), and thus, both reactive and unreactive silicon tips have the ability to image with submolecular resolution (20). It is important to note that submolecular contrast is achieved routinely without deliberate functionalisation of the tip.

4.2 Results: Preliminary Imaging and Force Data of NTCDI

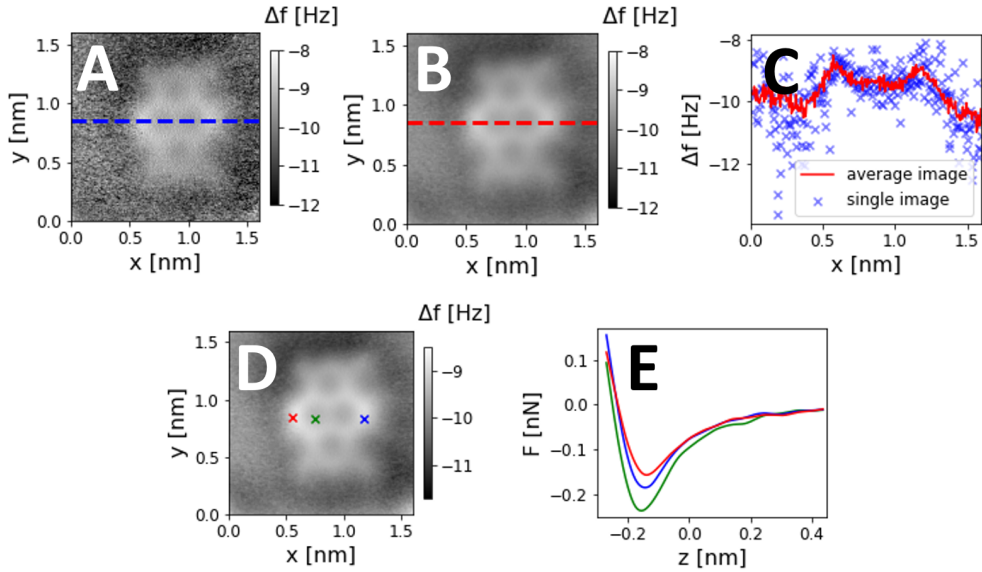


Figure 4.5: A) Constant height NC-AFM Δf image of a single NTCDI molecule at room temperature (raw data: tracking set point = -5.2 Hz, z height offset = -200 pm, $V_{gap} = 0.3$ V, $A_0 = 21$ nm, $t_{acq} = 120$ s). B) Averaged constant height NC-AFM Δf image of the same molecule, average of 20 scans (including forward and backward traces), total $t_{acq} = 22$ min. C) Plots of blue and red line profiles through single and averaged images showing signal-to-noise improvement. D) as B), with coloured markers indicating positions of single point Δf spectroscopy curves, which were converted into $F(z)$ curves and plotted in E). The $\Delta f(z)$ curves in were processed and inverted into $F(z)$ via the method discussed in Section 3.4, after subtracting the non-site specific forces by measurement of the tip-sample interaction over a corner hole site (18, 21).

4.2.2 Conventional Constant Height Imaging

Having assessed the contrast of the NTCDI via AH mode operation, conventional constant height Δf imaging and $\Delta f(z)$ point spectra would then be carried out. This helped gauge the appropriate parameters/dimensions of the scripted data sets. Using the early version of the drift correction procedure (see Section 3.1.2), even with optimised temperature regulation (Figure 3.5.B), limited the maximum acquisition time of a single scan frame. To ensure the drift in z remained under ~ 10 pm over the course of a single image, t_{acq} was limited to $\sim 1 - 2$ minutes for the constant height slices experiment.

However, with high f_0 Si cantilevers, it is possible to use a faster scan speed and acquire multiple images of the same area via regularly updated drift correction, and create a low-noise averaged image to help counteract the reduction in S/N that comes with higher scan speeds. With scripting, this can be done in a time comparable to that required to scan a single high quality image at low temperature with a qPlus sensor (> 5 minutes). This is depicted in Figure 4.5.A - C), wherein the averaging and improvement to S/N are plotted. Additionally, single point $\Delta f(z)$ spectroscopy curves were carried out on different locations of the molecule, indicated by the coloured markers in D). The calculated $F(z)$ curves plotted in E) show force minima ~ -100 pN, an order of magnitude smaller than what is typical for Si tips on Si adatoms (see Figures 3.13 & 3.16). This is indicative of a non-reactive tip interacting primarily via van der Waals and Pauli repulsive interactions. The force minima exhibit differences across molecular bonds of ~ 25 pN, and between bond and ring of ~ 45 pN, indicating the forces over different sites of the molecules could indeed be resolved in multi-dimensional maps. This, and routinely achieving submolecular contrast in constant height imaging, are prerequisites for success in the more demanding force mapping experiments.

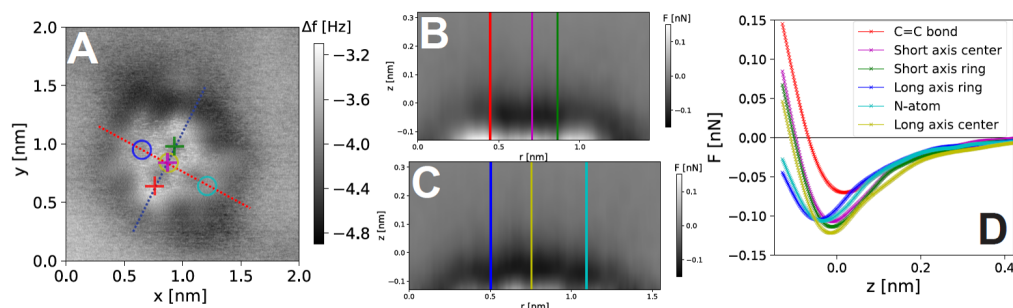


Figure 4.6: 2D grid spectroscopy experiment over short and long axes of NTCDI molecule on Si(111)-(7 \times 7). Map size: 300 \times 512 pixels, 1.8 nm \times 0.63 nm (r, z) tracking carried out on NTCDI molecule and resumed after every 5 spectra, total $t_{acq} \sim 90$ minutes. A) Constant height Δf image of a single NTCDI molecule adsorbed on the Si(111) – (7 \times 7) surface, showing the position of the 2D force maps subsequently acquired. Image parameters $V_{gap} = 0.15$ V, $z = -0.13$ nm relative to height at $\Delta f = -3.4$ Hz, $A_0 = 21$ nm. B) 2D force map acquired over the short axis of the molecule (blue line in A)). C) 2D force map acquired over the long axis of the molecule (red line in A)). D) Representative single point $F(z)$ curves extracted from both grids showing the force profiles over key sites on the molecule (positions marked on the Δf image and force maps). Details of $\Delta f(z)$ processing and inversion are discussed in Section 4.5.

4.3 Results: Intramolecular Force Mapping on NTCDI

4.3.1 2D Force Mapping

Sets of 2D force maps over a single NTCDI molecule were acquired (using grid spectroscopy) as shown in Figure 4.6. A) shows a conventional constant height image taken prior to scripting, overlaid with the positions of the cross-sectional maps across the short and along axes of the molecule (blue and red dotted lines). The positions of $F(z)$ curve extracted from the force maps are indicated by the 'o' and 'x' markers in A). B) & C) show the short and long axis force maps, respectively. Each shows the characteristic diffuse attractive halo arising from dispersion interactions surrounding the molecule, as

4 Intramolecular force mapping at room temperature

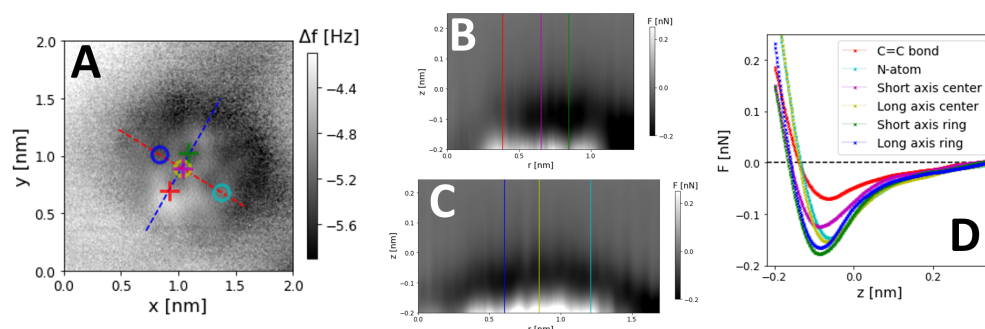


Figure 4.7: 2D grid spectroscopy experiment over short and long axes of NTCDI molecule on Si(111)-(7 \times 7). Map size: 400 \times 512 pixels, 2.0 nm \times 0.7 nm (r, z) tracking carried out on NTCDI molecule and resumed after every 5 spectra, $t_{acq} = 130s$, total $t_{acq} \sim 2$ hours. Additional 2D grid spectroscopy data set. A) Constant height Δf image of molecule prior to scripting. Image parameters $V_{gap} = 0.3$ V, $z = -200$ pm relative to height at $\Delta f = -3.1$ Hz, $A_0 = 21$ nm. B) 2D force map acquired over the short axis of the molecule (blue line in A)). C) 2D force map acquired over the long axis of the molecule (red line in A)). D) Representative single point $F(z)$ curves extracted from both grids showing the force profiles over key sites on the molecule (positions marked on the Δf image and force maps). Details of $\Delta f(z)$ processing and inversion are discussed in Section 4.5.

well as the more defined repulsive features due to Pauli repulsion at close approach. The force field over the long axis is roughly symmetric, with a mostly uniform attractive halo and repulsive features at close approach. D) shows representative $F(z)$ curves extracted from both grids over key sites on the molecule. Because the oxygen atoms of the molecule are bound to the surface, there are no strongly reactive sites present, and consequently only small attractive forces (~ 100 pN) and small variations in the force minima ($\sim 5 - 15$ pN) over the different areas of the molecule are detected. This demonstrates a comparable sensitivity to similar experiments carried out at cryogenic temperatures. The abnormally small minima on the left hand side of the molecular short axis (red curve in D)), likely arises from a tip asymmetry visible in the force field. A force difference of ~ 10 pN was observed between the bonds and rings, accounting for the tip asymmetry. Further discussion on the effect of tip asymmetries on quantitative force mapping is discussed in Section 4.5.3.

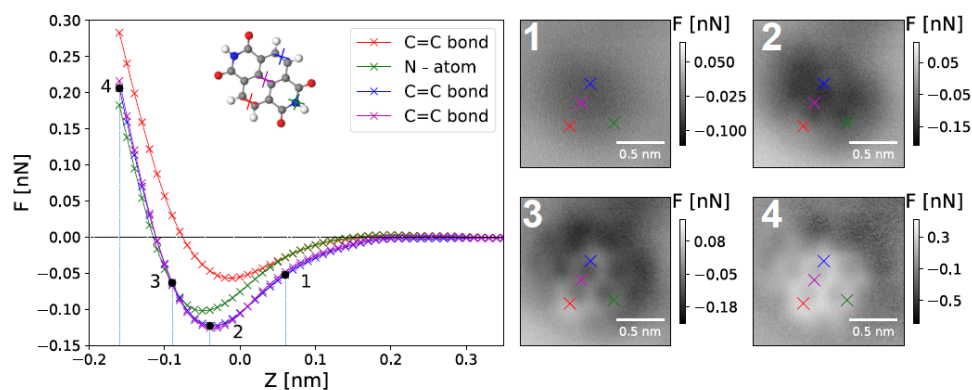


Figure 4.8: Data extracted from a full 3D force map $F_z(x, y, z)$ over a single NTCDI molecule. Map dimensions: $272 \times 272 \times 67$ pixels, $1.6 \text{ nm} \times 1.6 \text{ nm} \times 0.66 \text{ nm}$. Tracking set point -3.1 Hz , $V_{gap} = 0.3 \text{ V}$, $A_0 = 21 \text{ nm}$, scan time = 94 s , total $t_{acq} \sim 8 \text{ hours}$. Each height was scanned three times and the average image was calculated. (Left) $F(z)$ curves (averages of 10×10 pixel area) extracted over key sites on the molecule indicated by crosses on the images and inset molecular model. An insert of a stick & ball model of NTCDI is included to provide clarity for which sites of the molecule were chosen to extract the corresponding $F(z)$ curve. 1)-4) $F_z(x, y)$ images extracted at progressively closer tip-approach at heights indicated on the $F(z)$ graph. Data acquisition parameters $V_{gap} = +0.3 \text{ V}$, $\Delta f = -3.1 \text{ Hz}$, oscillation amplitude $A_0 = 21 \text{ nm}$.

This experiment was repeated with a different tip and plotted in Figure 4.7, demonstrating the reproducibility of the drift correction procedure. Here, the tip asymmetry was present again, and the attractive region top-right of the molecule is more pronounced, compared to Figure 4.6. The molecule in the latter of the two 2D forcing mapping experiments presented in Figure 4.7, was further characterised in a 3D force mapping experiment using the slices method.

4.3.2 3D Force Mapping

Figure 4.8 shows the first example of a 3D molecular force field captured at room temperature, taken on a different NTCDI molecule with a different tip apex, using the ‘slice’ method. Representative $F(xy)$ images extracted from

the 3D data set at decreasing tip-sample heights show a clear evolution in contrast, as previously described for similar systems at low-temperature (17, 18). Representative $F(z)$ curves extracted from the same data set at key sites over the molecule show a similar variation in minima and force resolution to those extracted from the 2D grids, confirming the correspondence between the two methodologies.

Previous room temperature measurements by Iwata et al. (2015) (20) were not precise enough to obtain differences in the tip-sample force with intramolecular resolution, but DFT simulations in the same work predicted a force difference of ~ 30 pN between the maximum interaction force over a C atom, and the centre of the carbon-ring. The force maps presented in Figures 4.6, 4.7 & 4.8 are able to detect ~ 10 pN differences between sites. The force sensitivity is discussed in further detail in Section 4.5.4. Although the interaction is of course dependent on the exact tip structure (which is not defined here) this nonetheless demonstrates that room temperature molecular force mapping has in principle sufficient accuracy to sense small chemical differences due to single atom substitutions in organic molecules or in graphene nano-ribbons (22).

4.3.3 Adsorption Geometry

Another key advantage of acquiring higher dimensional force maps as opposed to standard constant height imaging is the ability to perform more sophisticated analysis on the spectroscopic data to extract detailed quantitative information about the studied system. The conformation of the molecule adsorbed on the surface can be studied by following the method used by Mohn et al. (2011) (11, 12), which maps the minimum $\Delta f(z)$ or $F(z)$ value for each point in (x, y) across the molecule:

$$z_{\Delta f}^*(x, y) = \arg \min \Delta f_z(x, y, z) \quad (4.1)$$

$$z_F^*(x, y) = \arg \min F_z(x, y, z) \quad (4.2)$$

4.3 Results: Intramolecular Force Mapping on NTCDI

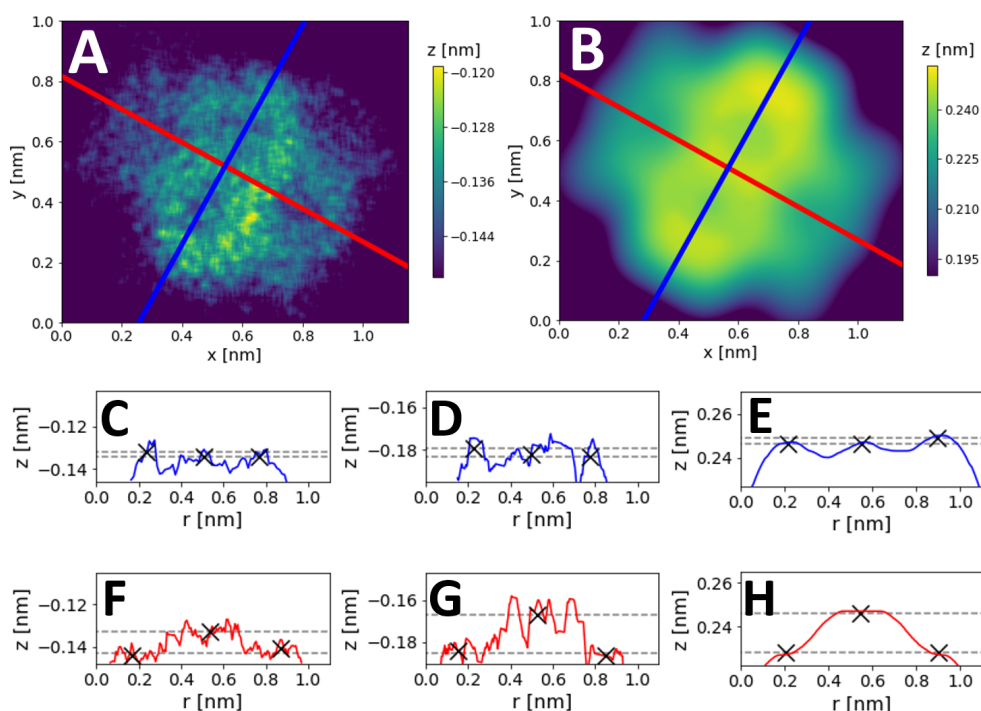


Figure 4.9: Analysis of structural distortion due to adsorption for a single NTCDI molecule. A) Experimental $z^*(x, y)$ map (main result in Figure 4.8. B) Simulated $z^*(x, y)$ map. C) Experimental (3D data set), D) Experimental (2D data set, main result in Figure 4.7), and E) Simulated, $z^*(x, y)$ profiles through the molecular short axis (blue line in A) and B)). F) - H) as for C) - E) but through the molecular long axis (red line in A) and B)). The extracted heights of the same central and outermost features (marked with an 'x') are plotted on each profile as grey dotted lines.

In Figure 4.9, Equation 4.1 was applied to the $\Delta f(z)$ data from the force map Figures 4.8 & 4.9, which were acquired on the same molecule using the same tip. The height of the $\Delta f(z)$ turnaround conveys the height above the surface of the molecular feature at that point, and the differences between the turnaround heights can be used to determine the conformation geometry of the molecule. Given the high symmetry of NTCDI, the analysis for the 3D Δf map can be simplified by considering just the short and long axes of the molecule, which allows for direct comparison with the 2D counterpart. Both experimental data sets were compared to a simulated force map using the Probe Particle Model (PPM). Details of the simulation are discussed in Section 4.4.

First, for the short axis it is known that NTCDI adsorbed on Si(111)-(7×7) can adopt both planar and tilted adsorption configurations with respect to the substrate, although from combined experimental and Density Functional Theory (DFT) studies it is expected that the planar configuration will be more commonly observed (10). In the data sets shown in Figure 4.9, the tilt of the molecule in the short axis is $\sim 2 - 4$ pm, as compared to the ~ 3 pm tilt predicted from combined DFT and probe particle model (PPM) simulation (23). This is flat within the experimental and computational error, and intuitively correct as the molecule and adsorption geometry are symmetric with respect to the surface along this axis.

In contrast, the long axis data shows a bowing downwards in the z^* maps, with the end nitrogen atoms being pulled down below the central aromatic rings. In the 3D data set the nitrogen atoms were determined to be 11 ± 7 pm below the central bond of the molecule, whereas for the 2D data set a similar analysis resulted in an estimate of 18 ± 9 pm. This is very similar to the results of the same analysis applied to the simulated PPM data set, which shows a height difference of 18 ± 4 pm. Examination of the DFT calculated geometries (see Section 4.4.1) shows that this molecular distortion arises from the strong bonding of the oxygen atoms at the end of the molecule with the underlying silicon adatoms, due to the almost perfect commensurability between the positions of the carboxylic groups and the adatom positions in this adsorption geometry (10). Due to the symmetry of the data and the experimental system, this effect cannot be ascribed to any tip asymmetry, and therefore provides strong evidence that quantitative observations of extremely subtle distortions in the molecular framework

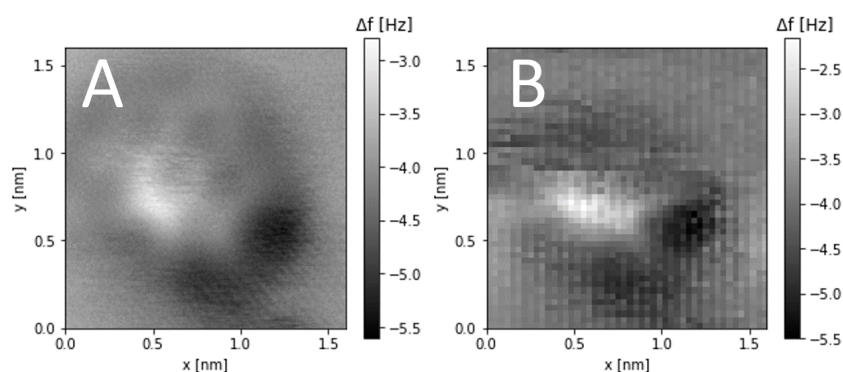


Figure 4.10: Images of closest approach across (x, y) , taken from concurrent 3D $\Delta f(x, y, z)$ maps gathering using the constant height slices method and grid spectroscopy methods. A) Constant height slices $\Delta f(x, y, z)$ map dimensions: $256 \times 256 \times 65$ pixels, $1.6 \text{ nm} \times 1.6 \text{ nm} \times 0.65 \text{ nm}$. Tracking set point -4.8 Hz , $V_{\text{gap}} = 0.45 \text{ V}$, $A_0 = 21 \text{ nm}$, scan time = 118 s , total $t_{\text{acq}} \sim 8 \text{ hours}$. Each height was scanned three times and the average image was calculated. B) Grid spectroscopy $\Delta f(x, y, z)$ map dimensions: $48 \times 48 \times 1024$ pixels, $1.6 \text{ nm} \times 1.6 \text{ nm} \times 0.65 \text{ nm}$. Tracking set point -4.8 Hz , $V_{\text{gap}} = 0.45 \text{ V}$, $A_0 = 21 \text{ nm}$, tracking was paused after every 5 spectra, $t_{\text{acq}} \sim 300 \text{ s}$, total $t_{\text{acq}} \sim 40 \text{ hours}$. A tip-change occurs part of the way through the experiment after 24 hours measurement, possibly due to repeatedly taking the tip to the point of closest approach.

can be made, despite the extremely challenging experimental conditions. This suggests that structural determination of complex molecules, and even chemical identification of atoms within molecules (14) is in principle achievable even during room temperature studies.

4.3.4 Supporting Data Sets

Further data sets are provided in this section to demonstrate the reproducibility of the experimental protocol. Figure 4.10, depicts the $\Delta f(x, y)$ images of closest approach extracted from 3D data sets gathered concurrently using the slices and grid spectroscopy methods respectively. The slices experiment reached the full intended volume of data successfully without fault, however, when it came to the grid spectroscopy, a tip-change occurred roughly halfway through. The acquisition time for the slice method was $\sim 8 \text{ hours}$, and $\sim 40 \text{ hours}$ for the grid spectroscopy. Approximately

4 Intramolecular force mapping at room temperature

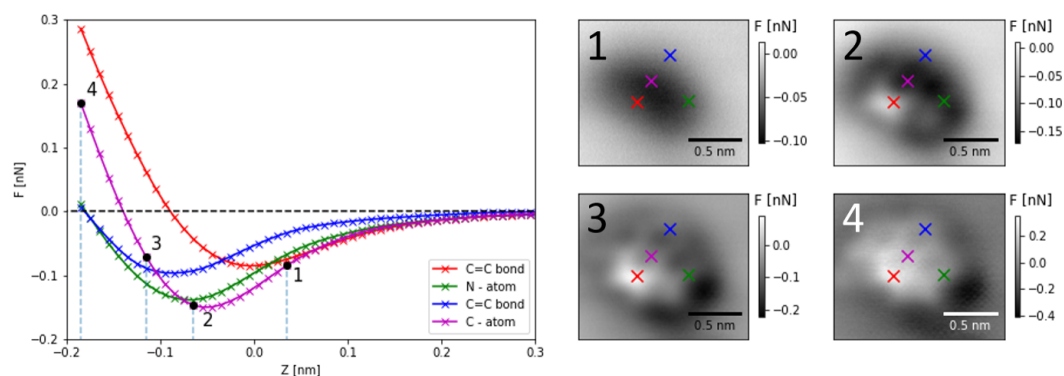


Figure 4.11: 3D force map (plotted in same way as Figure 4.8) constructed by inverting the Δf data from the slice experiment in Figure 4.10.A). Left) $\Delta F(z)$ curves plotted, extracted over key sites on the molecule. Positions of $F(z)$ are indicated on the images to the right. Images 1)-4) extracted at progressively closer tip-sample distances, at heights indicated on the $\Delta F(z)$ graph.

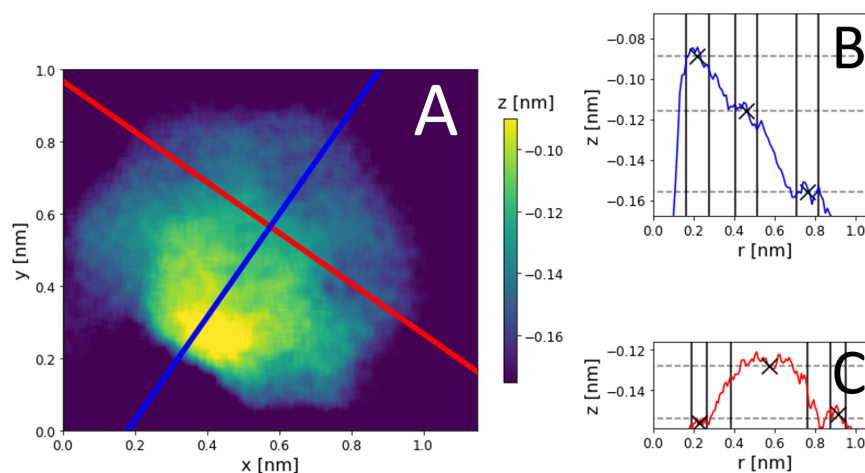


Figure 4.12: Extraction of $z^*(x, y)$ from Δf map data from Figure 4.10. A) $z^*(x, y)$ image, and line profiles through the short and long axes of the molecule plotted in B) & C). The heights across the features are calculated and indicated by the \times markers (average heights at each site are calculated ranges of data indicated by the vertical lines).

halfway through the grid spectroscopy method there was a tip-change, thus giving a discontinuity in the grid and subsequent resolution of the molecule, highlighting the difficulty with 3D grid spectroscopy. However, it is likely if the experiment was set to run quicker, it would have succeeded without a tip-change.

Using the slices 3D Δf map from Figure 4.10.A, a map of the $F_z(x, y, z)$ signal was generated. Figure 4.11 depicts the force map inverted from the 3D Δf map (via the slices method). The minima of the $F(z)$ curves extracted over the key sites of the molecules are of similar magnitude to Figure 4.8, and evidence of tip asymmetry is present again. It is worth noting that it was not the same tip (nor the same cantilever) used for the experiments in Figures 4.8 & 4.11.

As with Figure 4.9, the $z^*(x, y)$ map can be extracted from the 3D Δf signal and plotted (along with the line profiles of the short and long axes of the molecule) in Figure 4.12. The tip asymmetry is prominent in the $z^*(x, y)$ also, with an apparent drop in the short axis (left to right) of $67 \text{ pm} \pm 10 \text{ pm}$. This is discussed further in Section 4.5.3. The long axis appears more symmetrical, with the nitrogen atoms positioned $22 \pm 8 \text{ pm}$ on average, below the central carbon double bond, and is in good agreement with measurements performed with other tips (see Figure 4.9).

4.4 Simulated AFM data

4.4.1 DFT

Density Functional Theory (DFT) calculations of a single molecule of NTCDI adsorbed onto Si(111)-(7×7) were carried out to support the experimental force map data. The DFT calculated geometry that matched the most typical configuration observed in experiment (see Figure 4.3) was taken from Jarvis et al. (2015) (10). Figure 4.13 renders this geometry across orthogonal viewpoints using Ovito software (24). The adsorption geometry was evaluated using the atomic coordinates calculated from the DFT, revealing a bowing across the long axis which pulls the nitrogen atoms 20.2 pm below the

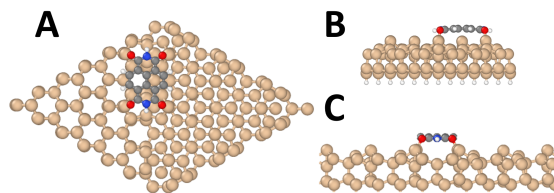


Figure 4.13: Potential adsorption geometry of NTCDI molecule on Si(111)-(7x7) surface rendered in Ovito software (24). A) the (x,y) plane, B) (y,z) plane (cross-section of the long axis of the molecule), and C) (x,z) plane (cross-section of the short axis of the molecule).

central carbon-carbon bond atoms. The profile across the short axis was found to be inclined toward the right side by 3.0 pm .

4.4.2 PPM

Using the probe particle model (PPM) (23), simulated AFM images were generated to construct a similar 3D force map as in Figures 4.8 & 4.11. Example $F(z)$ curves and x,y slices through the matrix are presented in Figure 4.14, in the same manner as Figures 4.8 & 4.11. The significant difference between force minima between experimental and simulated results was ignored, as the purpose of the simulation was for assessing the adsorption geometry of the NTCDI, rather than its interaction with the tip. Given the unknown exact geometry of the tip, a range of probe stiffnesses, k , and charges, Q , were tested. For the data presented in Figures 4.9 & 4.14, the set of parameters which most closely recreated the experimental bond length, $k = 1 \text{ N/m}$ and $Q = 0$ were chosen. DFT data & PPM simulations were performed by Jack Henry.

4.4.3 Estimating Tip Apex Stiffness

The lateral stiffness, k_{xy} of the tip apex will determine the degree to which it will deflect under strong tip-sample interaction. This deflection results in

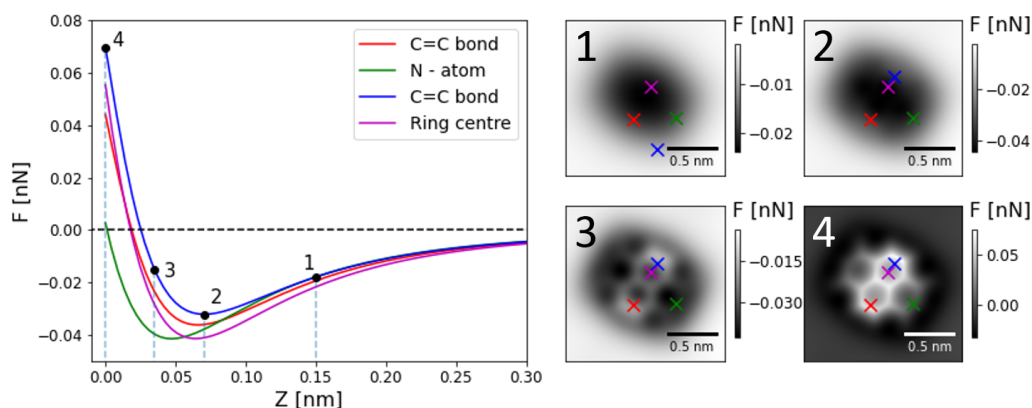


Figure 4.14: Map of the force from PPM simulation, spanning 0.3 nm above the NTCDI on $\text{Si}(111)-(7 \times 7)$, with a vertical spacing of 1 pm . (Left) Single point force spectra from the 3D data set, with positions in (x, y) indicated by the markers in images 1)-4) which show cross-sections of the 3D force map in the (x, y) plane at various heights. $k = 1 \text{ (N/m)}$, $Q = 0$. PPM simulation performed by Jack Henry.

| Line Profile | Experiment | | PPM ($k = 0.5 \text{ N/m}$) | | PPM ($k = 1 \text{ N/m}$) | |
|--------------|-------------------------|--------------|-------------------------------|--------------|-----------------------------|--------------|
| | Length (\AA) | Increase (%) | Length (\AA) | Increase (%) | Length (\AA) | Increase (%) |
| Short axis | 5.69 | 11 | 5.94 | 18 | 5.78 | 10 |
| Long axis | 7.70 | 10 | 7.92 | 14 | 7.43 | 8 |
| 2 rings | 5.60 | 11 | 5.69 | 15 | 5.44 | 10 |
| 2 rings | 5.35 | 8 | 5.63 | 14 | 5.38 | 9 |
| 2 rings | 5.42 | 11 | 5.72 | 16 | 5.35 | 8 |
| 2 rings | 5.57 | 12 | 5.66 | 15 | 5.41 | 10 |

Table 4.1: Table of lengths across various sites of the molecule measured using a Gwyddion line profile (see Figure 4.15), for both experimental image (Figure 4.4.B) and simulated PPM image (Figure 4.14.4). The lengths spanning the axes of the molecule, and all distances across two of the four rings were calculated from the line profile. % exaggerations of the DFT calculated structure are also tabulated. The average increase (as a %) in bond length from the experimental data set is 10.5 %. The average increase (as a %) in bond length from the PPM simulation for stiffnesses, $k_{xy} = 0.5 \text{ N/m}$ and $k_{xy} = 1 \text{ N/m}$, were 15.3 % and 10.2 % respectively. The simulated tips were uncharged: $Q = 0 \text{ e}$.

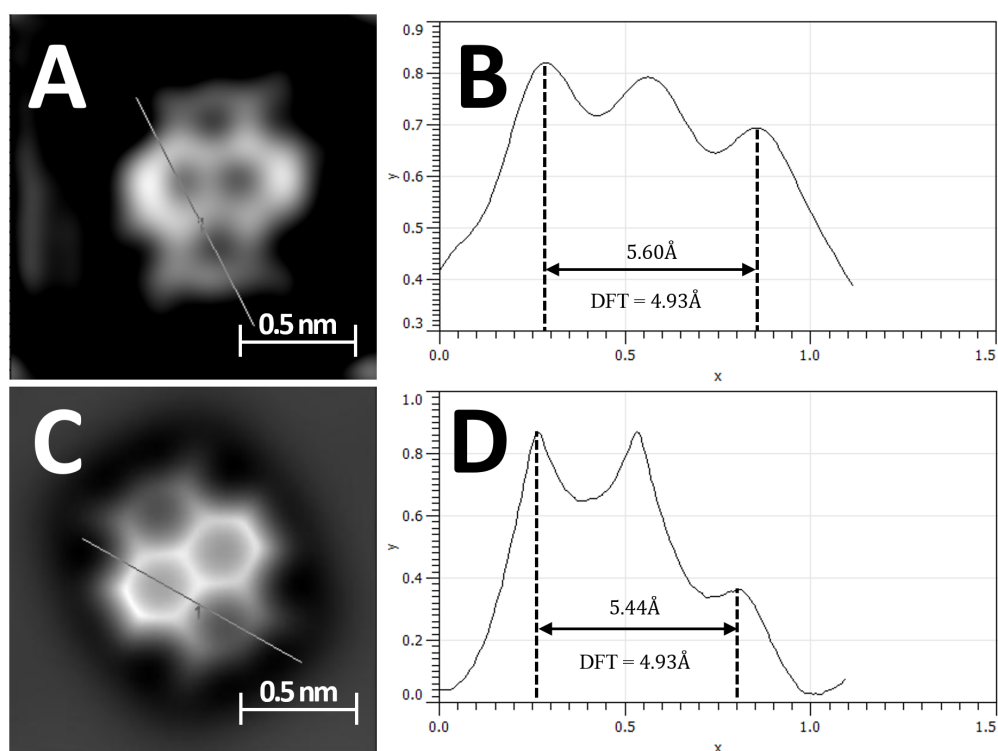


Figure 4.15: Example bond length measurement for experimental and PPM data. A) Average image of 20 constant height scans of NTCDI molecule from Figure 4.5.B. The line profile drawn (by eye, with thresholding to help) across two rings is depicted in B). Using the line profile, the distance across the two rings is calculated to be 5.60Å. C) & D) As for A) & B), for PPM calculated constant height image of NTCDI molecule (see Figure 4.14.4), with simulated stiffness, $k = 1 \text{ N/m}$ and charge, $Q = 0 \text{ e}$. The lengths and % exaggeration for all line profiles used across each constant height are included in Table 4.1.

the exaggeration of image features, i.e. the individual bonds of the molecule (25). A CO molecule adsorbed on the tip apex has been shown to have a low lateral stiffness (2, 25, 26), and thus deflects laterally to exaggerate bond lengths. A quantitative analysis of the high-resolution image in Figure 4.15.A shows that although the images fail to show the strong ‘sharpening’ of the bonds and other image distortions associated with imaging with CO terminated tips (2), the absolute bond lengths within the molecule are nonetheless exaggerated when compared to the DFT calculated structure. Using the same method as Mönig et al. (2018) (25), various lateral stiffness levels for the simulated data were used and compared to the experimental data, in order to estimate k_{xy} .

Table 4.1 compares various distances across the NTCDI using the averaged image from Figure 4.4.B, and a simulated probe particle model (PPM) (23) image (Figure 4.14.4), and presents the respective bond exaggerations as a % increase over the calculated DFT structure. A simulation using CO-level stiffness ($k_{sim} = 0.5 \text{ N/m}$) resulted in a PPM bond length exaggeration of 15.3%, whereas for a CuOx tip ($k_{sim} = 10 \text{ N/m}$), this exaggeration was 2%. The experimentally determined bond lengths are on average 10.5 % larger than DFT prediction. $k_{xy} = 1 \text{ N/m}$ simulated tips provided the closest approximation of the experimental data: 10.2 % exaggeration, a comparison is shown in Figure 4.7. This indicates the tips across these room temperature experiments have a level of stiffness between those typically estimated for CO terminated tips ($k_{xy} \sim 0.25 - 0.5 \text{ N/m}$) and the stiffer CuOx tip termination ($k_{xy} \sim 10 \text{ N/m}$) (25).

4.5 Data Processing

As with the data sets of the bare Si(111)-(7×7) substrate (see Section 3.4), the Nanonis images and spectroscopy data files were imported into appropriately sized numpy arrays using Python. For the 2D grid spectroscopy data sets (Figures 4.6 & 4.7), Δf curves were smoothed across the lateral dimension, r with a 10 pixel-wide averaging window (equating to 60 pm and 50 pm respectively). The respective first curves of the data sets were taken to be the background and subtracted from all other curves. Scipy

spline fits were made for each of the $\Delta f(z)$ curves, and inverted into $F(z)$ using Equations 1.23 & 1.24 (27). Further spline fits in z were applied to the $F(z)$ map, and the extracted $F(z)$ curves shown in subplots: D) were averaged across 10 pixels also.

For the slices method data sets (Figures 4.8 & 4.11), the repeat scans at equal heights (3×3) were averaged to improve the S/N. No *post-hoc* alignment was applied to the images gathered throughout this thesis. Sufficient alignment was already provided by the in-situ drift correction procedure. The 3D grid was smoothed in (x, y) first using a 10×10 pixel averaging window ($\sim 60 \text{ pm}^2$), then across z using a spline fit ($\lambda = 0.99$). In each $\Delta f(x, y, z)$ map, the position of the substrate corner holes could not be determined from the constant height images. Therefore the background signal (for force inversion) was taken from the upper right hand corner, to be as far as possible from the molecule. The force conversion was carried out in the same way as for the 2D data, for all points in (x, y) . The force data was then smoothed with an additional spline fit in z ($\lambda = 0.99$), and the single point $F(z)$ curves were extracted from an average of 10×10 pixels.

For extraction of the $z_{\Delta f}^*(x, y)$ images (Figures 4.9 & 4.12) from the $\Delta f(x, y, z)$ maps, the Δf signal was smoothed in (x, y) initially using a 20×20 pixel averaging ($\sim 120 \text{ pm}^2$) window. Spline fits were applied across $\Delta f(z)$ as before ($\lambda = 0.99$). After extracting the minimum value of Δf at each point in (x, y) , no further smoothing was done. The $z^*(x)$ line profiles in Figures 4.9.D & G) (extracted from the 2D grid spectroscopy experiment: Figure 4.7) were extracted from the raw $\Delta f(r, z)$ map, and then smoothed across r using a 3 pixel wide averaging window.

4.5.1 Noise Considerations

Preliminary measurements in NC-AFM evaluated the S/N in $\Delta f(z)$ spectra whilst oscillating the cantilever at 14 nm or 22 nm. Figure 4.16 reveals that slightly worse S/N was observed whilst oscillating at the smaller amplitude of 14 nm. Therefore, larger amplitudes ($\sim 20 \text{ nm}$) as used by Iwata et al. (2015) (20), were used across subsequent experiments to avoid the practical limitations that come with small amplitude oscillation. The

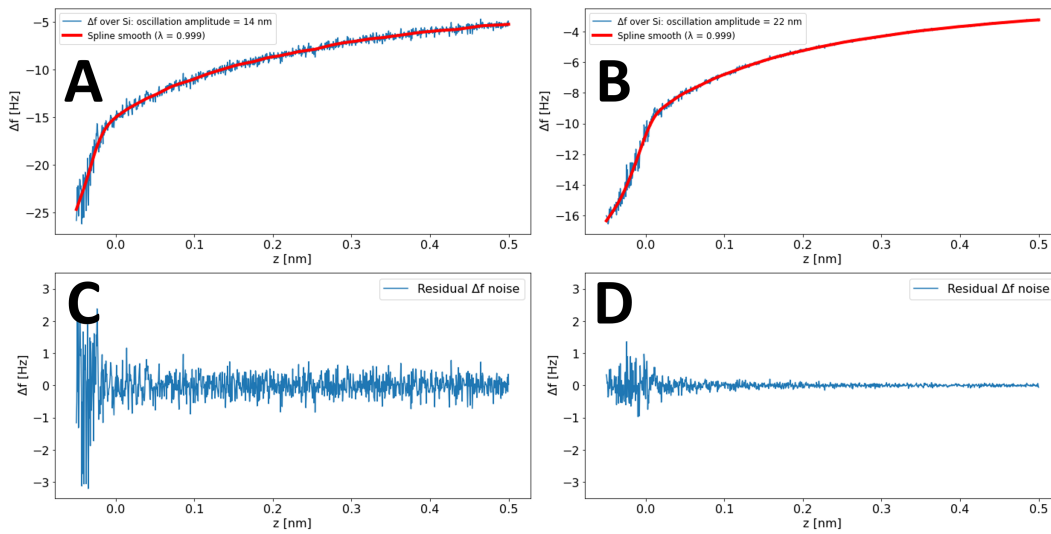


Figure 4.16: A) & B) single point $\Delta f(z)$ curves carried out using $A_0 = 14 \text{ nm}$ and $A_0 = 22 \text{ nm}$ respectively. Spline fits of the raw data ($\lambda = 0.9999$) are plotted in red. The residual $\Delta f(z)$ signals of A) & B) (raw data subtracted from the fit) are plotted in C) & D) respectively, as an estimate for the level of noise in $\Delta f(z)$.

theoretical advantages of smaller amplitude operation (higher sensitivity to short-range forces (28)) can be outweighed by the practical considerations: jump to contact, larger magnitudes of frequency shift signals (which can affect dissipation and the required PLL bandwidths), and a reduced detector signal.

The levels of noise for NC-AFM force mapping experiments conducted on the Si(111)-(7×7) adatoms, and on the NTCDI molecule, were analysed in Figure 4.17. $\Delta f(z)$ spectra acquired on samples are plotted in A) and B), with a spline fit to assess the level of noise. For both curves, there is a reduction in noise at the $\Delta f(z)$ turnaround. For A) in particular, the noise becomes negligible at the Δf minimum. This indicates the dominant source of noise at close approach in the NC-AFM experiments was the mechanical noise, δz_{mech} of the microscope, since the noise contribution from δz_{mech} is proportional to the slope of Δf (29).

The error signals in $\Delta f(z)$ for the Si adatom and NTCDI curves are plotted in Figure 4.17.C & D) (blue). Using the methodology proposed by Sugimoto

4 Intramolecular force mapping at room temperature

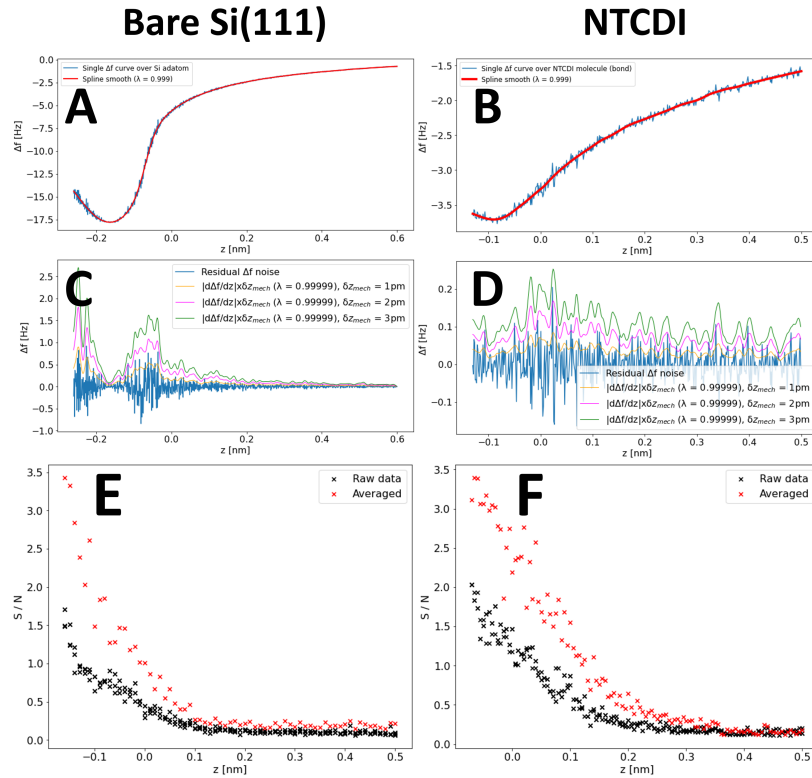


Figure 4.17: A) & B) Single point $\Delta f(z)$ curve taken over a Si adatom and NTCDI molecule respectively. Spline fit curves ($\lambda = 0.99$) are plotted to estimate the Δf noise. C) & D) The measured Δf noise (the differences between the raw $\Delta f(z)$ signal and the spline fits) are plotted for curves A) & B). Models of the mechanical noise are plotted using the method proposed by Sugimoto et al. (2010) (29) in order to estimate the δz_{mech} that best fit the experimental data. The raw output of Equation 4.3 was smoothed slightly for clarity via spline fitting ($\lambda = 0.9999$). E) & F) Δf noise levels (as S/N) in slices-based $\Delta f(x, y, z)$ mapping experiments conducted over E) bare Si(111)-(7 \times 7) and over F) NTCDI (main results seen in Figures 3.14, 4.8). The S/N was calculated for both raw data and averaged images (of 3 scans) in Python using a FFT filtration to extract the 'signal' image, from the 'noise'.

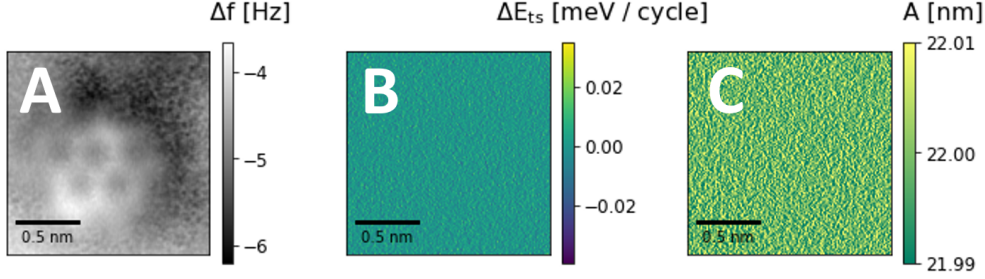


Figure 4.18: A) Raw Δf , B) dissipation, and C) amplitude channels of the scan of closest approach from force map experiment (main result in Figure 4.8).

et al. (2010) (29)), calculated models of the mechanical noise of the system were also plotted, for various values of δz_{mech} :

$$\Delta f_{noise} = \left| \frac{d\Delta f}{dz} \right| \times \delta z_{mech} \quad (4.3)$$

From Figure 4.17.C) & D), δz_{mech} values of 1 μm , and 2 μm respectively, provided the best fit. Thus, the dominant source of noise in the system is mechanical, and the magnitude of that mechanical noise can be estimated as 1 – 2 μm .

The evolution of the S/N, for both raw data and averaged images (of 3 scans) across z in the $\Delta f(x, y, z)$ maps, is depicted in Figure 4.17.E & F). For the raw data at far distances, the S/N approaches zero, and at the point of closest approach, $S/N \sim 1.5 - 2$. Averaging the image over 3 scans increases S/N by approximately a factor of 2.

4.5.1.1 Dissipation

The calculations carried out for force inversion only capture the conservative part of the interaction. Furthermore the calculations assume the oscillation amplitude, A_0 is constant. To verify the validity of the force inversion, the

dissipation and amplitude channels were checked for each molecular force map data set (in addition to an inflection point-test, see Section 1.2.3.1). An example (using data from Figure 4.8) is plotted in Figure 4.18. A) depicts the constant height Δf image of closest approach in the grid, and B) & C) are the dissipation and amplitude channels respectively associated with the scan. The dissipation, B) has been converted from the excitation channel (units of (V)) into the energy dissipation of the approach and retraction of the tip (units of (meV / cycle)) using Equation 1.26 for energy dissipation arising from the tip-sample interaction (28). A'_{drive} is the driving amplitude, observed in C), and A_{drive} is the 'free' damping signal, taken from a constant height scan at the furthest tip-sample distance from the molecule. The dissipation and driving amplitude signals are negligible and so do not affect the force reconstruction. This is typical for the other measurements of molecular systems at room temperature, and reflects the conservative nature of the interaction of a passivated tip with the molecule (similar to measurements with CO tips on molecules using a qPlus sensor at low temperature (2)), which is different to the chemically reactive (e.g. silicon on silicon (29–31)), or highly flexible (e.g. NaCl (32)) systems often imaged using room temperature NC-AFM.

4.5.2 f_0 Drift

In some experiments, a slow drift in the resonance frequency, f_0 of the cantilever, was observed. This is almost certainly a result of thermal fluctuation of the cantilever, whereby the change in f_0 , causes a shift in the $\Delta f(z)$ spectra.

Using the Equation presented in Giessibl (2003) (28), an estimate can be made for the deviation in f_0 due to temperature change:

$$\frac{\partial f_0}{\partial T} = f_0 \left(\frac{1}{v_s} \frac{\partial v_s}{\partial T} \right) \quad (4.4)$$

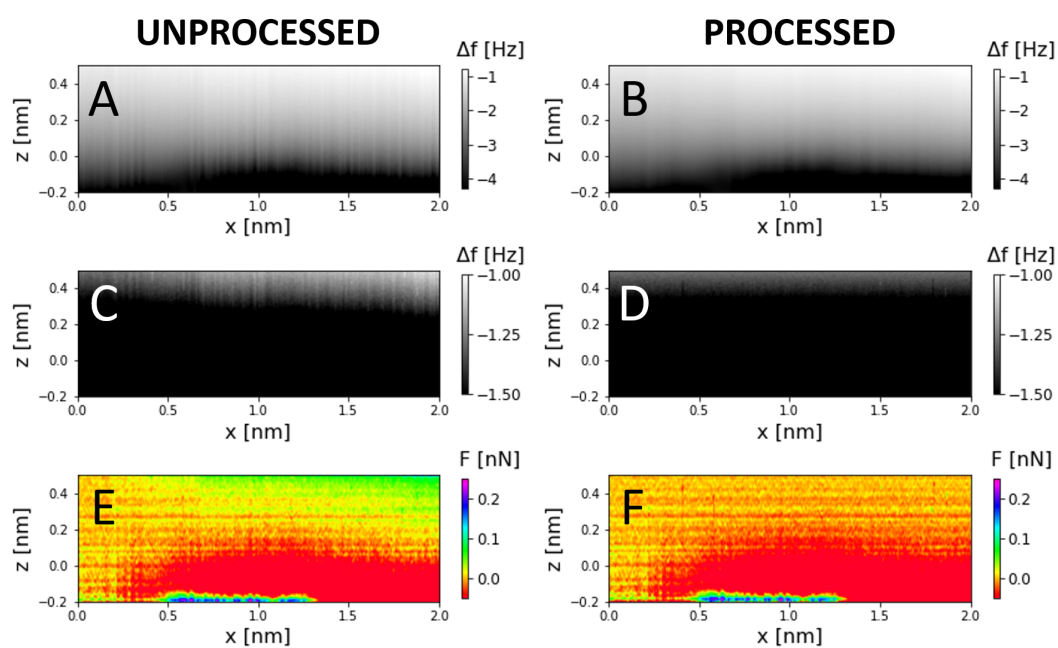


Figure 4.19: Processing of 2D grid spectroscopy Δf map conducted over NTCDI molecule (main result in Figure 4.7). A) raw Δf . B) Δf following processing via a 10 point rolling average in x , and alignment of the long range data in Δf . C) & D) as above but with colour bar of figure adjusted to highlight the behaviour of the Δf at large tip-sample separations. E) & F) are the outputs of the force inversion from the unprocessed and processed data sets respectively.

where v_s is the speed of sound in a Si cantilever at room temperature. Using Equation 4.4, $\frac{\partial f_0}{\partial T} \approx -9.4 \text{ Hz/K}$, thus, a change in temperature on the order of 10 mK can shift f_0 by 0.1 Hz (this was typical during moments where the temperature control PID loop was not fully stabilised).

Figure 4.19.A depicts the raw $\Delta f(x, z)$ map used for Figure 4.7, composed of 400 point spectra, measured over the course of 2 hours. The effect of f_0 drift can be observed in the tail end of the $\Delta f(z)$ spectra. The Δf colour threshold was changed and plotted in Figure 4.19.C to highlight the drift in signal far from the sample. The Δf signal in the long range regime systematically shifts $\sim -0.1 \text{ Hz}$ from the first curve to the last over the course of the experiment (from left to right, within the image). This effect carries over to and is observed in the force reconstruction (E)) of the $\Delta f(x, z)$ map, whereby the tail ends of the $F(z)$ curves become repulsive toward the right hand side of the map.

When such systematic shifts were observed, the $\Delta f(z)$ curves were shifted in the Δf axis in order to align the long range parts of the curves with that of the first $\Delta f(z)$ taken in the grid. This was to prevent the distortion of the inverted $F(z)$ data. Linear fits of only the furthest 50 points of the raw $\Delta f(z)$ curves were used to determine the required shift to have all $\Delta f(z)$ curves equal in the long range regime. From there, the $\Delta f(x, z)$ would be processed as described in Section 4.5. Figure 4.19.B, D), & F) depict the $\Delta f(z)$ map after alignment, and smoothed in x using a 10 pixel sized rolling average.

Thermal fluctuation of the cantilever may also occur during a slices based experiment, however it is less overt when in the (x, y) images, as the typical acquisition time for a single constant height image is too short to observe a noticeable shift in the Δf signal due to thermal drift of f_0 . The effect of f_0 drift would be apparent when comparing the $\Delta f(z)$ behaviour of the grid data with that of preliminary $\Delta f(z)$ point spectra. However, such systematic shifts were only observed during the grid spectroscopy experiments presented in Figures 4.7 & 4.10.B.

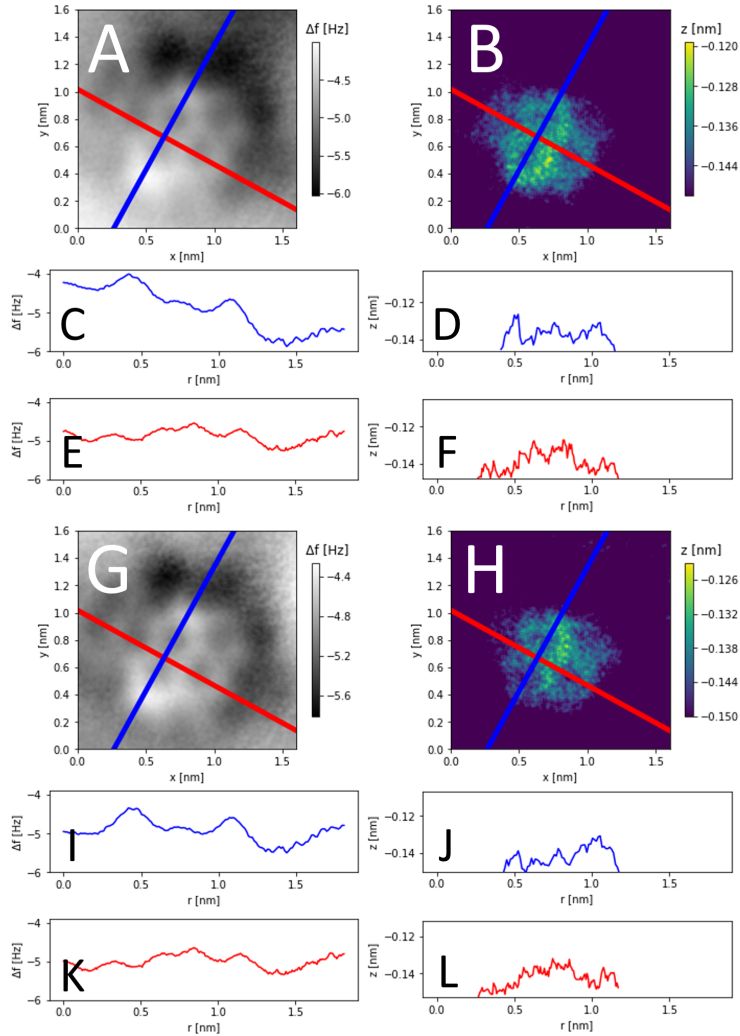


Figure 4.20: Δf^* and $z^*(x,y)$ map comparisons between uncorrected data and plane-corrected, using $\Delta f(x,y,z)$ data from Figure 4.8. A), C), E) Uncorrected $\Delta f^*(x,y)$ map and axes line profiles. B), D), F) Uncorrected $z^*(x,y)$ map and axes line profiles. G), I), K) plane-corrected $\Delta f^*(x,y)$ map and axes line profiles. H), J), L) plane-corrected $z^*(x,y)$ map and axes line profiles. The plane tilt was calculated using the 10×10 pixel averages of the four lateral corners of the $\Delta f(x,y,z)$ image at furthest approach.

4.5.3 Tip Asymmetry

When performing $z^*(x, y)$ and $\Delta f^*(x, y)$ mapping, it is important to consider the effect of tip asymmetry. Similar to all SPM, these maps are necessarily a convolution of the structure of the sample (molecule) and the tip apex. Under the assumption of a uniform symmetric tip, the $z^*(x, y)$ map provides an accurate approximation of the true molecular geometry (as demonstrated by the PPM simulation in Figures 4.9 & 4.14, for example). However, if the tip apex possesses an asymmetry this may affect the $z^*(x, y)$ map, and hence provide a distorted representation of the geometry.

The tips used sometimes show a slight asymmetry in the attractive halo of the molecule during imaging, which suggests a tip asymmetry. It is difficult to estimate the effect on the 3D data set from the halo present in a single constant height image. Moreover, because tips are restructured only via gentle indentation (rather than large scale indentation, as is common in STM measurements), the slight asymmetry for a given cantilever can often persist between measurements with nominally different tip terminations.

The $\Delta f^*(x, y)$ map (i.e. the 'depth' of the minima), was typically found to be more strongly perturbed than the $z^*(x, y)$ map (i.e. the vertical position of the minima), which intuitively corresponds to the fact the vertical position of the turning point is strongly governed by the onset of Pauli repulsion, which has an extremely strong distance dependence, compared to the more diffuse van der Waals forces which govern the depth of the minima. This is clearly demonstrated in Figure 4.6. The red curve in D) demonstrates an abnormally small force minima, but the vertical position of the red curve minima is almost unperturbed relative to similar sites on the molecule. Furthermore, Figure 4.20, shows side by side comparisons of $\Delta f^*(x, y)$ (left) and $z^*(x, y)$ (right) data from a $\Delta f(x, y, z)$ map (main result in Figure 4.8). Subplots A)-F) depict data without any alteration made to the plane tilt. While a tip asymmetry is observed in $\Delta f^*(x, y)$ map A), and short axis line profile C), this does not appear to carry through to the $z^*(x, y)$ map data. Conversely, subplots G)-L) use $\Delta f(x, y, z)$ data that has been plane-corrected to remove the apparent tilt observed in the region surrounding the molecule (the plane was modelled using the four lateral corners of the grid). The resultant $\Delta f^*(x, y)$ map G), and short axis line profile I), appear

significantly flatter after plane correction. However, this has the effect of tilting the molecule in the other direction in $z^*(x, y)$ map H) and line profile J). As the tip asymmetry in the uncorrected $\Delta f(x, y, z)$ map resulted in the flat adsorption geometry expected from the DFT, it was deemed that no plane adjustment should be applied to the Δf data in efforts to 'correct' asymmetry.

Nonetheless, for tips with strong asymmetries, distortions of the $z^*(x, y)$ maps were observed (as shown in Figure 4.12). For this tip apex, it appears the slope on the tip apex in the short molecular axis direction is greater than the slope on the molecule (which is nearly flat), and so the $z^*(x, y)$ map effectively provides an image of the tip apex rather than any tilt on the molecule. Along the short axis of the $z^*(x, y)$ map there is an apparent tilt in the molecule, the rightmost carbon bond is 67 ± 10 pm below the leftmost, subtending an angle of approximately 7° . Given the flatness of the substrate around the molecule, the tilt observed in the molecule is likely due to the asymmetrical shape of the tip used for this particular experiment. This tilt is observed in both the topography and magnitude of force minima across the short axis of the molecule. While the molecular geometry observed in the $z^*(x, y)$ map in Figure 4.14 does not exhibit any significant asymmetries, a residual asymmetry is observed in the $\Delta f^*(x, y)$ map. For this reason when discussing the quantitative variation in the $F(z)$ minima taken on different sites (Section 4.5.4), it was ensured that these were compared along the long axis of the molecule, as maps in this direction did not show any evidence of tip asymmetry in either $\Delta f^*(x, y)$ or $z^*(x, y)$ maps.

4.5.4 Estimating Force Resolution

The force resolution exhibited by the data can be estimated by determining the differences in minima across different sites of the molecule. Comparing the magnitude of force minima across the molecule must take into account the tip asymmetry that brings the signal more negative in Δf in the upper-right portion of the (x, y) plane. Hence, comparisons of differences in magnitude (to estimate the force resolution) are done along directions unaffected by the asymmetry (i.e. parallel to the long axis).

4 Intramolecular force mapping at room temperature

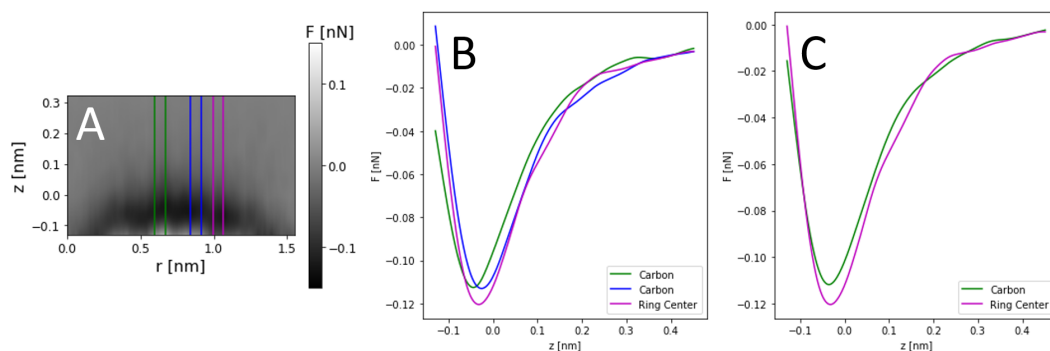


Figure 4.21: Estimating force resolution from Figure 4.6. A) Cross-sectional force map across long axis of molecule. B) Average single point $F(z)$ curves extracted over ranges indicated in A). C) Average of the blue and green force curves taken over bonds, for comparison to ring region force curves (purple). The difference in minima is $8pN$.

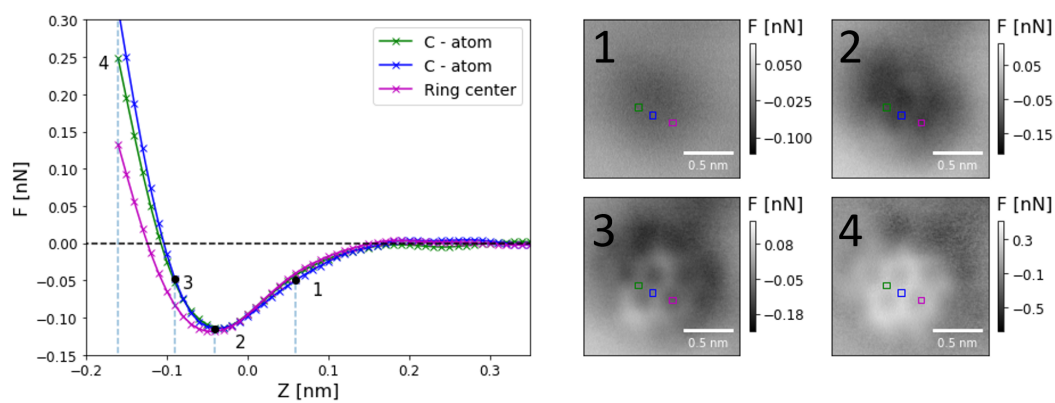


Figure 4.22: Extracted from the same data set as Figure 4.8. Force curves (left) extracted over carbon atoms and ring centre site on the side of the molecule to estimate force resolution. Lateral positions of $F(z)$ curves indicated by square markers in images 1)-4), which encompass the averaging window. The average difference in force minima between the ring and the points over the bond is $5pN$.

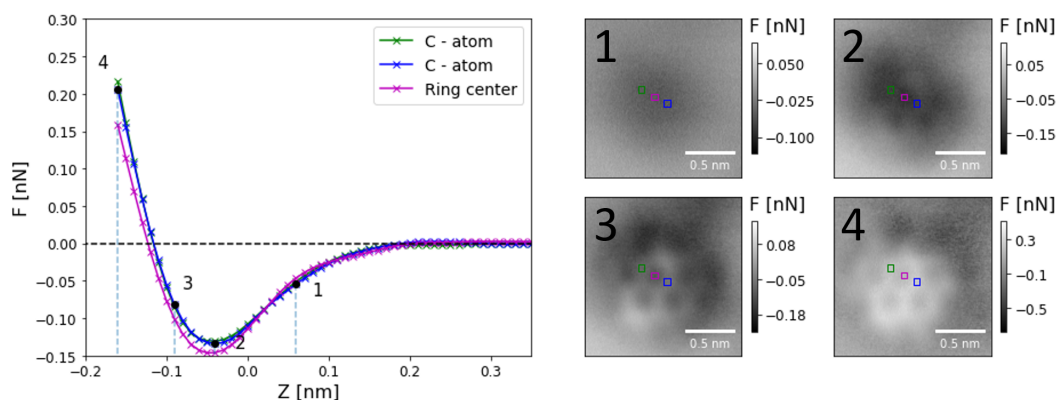


Figure 4.23: Extracted from the same data set as Figure 4.8. Force curves (left) extracted over carbon atoms and ring centre site on the side of the molecule to estimate force resolution. Lateral positions of $F(z)$ curves indicated by square markers in images 1)-4), which encompass the averaging window. The average difference in force minima between the ring and the points over the bond is 14 pN .

Figure 4.21 examines the force minima across three key sites of the molecule, along the long axis, extracted from the grid spectroscopy $F(z)$ presented in Figure 4.6.C. The minima across a ring centre (purple) and the central carbon atoms are -0.120 nN and -0.112 nN respectively. $F(z)$ curves taken over the same molecular sites (as Figure 4.21) were extracted from the 3D constant height slices data set presented in Figure 4.8 and plotted in Figure 4.22. There, the respective average minima of the rings and bonds are -0.119 nN and -0.114 nN . This was repeated for another set of points parallel to the long axis, in Figure 4.23, where the average minima of the rings and bonds are -0.146 nN and -0.132 nN respectively. The average difference in the force minimum between atoms and ring centers across Figures 4.21, 4.22 & 4.23 are 8 pN , 5 pN , and 14 pN respectively. From this, the force sensitivity of the system is estimated to be on the order of 10 pN . The features across Figures 4.22 & 4.23 are no smaller than $\sim 50\text{ pm}$, which serves as an estimate for the lateral resolution of the experiment. Thus, the extracted $F(z)$ curves are averages over 50 pm^2 areas (indicated by the size of the coloured squares in the images 1)-4)). This resolution has been previously reported in room temperature NC-AFM studies (33).

It is notable that DFT calculations from Iwata et al. (2015) (20) reported differences in force minima over PTCDA (a chemically similar molecule), between central carbon atoms and oxygen atoms of PTCDA molecules of 30 pN , assuming a silicon terminated tip. Across the carbon ring bonds and ring centres the difference in minima in their calculation was $\sim 50 pN$. The experimental data presented in this chapter suggest a smaller difference, although this of course is dependent on the precise structure of the tip.

4.5.4.1 Reproducibility

The reproducibility of experiments was assessed by comparing the force measurements at equivalent sites across different 2D grids with common intersections. In Figure 4.6, a difference of 15 pN was observed in the force minima at the equivalent central site of the short and long axes 2D grids (at their intersection in 4.6.A). Similarly with Figure 4.7 (acquired with a different tip and molecule), the difference between the force minima at the point of intersection is 30 pN , and they are also displaced in z by 20 pm .

Therefore while the measurements within a single grid are sensitive to force variations on the order of $\sim 10 pN$, systematic uncertainties can be observed in the absolute force measured over equivalent sites between subsequent grids of up to 15 – 30 pN . This is perhaps due to small differences in the tip structure or different locations of the ‘off’ curve used to remove the background signal.

There is good agreement between the force minima of equivalent sites between the 2D (Figure 4.7) and 3D grid (Figure 4.8), which were taken using the same tip and molecule. For example, the force minima of the leftmost C=C bond along the short axis are $-69 pN$ and $-68 pN$ respectively, and for the rightmost nitrogen atoms along the long axis, $-146 pN$ and $-130 pN$, demonstrating a similar systematic uncertainty observed between subsequent 2D grid measurements.

4.6 Conclusion

The results in this chapter present 2D and 3D force mapping of a planar organic molecule at room temperature, results which have not yet been reported elsewhere in the literature. The exact conformation of the molecule can be clearly identified using conventional silicon cantilevers with large oscillation amplitudes and without deliberate tip functionalisation.

Force mapping of the molecules allows direct quantitative analysis of the structure of the molecule, and also assessment of the quality of the tip. Using scripted data acquisition the quality of the intramolecular data achieved is comparable to that previously only obtained at cryogenic temperatures. These results open up the field of submolecular and 2D material characterisation to a wider community of experimentalists, and suggest the possibility of performing similar measurements under close to real-world conditions. In Chapter 5 the same force mapping methodology and analysis is applied to other, more challenging molecule - substrate systems.

References

1. T. Brown, P. J. Blowey, J. Henry, A. Sweetman, *ACS Nano* **17**, 1298–1304 (2023).
2. L. Gross, F. Mohn, N. Moll, P. Liljeroth, G. Meyer, *Science* **325**, 1110–1114 (2009).
3. L. Gross *et al.*, *Science* **337**, 1326–1329 (2012).
4. F. Mohn, L. Gross, N. Moll, G. Meyer, *Nat Nanotechnol.* **26** (2012).
5. D. G. de Oteyza *et al.*, *Science* **340**, 1434–1437 (2013).
6. K. Kaiser *et al.*, *Science* **365**, 1299–1301 (2019).
7. P. Ruffieux *et al.*, *Nature* **531**, 489–492 (2016).
8. A. Sweetman, N. R. Champness, A. Saywell, *Chem. Soc. Rev.* **49**, 4189–4202 (2020).
9. L. Gross *et al.*, *Angewandte Chemie International Edition* **57**, 3888–3908 (2018).

10. S. P. Jarvis *et al.*, *Journal of Physics Condensed Matter* **27** (2015).
11. F. Mohn, L. Gross, G. Meyer, *Applied Physics Letters* **99**, 53106 (2011).
12. L. Gross *et al.*, *Physical Review Letter* **111**, 106103 (2013).
13. M. Neu *et al.*, *Phys. Rev. B* **89**, 205407 (2014).
14. N. J. van der Heijden *et al.*, *ACS Nano* **10**, 8517–8525 (2016).
15. A. Sweetman *et al.*, *Nature Communications* **7**, 10621 (2016).
16. A. J. Heinrich, C. P. Lutz, J. A. Gupta, D. M. Eigler, *Science* **298**, 1381–1387 (2002).
17. A. M. Sweetman *et al.*, *Nature Communications* **5** (2014).
18. A. Sweetman, A. Stannard, *Beilstein Journal of Nanotechnology* **5**, 386–393 (2014).
19. C. Moreno, O. Stetsovych, T. K. Shimizu, O. Custance, *Nano Letters* **15**, 2257–2262 (2015).
20. K. Iwata *et al.*, *Nature Communications* **6**, 7766 (2015).
21. M. A. Lantz *et al.*, *Science* **291**, 2580–2583 (2001).
22. S. Kawai *et al.*, *Science Advances* **4**, eaar7181 (2018).
23. P. Hapala *et al.*, *Phys. Rev. B* **90**, 085421 (2014).
24. A. Stukowski, *Modelling and Simulation in Materials Science and Engineering* **18**, 015012 (2009).
25. H. Monig, S. Amirjalayer, A. Timmer, *Nature Nanotech*, 371 (2018).
26. F. Giessibl, *Review of Scientific Instruments* **90**, 011101 (2019).
27. A. Stannard, A. M. Sweetman, *A Considered Approach to Force Extraction from Dynamic Force Microscopy Measurements*, ed. by P. Moriarty, S. Gauthier (Springer International Publishing, 2015), pp. 63–79, ISBN: 978-3-319-17401-3.
28. F. J. Giessibl, *Reviews of Modern Physics* **75**, 949–983 (2003).
29. Y. Sugimoto *et al.*, *Physical Review B* **81**, 245322 (2010).
30. Y. Sugimoto, T. Namikawa, K. Miki, M. Abe, S. Morita, *Phys. Rev. B* **77**, 195424 (2008).
31. Y. Sugimoto, K. Ueda, M. Abe, S. Morita, **24**, 84008 (2012).

32. S. Kawai, T. Glatzel, S. Koch, A. Baratoff, E. Meyer, *Physical Review B - Condensed Matter and Materials Physics* **83**, 1–7 (2011).
33. P. Rahe *et al.*, *Review of Scientific Instruments* **82** (2011).

5 Force Mapping of Molecular Networks on B:Si(111) – ($\sqrt{3} \times \sqrt{3}$)R30°

The experiments in Chapter 4 succeeded in resolving the intramolecular structure of a single organic molecule. To further the limits of what is possible within room temperature NC-AFM, efforts were turned to map the force fields of ordered molecular networks, whose molecule - molecule interactions are weaker compared to covalent bonds. The results in this chapter demonstrate the versatility and flexibility of the drift correction procedures, showing they can be effectively applied to larger 3D force maps, over multiple molecules.

5.1 Molecular Self-Assembly

A wide variety of 2D supramolecular architectures on metal surfaces have been studied in the literature via STM, and their synthesis has become an important field of research within nanotechnology. Through self-assembly, distributions of molecules on surfaces can arrange into well-ordered networks, governed by molecule - molecule interactions. Self-assembly has received much attention (1–3), owing to its wide range of applications, ranging from providing selective ion exchange (4–6), to preparing functional materials (7–9) and fabricating novel nanodevices (10, 11). These molecular assemblies are typically made using metal surfaces, but have also been prepared on semiconducting surfaces (12, 13). Depending on the molecular monomer, these structures can be halogen (14, 15) or hydrogen (16, 17) bonded networks.

NC-AFM has previously been used to study intermolecular bonding in self-assembled systems (12, 18, 19), however, these measurements were performed at cryogenic temperatures. Force maps capable of resolving both intramolecular, and intermolecular bonding have not previously been reported for room temperature NC-AFM.

5.1.1 Substrate Selection

In Chapter 4, the Si(111)-(7×7) substrate was chosen for its dangling bonds that localised the NTCDI. These inhibited molecular diffusion, granting the necessary stability for the lengthy measurements needed to map the force field in 3D. However, diffusion is necessary for molecules to rearrange and form ordered networks, hence Si(111)-(7×7) could not be used as a substrate for NTCDI self-assembled networks.

Metal surfaces are typically used in STM studies to characterise molecular networks. However, while metal surfaces have been studied in room temperature NC-AFM using conventional Si cantilevers (20, 21), intramolecular force mapping relies on passivating the tip by some means, whether by controlled functionalisation at 5 K (22, 23), or an incidental restructuring of the tip at room temperature (24, 25). Unlike semiconducting surfaces, metals do not provide a means of chemically passivating the tip apex at room temperature. In operation, the Si tip of the cantilever would likely become coated in metal atoms, which interact with organic molecules more strongly compared to non-metals, and hence the user would struggle to approach close enough to the molecules to detect the Pauli repulsive forces for a complete force map. Additionally, any larger molecule on the tip apex might be unstable.

To circumvent this problem, the Ag:Si(111)-($\sqrt{3} \times \sqrt{3}$)R30° surface was a promising candidate for the study of molecular networks in room temperature NC-AFM, and has previously been used to characterise NTCDI molecules in hydrogen bonded networks (12, 26, 27). However, the VTSTM/AFM used for this thesis did not have a Ag deposition source. Consequently, the use of an alternative substrate was pursued: B:Si(111). This substrate is also a passivated, semiconducting substrate, but differs in that

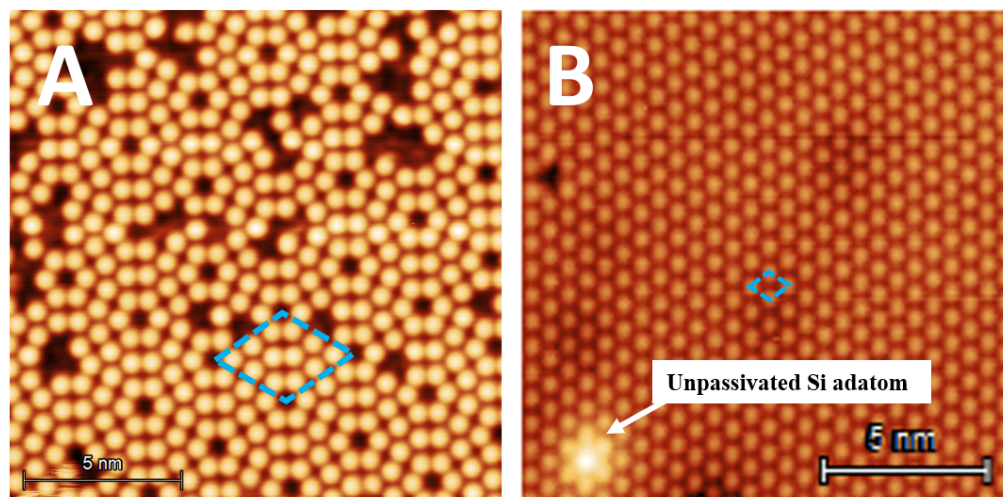


Figure 5.1: Typical STM images of p-type Si(111) reconstructions: Si(111)-(7 \times 7) and B:Si(111) - ($\sqrt{3} \times \sqrt{3}$)R30 $^\circ$. Image parameters: A) $V_{gap} = +2$ V, set point = 200 pA. B) $V_{gap} = +2$ V, set point = 20 pA. The respective unit cells of each substrate are indicated by the blue dotted lines. A surface defect associated with unpassivated Si adatoms is labelled in B).

surface could be passivated with the dopant without requiring a deposition source as for p-type silicon the boron is already present in the bulk crystal.

5.1.2 B:Si(111) - ($\sqrt{3} \times \sqrt{3}$)R30 $^\circ$ Substrate

Figure 5.1 shows the (7 \times 7) reconstruction of Si(111) A)) and the boron induced ($\sqrt{3} \times \sqrt{3}$)R30 $^\circ$ phase (B)). By extended annealing of the doped Si(111) sample, the B atoms from the bulk crystal preferentially segregate to the surface of the crystal. Due to a charge transfer from the Si adatom to the B atoms, the dangling sp³ bonds of the surface adatoms become saturated (29, 30). Hence, the previously reactive Si atoms at the surface / vacuum interface become passivated in the presence of underlying B atoms. The ($\sqrt{3} \times \sqrt{3}$)R30 $^\circ$ phase is the most energetically stable formation of B on the Si(111) surface, and is shown in Figure 5.1.B.

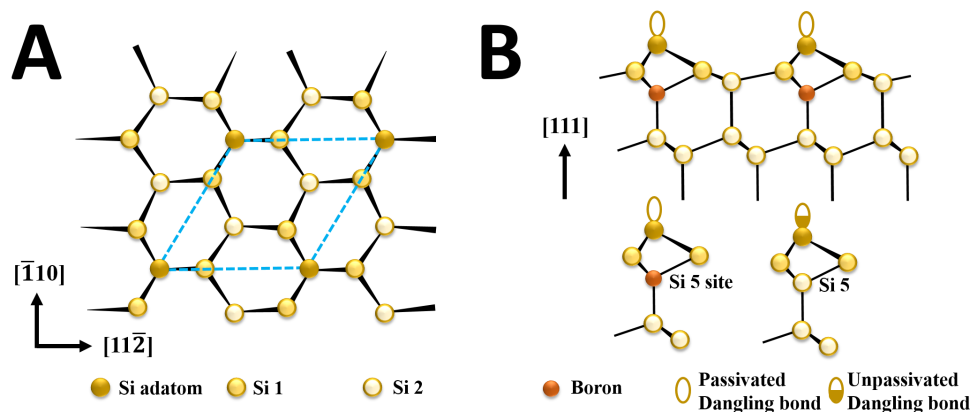


Figure 5.2: A) Plan view of ball-and-stick model of B:Si(111). The repeating unit visible in STM images is indicated by blue dotted line (see Figure 5.1.B). B) Top: Side view ball-and-stick model of complete substitution in B:Si(111) surface. Bottom: Depiction of complete and incomplete B substitutions of the S_5 site, the latter resulting in surface defects (unpassivated dangling bonds). Figure after Baumgärtel et al. (1999) (28) & Makoudi et al. (2017) (13).

Ball-and-stick models in Figure 5.2 reveal that B atoms occupy the substitutional (S_5) sites, directly beneath the Si adatoms (28) (in contrast to other group III elements that substitute the Si adatoms at T_4 sites (31)). Point defects on the surface can result from incomplete B substitution, wherein the Si atom underlying the adatom position remains, as does the sp^3 dangling bond of the Si adatom (13, 32). As a result these defects appear as bright protrusions in STM images, due to their increased electron density (see Figure 5.1.B).

In addition to Si atoms in S_5 sites underneath Si adatoms, other defects can also be observed in the surface reconstruction. Figure 5.3 depicts various defect types. These are: A) Si(S_5) atoms underneath Si adatoms, B) Si(S_5) atoms underneath vacancies, C) B atoms occupying S_5 sites underneath vacancies, D) B atom occupying sites in between and beneath three B(S_5) atoms (13). For adsorption and self-assembly of molecules, it is necessary to prepare the surface as clean and defect-free as possible.

5.1.2.1 Surface Preparation

While the reconstruction can be prepared via external boron deposition (33), the experimental set-up used for this thesis utilizes Si(111) crystals with high densities ($\sim 10^{20}/\text{cm}^3$) of B dopants (34). Boron segregation is thermally activated $\gtrsim 800^\circ\text{C}$ and the dopants move toward the surface. The maximum boron concentration at the surface is 1/3 of a monolayer (ML) (1ML being the surface atom density of Si(111): $7.8 \times 10^{14} / \text{cm}^2$) (35).

The exact parameters and protocols to achieve a B:Si(111) reconstruction differ between groups. Eom, Moon and Koo, (2015) report performing repeated flash anneal cycles of the Si(111) to 1473°C followed by a cool from flash temperature to room at a rate of $2^\circ\text{C}/\text{s}$ (36). Whereas Copie et al. (2014) prepared the reconstruction through annealing the sample above 900°C for several hours (37). A full summary of the various exact parameters used in key results across a range of groups can be found in a Ph.D. thesis by Marchese (2020) (38).

The procedure for substrate preparation adopted in this chapter emulated that used by Spadafora et al. (2014) (39), as this yielded the highest quality reconstructions, with lowest defect densities. Highly doped Si(111) crystals were initially cleaned via sonication in solution before introduction to the UHV chamber. They were then degassed in the UHV chamber overnight at 500°C . Next they were flash annealed to 1200°C , for 10 seconds at a time, until the $(\sqrt{3} \times \sqrt{3})$ reconstruction started to form (checking the sample in STM), indicating that a sufficient amount of B dopants in the bulk crystal had risen to the surface (35). The surface was then prepared by annealing the crystal at 900°C for 1 hour (having been flashed repeatedly at 1200°C), and then cooled to room temperature slowly ($< 1^\circ\text{C}/\text{s}$). Using this procedure yields an approximate surface defect density of $\sim 5\%$ (see Figure 5.3).

Figure 5.4, shows a 3D $\Delta f(x, y, z)$ map acquired using the constant height slices method, over the passivated Si adatoms of the bare B:Si(111) substrate, and a single dangling bond defect. Without a corner hole site on the reconstruction, or step edges within the scan frame, there is not a clear 'off' site to use here. Hence an extracted $F(z)$ map would contain residual non-site

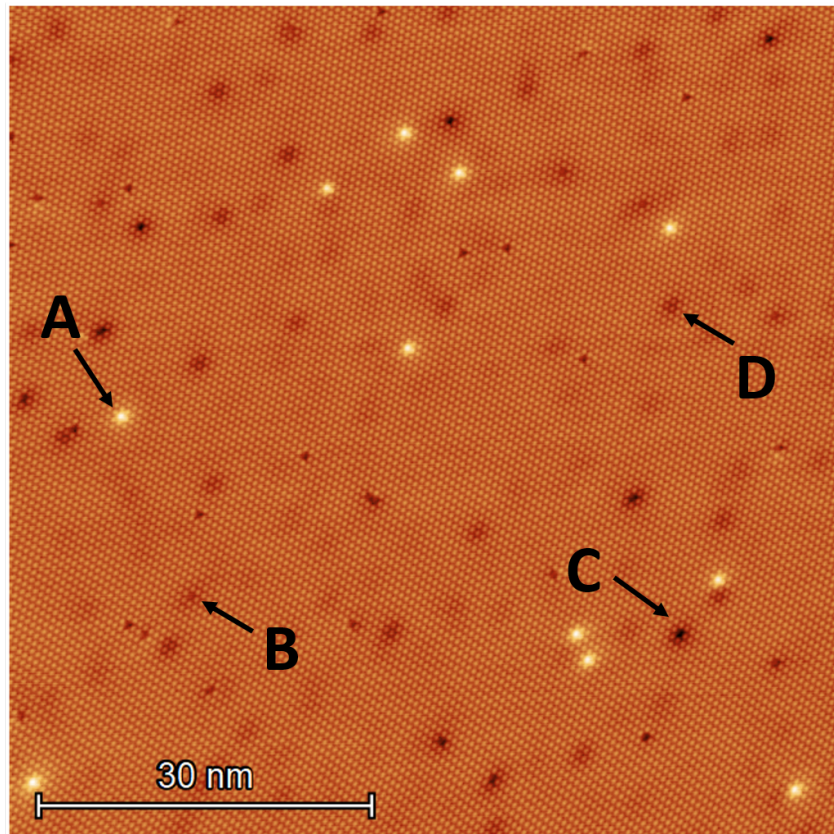


Figure 5.3: Overview STM image of B:Si(111). Image parameters: $V_{gap} = +2 V$, set point = $20 pA$. Various typical defects present in overview are labelled: A) Si(S_5) atoms underneath Si adatoms. B) Si(S_5) atoms underneath vacancies. C) B atoms occupying S_5 sites underneath vacancies. D) B atom occupying sites in between and beneath three B(S_5) atoms.

specific interactions. However, the experiment still affirmed the amenability of substrate for stable atom tracking and constant height imaging.

5.1.3 Molecular Self-Assembly on B:Si(111)

On passivated Si substrates, molecules are able to rotate, and diffuse across the surface, and hence interact with other molecules. As more molecules are deposited, the energetically favourable adsorption sites fill up, and depending on the balance of the molecule - substrate & molecule - molecule interaction energies, intermolecular interactions can start to govern the behavior of molecules, which can lead to formation of networks and architectures (42). There is a substantial body of work centered on molecular self-assembly on the B:Si(111) surface (13, 43–45). As an example, Figure 5.5 depicts the self-assembly of 1,3,5-tri(4'-cyanobiphenyl)-benzene and 1,3,5-tris(4'-bromophenyl)-benzene networks previously achieved (13). The molecules assemble in an open porous structure, allowing for further molecular deposition to occupy the pores. With the molecular self-assembly credentials of the substrate evident throughout the literature, it was pursued as a substrate for creating a hydrogen bonded island of NTCDI, as described for the Ag:Si(111) substrate in Sweetman et al. (2014) (12). C₆₀ and CoPc molecules were subsequently deposited, and studied in NC-AFM.

5.2 Results: NTCDI on B:Si(111)

For a partial coverage ($\sim 0.2ML$), NTCDI was deposited at 175°C for 2 hours, however the NTCDI was not observed to form ordered islands. This was true for a range of deposition protocols (also for: 190°C for 5 minutes), and also after annealing the sample at 200°C (for 30 minutes), there was no observable difference in the surface in STM. Figure 5.7 shows both STM and NC-AFM (via AH mode) overviews of disordered NTCDI islands on B:Si(111). A) The STM reveals that the majority of the surface defects are covered by the NTCDI, furthermore that the coverage of NTCDI (10 – 20 %) is greater than the defect density. Therefore, the NTCDI bonds to both the dangling bond defects, and the boron substituted sites of the surface.

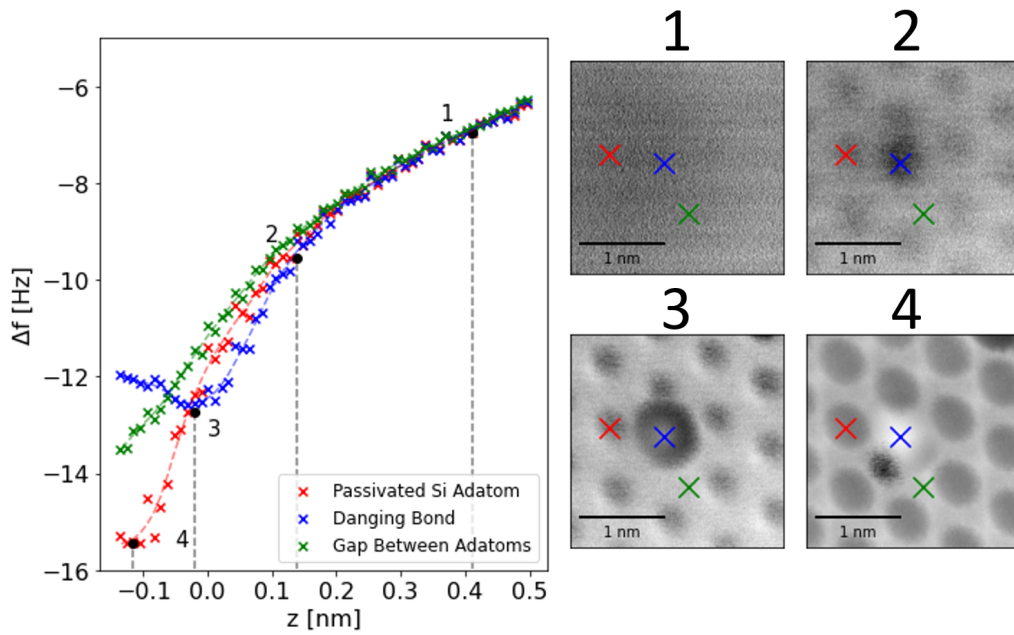


Figure 5.4: 3D Δf mapping of B:Si(111) in NC-AFM using constant height slices. Each slice in data set was scanned 3 times and an average image was calculated. Map dimensions: $272 \times 272 \times 61$ pixels, $2.5 \text{ nm} \times 2.5 \text{ nm} \times 0.64 \text{ nm}$. Image parameters: Tracking set point = -12.4 Hz , $V_{\text{gap}} = +0.4 \text{ V}$, $t_{\text{acq}} = 103 \text{ s}$, total acquisition time ~ 6 hours. Left) Extracted $\Delta f(z)$ curves across various sites in data set. Curves smoothed by initially averaging the 3D data set in x, y with 5×5 pixel average. Then Δf signal spline smoothed in z using the *splrep* function from the *scipy.interpolate* python library (smoothing parameter $\lambda = 0.99$). Right) Example images 1)-4) from data set, showing evolution in contrast of passivated Si atoms, and a dangling bond defect.

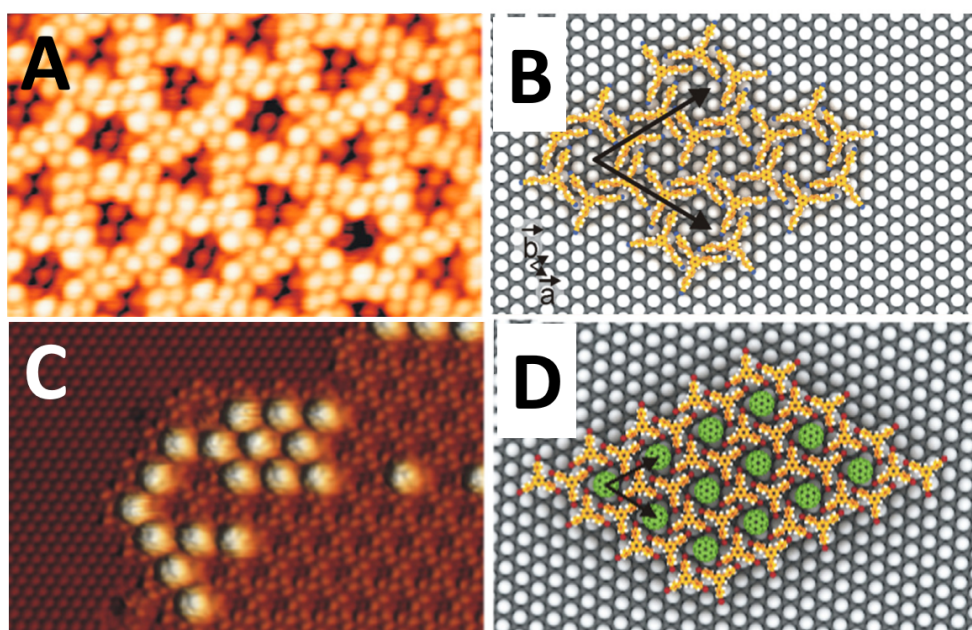


Figure 5.5: A) & B) STM image and ball-and-stick model of porous network of 1,3,5-tri(4'-cyanobiphenyl)-benzene molecules on B:Si. STM image parameters: $V_{gap} = +1.2$ V, set point = 300 pA. C) & D) STM image and ball-and-stick model of porous 1,3,5-tris(4'-bromophenyl)-benzene network on B:Si, partially filled with C_{60} . STM image parameters: $V_{gap} = +2.7$ V, set point = 15 pA, figure after Makoudi et al. (2017) (13).

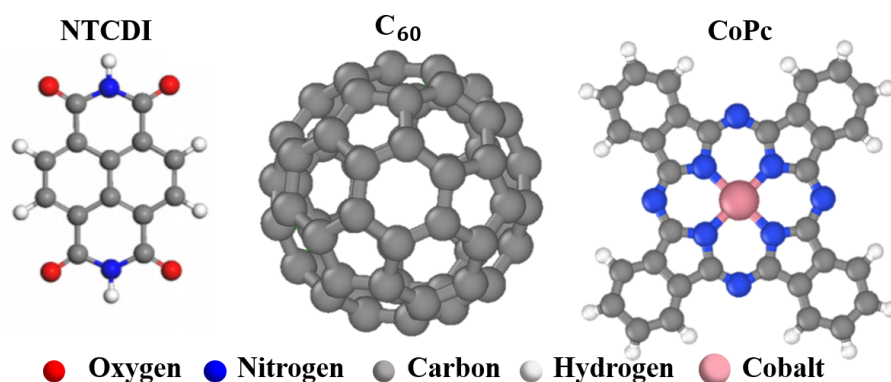


Figure 5.6: Overview of Molecules deposited on the B:Si(111) substrate (not to scale). Ball-and-stick models of NTCDI (40), C₆₀ & CoPc (41).

There is little evidence of molecular diffusion occurring during the scan. B) Reveals intramolecular features, not dissimilar from the AH overview observed previously for NTCDI (see Section 4.2.1) and which are likely the chemical structures of the molecules. Following that, a deposition (200°C for 30 minutes) was attempted to see if coverage approaching a monolayer would produce an ordered formation. Again, only disordered islands were observed (see representative STM images in Figure 5.8).

The group of Frederic Cherioux explained in private communication that they had previously attempted to form ordered islands of molecules containing carbonyl groups (ketones, aldehydes, acids) and OH groups (alcohols, phenols) without success. From their previous experiments they had found that the molecules bearing carbonyl group would form bonds between the O of the carbonyl groups with the Si adatoms, even over the passivated B(S₅) sites. The pinned molecules would therefore be unable to diffuse and form ordered islands. With this knowledge, focus turned to other molecules to study on B:Si(111), which would not pin to the surface.

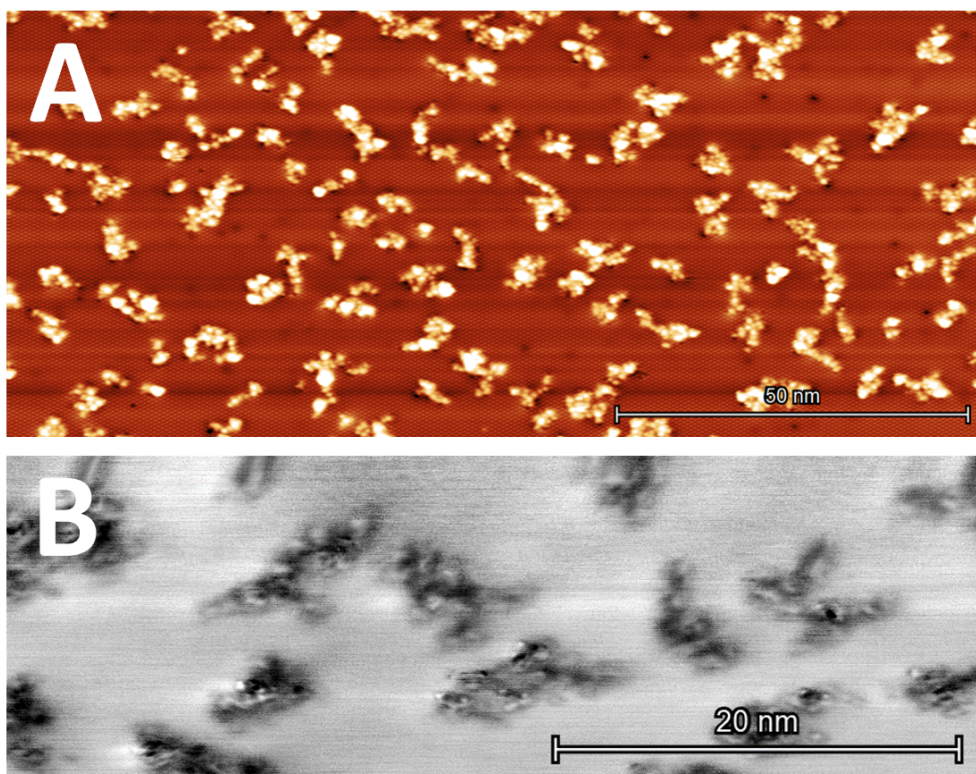


Figure 5.7: STM and NC-AFM (AH mode secondary pass) overviews of disordered NTCDI island formation on B:Si(111). Image parameters: A) $V_{gap} = +2$ V, set point = 20 pA. B) $V_{gap} = 0$ V, Oscillation amplitude 22 nm, set point = -6 Hz, second pass offset = -270 pm.

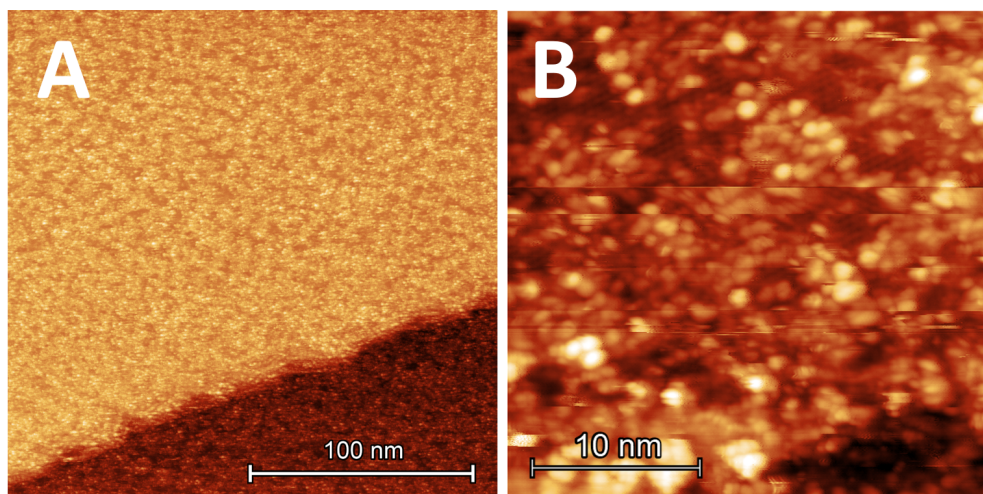


Figure 5.8: STM overview of disordered NTCDI island formation on B:Si(111). Image parameters: A) $V_{gap} = +2$ V, set point = 20 pA. B) $V_{gap} = +2$ V, set point = 20 pA.

5.3 Results: C_{60} on B:Si(111)

C_{60} is known to be amenable to forming ordered islands on the B:Si(111) surface (46). A partial coverage ($\sim 0.2ML$) of C_{60} was achieved following a 30 minute long deposition at $350^\circ C$ (see Figure 5.9). As discussed by Stimpel et al. (2002) (43), the C_{60} initially adsorbs to the defect sites (unsubstituted Si(S₅)), and along step edges. With sufficient coverage, well-ordered close packed islands formed via diffusion can be observed. The surface was checked in STM prior to NC-AFM (see Figure 5.9.A & B)).

Figure 5.9.C & D) depict constant Δf and constant height overview images of a close packed C_{60} island in NC-AFM. As the molecules are highly non-planar, it is difficult to resolve the chemical structure with constant height imaging. Nonetheless, clear submolecular features are resolved within each molecule in Figure 5.9.D) and various different adsorption geometries of the C_{60} can be observed. The contrast has similarities to the contrast observed in Sweetman et al. (2016) (47) & (48) and therefore it is difficult to

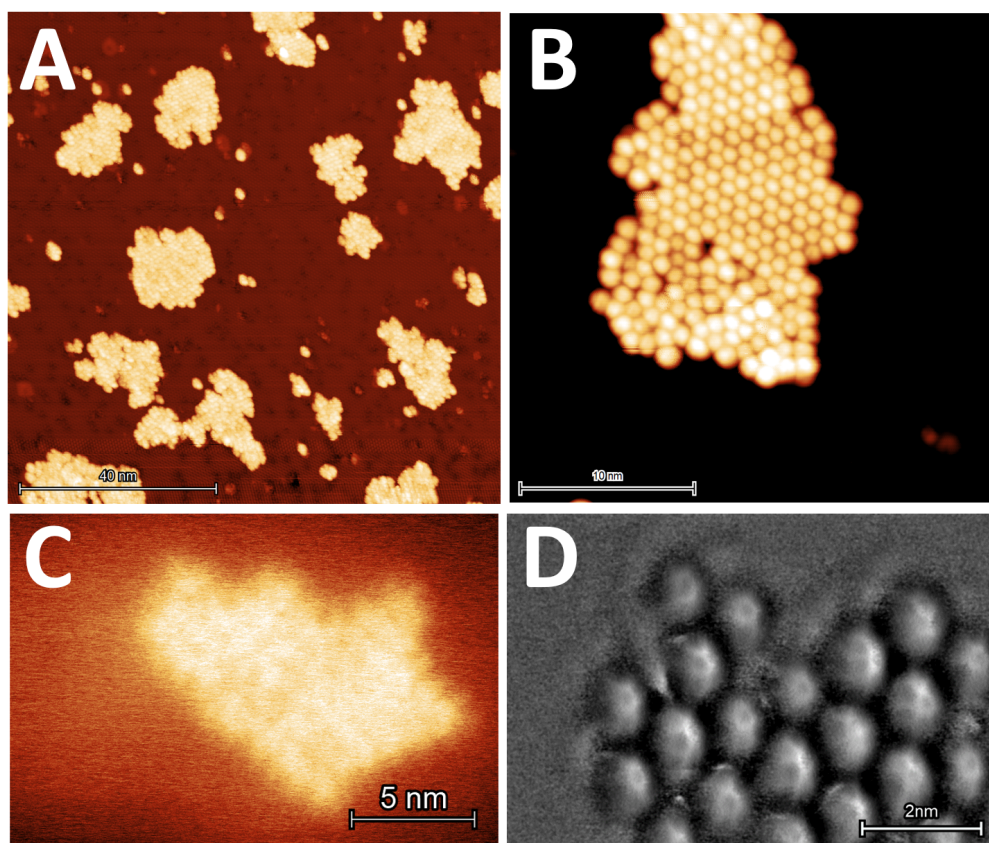


Figure 5.9: A) & B) STM overviews of C₆₀ island formation on B:Si(111). Image parameters: $V_{gap} = +2 V$, set point = $20 pA$. C) Constant Δf NC-AFM overview of C₆₀ island used for subsequent force mapping experiments. Image parameters: C) $V_{gap} = +0.2 V$, set point $\Delta f = -30 Hz$, $A_0 = 20 nm$. D) Constant height image of upper left corner of C₆₀ island. A high pass filter has been applied to highlight the submolecular contrast. Image parameters: $V_{gap} = +0.2 V$, $A_0 = 20 nm$, height = $-280 pm$ below tracking position ($\Delta f = -34 Hz$, on C₆₀ molecule).

5 Force Mapping of Molecular Networks on B:Si(111) – $(\sqrt{3} \times \sqrt{3})R30^\circ$

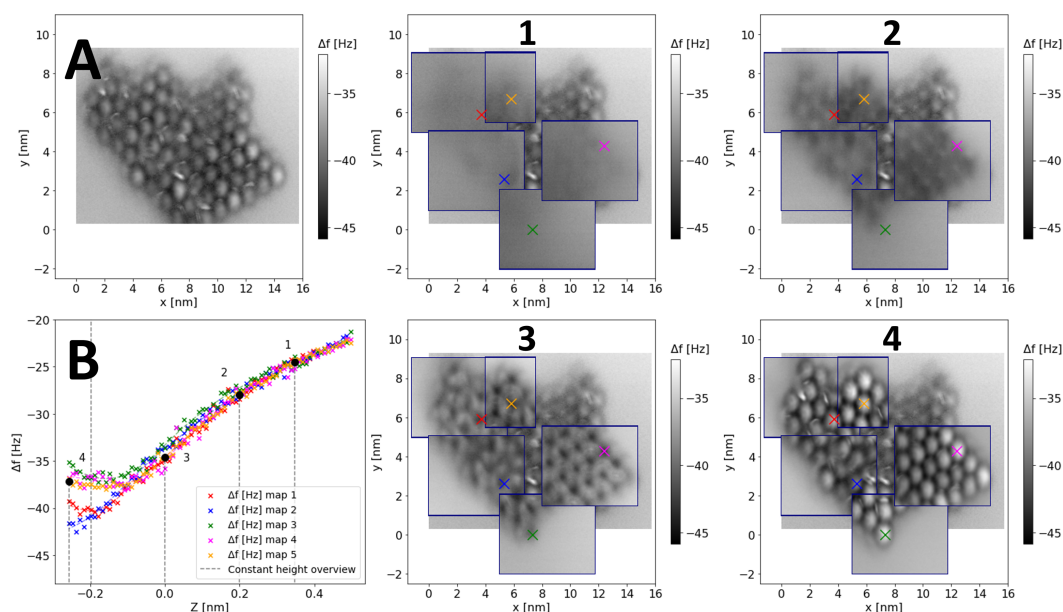


Figure 5.10: A) Constant height image of C₆₀ island Figure 5.9. Imaging parameters: $V_{gap} = 0.2 V$, $A_0 = 20 nm$, tracking set point $\Delta f = -34 Hz$. B) $\Delta f(z)$ curves extracted from all five Δf maps (1 curve from each). 1)-4) depict the constant height images across representative heights for all five maps, superimposed over the overview image. In each case the Δf map is positioned over its approximate position in x, y , superimposed over the overview image. The x, y positions of each $\Delta f(z)$ plotted in B) curve are indicated by the coloured markers in 1)-4). All slices in the 3D data sets are composed of average images of 3 scans.

unambiguously determine whether the tip terminates in a Si cluster or a C₆₀ molecule.

This island was further characterised with multiple 3D Δf maps. Figure 5.10 depicts five Δf maps, acquired via the constant height slices method, over various areas of the island from Figure 5.9.C & D). Figure 5.10.A is a constant height image of the island large enough to see most of the molecules within one image. It is important to note that, as a prerequisite, the system (in particular, the feedforward vectors) must be highly stable to minimise the z-drift during a constant height scan of this size ($15.7 nm \times 9 nm$). From each of the five Δf maps, a $\Delta f(z)$ curve was extracted over a molecule, aligned (using the same method as described in Section 4.5.2), and plotted

in Figure 5.10.B. Subplots 1)-4) depict the constant height images across representative heights for all five maps, superimposed over the overview image. In each case, the Δf maps are plotted at their corresponding position in (x, y) , superimposed over the overview image. The (x, y) positions of each $\Delta f(z)$ plotted in B) curve are indicated by the coloured markers in 1)-4). A single C₆₀ molecule within the island (indicated by the blue \times) was used as the tracking site for all Δf maps, hence the tip-sample distances plotted are all relative to the same position, with tracking set point of $\Delta f = -34$ Hz.

The shape of the $\Delta f(z)$ curves in Figure 5.10.B, and the image contrast systematically change between Δf map #2 and map #3. This would indicate the tip had likely changed in some way between these experiments, which were carried out concurrently over a period of days (each map took ~ 13 hours). This data set demonstrates the ability of the tracking scripts to take multiple $\Delta f(x, y, z)$ maps over areas large enough to encompass large assemblies of molecules, and potentially self-assembled networks.

5.3.1 3D Force Map Analysis on C₆₀

As an example, further analysis was carried out on $\Delta f(x, y, z)$ map #5, including inversion to create a 3D $F_z(x, y, z)$ map. Figure 5.11.A depicts the $\Delta f(x, y, z)$ map, with $\Delta f(z)$ curves extracted at various sites within the map (left), alongside representative constant height slices throughout the grid (1)-4)). B) follows the same format as A), for the inverted $F_z(x, y, z)$ map. The processing and inversion protocol follow Sections 3.4 & 4.5 for a 3D grid obtained via constant height imaging. Figure 5.11.C) & D) show the $z^*(x, y)$ map extracted from the $\Delta f(x, y, z)$ data, as a 2D image, and 1D line profile respectively. There is an apparent downward trend (left to right) in the line profile. The origin of this slope is discussed below in Section 5.3.1.1.

The same region depicted in Figure 5.11 was mapped again, using the same tip, via 3D grid spectroscopy, and plotted in Figure 5.12. This method had hitherto only yielded limited success (Figure 3.15 & Figure 4.10.B), due to needing not only a stable system and tracking correction for upwards of 10+ hours, but also due to the tip moving to the point of closest approach for each pixel in (x, y) . In this case, the grid spectroscopy experiment lasted 16 hours,

5 Force Mapping of Molecular Networks on B:Si(111) – $(\sqrt{3} \times \sqrt{3})R30^\circ$

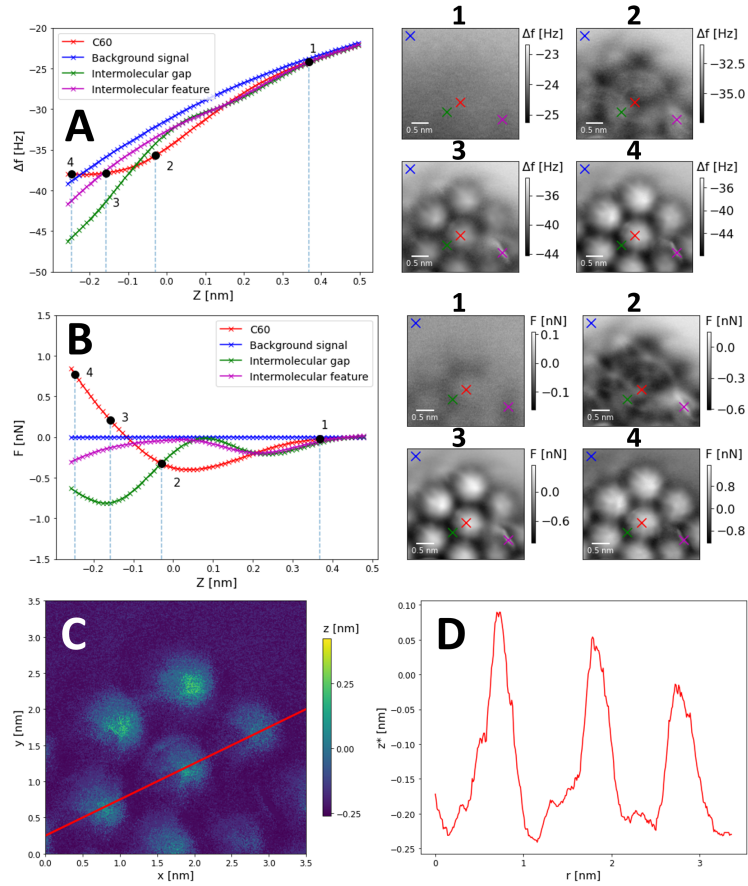


Figure 5.11: C₆₀ on B:Si(111) 3D $\Delta f(x, y, z)$, $F_z(x, y, z)$ maps taken via constant height slices method and $z^*(x, y)$ map data, map parameters: $352 \times 352 \times 77$ pixels, $3.5 \text{ nm} \times 3.5 \text{ nm} \times 0.76 \text{ nm}$, $V_{gap} = 0.2 \text{ V}$, $A_0 = 20 \text{ nm}$, tracking set point $\Delta f = -34 \text{ Hz}$, $t_{acq} = 186 \text{ s}$, total $t_{acq} \sim 8$ hours. Images are an average of 3 scans at each height. A) $\Delta f(x, y, z)$ map: $\Delta f(z)$ curves (Left) extracted from 3D grid over key sites. Each curve is an average of 10×10 pixels, and is smoothed in z via a spline fit ($\lambda = 0.999$). The positions of the curves are indicated by the coloured markers in representative image (Right) 1)-4). B) As for A) but for 3D grid of inverted $F_z(x, y, z)$ data. Each curve is an average of 10×10 pixel, and smoothed in z via a spline fit ($\lambda = 0.99$). C) $z^*(x, y)$ map extracted from $\Delta f(x, y, z)$ data, the image has been smoothed in (x, y) . D) Line profile cross-section through 2D $z^*(x, y)$ map. Line profile has been smoothed using 3 pixel wide rolling average to data (equating to 150 pm).

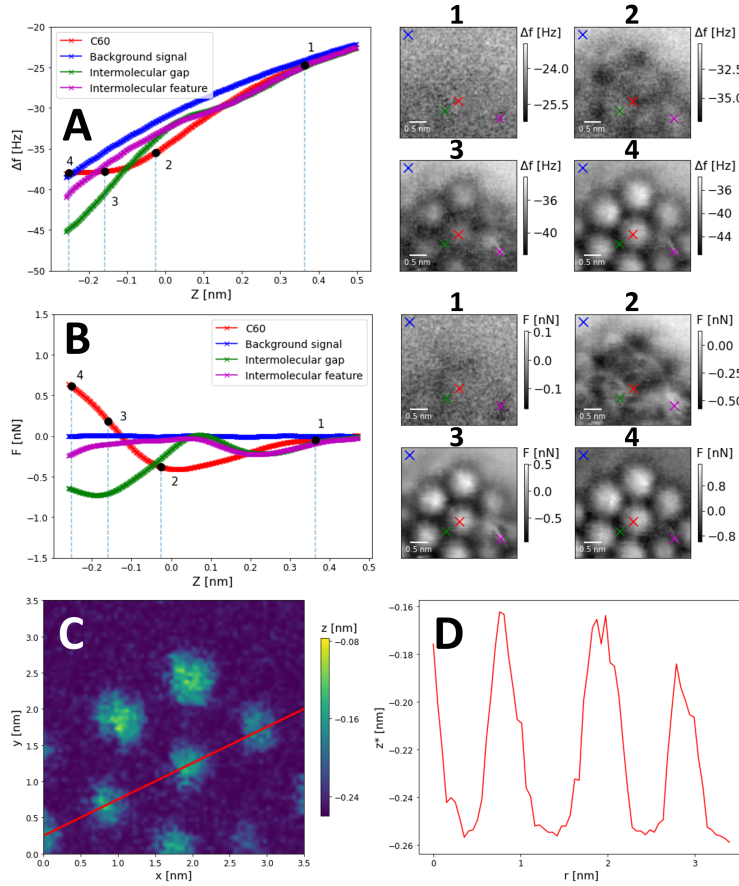


Figure 5.12: C₆₀ on B:Si(111) 3D $\Delta f(x, y, z)$, $F_z(x, y, z)$ maps taken via grid spectroscopy method and $z^*(x, y)$ map data, map parameters: $70 \times 70 \times 512$ pixels, $3.5 \times 3.5 \times 0.76 \text{ nm}^3$, $V_{gap} = 0.2 \text{ V}$, $A_0 = 20 \text{ nm}$, tracking set point $\Delta f = -34 \text{ Hz}$, $t_{acq} = 140$, total $t_{acq} \sim 16$ hours. Atom tracking was resumed after every 5 spectra. A) $\Delta f(x, y, z)$ map: $\Delta f(z)$ curves (Left) extracted from 3D grid over key sites. Each curve is an average of 10×10 pixels, and is smoothed in z via a spline fit ($\lambda = 0.9999$). The positions of the curves are indicated by the coloured markers in representative image (Right) 1)-4). B) As for A) but for 3D grid of inverted $F_z(x, y, z)$ data. Each curve is an average of 10×10 pixel, and smoothed in z via a spline fit ($\lambda = 0.999$). C) $z^*(x, y)$ map extracted from $\Delta f(x, y, z)$ data, the image has been smoothed in (x, y) . D) Line profile cross-section through 2D $z^*(x, y)$ map. Line profile has been smoothed using 15 pixel wide rolling average to data (equating to $\sim 150 \text{ pm}$).

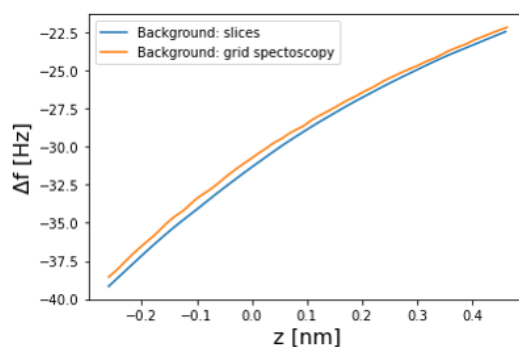


Figure 5.13: Respective 'off' curves used in slices and grid spectroscopy experiments, subtracted from $\Delta f(z)$ data for force inversion.

wherein 4900 single point spectra were compiled into a $70 \times 70 \times 512$ pixel 3D grid ($3.5 \times 3.5 \times 0.76$ nm). The data were then processed and presented in the same format as for Figure 5.11.

Theoretically, both methods of data acquisition should produce equivalent data sets when applied to the same region. In each data set, the single point curves extracted in Figure 5.12.A & B) were averaged with a 3×3 pixel sized window (equating to a physical area 150 μm^2). The two methods of data acquisition produce 3D maps that are markedly similar, likely owing to improvements made to the drift correction procedure having reduced the residual drifts in the system (see Section 3.1.2, and Figure 3.5.C). In some instances the systematic error in force minima of equivalent sites across the data sets is as small as 10 pN (comparing the force minima from the slices and spectroscopy grids, at the site indicated by the red \times , which are -401 pN and -411 pN respectively).

However, there are pervasive small quantitative differences between Figures 5.11 & 5.12. For example, the force minima of nominally equivalent points measured over the area indicated by the green cross (subplot B, images 1)-4)) is 90 pN more attractive for the slices data set. In addition, the point of closest approach for the slices method incurs a force ~ 200 pN more repulsive for the example C_{60} molecule than that of the grid method. This is possible due to slight differences in the respective background $\Delta f(z)$ curve for each data set (the blue curve in A) for each data set), as this would slightly alter the force inversion for all the other $\Delta f(z)$ curves.

Direct comparison of the background Δf signal in Figure 5.13 reveals that the data from the experiment is shifted in Δf by $\sim +0.2 - 0.3$ Hz. A possible explanation is that the signal of the first off curve is formed gradually, from constant height images, conducted over a period of ~ 8 hours, whereas the second off curve is gathered from one of the point spectra obtained toward the end of the experiment (the spectroscopy was performed line by line, from $y = 1$ to $y = 70$), hence there is an additional time difference between the background signals of nearly 16 hours. In that time, while it is not overt in the $\Delta f(x, y, z)$ maps, a slight drift in the f_0 of the cantilever (as discussed in Section 4.5.2) is enough to alter the latter background signal, and hence yield slightly different force measurements between the grids. Future lengthy experiments of this nature could potentially account for these errors by regularly measuring the resonance curves of the cantilever to monitor any changes to f_0 .

The respective $z^*(x, y)$ subplots C) and D) of both data sets depict the same apparent trend from left to right of lower heights of $\Delta f(z)$ turnaround over the C₆₀ molecules. This is physically unlikely to be the case for C₆₀ molecules adsorbed on B:Si(111). Given the same trend is observed in both methods, wherein the dimensional nature of data acquisition is different, it is highly unlikely to be an artefact of residual drift / creep. The phase, amplitude and excitation channels were checked across the region of closest approach (as for Figure 4.18) for both techniques. As before, these signals were negligible, hence neither technique suffers from errors in the PLL response, regardless of whether the tip gathers data across (x, y) in constant z , or *viceversa*.

Furthermore, the slope is also unlikely to be result of thermal fluctuation of f_0 over time, since the same trend is observed from (at the latest) the lower portion of the ~ 8 hour slices data set, and is maintained throughout the subsequent ~ 16 hour grid spectroscopy experiment. The timescales involved eliminate f_0 fluctuation as the cause of the apparent trend in these $z^*(x, y)$ maps.

5 Force Mapping of Molecular Networks on B:Si(111) – $(\sqrt{3} \times \sqrt{3})R30^\circ$

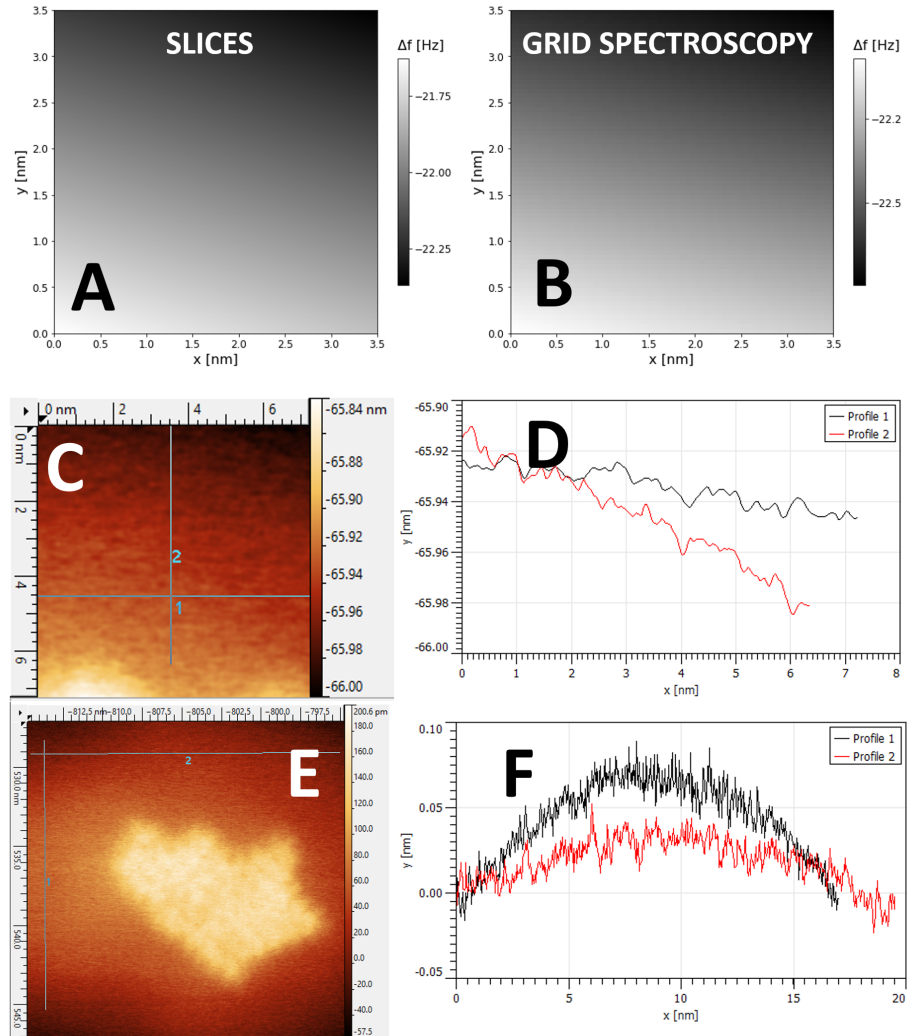


Figure 5.14: A) & B) Calculated Δf planes using the top slices in (x, y) of 3D slices and grid spectroscopy experiments respectively (from Figures 5.11 & 5.12). C) Zoom in of topographic image (from Figure 5.9.C), of substrate adjacent to region of island studied in Figures 5.11 & 5.12. D) Line profiles across substrate exhibiting an apparent sample tilt ($\sim -0.2^\circ$ in x , $\sim -0.6^\circ$ in y). E) & F) as for C) & D), but using entire span of topographic overview to assess the plane tilt. E) & F) reveal proximity to the island may be the cause of the apparent tilt. There is no significant plane error in y , and the measured tilt in $x \sim -0.05^\circ$.

5.3.1.1 Plane Analysis

The possible origin of the slope is a tilt in the sample relative to the piezo scanner coordinates. This was corroborated via examination of the plane error of the Δf signal from the respective highest (x, y) slice. For the slices data set: from the origin, the Δf signal changes magnitude by -0.18 Hz in x , and -0.44 Hz in y . A similar trend was observed for the grid spectroscopy data set: from the origin, the Δf signal changes by -0.17 Hz in x , and -0.64 Hz in y . Qualitatively, this is consistent with a plane measurement of the same region of substrate, using the topographic image depicted in Figure 5.9.C. The topographic data over the region of substrate adjacent to the mapped molecules, indicate a plane error, tilted downwards by $\sim 0.2^\circ$ across x , and $\sim 0.6^\circ$ across y . Figure 5.14.A & B) show the respective planes calculated using the top slice in (x, y) from each $\Delta f(x, y, z)$ grid. C) & D) depict the region and line profiles used to calculate the plane using the a topographic image. The similarity of long range Δf behaviour amongst each of the data sets indicates that there was a systematic error present during these experiments (rather than a fault of the drift correction procedure). It is difficult to calculate the physical plane error directly, with respect to z , (because the Δf signal cannot be assumed to change linearly with z). However, examination of the total overview area in Figure 5.14.E & F) revealed no significant tilt in the net plane, and the apparent tilt in C) & D) can likely be attributed to the interaction between the tip and the island.

While the resolution is such that the precise chemical structure and adsorption geometries of the C₆₀ molecules cannot be inferred from the $z^*(x, y)$ map, the fact that the same systematic error is observed across both methods, spanning 20+ hours of data acquisition, conveys the robust nature and reproducibility of both data acquisition methods using the drift correction procedure, even when they are applied to larger regions for mapping molecular networks. Figures 5.11 & 5.12 provide promising results that show the potential for similar methodologies applied to self-assemblies of more planar molecules, which would be more amenable to intramolecular force mapping.

5.4 Results: CoPc on B:Si(111)

Metal Phthalocyanines (MPc) are a well studied class of molecules, in part, due to their applications in industrial catalysis (50, 51), fabrication of organic thin film transistors (52, 53) and other novel functional materials (54, 55). Cobalt Phthalocyanine (CoPc) in particular, is used in the Merox process (removal of sulphur from petrol) (51). CoPc were used as a prototypical molecule for the experiments on the B:Si(111) surface (see Figure 5.6), because, unlike other Phthalocyanine (Cu, Zn) it has previously been shown to adsorb highly aligned to the B:Si(111) substrate, with benzene rings planar to the surface (13). This alignment is attributed to the strong overlap between the *d* orbital of the Co ion and the Si adatom dangling bond (32). Hence, unlike other Phthalocyanines (Cu, Zn), CoPc does not begin self-assembly into tilted networks (which would not be conducive to resolving the chemical structure) until a sufficient number of molecular layers are deposited on the B:Si(111) surface (56). Thus, a low coverage of CoPc on B:Si(111) would theoretically allow for fully mapping the chemical structure of multiple molecules in 3D at room temperature.

A low coverage (< 0.1 ML) of CoPc on B:Si(111) was achieved following a 30 second deposition at 380°C. As with previous surfaces prepared, the CoPc deposition was studied in STM prior to NC-AFM. Figures 5.15.A-C) show representative STM images of CoPc on B:Si(111). According to Wagner et al. (2015) (32), the CoPc molecule pins to the dangling bond sites of the substrate first. This is corroborated by overview image Figure 5.15.A, as the majority of dangling bond defects are not visible, indicating that a relatively small coverage of CoPc molecules covers them. The circular shape of some molecules suggests they may be rotating about these dangling bond sites. Other, more square shapes seen amongst A)-C), indicate a more static adsorption geometry. The coverage of CoPc was not high enough to see any island formation of molecules.

The bright centres of the molecules in Figure 5.15.B) & C) indicate the position of the central Co core of the molecule. In Figure 5.15.C, two flat lying molecules are imaged, with their four benzene rings also resolved. The flat molecules exhibit three stable orientations, in accordance with the symmetry of the $\sqrt{3} \times \sqrt{3}$)R30° surface, indicated by the white lines in C).

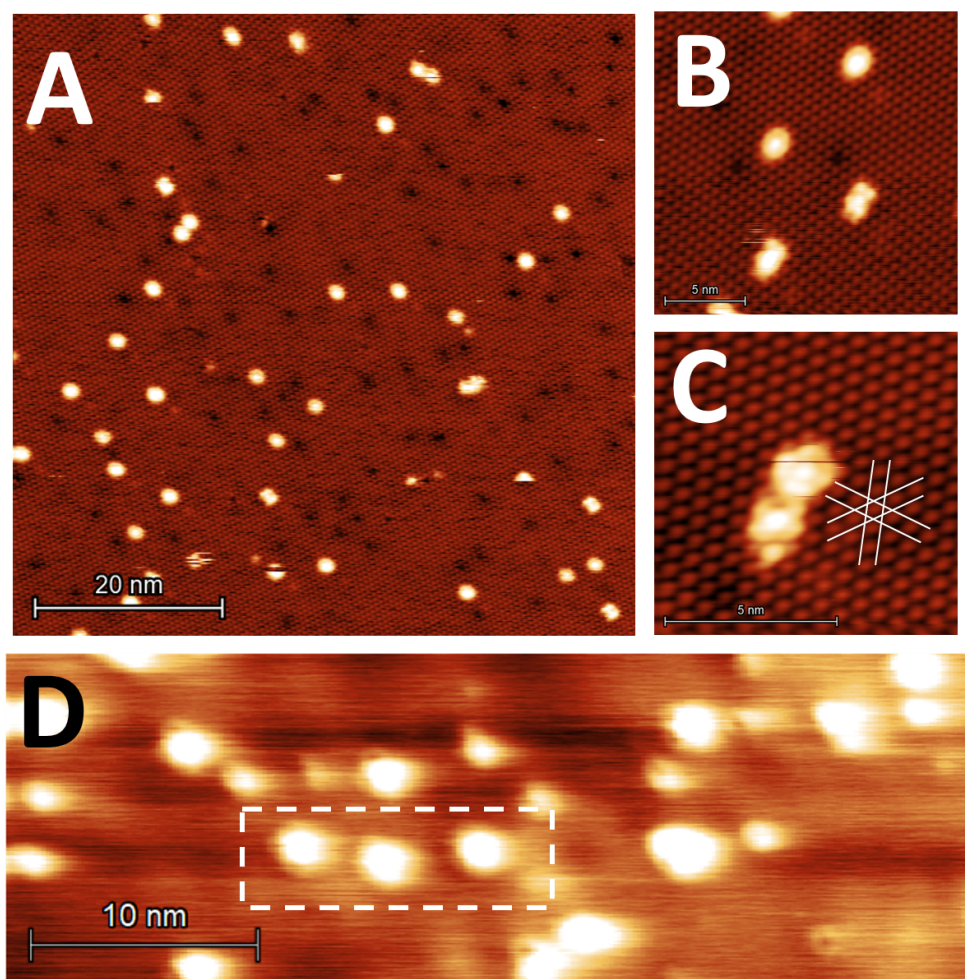


Figure 5.15: STM & NC-AFM overview of CoPc molecules on B:Si(111). Image parameters: A)-C) $V_{gap} = +2 V$, set point = $20 pA$. D) $V_{gap} = +0.4 V$, $A_0 = 20 nm$, set point $\Delta f = -0.8 Hz$.

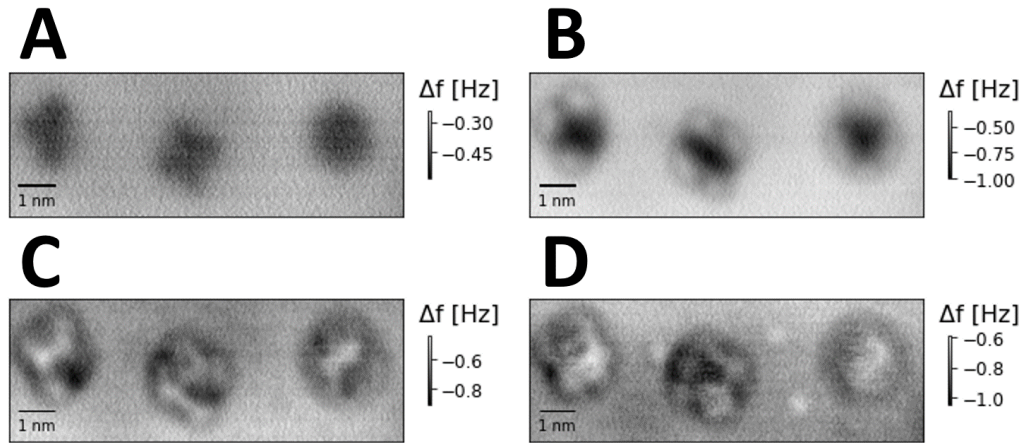


Figure 5.16: Constant height NC-AFM images of CoPc on B:Si(111) acquired at room temperature. Image parameters: $V_{gap} = +0.4$ V, $A_0 = 20$ nm, tracking set point $\Delta f = -1.4$ Hz. Heights relative to tracking position: A) +500 pm, B) +320 pm, C) +220 pm, D) +120 pm.

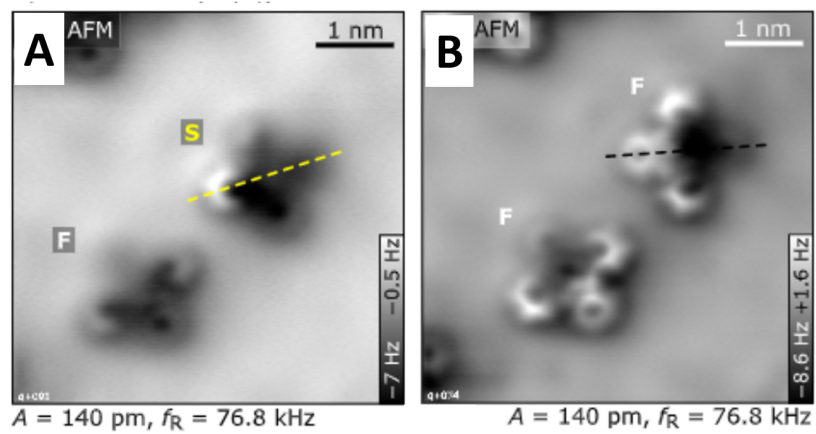


Figure 5.17: Constant height NC-AFM of CoPc on $\text{In}_2\text{O}_3(111)$. Images acquired at low temperature (4.8 K), using a qPlus sensor prepared on the $\text{In}_2\text{O}_3(111)$ surface, $A_0 = 140$ pm, $V_{gap} = 1$ V. Figure from Wagner et al. (2022) (49).

D) depicts a constant Δf image taken in NC-AFM of the CoPc on B:Si(111) surface. The three molecules in the region indicated by the white dotted line were imaged in constant height. Representative images, showing the evolution of the contrast with tip-sample distance are shown in Figure 5.16.

In this thesis, the middle molecule of the three in Figure 5.16, most closely resembles the expected geometry, observed in previous, low temperature experiments. Images from Wagner et al. (2022) (49), depict two CoPc molecules adsorbed on the $\text{In}_2\text{O}_3(111)$ surface, scanned in constant height at 4.8 K using a aPlus sensor prepared on the substrate. These are shown in Figure 5.17, wherein most of the chemical structure is clearly resolved. For both of the molecules shown in Figure 5.17, the Δf signal over one of the four benzene rings is comparatively less intense, indicating those corners of the molecules are tilted down toward the surface relative to the rest of the molecule. This can be seen in Figure 5.16, for the leftmost CoPc molecule. In subplots B) & C), the lower right 'leg' of the molecule appears to be bent downwards to the surface. This is unlikely to be the result of a tip asymmetry, as this feature is not shared with the other molecules in Figure 5.16.

5.4.1 3D $\Delta f(x, y, z)$ Mapping of CoPc on B:Si(111)

With a different tip apex, a Δf map was carried out over a single CoPc molecule via the slices method and plotted in Figure 5.18. The constant height images did not reveal the clear, internal chemical structure as the results on NTCDI on Si(111)-(7 \times 7) in Chapter 4 did. Below a certain tip-sample distance (approximately -0.3 nm) the contrast evolves in an unusual way, and becomes a more complex convolution of the tip shape and molecule. The Δf contrast in images 3) & 4) shows an apparent tilt in the molecule, indicating the lower left side of the molecule is tilted further up than the upper right side of the molecule. A comparison of the images at close tip-sample distance from Figure 5.18, to example constant height scans of FePc molecules on a Ag(111) surface at 5 K using a tip of unknown (possible molecular) termination, seen in Figure 5.20, reveals that similar initial contrast is observed for both data sets. The characteristic attractive

5 Force Mapping of Molecular Networks on B:Si(111) – $(\sqrt{3} \times \sqrt{3})R30^\circ$

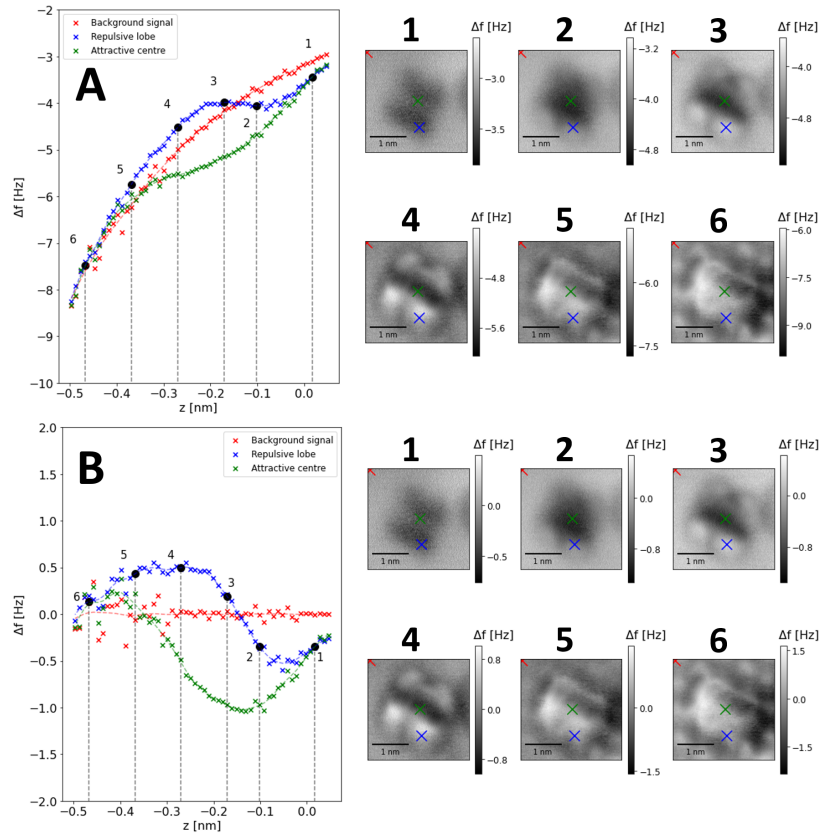


Figure 5.18: 3D Δf map over single CoPc on B:Si(111) taken via the slices method in NC-AFM. A) Single point $\Delta f(z)$ data, extracted from averages of 10×10 pixel area (equating to 100 pm^2). Images 1)-6) depict the contrast evolution of the molecule across tip-sample distance. Image parameters: $V_{gap} = 0.4 \text{ V}$, $A_0 = 20 \text{ nm}$ tracking set point = $\Delta f = -3.5 \text{ Hz}$, $t_{acq} = 111 \text{ s}$, total $t_{acq} \sim 8 \text{ hours}$. Each scan was repeated 3 times and an average was calculated to improve the S/N. B) As for A), but data shows single point curves of background subtracted $\Delta f(z)$ data. The data red curve in A) is taken to be the background signal.

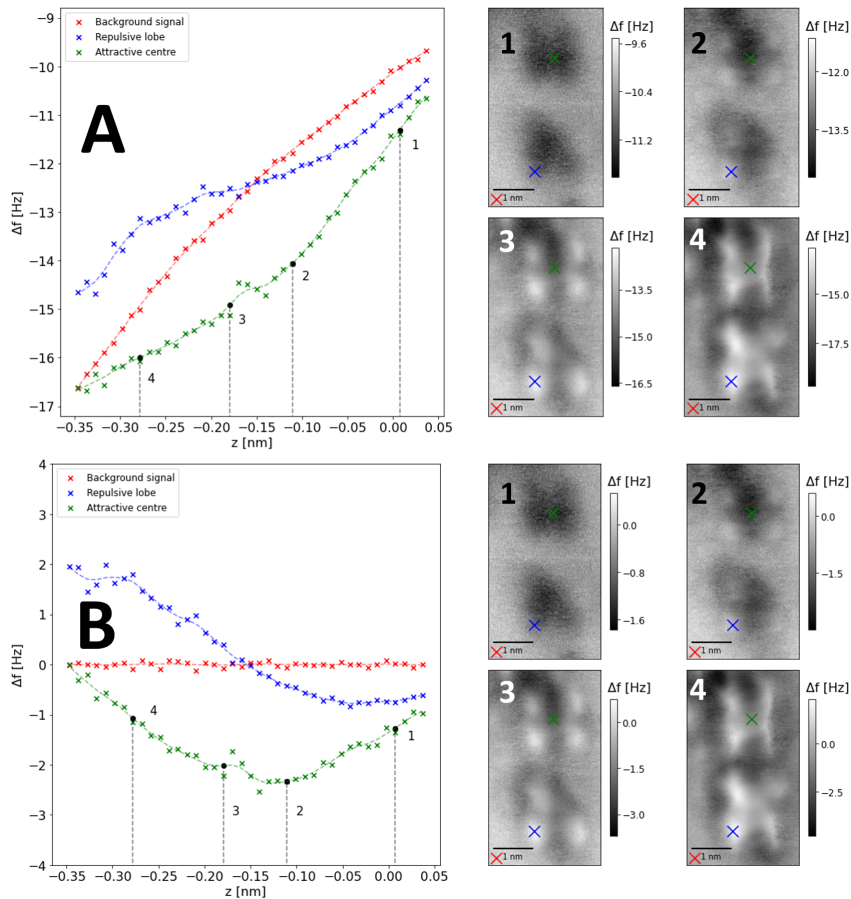


Figure 5.19: 3D Δf map over a pair of CoPc on B:Si(111) taken via the slices method in NC-AFM. A) Single point $\Delta f(z)$ data, extracted from averages of 10×10 pixels (equating to 120 pm^2). Images 1)-4) depict the contrast evolution of the molecules across the tip-sample distance. Image parameters: $V_{gap} = 0.4 \text{ V}$, $A_0 = 20 \text{ nm}$ tracking set point $\Delta f = -11 \text{ Hz}$, $t_{acq} = 108 \text{ s}$, total $t_{acq} \sim 8 \text{ hours}$. Each scan was repeated 3 times and an average was calculated to improve the S/N. B) As for A), but data shows single point curves of background subtracted $\Delta f(z)$ data. The data red curve in A) is taken to be the background signal.

centre and repulsive lobes at the four corners of the molecule are common across both data sets. Similarly, for both Figures 5.18 & 5.20, there are tip relaxations at close tip-sample distances that convolute the image signal. This is exemplified in the blue short range $\Delta f(z)$ curve in Figure 5.18.B, which has an initial turn at $z \sim -0.05 \text{ nm}$, followed by an increase in Δf . At $z \sim -0.25 \text{ nm}$, it begins to turn back downward, decreasing in Δf signal again. The most likely explanation for this is that the tip is compressing or deflecting as it approaches the molecule. The highly stable levels of drift during the course of this experiment, owing to the optimised correction procedure, are plotted in Figure 3.5.D as a further example of the improved results.

The 3D $\Delta f(x, y, z)$ mapping was repeated over a pair of CoPc molecules and plotted in Figure 5.19 with both raw Δf and short range Δf . As with Figure 5.18, the constant height images did not resolve the internal chemical structure of the CoPc. Likewise, the molecules appear distorted at close tip-sample distances (see image 4)). This can be seen again in the blue curve in B), in which the $\Delta f(z)$ signal starts to turn more negative at the point of closest approach. Similar to the CoPc seen in Figure 5.17, the contrast over one of the corners or, 'legs', of the lower molecule (upper right) indicates it is closer toward the surface.

The adsorption geometries of the molecules across Figures 5.18 & 5.19, and the tilts of their respective corners, were further investigated.

5.4.2 Conformation of CoPc Molecules on B:Si(111)

From the short range $\Delta f(x, y, z)$ map seen in Figure 5.18, the $z^*(x, y)$ map was extracted and plotted in Figure 5.22 (left). Given the complex $\Delta f(z)$ behaviour at closer tip-sample distances, the data were processed to ensure that for each point in (x, y) , only the position of the first $\Delta f(z)$ turnaround is extracted and plotted. Points in (x, y) that do not have a $\Delta f(z)$ turnaround were also screened from the $z^*(x, y)$ map. The $z^*(x, y)$ map reveals that two legs of the CoPc toward the lower left side, protrude further up above the surface than the other two legs, i.e. there is an apparent tilt to the molecule.

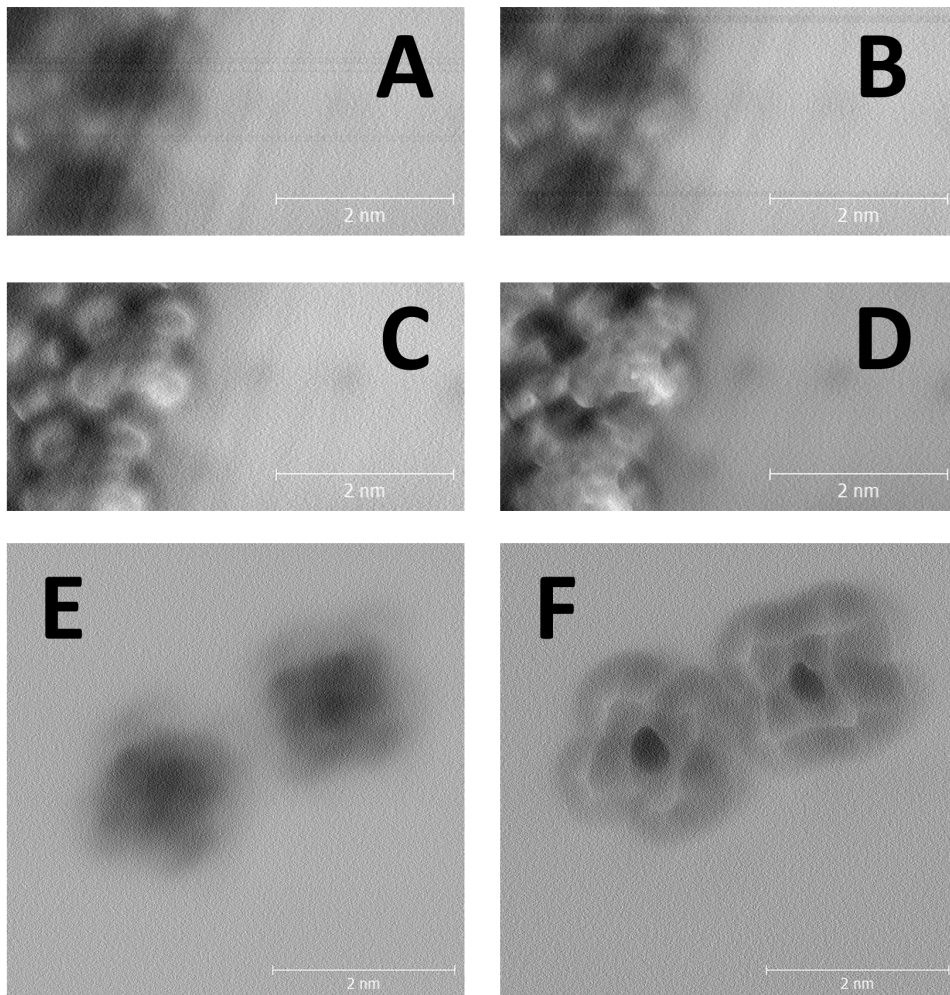


Figure 5.20: Example constant height images in NC-AFM of FePc on Ag(111) at 5 K using qPlus sensor. Figure printed with permission from Sweetman (2015) (unpublished). A)-D) Constant height images, of progressively smaller tip-sample distance, of island of FePc molecules. E) & F) Two constant height images of isolated FePc molecule, showing the attractive contrast over the metal core.

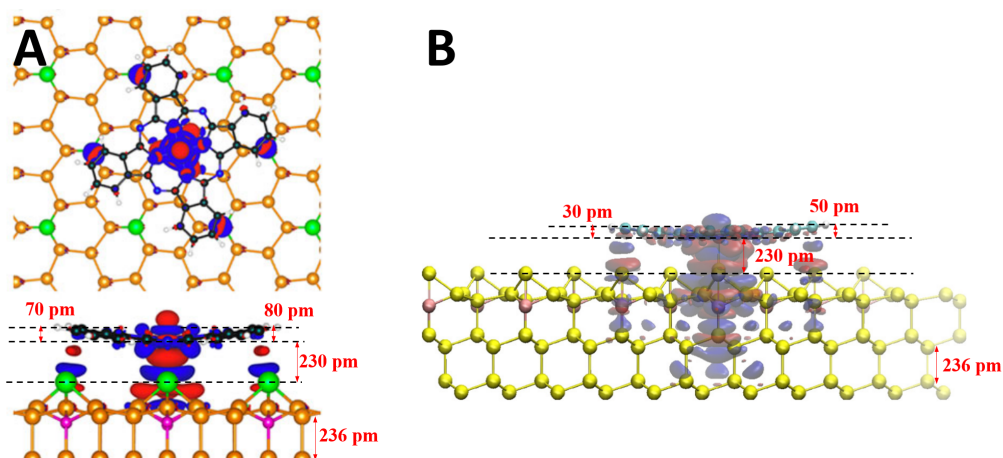


Figure 5.21: DFT calculated structures and charge distributions of Cobalt Phthalocyanine on B:Si(111). A) Top down and side views presented by Wagner et al. (2015) (32). Red regions indicate electron accumulation, blue regions indicate electron depletion. The green balls represent silicon adatoms, and pink balls boron substitutions. B) Side view presented by Veiga et al. (2016) (57). Blue regions indicate electron accumulation, red regions indicate electron depletion. Estimations of molecular tilt were made graphically using the Si bond length (236 pm) as scale.

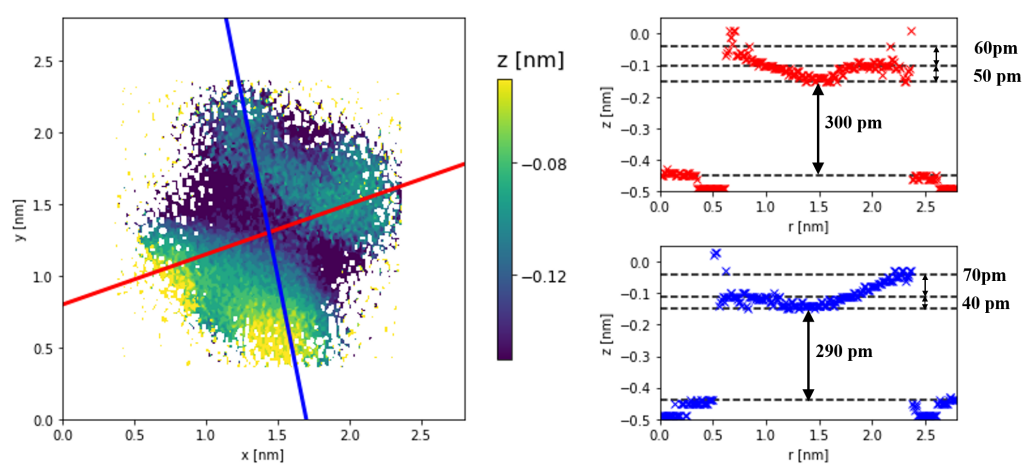


Figure 5.22: (Left) Processed $z^*(x, y)$ map of single CoPc plotted using data from Figure 5.18. (Right) Diagonal line profiles across the molecules are plotted for estimation of the molecular distortion. The black dotted lines indicate the relative height of the molecular legs, Co core, and approximate point of $\Delta f(z)$ turn around of the Si adatoms.

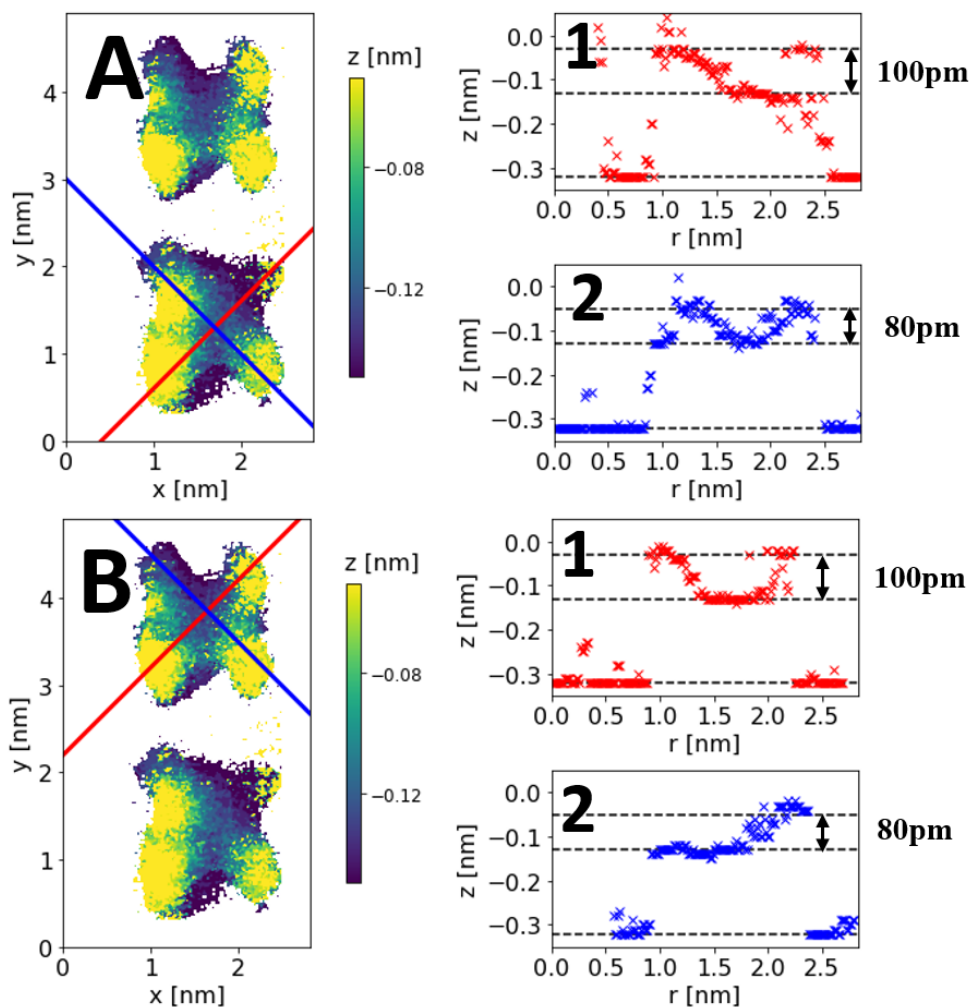


Figure 5.23: (Left) Processed $z^*(x, y)$ map of pair of CoPc molecules on B:Si(111) plotted using data from Figure 5.19. (Right) Diagonal line profiles across the molecules are plotted for estimation of the molecular distortion. The black dotted lines indicate the relative height of the molecular legs and Co core. For this data set there was no turnaround observed over the substrate.

The tilts of each leg were calculated by extracting the line profiles through the $z^*(x, y)$ data (right).

From the $z^*(x, y)$ map it was found that the lower left legs of the molecule tilt up above the Co core by approximately 110 pm. Conversely, the other two legs tilt up less so, by $\sim 40 - 50$ pm, which is consistent with the trend observed in the Δf signal of the constant height images (see Figure 5.18). Figure 5.21 depicts the results of DFT calculations carried out by Wagner et al. (2015) & Veiga et al. (2016) (32, 57), for a CoPc molecule adsorbed on the B:Si(111) surface. Using Figure 5.21, estimations were made (graphically) for the heights of the legs of the molecule relative to the Co core. These estimations (A) $\sim 70 - 80$ pm, B) $\sim 30 - 50$ pm) are of the same order as those determined from Figure 5.22. The level of tilt / buckling estimated from the experimental $z^*(x, y)$ map ($\sim 40 - 110$ pm), is slightly larger than for the previous DFT results ($\sim 30 - 80$ pm). This trend is mirrored in Schuler et al. (2013) (58), whereby the experimentally determined buckling of a pentacene molecule on a Cu(111) surface are similarly exaggerated approximately 25 % compared to DFT results.

Using the position of the Δf turnaround over the substrate atoms in the Δf map (which can be observed in image 6) in Figure 5.18), an estimate can be made for the adsorption height of the molecule as ~ 290 pm. This is slightly larger than the DFT results depicted in Figure 5.21 (~ 230 pm), and other DFT results for CoPc adsorbed on Cu(111) (~ 250 pm) (59). The apparent height differences determined from the topographic STM image shown in Figure 5.15.B is also closer to the DFT, with molecules having an apparent height of 200 – 250 pm above the substrate. However with STM, the apparent height of signal arises from the LDOS of the sample, not the true topography of the molecule. Consequently, height differences measured in STM can only serve as an approximation of the true topography. Nevertheless, the methodology applied is capable of elucidating the conformation of the CoPc using 3D $\Delta f(x, y, z)$ maps, despite room temperature conditions.

Similarly, the $z^*(x, y)$ map was extracted from the short range $\Delta f(x, y, z)$ map in Figure 5.19, and plotted in Figure 5.23. The processing of these data followed the same analysis and filtration process for Figure 5.22. The $z^*(x, y)$ map of the short range Δf minima is plotted in Figure 5.23. Diagonal line profiles for each molecule are plotted (A) & B) and show the relative

buckling of the molecules. For each molecule A) & B) there is a corner / leg that appears to be pulled down toward the surface. This is unlikely to be an artefact of tip asymmetry as these particular legs are in different relative positions on the two molecules. For the lower molecule, this relative buckling was also present in the Δf signal in Figure 5.19 (as for the constant height images seen in Figure 5.17 also), whereas the upper molecule appears flat in the constant height images, and the buckling is only observed following extraction of the $z^*(x,y)$. Where the molecular legs tilt up, they do so approximately 80 – 100 pm above the Co core. These values are similar to that of Figure 5.22, and are of the same order as the level of tilt inferred from the DFT results in Figure 5.21. In the other cases, the molecule legs (the top left leg of the upper molecule, and the top right molecule of the lower molecule) remain approximately at the same level as the core. As there was not a convincing $\Delta f(z)$ turnaround observed over the Si adatoms, an estimate for the adsorption height of the molecule cannot be made, beyond stating that it is likely to be > 200 pm (the distance from the Δf turnaround at the core to the point of closest approach).

5.5 Conclusion

NTCDI deposition on B:Si(111) did not succeed in producing ordered networks, likely owing to the high reactivity of the carobyl group with the Si adatoms. As such, submolecular resolution force maps could not be acquired on NTCDI island. It may be possible to create the necessary conditions for room temperature force mapping of NTCDI (or other oxygen containing molecules) by instead growing molecular islands on the Ag:Si(111) surface (12, 60). This would require a Ag deposition source, which was a technical limitation of the VT-STM/AFM at the time of this thesis.

The experiments covered in this chapter on C_{60} and CoPc affirm the stability and reliability of the LabVIEW tracking procedure for lengthy data acquisition in NC-AFM. Figure 5.10 demonstrates that this procedure can also be applied, in a piecemeal method, to create $\Delta f F(z)$ maps over areas larger than the limiting confines of the scan area. The experimental protocol used to gather data presented in Figures 5.11 & 5.12 shows that, save for some

minor differences in the calculated force minima, both the slices and grid spectroscopy methods yield equivalent data as expected. Hence the user is free to choose the method that is best suited to the aims of the experiment and the practical considerations involved.

While the experiments on the CoPc molecules in NC-AFM did not achieve the same level of resolution observed in either low temperature experiments (49, 59) nor that of single NTCDI molecules in Chapter 4 (which resolved intramolecular features ~ 50 pm), information concerning the adsorption geometry of the molecules can still be determined in room temperature conditions. The reason for poorer intramolecular contrast across the CoPc experiments likely arose from the tip state. However, it should be possible for future studies in room temperature, to pair the tip state observed over the middle molecule in Figure 5.16, with the long term stability exemplified in the subsequent Δf mapping experiments Figures 5.18 & 5.19.

References

1. A. Ulman, *Chemical Reviews* **96**, 1533–1554 (1996).
2. N. Seeman, A. Belcher, *Proc. Natl. Acad. USA*, 6451–6455 (2002).
3. S.-S. Li *et al.*, *Journal of the American Chemical Society* **129**, 9268–9269 (2007).
4. K. D. Hammonds, V. Heine, M. T. Dove, *The Journal of Physical Chemistry B* **102**, 1759–1767 (1998).
5. M. Davis, *Nature* **417**, 813–821 (2002).
6. F. Silly, *The Journal of Physical Chemistry C* **117**, 20244–20249 (2013).
7. S. M. Kuznicki *et al.*, *Nature* **412**, 720–724 (2001).
8. T. N. Hoheisel, K. Hur, U. B. Wiesner, *Progress in Polymer Science* **40**, Progress in Polymer Hybrid Materials, 3–32, ISSN: 0079-6700 (2015).
9. L. Wang, Y. Sun, Z. Li, A. Wu, G. Wei, *Materials* **9** (2016).
10. G. de la Torre, C. Claessens, T. Torres, *Chemical Communications* **20**, 2000–2015 (2006).

11. R. Otero, J. M. Gallego, A. L. V. de Parga, N. Martín, R. Miranda, *Advanced Materials* **23**, 5148–5176 (2011).
12. A. M. Sweetman *et al.*, *Nature Communications* **5** (2014).
13. Y. Makoudi *et al.*, *Surface Science Reports* **72**, 316–349 (Sept. 2017).
14. Y. Kikkawa, M. Nagasaki, E. Koyama, S. Tsuzuki, K. Hiratani, *Chem. Commun.* **55**, 3955–3958 (2019).
15. D. Peyrot, F. Silly, *ACS Nano* **10**, 5490–5498 (2016).
16. T. Yokoyama, S. Yokoyama, T. Kamikado, Y. Okuno, S. Mashiko, *Nature* **413**, 691–621 (2001).
17. J. A. Theobald, N. S. Oxtoby, M. A. Phillips, N. R. Champness, P. H. Beton, *Nature* **424**, 1029–1031 (2003).
18. J. Zhang *et al.*, *Science* **342**, 611–614 (2013).
19. N. Turek *et al.*, presented at the Journées du GdR Nanosciences en champ proche sous ultra-vide 2021, oral.
20. C. Loppacher *et al.*, *Applied Surface Science* **140**, 287–292, ISSN: 0169-4332 (1999).
21. S. Orisaka, T. Minobe, T. Uchihashi, Y. Sugawara, S. Morita, *Applied Surface Science* **140**, 243–246 (1999).
22. L. Gross, F. Mohn, N. Moll, P. Liljeroth, G. Meyer, *Science* **325**, 1110–1114 (2009).
23. H. Monig, S. Amirjalayer, A. Timmer, *Nature Nanotech*, 371 (2018).
24. K. Iwata *et al.*, *Nature Communications* **6**, 7766 (2015).
25. T. Brown, P. J. Blowey, J. Henry, A. Sweetman, *ACS Nano* **17**, 1298–1304 (2023).
26. D. L. Keeling *et al.*, *Nano Letters* **3**, 9–12 (2003).
27. L. M. A. Perdigão *et al.*, *Phys. Rev. B* **76**, 245402 (2007).
28. P. Baumgärtel *et al.*, *Phys. Rev. B* **59**, 13014–13019 (1999).
29. P. Bedrossian *et al.*, *Phys. Rev. Lett.* **63**, 1257–1260 (1989).
30. J. T. Y. Jr, *Journal of Physics: Condensed Matter* **3**, S143 (1991).

31. J. Ricart, J. Rubio, F. Illas, *Phys. Rev. B Condens. Matter* **42**, 5212–5220 (1990).
32. S. R. Wagner *et al.*, *Physical Review Letters* **115** (Aug. 2015).
33. I. W. Lyo, E. Kaxiras, P. Avouris, *Physical Review Letters* **63**, 1261–1264 (1989).
34. W. R. Thurber, R. L. Mattis, Y. M. Liu, J. J. Filliben, *Journal of The Electrochemical Society* **127**, 2291 (1980).
35. B. Baris *et al.*, *ACS Nano* **6**, 6905–6911 (2012).
36. D. Eom, C.-Y. Moon, J.-Y. Koo, *Nano Letters* **15**, 398–402 (2015).
37. G. Copie *et al.*, *The Journal of Physical Chemistry C* **118**, 12817–12825 (2014).
38. D. Marchese, MA thesis, Lakehead University, 2020.
39. E. J. Spadafora *et al.*, *The Journal of Physical Chemistry C* **118**, 15744–15753 (2014).
40. S. P. Jarvis *et al.*, *Journal of Physics Condensed Matter* **27** (2015).
41. P. Ballirano, R. Caminiti, C. Ercolani, A. Maras, M. A. Orrù, *Journal of the American Chemical Society* **120**, 12798–12807 (1998).
42. L. Grill *et al.*, *Nat. Nanotechnol* **2**, 687–691 (2007).
43. T. Stimpel, M. Schraufstetter, H. Baumgartner, I. Eisele, *Materials Science and Engineering* **89**, 394–398 (2002).
44. A. Tan, S. R. Wagner, P. P. Zhang, *Physical Review B* **96** (July 2017).
45. G. Zhan *et al.*, *Journal of Physical Chemistry C* **121**, 8427–8434 (Apr. 2017).
46. P. J. Moriarty, *Surface Science Reports* **65**, 175–227 (July 2010).
47. A. Sweetman *et al.*, *Nature Communications* **7**, 10621 (2016).
48. A. Sweetman, J. Stirling, S. P. Jarvis, P. Rahe, P. Moriarty, *Phys. Rev. B* **94**, 115440 (2016).
49. M. Wagner *et al.*, *Surface Science* **722**, 122065, ISSN: 0039-6028 (2022).
50. A. B. Sorokin, *Chemical Reviews* **113**, 8152–8191 (2013).

51. B. Basu, S. Satapathy, A. K. Bhatnagar, *Catalysis Reviews* **35**, 571–609 (1993).
52. O. A. Melville, B. H. Lessard, T. P. Bender, *ACS Applied Materials & Interfaces* **7**, 13105–13118 (2015).
53. W. Zhou, N. J. Yutronkie, B. H. L. logoa, J. L. Brusso, *Materials Advances* **2**, 165–185 (2021).
54. S. Y. Flores *et al.*, *ACS Applied Nano Materials* **5**, 4688–4699 (2022).
55. Z. J. Comeau, N. A. Rice, C. S. Harris, A. J. Shuhendler, B. H. Lessard, *Advanced Functional Materials* **32**, 2107138 (2021).
56. S. Lindner *et al.*, *Phys. Rev. B* **100**, 245301 (2019).
57. R. G. A. Veiga, R. H. Miwa, A. B. McLean, *Phys. Rev. B* **93**, 115301 (2016).
58. L. Gross *et al.*, *Physical Review Letter* **111**, 106103 (2013).
59. P. Chen *et al.*, *Nat. Commun.* **14** (2023).
60. S. Menzli *et al.*, *Applied Surface Science* **369**, 43–49, ISSN: 0169-4332 (2016).

Conclusion

The robust and versatile procedure for drift correction described in Chapter 3, was refined, from rough versions, into a better optimised process, over the course of the Ph.D. project, whilst re-creating key results throughout the literature. The LabVIEW program used for the scripting was also made increasingly generalised, to allow for a variety of data set types (easily configurable number of dimensions, directions, changes to bias etc.), and was made more user-friendly.

These scripts, in tandem with properly regulated temperature ($\pm 2 \text{ mK}$), had the result of massively stabilising the tip-sample system despite operating at room temperature. The final program was able to achieve long term data acquisition (on the order of days), with residual values of thermal drift across x, y and z of the order of $1 \text{ pm}/\text{min}$. While sub-optimal temperature regulation could be observed carrying its oscillatory nature to the thermal drift, the program was still nevertheless able to suppress the displacement due to thermal drift to less than that of both our lateral resolution ($< \Delta g \sim 50 \text{ pm}^2$) and vertical resolution ($< 10 \text{ pm}$).

This thesis reports the development and optimisation of a scripted drift correction procedure (in LabVIEW) for a VT-STM/AFM, allowing for acquisition of 3D force maps with residual drifts on the order of $\sim 1 \text{ pm}$. In Chapter 4, this procedure (alongside other techniques) afforded the necessary stability for high resolution force mapping for the first time, in both 2D & 3D, of a single NTCDI molecule in room temperature conditions. The reproducibility of the technique not only allowed for the assessment for the variety in geometries present, both of the particular molecular adsorption on the (7×7) surface, but also of the effects of the tip shape / asymmetries on the Δf , F and z^* data. The force sensitivity achieved ($\sim 10 \text{ pN}$) was comparable to both DFT studies and those acquired at low temperature.

Thus, the experimental method permitted a quantitative analysis of the adsorption induced changes in the geometry of the molecule at the picometer level. The results of Chapter 4 suggest the possibility of performing similar measurements under conditions closer to real-world applications.

Future work in this vein could aim to recreate these force maps over single molecules in addition to a more rigorous characterisation or chemical fingerprinting of the tip, in order to gain a better understanding of the tip-sample interaction, and how it governs the observed contrast. This would also give insights into the lateral stiffness of the tip and the origin of the apparent bond exaggerations due to deflection. While data to characterise the tip was attempted, there were practical difficulties in carrying out the 'on minus off' method of force spectroscopy over a substrate of typically uniform contrast, and which would frequently inadvertently change the tip in the process. However, the contrast shown in Figure 4.4.B wherein the intermolecular bonds and substrates are resolved simultaneously, would suggest that force spectroscopy over the molecule, the adatoms, and the corner hole would be feasible. Alternatively, it could be possible to use the notable force sensitivity of Si cantilevers, in similar force mapping experiments, in order to chemically identify individual atoms within molecules.

In Chapter 5, efforts were turned to larger systems: assembled networks of organic molecules on a passivated semiconducting B:Si(111) surface. The objective, similar to that in the experiments of Chapter 4, was to demonstrate that force mapping, at room temperature, was feasible even when applied on the scale of larger surface structures. Characterisation of self-assembled molecular networks are of particular interest in the field of SPM, as they can serve as the basis of catalytic reactions.

While B:Si(111) is an established substrate surface in the field of studying self-assembly of molecules in SPM, attempts to create intermolecular-bonded networks of NTCDI failed. This is likely due to the strong interaction between the Si adatoms and the carbonyl groups of the molecule, despite the Boron dopants of the material saturating the dangling bonds of the Si adatoms. Following deposition, only disordered and dendritic islands of molecules were observed, as opposed to the hydrogen-bonded assembly of NTCDI reported on the Ag:Si(111) surface. It was not possible to create

the Ag:Si(111) surface, as the system used during the project lacked a Ag deposition source.

Despite the set back, Chapter 5 details the continued work carried out on B:Si(111). On an assembled island of C₆₀ molecules, the force mapping script, having been further optimised than for Chapter 4, was capable of imaging much larger areas in constant height (whilst keeping vertical resolution < 10 pm). In particular, it was shown that the force mapping procedure can be applied in piecemeal fashion, in order to cover these larger areas cumulatively (~ 100 nm²). The larger area Δf maps demonstrate the freedom granted to the room temperature experimentalist.

In the process, stable tracking was performed over the course of days, a longer duration than any previously reported experiments of this nature at room temperature. This was sufficient duration to acquire force maps over the same region of C₆₀ molecules, using both of the methods, constant height imaging and grid spectroscopy, in order to compile 3D data sets. These force maps exhibit marked similarity to each other, both qualitatively and quantitatively, and allow for a direct comparison between the methods. The analysis of both data sets, suggests that for most situations, constant height imaging is the more robust method for gathering 3D data in constant height, except perhaps in instances where, due to symmetries, most information can be attained with 2D cross-sections, in which case grid spectroscopy may be preferable.

Lastly, Chapter 5 presents NC-AFM data of CoPc molecules. While the resolution observed did not match that of the measurements on single NTCDI molecules, the measurements were still able to reveal the broad conformation of the molecule on the surface, wherein the relative heights of the Phthalocyanine 'legs' were extracted. The poorer contrast over the intramolecular features is likely due to the tip geometry. With the benefit of further study, it should be possible to repeat these experiments with a tip more conducive to resolving the finer structure of the CoPc.

The performance of the experimental scripting throughout Chapter 5 serves as a proof-of-concept for intramolecular force mapping of assembled networks of interest, in conditions closer to real-world application. Subsequent studies may use the Ag:Si(111) substrate in order to grow ordered networks

of NTCDI or other molecules featuring carbonyl or hydroxide groups, for study in room temperature NC-AFM.

The experimental results presented in this thesis open up the field of imaging and force mapping in NC-AFM to a wider array of experimentalists. This work asserts that the study of certain systems and samples using STM / NC-AFM need not be beholden to apparatus that enable cryogenic cooling. The writer feels this work is a key step made toward advancing also, what is potentially possible in ambient / liquid AFM systems.